Conductive Microneedle Patches: Developing New Approaches to Controlled Drug Delivery

Amy Devine

BSc

Faculty of Computing, Engineering and the Built Environment of Ulster University

Thesis submitted for the degree of

Doctor of Philosophy

March 2023

I confirm that the word count of this thesis is less than 100,000 words

Contents

List of Figures ix

List of Tables xviii

Acknowledgements xix

Copyright / Credit Notices xx

Abstract xxii

Abbreviations xxiii

Notes on Access to Contents xxv

Chapter 1 1

Overview 1

1.0 Introduction 2

1.1 Aims and Objectives 7

1.2 Thesis Overview 7

Chapter 2 10

Literature Review 10

Overview 10

2.0 Traditional Approaches to Drug Delivery 11

2.0.1 Oral 11

2.0.2 Injections 13

2.0.3 Sharps Waste 17

2.0.4 Compliance 17

2.1 Emerging Approaches 18

2.1.1 Implantable 18

2.1.2 Nanoparticles 21

2.2 Opportunities for Transdermal Drug Delivery 24

2.2.1 Physiology of the Skin 26

2.2.2 Commercial Transdermal Drug Delivery 26

2.3 Innovative Approaches to Transdermal Drug Delivery 29

2.3.1 Iontophoresis 29

2.3.2 Electroporation 31

2.3.3 Chemical Enhancement 32

2.3.4 Ultrasound 32

2.3.5 Thermal Ablation 34

2.4 Microneedles 35

2.4.1 Classification 36

2.4.1.1 Solid / Coated 36

2.4.1.2 Dissolvable 37

2.4.1.3 Hollow 39

2.4.1.4 Swellable 40

2.4.1.5 Conductive Microneedles 42

2.5 Conclusion 42

Chapter 3 44

Experimental Techniques and Methodology 44

Overview 44

3.0 Materials and Instrumentation 45

3.1 Electrochemical Instrumentation and Methods 47

3.2 Fundamental Electrochemistry 48

3.2.1 Underpinning Concepts 48

3.2.2 Electron Transfer Kinetics – Butler Volmer Equation 52

3.3 Mass Transport Mechanisms 57

3.3.1 Diffusion 58

3.3.2 Convection 59

3.3.3 Migration 59

3.4 Electrochemical Instrumentation 59

3.4.1 Working Electrode 60

3.4.2 Reference Electrode 61

3.4.3 Counter Electrode 62

3.5 Electrochemical Techniques 63

3.5.1 Potential Step Chronoamperometry 63

3.5.2 Cyclic Voltammetry 64

3.5.3 Square Wave Voltammetry 68

3.6 Surface Characterisation Methods 71

3.6.1 Raman spectroscopy 71

3.6.2 Scanning Electron Microscopy 73

3.6.3 Energy Dispersive X-ray Analysis 75

3.6.4 X-Ray Computed Tomography 76

3.7 Surface Modification Techniques 77

3.7.1 Electrochemical Anodisation 77

3.7.2 Laser Ablation 77

3.8 Assay Validation Methods 78

3.8.1 Ultraviolet-Visible Spectrophotometry 78

Chapter 4 80

Laser Ablation of Nanocomposite Microneedles for Enhanced Electrochemical Performance Combined with Dual-layer Microneedle Approach using Biocompatible and Dissolvable Array 80

Overview 80

4.0 Introduction 81

4.1 Experimental Details 83

4.1.1 Materials and Instrumentation 83

4.1.2 Preparation of Carbon Nanocomposite Microneedles 83

4.2 Results and Discussion 86

4.2.1 Preliminary Electrochemical Analysis 86

4.2.2 Raman Analysis of Surface Modification 88

4.2.3 Contact Angle Analysis 89

4.2.4 Influence of Laser Treatment on MN Structure and Performance 90

4.2.5 Design of a Multilayer MN Patch 93

4.2.6 Cellulose Acetate Phthalate MNs 96

4.2.7 Multilayer Assembly 97

4.2.8 Characterisation of Multilayer Assembly 98

4.3 Conclusions 100

Chapter 5 102

Nanocomposite Microneedles Based on Cellulose Acetate Phthalate and Carbon Nanoparticles Decorated with Laser Induced Graphene to Improve Electrochemical Performance 102

Overview 102

5.0 Introduction 104

5.1 Experimental Details 107

5.1.1 Materials and Instrumentation 107

5.1.2 Production of Laser Induced Graphene 107

5.1.3 Production of Carbon Composite Microneedles 108

5.2 Results and Discussion 108

5.2.1 Laser Scribing of Polyimide – A Preliminary Study 108

5.2.2 Influence of Laser Power on LIG Formations 110

5.2.3 Influence of Multiple Passes on LIG Formations 110

5.2.4 Cross Sectional Investigation of LIG Formations 112

5.2.5 Electrochemical Characterisation of LIG Substrates 112

5.2.6 Cellulose Acetate Phthalate Based MN 113

5.2.7 Layered LIG Approach 115

5.2.8 CAP-LIG Urate Acid Analysis 118

5.2.9 Biodegradability – Justification 121

5.2.10 Waste Impact Assessment 126

5.2.11 Biodegradability Preliminary Evaluation 129

5.3 Conclusions 131

Chapter 6 132

Electrochemically Initiated Release: Exploring New Modalities for Controlled Drug Release 132

Overview 132

6.0 Introduction 133

6.1 Experimental details 136

6.1.1 Materials and Instrumentation 136

6.1.2 Preparation of Naphthoquinone Derivatives 136

6.2 Results and Discussion 140

6.2.1 Release Mechanism 143

6.2.2 Microneedle Substrates 144

6.2.3 Potential Drug Candidates 146

6.3 Conclusions 149

Chapter 7 151

Activation of Carboxylic Groups *via* DMAP / DCC for Controlled Release of Ester Bound Drugs *via* Electrochemical Trigger 151

Overview 151

7.0 Introduction 152

7.1 Experimental Details 154

7.1.1 Materials and Instrumentation 154

7.2 Results and Discussion 155

7.2.1 Selection of Model Drug Targets 155

7.2.2 Oxidative Release of Drug Candidates 156

7.2.3 Ester Hydrolysis through Localised Changes in pH 162

7.2.4 Initial Electro-Hydrolysis of Drug Loaded LIG 163

7.2.5 Electrochemical Hydrolysis of Salicylic Acid Loaded LIG 163

7.2.6 Poly(Anthranilic Acid): Increasing Drug Loading 166

7.3 Conclusions 169

Chapter 8 170

Conclusions and Further Work 170

8.0 Conclusions 171

8.1 Further Work 174

References 176

List of Figures

Figure 1.0.1 Example of a microneedle array A) compared to a hypodermic needle B) electron micrograph of the array.

Figure 1.0.2 Illustration of how a microneedle array could ultimately be incorporated into a wearable smart watch capable of autonomously controlling the initiation and duration of drug release.

Figure 2.0.2.1 Needle insertion angles for intramuscular, subcutaneous, intravenous, and intradermal injections.

Figure 2.0.2.2 The number of drugs that can be delivered by intramuscular, subcutaneous, and intradermal or all types of needles using data from the British National Formulary (BNF).

Figure 2.0.2.3 The range of conditions where the therapeutics can be delivered by injections and the type of injection used.

Figure 2.1.1.1 Examples of commercially available implantable drug delivery systems.

Figure 2.1.2.1 Proposed schematic of the synthesis of the polypyrrole (PPy) particles. A) assembly of sodium dodecyl benzene sulfonate (SDBS) into micelles, B) preferential association of dexamethasone base (Dex) with the core and dexamethasone sodium phosphate (DexP) with the outer shell of the micelles, C) association of pyrrole with the outer shell of the micelles and D) chemically driven polymerisation of PPy over the micellar template.

Figure 2.2.2.1 General first-generation transdermal drug delivery patch assembly.

Figure 2.3.1.1 The mechanism used by iontophoresis to delivery drugs transdermally.

Figure 2.3.4.1 The mechanism used by ultrasound to delivery drugs transdermally.

Figure 2.3.5.1 The mechanism used by laser ablation to delivery drugs transdermally.

Figure 2.4.1 Different categories of microneedles, solid, coated, hollow, dissolving and hydrogel forming.

Figure 2.4.1.4.1 Schematic of polystyrene-block-poly(acrylic acid) swellable tip and a non-swellable polystyrene core as mechanical interlock in the skin.

Figure 3.0.1 Silicone mould and resultant microneedle array.

Figure 3.0.2 Typical dimensions of the A) microneedle patch and B) individual needles.

Figure 3.2.1.1 Typical electrode reaction and the sequence of steps involved.

Figure 3.2.1.2 Schematic highlighting the reduction and oxidation processes of a target analyte in solution. Where (A) represents a negative potential raises the Fermi level (*EF*) of the electrode and thereby the reduction of the analyte; (B) highlights the lowering of the *EF* of the electrode by a positive potential bias thereby inducing oxidation of the analyte.

Figure 3.2.2.1 Free energy (G) plot for the reduction of species $O_{(aq)}$ to product $R_{(aq)}$.

Figure 3.2.2.2 A) Influence of applied potential on the activation standard free energies for the reduction and oxidation reactions, B) is simply a magnification of the intersection region depicted in figure A.

Figure 3.3.1.1 Impact of diffusion on movement of analytes during electrochemical reaction.

Figure 3.3.3.1 Ionic behaviour when cathodic potential is applied.

Figure 3.4.1 Schematic of A) a generic potentiostat and B) a conventional three electrode cell.

Figure 3.4.2.1 Components of the commercial Ag/AgCl half cell reference electrode.

Figure 3.5.1.1 A) Single step amperomertic waveform. B) Generic amperometric response profile for an oxidation process.

Figure 3.5.2.1 Waveform for a conventional cyclic voltammogram where E1 is the start and end point and E2 is the switching potential.

Figure 3.5.2.2 Classic “duck” shaped cyclic voltammogram for a reversible electrode process.

Figure 3.5.2.3 Typical trace from reversible, quasi-reversible and irreversible systems.

Figure 3.5.3.1 Potential applied during square wave voltammetry in relation to time.

Figure 3.5.2.2 Resultant square wave voltammogram taking the switch in current direction.

Figure 3.6.1.1 Diagram of Raman scattering processes. The lowest energy state is denoted as m with energy levels increase upwards. Energy of incident radiation (upwards arrows) and energy of scattered radiation (downwards arrows) posses' larger energy than the vibrational states.

Figure 3.6.1.2 Difference in energy of incident radiation and scatter radiation for different Raman processes.

Figure 3.6.2.1 Scanning electron microscope configuration and electron path.

Figure 3.6.3.1 Electron transitions that can occur from bombardment from electrons.

Figure 4.0.1 Structure of cellulose acetate phthalate.

Figure 4.1.2.1 Schematic of conductive microneedle array dimensions produced using Micropoint Technologies Pte Ltd (Singapore) moulds.

Figure 4.1.2.2 Electron micrograph of A) polystyrene-carbon microneedle array, B) single needle from polystyrene-carbon microneedle 200(base) x 500(pitch) x 700(height).

Figure 4.1.2.3 Electron micrograph cross-section of polystyrene-carbon microneedle array.

Figure 4.2.1.1 Cyclic voltammograms of detailing the response of polystyrene-carbon microneedles to ferrocyanide (2mM,0.1 M KCl, 50mV/s) before and after electrochemical anodisation in NaOH (0.1 M, +2V, 60s).

Figure 4.2.1.2 Summary of the functional groups present on the surface of carbon nanoparticles within the polystyrene microneedle matrix.

Figure 4.2.2.1 Raman spectra of unmodified and anodised polystyrene-carbon microneedle.

Figure 4.2.3.1 Contact angle measurements of a polystyrene-carbon (Ps-C) microneedle A) before drop release, B) at the unmodified Ps-C MN and C) at the anodised Ps-C MN.

Figure 4.2.4.1 Electron micrograph of polystyrene-carbon microneedle array A) post laser ablation (power 25%, speed 30, PPI 1000), B) post laser ablation (power 25%, speed 30, PPI 1000), C) post laser ablation (power 50%, speed 30, PPI 1000)

and D) Oxygen percentage of polystyrene-carbon microneedle array as a consequence of laser ablation at increasing powers obtained from energy dispersive X-ray analysis.

Figure 4.2.4.2 Cyclic voltammogram of A) modified polystyrene-carbon microneedle to ferrocyanide (2mM,0.1 M KCl, 50mV/s) following laser ablation of varying power (Raster mode, speed 30, PPI 1000), B) unmodified polystyrene-carbon microneedle to ferrocyanide (2mM,0.1 M KCl, 50mV/s) versus anodised in NaOH (0.1 M, +2V, 60s) and laser ablated (Power 50 %, raster mode, speed 30, PPI 1000).

Figure 4.2.5.1 Schematic of multilayer microneedle patch with biocompatible layer to pierce the skin and laser processed layer for sensing or controlled drug delivery.

Figure 4.2.6.1 Electron micrograph of cellulose acetate phthalate microneedle 200(base) x 500(pitch) x 700(height).

Figure 4.2.6.2 Electron micrograph of cellulose acetate phthalate microneedle submerged in pH 7 buffer for A) 5 minutes, B) 10 minutes, C) 30 minutes, D) 30 minutes displaying fractures in baseplate, E) 30 minutes displaying ambiguous/smooth needle and F) 30 minutes displaying fracture on baseplate.

Figure 4.2.7.1 Sliced X-ray image of cellulose acetate phthalate microneedle layered on top of laser modified polystyrene-carbon microneedle.

Figure 4.2.8.1 Electron micrographs of dual layer microneedle after 30 minutes in Britton Robinson pH 7 buffer showing A) the flexibility of the CAP MN bending, B) the alignment of the CAP and underlaying modified Ps-C MN, C) the large cavity in the CAP MN exposing the underlaying sensing MN and D) the intact laser modified Ps-C MN.

Figure 4.2.8.2 Cyclic voltammogram of cellulose acetate phthalate layered laser modified polystyrene-carbon microneedle to ferrocyanide (2mM,0.1 M KCl, 50mV/s) with

increasing time in pH7 (Black 0 minutes, red 1 minute, green 15 minutes and blue 30 minutes).

Figure 5.0.1 Structure of polyimide.

Figure 5.1.2.1 Schematic of planar LIG electrode.

Figure 5.2.1.1 Electron micrograph of polyimide film with laser induced graphene (LIG) tracks.

Figure 5.2.1.2 Cyclic voltammogram of laser induced graphene electrode to ferrocyanide (2 mM,0.1 M KCl, 50mV/s). Inset: LIG electrode configuration.

Figure 5.2.2.1 Electron micrograph of laser induced graphene A) power 25 %, B) power 30 %, C) power 35 % and D) power 50 %.

Figure 5.2.3.1 Electron micrograph of laser ablated polyimide after A) 1 pass, B) 2 passes, C) 3 passes and D) 4 passes (PPI 1000, speed 40 and power 30 %).

Figure 5.2.4.1 Electron micrograph of laser induced graphene electrode after stripping with carbon tape (PPI 1000, speed 40 and power 30 %).

Figure 5.2.5.1 Cyclic voltammogram of laser induced graphene electrode to ferrocyanide (2mM,0.1 M KCl, 50 mV/s) at varying powers, 30 % (Black), 40 % (Red) and 50 % (Blue).

Figure 5.2.6.1 Electron micrograph of cellulose acetate phthalate carbon microneedle (CAP-C MN).

Figure 5.2.6.2 Cyclic voltammograms of A) CAP-C MN and Ps-C MN and B) CAP-C MN loaded with LIG response to towards ferrocyanide (2 mM, 0.1 M KCl).

Figure 5.2.6.3 Raman spectra of CAP-C LIG MN and planar LIG electrode.

Figure 5.2.7.1 A) Schematic of CAP-C-LIG MN fabrication process and B) cyclic voltammograms of CAP-C-LIG MN response to towards ferrocyanide (2 mM, 0.1 M KCl, 50 mV/s).

Figure 5.2.7.2 Electron micrograph of layered CAP-C-LIG MN after NaOH rinse.

Figure 5.2.7.3 Cyclic voltammograms comparing the response of unmodified CAP-C MN versus NaOH rinsed CAP-C MN to towards ferrocyanide (2 mM, 0.1 M KCl, 50 mV/s).

Figure 5.2.8.1 Breakdown pathway of uric acid resulting from oxidation at the electrode.

Figure 5.2.8.2 Square wave voltammogram detailing the response of modified and unmodified polystyrene-carbon microneedle towards uric acid in pH 6 buffer.

Figure 5.2.8.3 Square wave voltammogram detailing the response of CAP-C MN after dipping in NaOH towards uric acid in pH 6 buffer after repetitive cycling.

Figure 5.2.8.4 Square wave voltammogram detailing the response of CAP-C LIG MN after dipping in NaOH towards uric acid in pH 6 buffer after repetitive cycling.

Figure 5.2.9.1 Cyclic voltammograms detailing the response towards ferrocyanide (2 mM, 0.1 M KCl, 50 mV/s) at A) a carbon screen printed electrode and B) a polystyrene-carbon microneedle (Ps-C MN). The responses before and after anodisation in 0.1M NaOH are compared in each case.

Figure 5.2.9.2 Electron micrographs of the CAP-C MN after exposure to pH 8 BR buffers for A) 1 min and B) 30 min. C) Voltammetric responses of the CAP-C MN to ferrocyanide (2 mM, 0.1 M KCl, 50 mV/s) pre and post treatment with NaOH (0.1 M,10 s).

Figure 5.2.9.3 A) Cyclic voltammetric response of a CAP-C MN array to ferrocyanide (2 mM, pH 7 BR buffer, 50 mV/s) over a period of 40 minutes. B) Quantitative analysis of the changes in ferrocyanide oxidation peak height with time for both CAP-C and PS-C MN arrays.

Figure 5.2.9.4 Chronoamperometric responses of the CAP-C MN systems towards peroxide (25 mM additions, pH 7 BR buffer, +1V) over a period of 10 seconds.

Figure 5.2.10.1 A) Braun lancet for capillary blood sampling and B) the individual constituents.

Figure 5.2.11.1 Electron micrographs of the breakdown of CAP-C MN after 1 week in loam soil.

Figure 5.2.11.2 Electron micrographs of Ps-C MN after 1 week in loam soil.

Figure 6.0.1 Oxidative pathway leading to the release of the tethered drug.

Figure 6.1.2.1 Reaction scheme used in the preparation of the naphthoquinone derivatives.

Figure 6.2.1 Cyclic voltammograms detailing the response of the naphthoquinone derivatives (182 µM) at a glassy carbon electrode in pH 7 PBS buffer. Scan rate 50 mV/s.

Figure 6.2.2 Influence of scan rate on the peak height of the aminophenol component of the conjugate pre-adsorbed onto glassy carbon electrode.

Figure 6.2.1.1 Cyclic voltammograms detailing the response of the 1,4-methoxyaniline (182 µM) at a glassy carbon (dashed line) electrode in pH 7 PBS buffer. The response to 1,4-aminophenol (solid line) has been included for comparison. Scan rate: 50 mV/s.

Figure 6.2.2.1 A) Scanning electron micrograph of the nano particulate carbon – polystyrene microneedle array. B) Cyclic voltammograms detailing the response of the methoxy-naphthoquinone derivative (185 µM) at unmodified (dotted line) and anodised (solid line) carbon-polystyrene microneedle arrays in pH 7 buffer. Scan rate: 50 mV/s.

Figure 6.2.2.2 Proposed reaction mechanism attributed to the redox transitions (I→V) observed at the electrode for the methoxy conjugate.

Figure 6.2.3.1 Cyclic voltammograms comparing the response of a glassy carbon electrode to codeine (1 mM, pH 7 PBS) and the naphthoquinone-methoxy conjugate. Scan rate: 50 mV/s.

Figure 7.0.1 Activation of carboxylic groups on laser induced graphene (LIG) by dicyclohexylcarbodiimide (DCC) in the presence of 4- N, N-dimethylaminopyridine (DMAP) which is displaced by a drug candidate possessing hydroxyl group to facilitate esterification.

Figure 7.2.1.1 Cyclic voltammograms detailing response of A) codeine (0.19 mM), B) salicylic acid (1.15 mM) and C) acetaminophen (1.87 mM) towards glassy carbon electrode in pH 5 BR buffer. Scan rate: 50mV/s.

Figure 7.2.2.1 Immobilisation of electro-oxidative release of acetaminophen.

Figure 7.2.2.2 Acetaminophen release mechanism facilitated by DMAP / DCC ester activation and cyclic voltammogram detailing the response of LIG versus LIG DMAP / DCC loaded with acetaminophen in pH 5 BR buffer. Scan rate: 50 mV/s.

Figure 7.2.2.3 Cyclic voltammograms detailing the response of LIG DMAP / DCC loaded with acetaminophen with repetitive cycling in pH 5 BR buffer. Scan rate: 50 mV/s.

Figure 7.2.2.4 Cyclic voltammograms detailing the response of Ps-C MN DMAP / DCC loaded with acetaminophen with repetitive cycling in pH 5 BR buffer. Scan rate: 50 mV/s.

Figure 7.2.2.5 Salicylic acid release mechanism facilitated by DMAP / DCC ester activation.

Figure 7.2.2.6 Square wave voltammograms detailing the response of LIG DMAP / DCC loaded with salicylic acid with repetitive cycling in pH 5 BR buffer.

Figure 7.2.2.7 Chemical structure of the possible by-products that can arise due to the application of an oxidative potential towards salicylic acid. (A) polymeric deposits (PSA) and (B) biphenylsalicylic acid (BPSA).

Figure 7.2.3.1 Alternative release mechanism where the local pH is increased by the application of a cathodic potential to hydrolyse the ester bound to the drug.

Figure 7.2.4.1 Cyclic voltammograms detailing the response of LIG DMAP / DCC loaded with acetaminophen (Left) and salicylic acid (Right) after the application of –2 V (Red) versus the control where there was no pre-treatment potential of -2 V (Black) in pH 5 BR buffer. Scan rate: 50 mV/s.

Figure 7.2.5.1 Methodology employed to verify release of drugs following application of -2 V to LIG DMAP / DCC loaded with salicylic acid.

Figure 7.2.5.2 UV Vis spectrum of salicylic acid in pH 5 and the resulting calibration curve.

Figure 7.2.5.3 UV Vis spectrum following the electro-hydrolysis of salicylic acid from LIG DMAP / DCC loaded with salicylic acid after applying -2 V in pH 5 BR buffer.

Figure 7.2.6.1 Modification of poly(anthranilic acid) (A) with salicylate (B).

Figure 7.2.6.2 Cyclic voltammograms detailing the response of a LIG electrode towards anthranilic acid in 0.1 M sulfuric acid. Scan rate: 50 mV/s.

List of Tables

Table 2.2.2.1 Commercially available transdermal drugs.

Table 2.2.2.2 Commercially available transdermal drug delivery devices.

Table 6.2.3.1 Common prescription drugs which could be considered potential candidates for linkage to the naphthoquinone-aminophenol linker.

Acknowledgements

I would like to express my gratitude and thanks firstly to my supervisor Prof. James Davis, who has been the voice of reason during the most challenging moments of my PhD. James has been a source of guidance throughout my entire university career and had initially encouraged me to apply to the PhD program. James exhibits immense patience, answering any queries without judgement – when perhaps judgement would have been justified. Without his encouragement and creativity this process would not have been as enjoyable as it was. I couldn't imagine having a better mentor and supervisor.

My gratitude extends all the NIBEC staff and academics who have contributed to my PhD either through collaboration or technical assistance including: Miss Ruth Holman, Mr. Damian McDonald, Mr. Brian McGrath, Miss Charly Mifsud and Mrs. Ann Blair.

Thank you to my lab fam – Robert, Sarah, Cameron, Charnete and Catherine for sharing your knowledge, experience and most importantly thank you for sharing the laughs, the gossip and listening to the occasional rant. I have made memories that I'll laugh about for years to come, it has been a pleasure working with you all.

I would like to thank my family and friends. To Mum, Dad and Kerrie for your endless love and support, always pushing me beyond what I think I can achieve. Last but not least, to Danny, for dealing with the brunt of my stress and always putting things into perspective. I know you always have my back.

Copyright / Credit Notices

Within this thesis material (*i.e.*, text, figures, or tables) from the author's publications is reprinted. The copyright / credit notices are listed at this place in common for all the related chapters, paragraphs or sections. The material might have been modified slightly, however these copyright / credit notices still apply.

Acknowledgement is given to the original source of publication for:

Robert Barber, Sarah Cameron, **Amy Devine**, Andrew McCombe, L. Kirsty Pourshahidi, Jill Cundell, Souradeep Roy, Ashish Mathur, Charnete Casimero, Pagona Papakonstantinou, James Davis, 2021. Laser induced graphene sensors for assessing pH: Application to wound management. *Electrochemistry Communications*. 123.

The final publication is available at Science Direct *via*

https://doi.org/10.1016/j.elecom.2020.106914

Acknowledgement is given to the original source of publication for:

Amy Devine, Ellen Hegarty, Catherine Hegarty, James Davis, 2023. Conductive Composite Microneedle Sensors based on Cellulose Acetate Phthalate: Investigating Performance and Biodegradability. *IEEE Sensor Letters*.

The final publication is available at IEEE Xplore *via*

https://doi.org/10.1109/LSENS.2023.3245024

Acknowledgement is given to the original source of publication for:

Amy Devine, Catherine Hegarty, Charnete Casimero, Rebecca Louise Molyneaux, Robert B. Smith, Marco F. Cardosi, James Davis, 2020. Electrochemically initiated release: exploring new modalities for controlled drug release. *Journal of electroanalytical Chemistry*. 872.

The final publication is available at Science Direct *via*

https://doi.org/10.1016/j.jelechem.2020.113926

Abstract

Conventional controlled drug release methodologies largely centre around the encapsulation of therapeutics within a polymer or gel, where the physiological conditions in which the delivery vehicle is placed, results in their expulsion. The trigger is, more often than not, physio-chemical (*i.e.*, pH or temperature) which interacts with the smart material, releasing the loaded drug. As of late, external stimuli have been explored (electrode potential, temperature, pH *etc.*) to trigger the release of loaded therapeutics. In this work, an electrochemical trigger is employed, which leads to the release of an attached drug, for use in the next generation of transdermal smart patches.

The approach is based on conductive polymer nanocomposite microneedle arrays where the conductivity is improved by anodisation, laser ablation and laser induced graphene. Following the tuning of the conductivity, various chemical tethers are employed (*i.e.*, ether and ester bonds) which are broken following the application of an appropriate oxidative potential or control of local pH.

The design and characterisation of the nanocomposite microneedle arrays, and chemical tethers are described, and the release of model drugs validated electrochemically and by UV-Visual spectrophotometry. The novel microneedle formulations are assessed for the degree of conductivity they provide as well as their structural merits and the novel chemical tethers critically appraised.

Abbreviations

Ag	Silver
AgCl	Silver Chloride
BNF	British National Formulary
BR	Britton Robinson
CAP	Cellulose Acetate Phthalate
CAP-C	Cellulose Acetate Phthalate - Carbon
CE	Counter Electrode
CNT	Carbon Nanotube
DCC	Dicyclohexylcarbodiimide
DMAP	4- N, N-Dimethylaminopyridine
E	Electrode Potential
EDX	Energy Dispersive X-Ray Analysis
Eq	Equation
FDA	Food and Drug Administration
GI	Gastrointestinal
GOx	Graphene Oxide
HOMO	Highest Occupied Molecular Orbital
IoT	Internet of Things
KCl	Potassium Chloride
LCST	Lower Critical Transition Temperature
LIG	Laser Induced Graphene
MEMS	Micro Electromechanical System
MN	Microneedle
mV	Millivolt
mV/s	Millivolts per Second
MW	Molecular Weight

NaOH	Sodium Hydroxide
PDMS	Polydimethylsiloxane
PEG	Poly (ethylene glycol)
PGLA	Poly (lactic-co-glycolic acid)
PI	Polyimide
PNIPAAm	Poly (N-isopropyl acryl(amide)
POCT	Point of Care Testing
Ps-C	Polystyrene - Carbon
RE	Reference Electrode
SC	Stratum Corneum
SPE	Screen Printed Electrode
TDDS	Transdermal drug delivery system
UV-Vis	Ultraviolet-Visible
V	Volts
WE	Working Electrode
WHO	World Health Organisation
wt%	Percentage by weight

Notes on Access to Contents

"I hereby declare that with effect from the date on which the thesis is deposited in

Research Student Administration of Ulster University, I permit

1. the Librarian of the University to allow the thesis to be copied in whole or in part without reference to me on the understanding that such authority applied to the provision of single copies made for study purposes or for inclusion within the stock of another library.
2. the thesis to be made available through Ulster Institutional Repository and/or EThOS under the terms of the Ulster eTheses Deposit Agreement which I have signed.

IT IS A CONDITION OF USE OF THIS THESIS THAT ANYONE WHO CONSULTS IT MUST RECOGNISE THAT THE COPYRIGHT RESTS WITH THE AUTHOR AND THAT NO QUOTATION FROM THE THESIS AND NO INFORMATION DERIVED FROM IT MAY BE PUBLISHED UNLESS THE SOURCE IS PROPERLY ACKNOWLEDGED"

Chapter 1

Overview

It has been long recognised that it would be advantageous in a number of clinical contexts for drug delivery systems to autonomously control the delivery of therapeutic agents to patients thereby circumventing issues related to poor adherence. This removes the burden from the patient whilst offering independence to elderly people and those who suffer with chronic conditions requiring regular medication. In addition, it has been proffered that the transdermal route can deftly avoid the complications common to gastro-intestinal process such as bioavailability, absorption efficiency and mucosal irritation. First pass metabolism can also be overcome allowing the possibility of greater efficiency in the yield of the therapeutic. This chapter briefly introduces the primary concerns associated with drug delivery, places the research in context and summarises the aims and objectives of the project.

1.0 Introduction

The World Health Organisation (WHO) defines the term adherence to long term therapy as: "the extent to which a person's behaviour – taking medication, following a diet and / or executing lifestyle changes aligns with the agreed recommendations from a health care provider" (1). Within discussions of adherence, it is important to appreciate the difficulty in obtaining objective data as patients often over-estimate their level of adherence to therapies (2). With that in mind, it is estimated that, in developed countries, rates of adherence are 26 - 60% (3), and even lower in developing countries due to inequalities in access to health care (4; 5). Adherence plays an important role in the clinical benefit of therapies and poor adherence is the primary reason for suboptimal clinical benefit (1).

Illnesses can be classified into different types such as acute (6), chronic (7), infectious and non-infectious (8). Adherence is especially important for chronic diseases that in order to be classified as such must meet one or more of the following characteristics: be permanent, leave residual disability, be caused by irreversible pathological alteration, require special training of the patient for rehabilitation or may be expected to require a long period of supervision, observation or care (9). Common examples of chronic illnesses include asthma (10), hypertension (11), diabetes (12), chronic obstructive pulmonary disease (COPD) (13) and HIV/AIDs (14), and patients living with chronic conditions more often than not, display difficulties in adhering to their recommended regimes resulting in poor management and control of the illnesses (1; 5).

A high proportion of the elderly population suffer with chronic disease, and often multiple conditions simultaneously known as comorbidities (15). A consequence of which is polypharmacy, where patients have many treatment regimens to follow (16). For example, the average geriatric patient takes 4 – 5 different medications a day and, in this instance, adherence becomes difficult (17). During long term therapies, motivation to adhere to treatment plans can become strained (18). Punnapurath *et al.*, (2021) found that, of 100 geriatric patients, 44% had been on medicinal therapy for 5 – 15 years and many stopped taking their medication

early when symptoms had appeared to subside, rather than continuing to follow their health care providers' advice (19). Additional challenges elderly patients face is diminishing cognitive and physical abilities like memory, hearing, vision, and movement. Thus, they can become more reliant on external assistance and are less able to manage their own treatment (19).

Numerous chronic conditions require injections to manage their illness, for example, patients with type 1 diabetes must inject insulin and cancer patients often receive therapy *via* intravenous lines. Subcutaneous and intravenous injections can provide rapid delivery of a wide range of drugs, but these are predominantly administered by a trained professional (20). One major drawback to this approach, is the spread of deadly bloodborne diseases like hepatitis B, hepatitis C, syphilis, and herpes due to contaminated needlesticks, sharps or splashes putting health care workers at risk (21). Moreover, needles are invasive causing pain, bleeding, and bruising, which can exacerbate common fears and phobias and further impact adherence to these therapies (22; 23; 24). A study by Rzeszut *et al.*, (2011) found that 50 % of children and teenagers with diabetes reported being highly stressed when administering their insulin shots. This directly resulted in fewer endocrinology appointments, due to their heightened anxiety surrounding treatment, inevitably impacting the management of their condition (25).

Oral medication is the most common method of drug delivery due to its convenience and, unlike injections, it is minimally invasive with little risk of infection or pain (26; 27; 28). The key problem with oral medication is that it must pass through the gastrointestinal tract and be absorbed in the small intestine. The latter is dependent on physiological factors that include peristaltic movement within the intestine, pH, and the presence of food (26). High levels of enzymes are present in the small intestine to metabolise drugs, which can result in their inactivation markedly reducing the therapeutic yield. The extent of this is highlighted when considering the HIV protease inhibitor saquinavir and immunosuppressant tacrolimus, which are used to manage HIV. Upon ingestion they have been found to be only 20 % bioactive with, as of yet, no alternative means of delivery (28). To ensure the molarity and bioavailability of

delivered drugs remains intact, avoiding the gastrointestinal tract is recommended, and thus, transdermal approaches have been increasingly viewed as a more appropriate delivery route. Transdermal drug delivery is the application of drugs topically to healthy, intact skin which diffuses through the stratum corneum into the interstitial fluid and eventually the blood stream. This can be explained by their minimally invasive nature, ease of use/application and their ability to offer greater dose control. There are, however, a number of limitations in that: the array of drugs that possess the niche characteristics that can enable penetration of the stratum corneum are limited. For a drug to successfully diffuse through the skin it must be lipophilic, small in molecular weight and highly potent. Hence, to expand this range, the stratum corneum must be interrupted physically *via* either microporation or microneedles which create microchannels for the drug to pass (23; 29; 30; 31).

Microneedles can be either single needles or needle arrays typically ranging from 300 to 900 µm in length, with diameters in the order of microns which can pierce the uppermost layer of the skin. An example of a microneedle array is shown in **Figure 1.0.1** alongside a conventional hollow-bore needle (20). In contrast to subcutaneous injections, their miniature size allows them to disrupt the stratum corneum without irritating nerve endings in the dermis, therefore, causing no pain beyond the physical sensation of the patch being pressed onto the skin (22; 29).

Microneedles can be fabricated using a myriad of materials producing solid (32), dissolvable (33), hollow (34) and swellable (35) arrays. Solid microneedles can be produced using metal like stainless steel (36) or silicon (30) and are used simply to pierce the skin barrier. Drug delivery can be accomplished *via* two different methodologies. The “poke and patch” method relies on the addition of the drug to the skin after removal of the microneedle array. The microchannels created by the microneedles allow the drug salve to diffuse into tissue layers (37). The alternative approach is to coat the exterior of the microneedles with the drug such that the latter is inserted directly into the tissue on penetration (38). Dissolvable microneedles are often fabricated using biocompatible polymers or polysaccharides, whereby the needles dissolve

upon piercing the skin (39). In this case, the drug is usually incorporated into the microneedle formulation at the time of manufacture. A similar methodology is employed with swellable microneedles, whereby upon hydration the needles swell and expel immobilised drug (40). Finally, hollow microneedles are like miniature hypodermic needles where drug is often released from a reservoir upon piercing the skin (22; 29). These methods of drug delivery rely on passive diffusion, which is initiated immediately upon the insertion of the needles with little control over quantity and timing of drug release, therefore, fabricating microneedles that exploit smart materials could allow for expulsion of drug following an external stimulus like light (41), temperature (42) or voltage (43) which could be integrated into smart wearable systems.

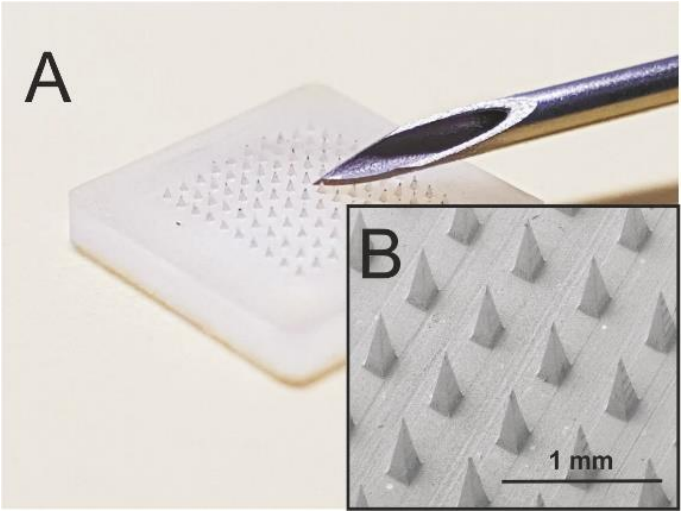

Figure 1.0.1 Example of a microneedle array A) compared to a hypodermic needle B) electron micrograph of the array (20).

Smart wearable systems are becoming more widespread within the health sector, which reduces the burden placed on patients when managing their therapy. They aim to support independence for the elderly population and people with disabilities, by providing real time data for health care professionals to monitor and adjust treatment in addition to notifying compliance (44). Automated drug delivery systems are encompassed under the canopy of smart wearable systems, where dose timing and frequency can be controlled, bettering adherence to complex regimens and anxiety surrounding administration. Typically, automated

transdermal drug delivery systems consist of sensors, memory, electronic circuit, and the drug delivery portion which can store data to be accessed by the patient or physician (45).

It could be anticipated that, through combining transdermal patches with smart wearable systems, autonomous drug delivery can be achieved that can facilitate improvements in adherence and offering patient friendly option to manage their therapy. **Figure 1.0.2** is a conceptual illustration of how microneedles could ultimately be incorporated into a wearable system to control transdermal drug delivery. This combination of smart materials and microneedles structures could also widen the range of molecules and drugs that can be delivered through the stratum corneum. At the outset of the present investigation, it was hoped that the work would provide the groundwork for a smart patch system that exploits microneedle technology to control transdermal drug delivery *via* electrochemical stimulus. This thesis documents the approaches taken, and the advances made to counter some of the problems that current therapeutic methods face.

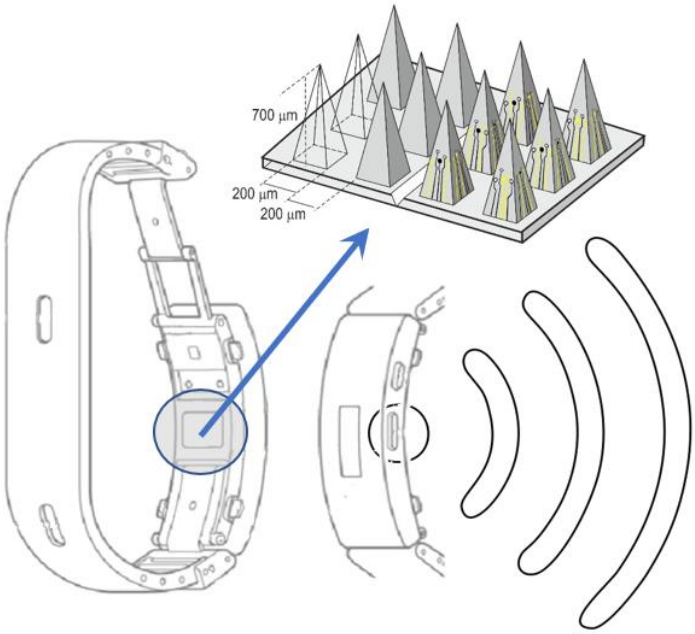

Figure 1.0.2 Illustration of how a microneedle array could ultimately be incorporated into a wearable smart watch capable of autonomously controlling the initiation and duration of drug release.

1.1 Aims and Objectives

The aim of this project was to investigate and develop novel methods of transdermal drug delivery that could be employed into the design of a “smart patch”, that would allow the controlled release or dosing of therapeutics. The focus of the research targeted microneedle structures and sought to explore new concepts in their design and formulation, as well as new drug release mechanisms. The core approach centred on electrical/electrochemical transduction as the release mechanism and the challenge lay in developing new materials that were consistent with microneedle fabrication, but which could enable the controlled delivery.

The objectives set out for the project were:

- to design and characterise various microneedle compositions promoting high conductivity and surface area;
- to characterise the surface morphologies of electrically conductive material and optimise their electrochemical properties and drug loading abilities;
- to develop drug release models that act as a tether to a given drug that can be released following the application of an appropriate potential;
- to optimise drug loading capabilities and increase yield of released drugs and;
- to assess the model’s ability to delivery drugs “on demand” and ability to provide multiple doses/therapeutic agents.

1.2 Thesis Overview

Chapter 2 entitled “Literature Review” discusses the issues that traditional approaches like oral medication and hypodermic needles face, and how these issues inspire research to help solve them. It looks critically at emerging technologies detailing their advantages and limitations in order to establish opportunities to develop the field further.

Chapter 3 entitled “Experimental Techniques and Methodology” outlines the scientific principles through which the project is based, and details the experimental methods employed

throughout the project. It is important to note that specific additions to the various experimental set-up are detailed in each chapter.

Chapter 4 entitled “Laser Ablation of Nanocomposite Microneedles for Enhanced Electrochemical Performance Combined with Dual-layer Microneedle Approach using Biocompatible and Dissolvable Array” investigates an alternative method to improve electrochemical properties of polystyrene-carbon (Ps-C) microneedles (MN) by way of electrochemical anodisation and laser ablation. Various techniques are used to assess the suitability of the laser modification method such as cyclic voltammetry, Raman spectroscopy, energy dispersive X-ray analysis (EDX) and scanning electron microscopy (SEM). In addition, a multi-layered approach is investigated using cellulose acetate phthalate (CAP) microneedle as means to create microchannels for interstitial fluid to access the laser modified microneedle below for sensing and controlled drug delivery applications.

Chapter 5 entitled “Nanocomposite Microneedles Based on Cellulose Acetate Phthalate and Carbon Nanoparticles Decorated with Laser Induced Graphene to Improve Electrochemical Performance” investigates various laser induced graphene formations to be harvested and added to cellulose acetate phthalate-carbon microneedles in order to improve their electrochemical performance. Electrochemical analysis such as cyclic voltammetry and square wave voltammetry are employed to test the response of the system to ferrocyanide and uric acid retrospectively. Electron micrographs detail the morphology of the LIG formation and illustrate the sharpness of the microneedle systems. As well as preliminary studies into the biodegradability of CAP as a binder to address issues of waste generated by sharps using blood glucose sensors used by diabetic patients as a way to quantify waste generated. The biosensing capability of the CAP system is preliminary assessed through the measurement of peroxide.

Chapter 6 entitled “Electrochemically Initiated Release: Exploring New Modalities for Controlled Drug Release” details a series of naphthoquinone-aminophenol derivatives synthesized on the basis that their conjugation with a suitable drug candidate, could provide

a means through which the latter could be released upon the imposition of an appropriate oxidation potential. The approach is based on a three-component assembly in which the naphthoquinone redox centre serves as a reporter unit allowing interrogation without release of the drug. The central aminophenol serves as the tether to which the drug is linked *via* an ether bond. Upon oxidation of the aminophenol - ether component, transition of the latter to quinone imine results in the release of the drug. The electrochemical properties of the model system are investigated and the impact of the release process on the functional groups intrinsic to the drug component is critically considered.

Chapter 7 entitled "Activation of Carboxylic Groups *via* DMAP / DCC for Controlled Release of Ester Bound Drugs *via* Electrochemical Trigger" employs dicyclohexylcarbodiimide (DCC) and 4- N, N-dimethylaminopyridine (DMAP) which is known to readily activate the carboxylic groups towards ester formation. Given the presence of such groups on the carbon surfaces, the subsequent activation could be exploited as a means of immobilising drug candidates at the electrode surface. Laser induced graphene (LIG) and polystyrene-carbon (Ps-C) were used as the test substrates. Following the esterification of the drug candidate to the substrate, the application of oxidative and reductive potentials can be used as a means to control drug delivery. Acetaminophen (paracetamol) and salicylic acid were employed as model drug agents and were used to validate the release system in real time by way of cyclic voltammetry and UV-visual spectrophotometry. While oxidative release exploits the inherent electrochemical properties of the drug, cathodic potential changes brought out changes in the local pH which in turn hydrolyse the ester bond. The use of poly(anthranilic acid) was also explored as an electrode modifier which would increase the population of carboxylic groups and thereby increase the drug loading potential and eventual yield.

Chapter 8 entitled "Conclusions and Further Work" provides a summary of the outcome arising from the previous chapters and suggestions as to how the area would be expanded further.

Chapter 2

Literature Review

Overview

This chapter discusses the traditional approaches to drug delivery and their limitations, whilst critically analysing up and coming drug delivery mechanisms like implantable and nanoparticles, which can achieve targeted release. This chapter also discusses the opportunities for transdermal drug release and the novel approaches within the field, their commendable attributes, and shortcomings.

2.0 Traditional Approaches to Drug Delivery

2.0.1 Oral

Medication taken orally is the most convenient and simple administration route, and it is therefore unsurprising that it is the most widely used method (46; 47; 48). Upon reaching the small intestine, the dissolved drug permeates the epithelium, followed by absorption into the blood or lymphatic system (49; 50). However, it is paramount that the orally administered drug has disintegrated and dissolved within the small intestine in order to be absorbed. Dissolution and absorption are hugely influenced by physiological conditions such as pH (51; 52; 53) and the volume of fluid (54; 55; 56), and in turn, the rate of intestinal absorption is key in deciding the bioavailability of a drug (49; 57). Changes within the physiology of the gastrointestinal (GI) tract can be the result of local diseases like inflammatory bowel disease (IBD) (58; 59) or systemic diseases like diabetes (58; 60; 61). Moreover, differences in physiological conditions in the GI tract of the population exist due to age, sex, ethnicity, or lifestyle and, as such, a "standard" patient population is difficult to achieve (62; 63). This can contribute to situations of over or under estimating absorption, which poses safety concerns and efficacy issues for a given drug. For example, children typically have less fluid in their GI tract, thereby influencing rates of dissolution of a drug and influencing the absorption kinetics (57; 64). The pH of the small intestine is typically neutral when fasted (51), but this varies greatly when food or water is present and can go as low as pH 3 (65). Elderly people also tend to have a more acidic GI tract (66) such that drugs intended to be absorbed in the small intestine may not even dissolve if they were formulated for dissolution in neutral conditions (49; 57).

Another important factor influencing absorption is volume of splanchnic circulation, referring to the blood flow to the abdominal gastrointestinal organs. It is controlled by the autonomic nervous system and is influenced by lifestyle (67), however, some drugs modify the splanchnic blood flow in turn impacting absorption. For example, digitalis is a strong vasoconstrictor and, once absorbed, can result in a decrease of 30 – 40 % splanchnic blood flow (68). As polypharmacy is common among people with comorbidities, it is likely that drug absorption is

altered due to other drugs being administered. This is not taken into consideration when developing pharmaceutical drug products (49).

Pharmaceutical drug products contain a myriad of ingredients to aid manufacturing and physical handling by the patient. Moreover, they can also include ingredients to enhance the taste / acceptability (particularly for younger children), to offset the bitterness of the basic components (69). The latter are typically inactive and do not alter the active component (70). There are, however, certain supplements that alter the drugs solubility, dissolution, wettability, and intestinal permeability. An example is sugar alcohols, which are known to affect absorption and reduce bioavailability (71). The small intestine is also inhabited by a microbiome of bacteria, which aid in the digestion of food, but can also inactivate some drugs (*e.g.*, cardiac glycoside digoxin), with the result that higher doses are often required and which, potentially, can be more harmful (49; 72). Generally, the geriatric population tend to be the predominant users of medication and can be vulnerable to the consequences of an ever-aging population, carrying a variety of chronic conditions (diabetes, heart disease etc) (73). While they represent 20 % of the entire global population, they are under-represented in clinical trials and their needs are often disregarded (74). Elderly patients often suffer with dysphagia: difficulty in swallowing, amounting in roughly 27 % population afflicted (57; 75; 76). This makes taking oral medication difficult and can reduce adherence to these therapies.

Another well documented issue associated with taking medication orally discussed by Pond *et al.*, (1984), is the role of the first-pass metabolism, which refers to a drug being metabolised by tissues in the body resulting in a decreased concentration and bioavailability of the drug reaching its desired site / systemic circulation (77). Drug metabolising enzymes are present in various tissues like the lungs, vasculature, the gastrointestinal tract, and many metabolically active tissues, however, the liver is primary site responsible for first-pass elimination (78). Despite the first pass metabolism being advantageous to prodrugs, (drugs that are converted from an inactive form to an active form by first-pass metabolism) *e.g.*, codeine which undergoes demethylation to morphine. Many extensively used drugs like morphine,

buprenorphine, diazepam, and midazolam are victims of the first pass metabolism, which greatly reduces their concentration before reaching systemic circulation (79). The metabolising power of the gastrointestinal tract and the liver is impressive, eradicating the oral bioavailability of HIV protease inhibitor, saquinavir and the immune suppressant, tacrolimus < 20 % (80). Not to mention, the denaturation and chemical degradation of macromolecules that occurs in the stomach before even reaching the small intestine or liver (81; 82). The highly acidic environment in the stomach (pH 1-2 when fasted), denature most proteins and begin their enzymatic degredation (82; 83).

The key issue with oral medication, is degradation of molecules in the stomach, and maintaining a high level of bioavailability of the drug to be absorbed within the small intestine. This is extremely dependent on physiological conditions, that vary from patient to patient due to age, food, fluid, disease, and polypharmacy. To avoid these issues, there have been considerable efforts to avoid delivery *via* the gastrointestinal tract when delivering therapeutics and ideally aim to be delivered to the blood *via* a more direct route.

2.0.2 Injections

Injection of therapeutics can be accomplished *via* an array of possibilities for example, intramuscular, subcutaneous, intravenous, and intradermal. The distinction for each method is the depth and angle at which the needle punctures the skin and is illustrated in **Figure 2.0.2.1**. Injections offer rapid delivery of drugs and molecules which avoid the gastrointestinal route, and thus, its limitations. After collating drugs delivered *via* needles from the British National Formulary (BNF), it was established that some 165 drugs are delivered by intramuscular, subcutaneous, and intradermal or all three, and a breakdown of the percentage of the proportion of drugs delivered by each kind of injection is illustrated in **Figure 2.0.2.2.**

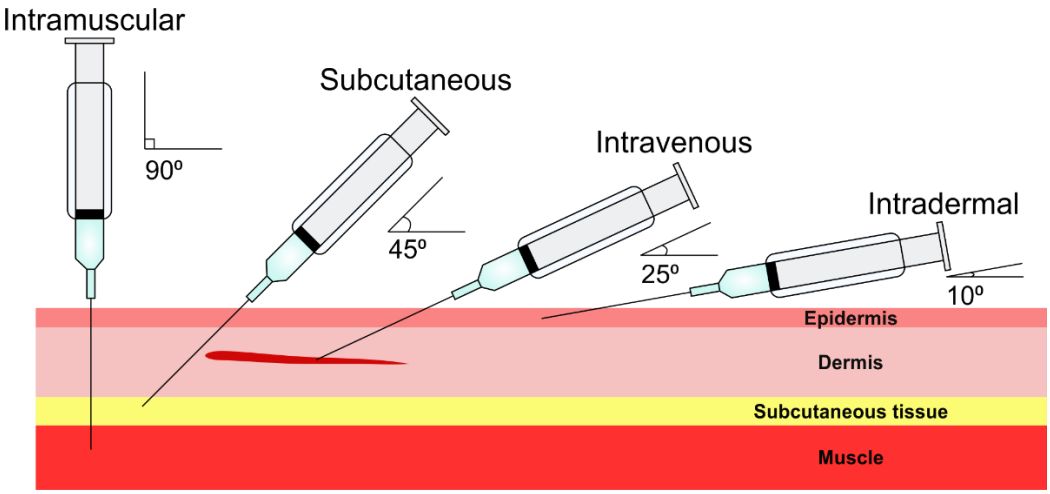

Figure 2.0.2.1 Needle insertion angles for intramuscular, subcutaneous, intravenous, and intradermal injections.

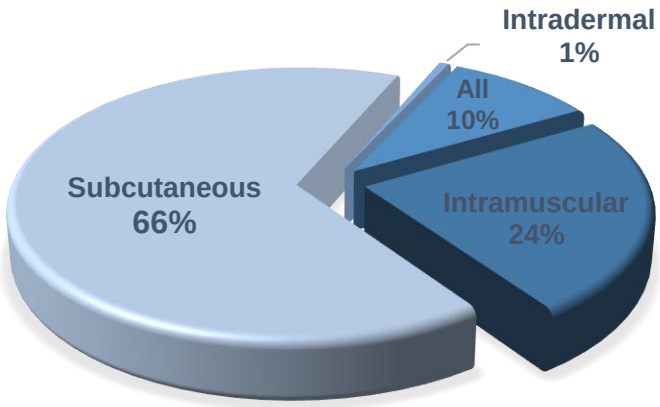

Figure 2.0.2.2 The number of drugs that can be delivered by intramuscular, subcutaneous, and intradermal or all types of needles using data from the British National Formulary (BNF).

The data can be broken down further to highlight the predominant delivery method for common conditions and these are illustrated in **Figure 2.0.2.3** (84).

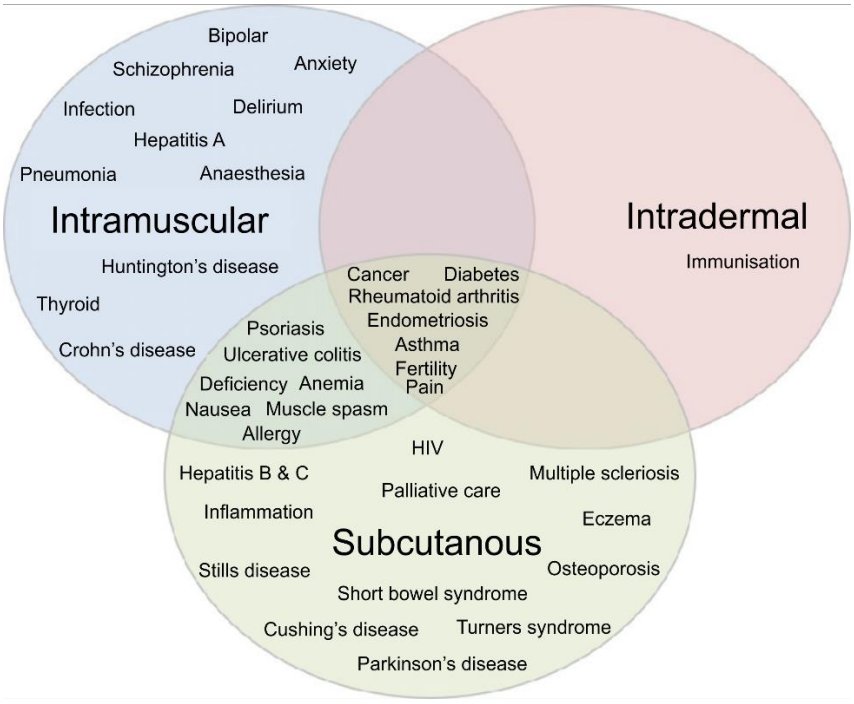

Figure 2.0.2.3 The range of conditions where the therapeutics can be delivered by injections and the type of injection used.

Despite providing rapid delivery, injections are an invasive procedure which are painful and can cause bleeding, bruising and muscle tenderness. While the prospect of injections can be worrisome for adults, it can be particularly problematic for children where it has been estimated that some 63 % exhibit needle fear (85). Needle fear in children can impact a parents' willingness to take their children to receive vaccinations if their child displays distress due to needle phobia. A survey of 120 children by Baxter *et al.*, (2017), found that many hospitalised children stated, that apart from their disease, injections are their main source of pain. This problem is not limited to children, this fear and phobia is carried on through adulthood and becomes intensified with age. It has been estimated that within the geriatric population, 15 % patients refuse flu shots due to their needle fears, and 28 % of people with HIV delayed getting tested due to fear of needles (86). Poor adherence to injections, not only has a negative implication for the individual, but also the general population. Outbreaks of preventable diseases has been well documented due to individuals refusing vaccinations, in part due to fear generated evasion (87).

Often diabetic patients self-administer injections, which requires a level of training and expertise in order to deliver the dose correctly to obtain the full clinical benefit of the therapy. Even experienced patients can encounter minimal improvement to glycaemic control due to simple errors like forgetting to remove the inner needle cap or having poor understanding of the needle pen (88). When delivering insulin, it is critical to leave the needle in the skin for at least 10 seconds to ensure the entire dose has been expelled. A survey of 13,289 patients by Frid *et al.*, (2016), found that only 32 % of diabetic patients left the needle in for the recommended time. Another frequent error is improper resuspension of the insulin vial by way of rolling 20 times for adequate mixing of the solution. This critical step is skipped by 10 % of patients, and the insufficient mixing results in large dosing errors, affecting the clinical gain of the therapy therefore patients experience poor glycaemic control (89).

The risk of spreading bloodborne pathogens like hepatitis B, hepatitis C and bacterial infections due to contaminated needles is also a very serious problem that thousands of patients have suffered. The contamination can occur due to reuse of single use syringes or through backwash into multiple use vials on one or multiple patients. These diseases have major health implications and can be detrimental not only to the patient but to the health care worker handling the contaminated needle (90). Despite the prevalence of unsafe injections falling by an estimated 88 % between 2000 and 2010, resulting in 874 million instances worldwide, the estimated figure cannot be disregarded. There is no doubt that unsafe injection practices are a universal problem. However, the impact is felt especially in countries facing economic austerity, limited resources, and availability of appropriate expertise, for example, it is common practice to reuse unsterilized equipment in countries like Pakistan. Unsurprisingly, improper usage and unsafe administration is often linked, but not limited to the reuse of needles, leading to accelerated spread of infection or disease. The inappropriate disposal of medical waste and injury as a result, is another issue that exacerbates the spread of injections due to improper handling of needles (91; 92). Although needles have their limitations, notable attributes are their ability to effectively bypass the skins protective barrier and achieve rapid

drug delivery to systemic circulation whilst maintaining a high level of bioavailability, thus, it remains a popular approach.

2.0.3 Sharps Waste

A factor that has only been considered in recent years, is the waste produced due to needles and syringes. It can appear obvious when reflecting on the size of needles, the syringe attached, the cap and the bottle of therapeutics. Vaccines predominantly delivered by needle and syringe like the vaccine for influenza which requires an annual booster. The waste produced by injections and vaccines must be disposed in a sharps waste bin and incinerated expelling carbon dioxide (and other potentially toxic materials such as dioxins) into the atmosphere. Although injections provide rapid delivery of therapeutics, there are clearly many issues and hence there is a continuing need to find alternative methods that bypass the gastrointestinal route without provoking a pain response. Microneedles have been envisaged to replace injections for the delivery of many therapeutics traditionally delivery *via* injection. Due to the large different in size, a microneedle would produce a much smaller carbon footprint than needle and syringes after incineration and this is discussed in **Chapter 5**.

2.0.4 Compliance

Although the bioavailability of a drug and its absorption pathway are key factors to consider when developing drug delivery systems, neither are of any use if the patient is unable to administer their medication as advised by their physician. Non-adherence to prescribed therapies is regarded as the foremost hurdle to preferred health outcomes in chronic conditions (93). For adherence to be considered satisfactory, over 80 % of the drug must be absorbed, and within rheumatoid arthritis patients for example, this is far from the case with adherence rates of 20 – 80 %. This compromises the therapeutic efficiency resulting in heightened disease activity and can lead to unnecessary treatment switches (94). Similarly, low adherence rates have been observed in children with asthma where some 50 – 70 % coincide with poor disease control (95).

Within stroke survivors, adherence is necessary to prevent a recurrent episode, however, Saade *et al.*, (2021) found that 50 % of patients with chronic conditions are non-adherent. The reasons for poor adherence are complex and depend on a patient's cognitive abilities and disabilities which can result in being unable to administer and manage their own treatment regimes, this is supported by the fact that non-housebound patients display higher adherence rates (96). In another example, Rajurkar *et al.*, (2018) found that forgetfulness is a commonly observed cause of non-adherence to glaucoma medication in addition to improper administration (97).

Drug delivery systems at present, fail to consider individual patient needs, as compliance is a complex issue. Going forward, a patient centric approach is required to deliver the best possible health outcomes, where patients are freed from the burden of managing their medication schedule by way of controlled drug delivery systems (98).

2.1 Emerging Approaches

Research in drug delivery has come a long way from those methods employed in antiquity, with more focus on diminishing side effects for patients and creating the most convenient experience.

2.1.1 Implantable

Recent advances in material chemistry and biomedical engineering, have permitted the transition of implantable devices from passive structural components to smart sensors and drug delivery actuators. Implantable drug delivery devices are available in a range of forms that can include: miniaturized hormone implants (99), larger drug carrying scaffolds (100), drug eluting stents (101) or drug wafers (102) as illustrated in **Figure 2.1.1.1**. Implantable devices are particularly advantages when considering the treatment of soft tissues for complex medical conditions in a patient friendly manner (103). This is especially evident where long term medical attention is required for the condition, such as diabetes, ocular diseases, cardiovascular

diseases, cancer, and contraception. To ensure the implantable device is fit for purpose, it is essential that the material is biocompatible in order avoid inducing an immune response (104). It must also adequate adhesive properties to integrate with the target tissue and is sufficiently durable to sustain long term dosing (103; 104).

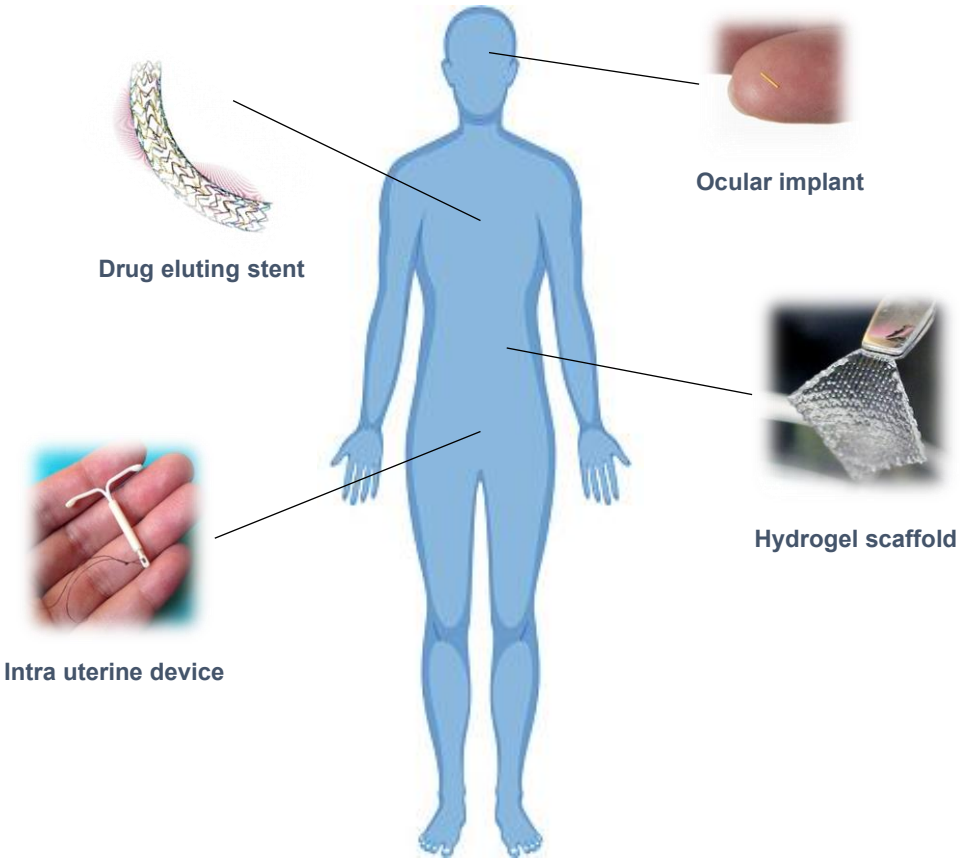

Figure 2.1.1.1 Examples of commercially available implantable drug delivery systems (Adapted from (103)).

Implantable scaffolds produced *via* electrospinning, have been extensively researched as the nanofibers have a high loading capacity for drugs (105) due to a high volume to surface ratio (106) and high flexibility. Drug loading can be achieved by several methods such as, mixing with polymers, coating/surface immobilisation (107) or encapsulation (105; 108). Each method has its own applications and limitations, simple fabrication methods typically produce burst release profiles with limited control *i.e.*, drugs attached by van der Waals', hydrogen bonds (109) or electrostatic interaction (110). However, affinity for drugs can be improved by surface modifications, for example the addition of functional groups including amine, thiol, hydroxyl,

and carboxyl can provide a more controlled release profile (111). Drug attributes can influence which polymer/solvent is employed and which drug incorporation method is used. For example, whether the drug is hydrophilic or hydrophobic influences which solvent is chosen to dissolve/process it. If the drug is sensitive to high voltage or organic solvents, it may be coated rather than mixed (112).

Polymeric implants are often injected into the target tissue or inserted during a minor surgery, so it is imperative that they have long lasting effects to circumvent non-compliance. Chitosan based implants have been examined, which have been used to release Ketorolac, an anti-inflammatory. The subcutaneous implant released Ketorolac passively for up to 45 days, an adequate length of time to provide long term treatments (113). The properties of biomaterials used for implantable drug delivery devices can be tuned to determine the response of cells *in vivo.* For example, proteins can be delivered as drugs to initiate processes within the cells, or the scaffold can be absorbed to help regrow tissues. Poly (lactic-co-glycolic acid) (PGLA) was employed as a scaffold modified by polydopamine loaded with nerve growth factor (NGF). It offered sustained release and adsorption power to implement in spinal cord injury to help repair nerve cells (114; 115).

Cancer treatment is an increasingly relevant area of research for implantable drug delivery systems, as the scaffolds can be implanted to the site of action. This is significant as anti-tumour medication is often extremely toxic to normal cells. Local and controlled delivery can address the shortcomings faced by oral and intra-venous delivery of the same medication, reducing some of the unwanted side-effects on normal tissue. In addition, the targeted/controlled approach gives the opportunity of higher dosing so that the implant will be effective for longer periods of time (116).

There are many ways to control dosing of implantable drug delivery systems which have been categorized into “on-demand” or “programmed” release. The use of “on-demand” release, is typically where the therapeutic agent is released following an external stimulus such as ultrasound (117), electric field (118), magnetic field (119) or near infra-red light (120). This allows

a physician to control dosing in a non-invasive way. In contrast “programmed” release is where the therapeutic agent is released based on stimuli intrinsic to the body such as: enzyme activity (121), pH (122) or redox interactions (123). The physiological conditions within tumour cells are often greatly different than that of normal tissue. Changes in intracellular pH and the over expression of enzymes are common and in one scenario, it is possible to envisage the therapeutic agent being triggered once enzyme products are above a certain threshold. Conversely, this over expression of enzymes is also a dual control mechanism such that when products are increased, changes in the pH and redox interactions can be observed (116). Similarly, starch nanoparticles are pH dependant and can exploit the variation in pH common to tumour cells to deliver the entrapped drug within the correct tissue (124) and enhance the efficacy of chemotherapies (125).

While implantable drug delivery systems provide targeted drug delivery and a structure whereby tissue can repair, the procedure can be very invasive requiring a needle at the very least, or surgery in severe cases for insertion. Although the implants can be long lasting, and ultimately more convenient for patients, it is not always appropriate or feasible financially. More simplistic methods which does not require any expertise or physicians time can be useful for more manageable chronic conditions.

2.1.2 Nanoparticles

Polymers that can be configured into nanoparticles and micelles have grained enormous interest in developing drug delivery systems to provide targeted therapy. Polymers enhance controlled release mechanisms, improve biocompatibility, bioavailability and solubility of drugs thus improving their efficacy (126). Smart polymers such as hydrogels change physically or chemically based on the environment in which they are placed (127). One example is poly(N-isopropyl acryl(amide) (PNIPAAm) which is thermosensitive such that when it is below its lower critical transition temperature (LCST) it is observed in a coil state. Upon heating however, it is globular and swells (127; 128; 129; 130). It is important to also note that the LCST is tuneable, by the addition of co-monomers such that it can be adapted to suit a particular application (125).

This characteristic change in structure above LCST temperature was also exploited for chitosan-g-poly(N-vinyl caprolactam) nanoparticles. These were injected into mice and the rate of drug release found to increase following a temperature increase above the LCST temperature of the polymer. This was confirmed by monitoring a fluorescent marker present in the cells which indicated 95 % of loaded drug had successfully been delivered (131). Temperature and pH are significant release factors as they are important states within the body and disease often alters both.

In addition to enhancing the control of drug delivery systems through smart polymers, nanoparticles expand the range of deliverable drugs and influence efficacy. For instance, there have been promising anti-cancer drugs derived from plant extracts that achieve high therapeutic action with minimal side effects such as umbelliferon (132) and curcumin (131). This is encouraging, as the drugs can be produced in high abundance resulting in affordable treatments. However, these extracts exhibit poor solubility and bioavailability, and cellular uptake is key to diminish tumour cells. These derivatives require assistance from nanoparticles to cross physiological barriers in order to be effective cancer treatments (132). Traditional cancer treatments like chemotherapy or photothermal therapy are extremely toxic and cannot differentiate between tumour cells and healthy cells, resulting in severe side effects. For this reason, it is paramount that delivery of anti-cancer drugs provides targeted release to minimise damage to healthy tissues. Nanoparticle therapy, in addition to improving the solubility of less toxic drugs for cancer treatment, also provides a level of control for the toxic drugs.

Controlled drug release *via* nanoparticles can be initiated not only by internal physiological stimuli, but external sources like electricity, near infrared light or magnetic field. Electropolymerized polypyrrole nanoparticles produced over dexamethasone (steroid) loaded micelles shown in **Figure 2.1.2.1** exhibited greatest yield of drug following a pulsated electrical signal for electrically triggered release (133).

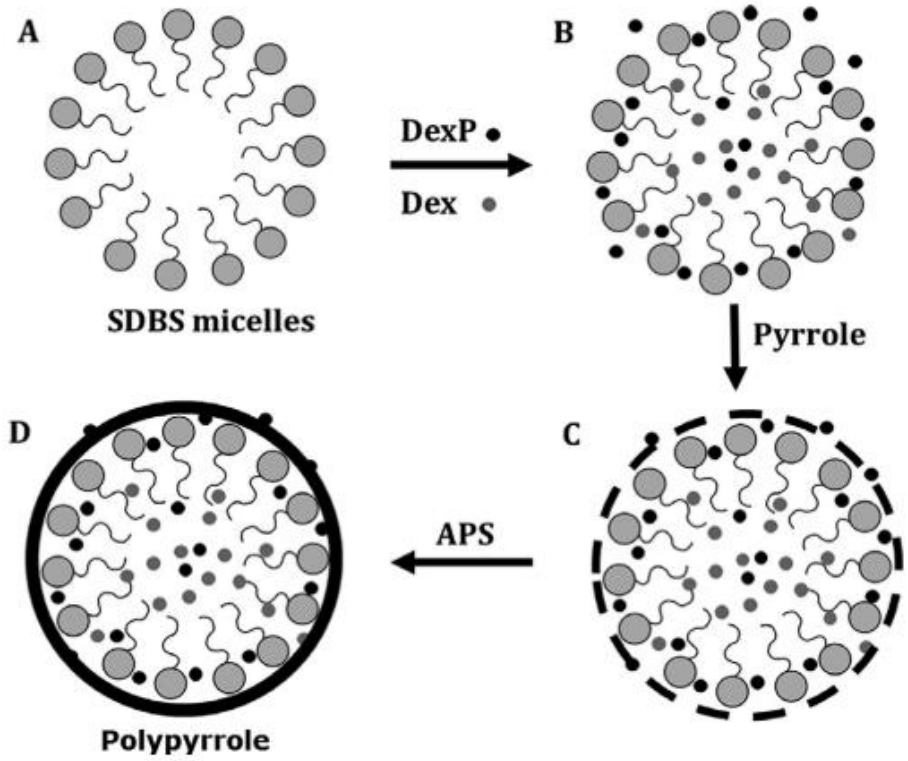

Figure 2.1.2.1 Proposed schematic of the synthesis of the polypyrrole (PPy) particles. A) assembly of sodium dodecyl benzene sulfonate (SDBS) into micelles, B) preferential association of dexamethasone base (Dex) with the core and dexamethasone sodium phosphate (DexP) with the outer shell of the micelles, C) association of pyrrole with the outer shell of the micelles and D) chemically driven polymerisation of PPy over the micellar template (133).

Interest in the use of graphene oxide (GOx) nanoparticles, a derivative of graphene, has increased due to its drug loading capacity and its antibacterial properties. Work by Khan *et al.*, (2017) reduced graphene oxide by stirring with gum arabica, thus, making hydrophilic. Following this, the hydrophilic GOx was combined with gold nanorods covalently bonded to doxorubicin (chemotherapy). The approach had a dual effect, whereby the GOx increased the absorption of near infrared light employed as phototherapy to kill cancer cells and the delivery controlled of doxorubicin from the gold nanorods provided chemotherapy (134). Freund *et al.*, (2012) found that magnetic nanoparticles could be directed to the target area *via* an applied magnetic field and hence are promising for cancer therapies (135). At present, however, their application is limited to the latter as they prove to be a challenge for cardiovascular treatments

due to the complex interactions between magnetic forces and fluid flow drag forces in arteries (136). Alternative nanoparticle formulations have been researched whereby the unique haemodynamic environment present in stenosed arteries are taken advantage of. In such cases, the release of therapeutics only occurs when a predefined threshold of abnormal shear rates is experienced – *i.e.*, those shear rates typically observed in blocked arteries (137). The mechanical aberrations experienced by the nanoparticle causes release of the medication to help remove the blockage (138).

Nanoparticles have been extensively researched for cancer treatment, offering enhanced efficacy, and widening the range of therapeutics available in order to circumvent the harmful side effects of chemotherapy and photothermal therapy. However, for other chronic conditions, where the treatment is not as toxic to normal tissue, they are still an invasive procedure as they are often injected by conventional hollow-bore needles. This does not offer an alternative for people who have phobias and does not address issues due to adherence or non-compliance.

2.2 Opportunities for Transdermal Drug Delivery

The skin is the body's largest organ and is highly accessible, providing an extensive surface area that could address some of the limitations associated with more traditional approaches discussed previously. Interest has grown in the development of pharmaceuticals as transdermal agents in recent years. The increased attention towards transdermal drug delivery systems has generated novel approaches with the aims to improve skin permeation, drug transport and drug release mechanisms, which could be combined with future transdermal patch technologies. When compared to drugs delivered orally or by injection, transdermal drug delivery possess numerous beneficial attributes, including control, time-release delivery, prevention of spikes in concentration in the blood (139) and evading premature metabolising by first-pass elimination (140). Moreover, transdermal routes are minimally invasive, and pain

is almost non-existent when compared to injections (141), as well as reduced waste production and the spread of diseases due to reuse of needles (140).

Transdermal drug delivery has traditionally referred to drugs that initially penetrate the stratum corneum, passing through the epidermis and deeper dermis which can then diffuse into the vascular system to be absorbed by the systemic circulation and therein transport the drug to its target site (142). Since transdermal drug delivery avoids the gastrointestinal tract, a lower dose can be administered as there is a short diffusion path to reach the vasculature. Not only that, it's also a non-invasive method which is virtually painless and permits repeated administration. However, since the stratum corneum is such an effective barrier to foreign molecules, very few drugs are favourable to diffuse through the lipid matrix. Only molecules that are small in molecular weight, lipophilic and potent can cascade through the stratum corneum into the deep tissue (143).

Aside from providing an alternative route from the GI tract, transdermal drug delivery is highly favoured among patients and has high adherence rates. Elderly people, especially, display high acceptability and satisfaction following transdermal drug application as their veins are often hard to find for intravenous injection due to dehydration (144). Furthermore, a study by Molinuevo *et al.*, (2014) found that in a sample of 649 Alzheimer patients, higher adherence rates were displayed for transdermal patches rather than oral medication over a six-month period (145). This is very significant as failure to follow medication properly disproportionately affects patients with memory issues. This has a detrimental impact on physical, mental, and social circumstances and can reduce the bioavailability of the drug.

Transdermal drug delivery provides a simple, patient centric approach to therapies granting self-administration providing patients with confidence and a sense of control over their own health care. Transdermal patches are portable, and wearable therefore offer freedom and independence with less of a burden. Lesser considered advantages to transdermal delivery are the fewer side effects and the lower chance of overdose as the patch can easily be removed (146).

2.2.1 Physiology of the Skin

The stratum corneum is the outer most layer of the epidermis which acts as a physical barrier preventing pathogens and irritants from getting into the body (147). It is comprised of extremely keratinized dead cells which form a lipid envelope some 900 µm thick, where the lipid matrix fills the extracellular space responsible for the skin's barrier effect. If a molecule penetrates the physical barrier, the lipid matrix can significantly hinder its diffusion. The diffusion rate within the lipid matrix has been estimated to be 10^{-3} cm h^{-1}. This is in contrast to a regular phospholipid membrane, which is two orders of magnitude faster of 10^{-3} cm^{-1} s^{-1} (148). There are very few nerve fibres within the stratum corneum, instead, they are bundled in the subcutaneous tissue and branch outwards from there (147) . For this reason, transdermal drug delivery has often been promoted as an attractive option to circumvent pain from injections.

2.2.2 Commercial Transdermal Drug Delivery

Transdermal drug delivery began with the use of creams, gel and ointments applied topically on the skin. At present, some 20 drugs have been adapted to the TDDS format (139), and this small number can be largely attributed to the difficulties associated with the drug being able to penetrate the stratum corneum (SC) and subsequent layers. At the time of writing, over 500 clinical trials relating to transdermal studies have been listed by the U.S National Library of Medicine, and around 80 of those are currently listed as open (149). In 2010, the international market for transdermal drug delivery was valued at $21.5 billion, of which the U.S alone contributes $3 billion per annum. Market analysis has attributed more than 12 % of the global drug delivery market to transdermal formulations (150). Some of the systems approved by the U.S Food and Drug Administration (FDA) are outlined in **Table 2.2.2.1** and consists largely of first-generation mechanisms relying on passive diffusion of small, lipophilic molecules. At present, most currently approved transdermal drug delivery systems are first-generation designs, featuring the primary components shown in **Figure 2.2.2.1**. These methods rely on the physiochemical qualities of drug being delivered, that permit transdermal diffusion. In order for drugs to be delivered this way, they must be lipophilic and possess a low molecular weight,

so it is unsurprising that a small range of drugs can be delivered by these means. Other approved transdermal drug delivery methods include topical creams and sprays which do not make use of a patch at all. For example, testosterone gel is applied topically to achieve slow release to the underlying blood supply following absorption by the stratum corneum (151; 152). The limitations of first-generation transdermal drug delivery systems have led to the development of second and third generations which have included numerous enhancements.

Year	Drug	Product	Application
1979	Scopolamine	Transderm Scop	Motion sickness
1984	Clonidine	Catapres	Hypertension
1986	Estradiol	Estraderm	Menopausal symptoms
1990	Fentanyl	Duragesic	Chronic pain
1993	Testosterone	Testroderm	Testosterone deficiency
1995	Epinephrine; Lidocaine HCl	Iontocaine	Local dermal analgesia
1995	Nitroglycerine	Nitro-Dur	Angina pectoris
1996	Nicotine	Nicoderm	Smoking cessation
1998	Estradiol; Norethindrone Acetate	CombiPatch	Menopausal symptoms
1999	Lidocaine	Lidoderm	Postherpetic neuralgia
2001	Ethinyl Estradiol; Norelgestromin	Ortho Evra	Contraception
2003	Oxybutynin	Oxytrol	Overactive bladder
2005	Lidocaine; Tetracaine	Synera	Local dermal analgesia
2006	Methylphenidate	Daytana	Attention deficit hyperactivity disorder
2006	Selegiline	Emsam	Major depressive disorder
2007	Diclofenac Epolamine	Flector	Nonsteroidal anti-inflammatory
2007	Rivastigmine	Exelon	Dementia
2007	Rotigotine	Neupro	Parkinson’s disease
2008	Granisetron	Sancuso	Chemotherapy induced nausea
2008	Menthol; Methyl Salicylate	Salonpas	Topical analgesic
2009	Capsaicin	Qutenza	Peripheral neuropathic pain
2010	Buprenorphine	Butrans	Chronic pain
2013	Sumatriptan Succinate	Zecuity	Acute migraine pain

Table 2.2.2.1 Commercially available transdermal drugs.

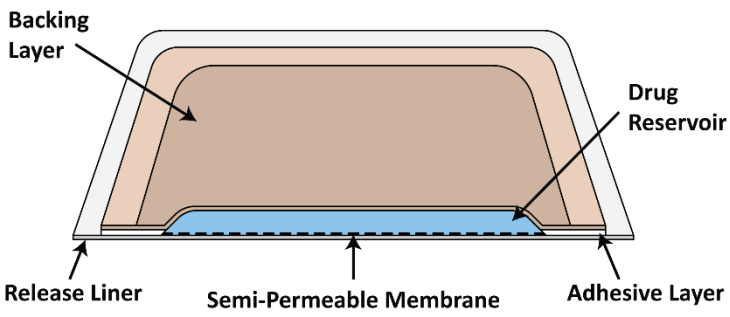

Figure 2.2.2.1 General first-generation transdermal drug delivery patch assembly.

Following the commercial success of some of those listed in **Table 2.2.2.1**, more research focused on widening the range of drugs to be delivered transdermally, and enhanced methods have focused on utilising pressure jets, iontophoresis, ultra-sound, laser ablation and microneedles, some of which have been released commercially and have clinical uses summarised in **Table 2.2.2.2** below (153; 154). Although there have been some commercially available enhanced transdermal drug delivery systems, they are still not widespread and innovation in this area continues which is discussed in more detail in the next section.

Type	Method	Drug	Use	Brand name	Limitations
Passive patches	Patch applied topically and therapeutics diffuse across the skin	Nitro-glycerine Estradiol Fentanyl Scopolamine	Prevent angina Hormone replacement Pain relief Motion sickness	Nitro-Dur Vivelle-Dot® Duragesic Transderm Scop	Range of drugs are limited
Pressure driven jets	Pressure applied at velocity 100-200 m/s to puncture skin	Somatropin	Human growth hormone	TJet ®	Limited acceptance due to bruising, pain, cross-contamination issues
Iontophoresis	Electric current applied 0.1-1 mA cm^{-2} drives molecules through skin	Lidocaine Epinephrine Fentanyl Sumatriptan	Local anaesthetic Allergic reactions Pain relief Headaches	Phoresor®	Not adapted for larger molecules, can cause cell death, damage proteins thus bioactivity
Ultra-sound	Generate microbubbles that mechanically interrupt the skin		Local anaesthesia	Sonoprep®	High intensity ultra-sound can cause second degree burns
Laser ablation	Removes local areas of the stratum corneum				Lack of control, painful, causes skin irritation
Microneedles	Pierce the stratum corneum creating micro-channels for drug to diffuse	Teriparatide	Osteoporosis	MicroCore® PTH Admin Patch ®	Made from stainless steel so risk of needles breaking and remaining in the skin

Table 2.2.2.2 Commercially available transdermal drug delivery devices.

2.3 Innovative Approaches to Transdermal Drug Delivery

For transdermal drug delivery to be feasible to a much wider range of drugs, the stratum corneum must be disrupted. Technology like iontophoresis has been developed to improved permeation of drugs by way of applying a low intensity current around a drug reservoir to encourage drugs to be transported (155). Electroporation, chemical enhancement, ultrasound, and thermal ablation have also been applied but, in many cases, the procedural and instrumentational requirements are significant and inappropriate for everyday application. More recently, the increasing accessibility of manufacturing methods for the production of microneedles has provided an alternative means through which to disturb the stratum corneum physically creating a microchannel through which drugs, regardless of size, can diffuse (156). These approaches are considered in more depth in the subsequent sections and their merits/limitations in terms of drug release are critically appraised.

2.3.1 Iontophoresis

Iontophoretic drug delivery is the application of low intensity current (0.3 – 0.5 mA / cm^2) to a biological barrier and a drug reservoir, which the drives the stored therapeutics into the desired tissue. The typical set-up encompasses a power supply and two electrodes – the drug delivery electrode and a returning electrode, which facilitates the transportation of drugs *via* electromigration and electroosmosis illustrated in **Figure 2.3.1.1** (155; 157; 158).

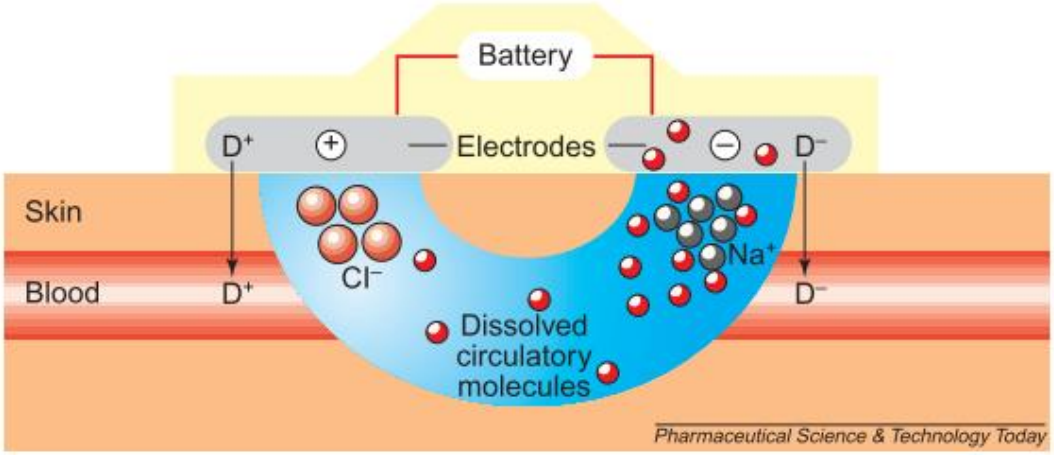

Figure 2.3.1.1 The mechanism used by iontophoresis to delivery drugs transdermally (158).

Electromigration refers to the repulsive/attractive force between the two electrodes employed - the drug electrode and the returning electrode, which drives therapeutics through the tissue and towards the returning electrode. Electroosmosis refers to the transportation of drugs within a solvent by convection flow that is induced by the potential difference of the charged tissue (155). For instance, when the skin shifts above its isoelectric point which is pH 4 – 4.5, the carboxylic groups ionise becoming negatively charged. When current is applied, internal anions like Ca^{2+} are drawn towards the skin changing the potential. This subsequent solvent flow can then carry dissolved drugs towards the cathode – the returning electrode. However, when the skin is below the isoelectric threshold, electroosmosis plays a negligible role in drug delivery therefore pH greatly influences which mechanism is at play during iontophoresis (155; 157).

Initially, transdermal drug delivery that exploited iontophoresis was used to treat topical conditions like psoriasis, alopecia, skin cancers and acne (155). Through combining iontophoresis with nanoparticles encapsulating therapeutics, larger hydrophilic molecules can be delivered. Moura *et al.*, (2022), formulated a lipid-based nanoparticle loaded with lopinavir (antiretroviral for HIV) which historically has poor oral bioavailability and digestive side effects which can be avoided by delivering *via* the transdermal route (159). The effects of iontophoresis on lipid dynamics were examined and the drug remained viable even after applying current for six hours. No passive release was observed within a Franz cell set-up due to the lipophilicity of the nanoparticles. Following the application of 0.5 mA/cm^2, significant drug release was observed, a distinction was noted between cathodic and anodic iontophoresis and in this instance anodic iontophoresis was favourable with the highest flux of release, enabled by electromigration (159). Since release *via* iontophoresis is controllable, individualistic, and pulsed release profiles are achievable and Djabri *et al.*, (2019), explored the delivery of midazolam by transdermal iontophoresis within the paediatric population. The solubility of midazolam (anaesthesia) is very low at pH 5, which is increases in more acidic environments

as the drug is in its ionized form. Through the application of current the drug can penetrate porcine skin and a linear relationship is observed between drug flux and current (160).

Iontophoresis improves transdermal drug delivery particularly when the drug fits the desired characteristic to move across the stratum corneum such as low molecular weight, lipophilicity non-polar. Through combining with nanoparticles, more variation is attainable however, the process can result in irritation and blistering, and the site must be changed if multiple doses are applied to avoid trauma (161).

2.3.2 Electroporation

Electroporation is regarded as an active drug delivery enhancement. The technique applies a high pulsating voltage for a given length of time to biological tissue, the pulses alter the structure of lipid bilayer creating aqueous pores to improve drug permeation. Various electrode styles have been employed such as: needles, plates, needle-free microelectrode arrays, and multi-electrode arrays. The quantity and frequency of drug dosing is controlled by varying the magnitude of the voltage applied, the duration of the applied voltage and the number of pulses. When applied to the skin, electroporation reduces the resistance across the stratum corneum, and the electric field can penetrate the deeper layers of the dermis enhancing the diffusion of molecules into the interstitial fluid (162). When the method is used on mice skin for five minutes pores formed to allow drugs to pass and closed gradually over twelve-hour period, thus electroporation is reversible making it safer (162; 163). The formation of pores enhances the delivery of topical drugs applied after electroporation treatment. However, the method can be used in combination with polymer films loaded with therapeutics. Anirudhan *et al.*, (2019), developed a polymer film loaded with carbon nanotubes decorated with gold nanoparticles to deliver diclofenac sodium (anti-inflammatory) through the dermis. The application of electroporation method improved the yield of drug, and 10 V was the most favourable for drug permeation (164).

2.3.3 Chemical Enhancement

Ionic liquids are composed of salts with a melting point below 100°C, of distinct cations and anions which determine the lowered melting point (165; 166). They have numerous uses within the pharmaceutical industry as solubility enhancers, antibacterial agents, stabilisers, and skin penetration enhancers for active therapeutic ingredients (165). Ionic liquids enhance transdermal drug delivery by chemically reducing the stratum corneum, disrupting the regular arrangement of keratin for drugs to pass (167).

Choline cation ($[CH]^+$) is commonly employed for the use in ionic liquids as it is non-toxic and readily available in many living organisms as a basic component of vitamin B4 which is ideal for biomedical applications and transdermal drug delivery (165). Ionic liquids have been combined with an oil phase as a microemulsion to enhance transdermal delivery, where midazolam is the ionic liquid component and 1-hydroxyethyl-3-methylimidation chloride as the transdermal enhancer to deliver artemisinin (anti-malarial) (167). The use of ionic liquids increases the solubility of the drug as well as changing the physiochemical properties of the stratum corneum for example the solubility of ketoprofen, flurbiprofen and loxoprofen (nonsteroidal anti-inflammatory drugs) was enhanced 4.5-fold and permeation of the drugs was enhanced 9.3-fold when delivered exploiting triethylamine ionic liquid (166).

Although ionic liquids can have numerous advantages to the pharmaceutical field, particularly transdermal drug delivery, their safety is a concern. The effect that ionic liquids have on the skin has not been thoroughly evaluated at present. There is evidence that organic substances produce oxidative stress on the skin causing dermatitis and skin lesion. In addition, studies indicate that ionic liquids can be toxic on the environment (168). Another challenge with the use of ionic liquids for transdermal drug delivery is their stability, as they must be stored under inert gas and in 4°C fridge (169).

2.3.4 Ultrasound

Ultrasound initiated drug delivery makes use of the longitudinal sound waves and mechanical energy transferred by particles oscillating from one point to another. The frequencies of the

oscillations have been classified into low frequency (20 – 100 kHz), therapeutic frequency (0.7 – 3 MHz) and high frequency (>3 MHz), in recent years it has been found that low frequency is optimum for transdermal drug permeation. The mechanism in which ultrasound waves interrupt the stratum corneum is somewhat unclear, however, it is recognised that cavitation occurs. This process induces particle oscillations and create pressure forming bubbles that result in a disturbance in the skin's lipid barrier allowing molecules to penetrate (170). Additional processes that enrich drug permeation following ultrasound application relate to acoustic streaming, rectified diffusion and the thermal effects associated with ultrasound. These processes also produce strong shockwaves that interrupt the stratum corneum (171). Acoustic streaming is a phenomenon where unidirectional flow currents are produced in fluids as a result of the applied sound waves. The currents are due to ultrasound reflections and distortions that occur during wave propagation (172; 173). Rectified diffusion relates to the cavitation that occurs due to the application of ultrasound. During the application of ultrasound the bubbles repeatedly expand and compress and the diffusion of dissolved gases into and out of these bubbles refers to rectified diffusion (174; 175).

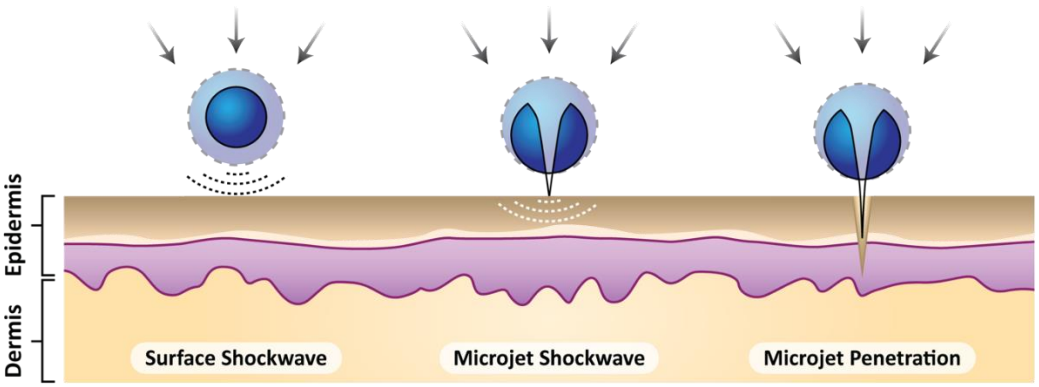

Figure 2.3.4.1 The mechanism used by ultrasound to delivery drugs transdermally.

Ultrasound initiated drug delivery can deliver non-ionized and non-magnetic therapeutics in addition to increasing the permeability of macromolecules like insulin, glucose and vaccines which depends on the frequency and acoustic pressure of the ultrasound. A nanoparticle of diameter 200 nm penetrated more deeply into skin tissue, following a 42 kHz ultrasound application (176). The ultrasound parameters must be tuned depending on the component

being delivered, for example, econazole nitrate (antifungal) has optimum topical permeation on porcine skin model post application of 20 kHz for two minutes (170). The methods just described discuss how ultrasound alters the skin to allow molecules to penetrate, however smart materials can also be exploited. Ultrasound responsive poly(lactic-co-glycolic acid) microplates containing curcumin (anti-inflammatory) were treated with 1 MHz frequency – close to the material resonance frequency, causing degradation of the vehicle to expel the drug with a 200 % increase in delivery. The use of such materials is appropriate for smart wearable systems that provided triggered transdermal delivery (177). Examples of long-term drug delivery have been achieved in porcine skin model for the delivery of enfuvirtide (anti-retroviral) over one month, where ultrasound of 24-26 kHz was applied for thirty minutes every day (178).

2.3.5 Thermal Ablation

Transdermal drug delivery can be achieved by passing a precise laser epidermal system laser over the skin ensuring the beam diameter is as small as possible to avoid unnecessary destruction. The method works by exciting water within the dermis inducing evaporation and creating micropores and thereby allowing therapeutics to travel through.

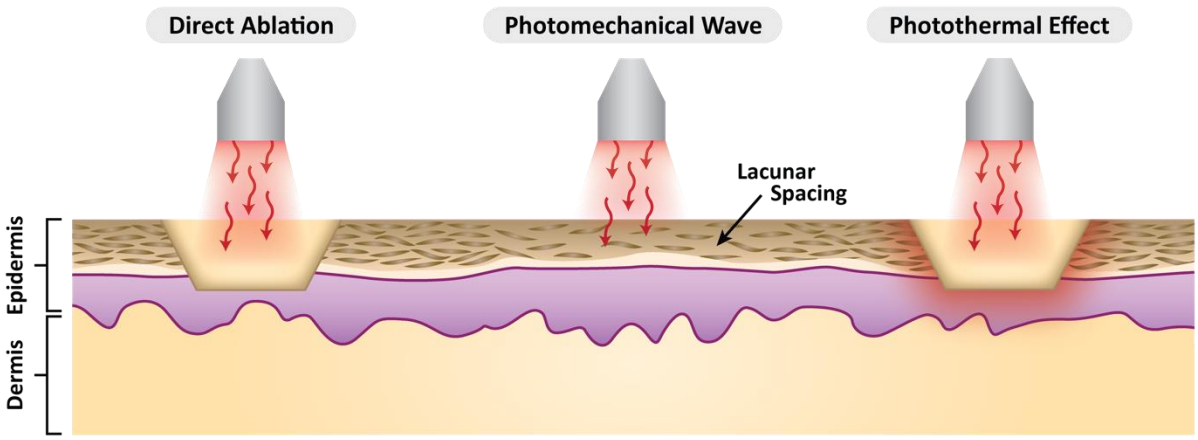

Figure 2.3.5.1 The mechanism used by laser ablation to delivery drugs transdermally.

An important note to make, is that the energy pulse applied by the laser is shorter than the thermal relaxation time of water so there is negligible heat transfer and Lee *et al.*, (2011),

recommended applying pulses for milliseconds at a time to avoid significant cell damage to deeper tissues (179; 180). Gou *et al.*, (2019) delivered pentoxifylline (blood circulation medication) to laser porated skin (where the outermost barrier layer is removed), for forty hours as the medication has low oral bioavailability, and after time had passed the pores closed circumventing the risk of infection (181). Although the selective destruction of the epidermis by microscopic ablation zones allows for deeper penetration and absorption of topically applied medication, there are some mild side effects like burning, pain, acne and dyspigmentation in darker skinned patients that could reduce compliance at best, or at worst, severe symptoms like scarring, local infection or systemic infection due to the compromised skin barrier (182).

Although there is merit to these innovative approaches to transdermal drug delivery, the approaches require complex instrumentation which, in most cases, have not yet been miniaturized to provide point of care treatment. They require training and have not yet been automated to remove the burden of dosing from the patient and they are a two-step process of altering the stratum corneum and followed by topically applied medication as a cream/ emulsion or nanoparticles.

2.4 Microneedles

Microneedle's blend traditional injections on a microscale with transdermal patches. Generally, microneedles are 25 – 2000 μm in height, with a 20 – 250 μm base and 1 – 25 μm tip diameter with the shorter variations minimising the risk of aggravating nerves making them painless and minimally invasive (142; 156; 183; 184). Microneedles can be categorized by their function, and it is widely accepted that there are five broad categories: solid, coated, hollow, dissolving and hydrogel forming (142; 183) as presented in **Figure 2.4.1**. A more detailed consideration of each type is presented in the following subsections.

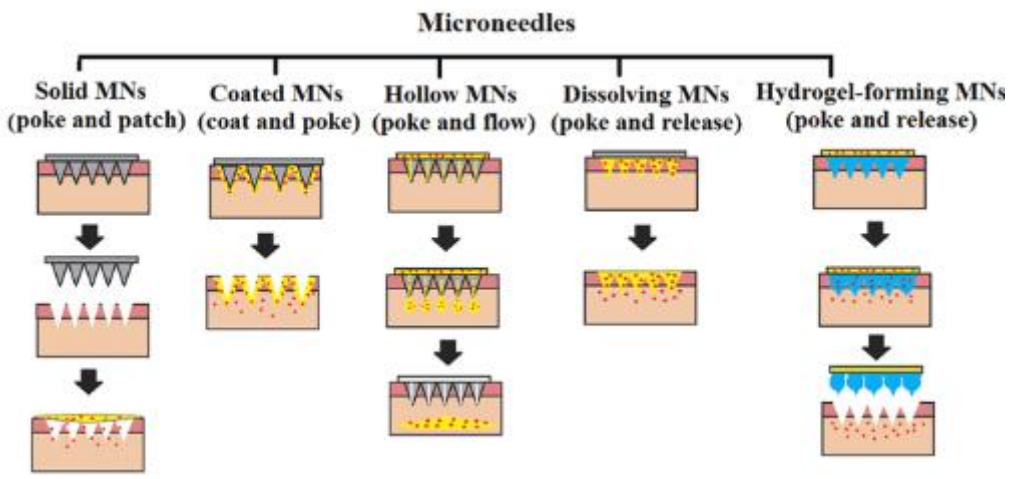

Figure 2.4.1 Different categories of microneedles, solid, coated, hollow, dissolving and hydrogel forming (183).

2.4.1 Classification

2.4.1.1 Solid / Coated

Solid microneedles are typically fabricated using metals or silicon and have two main functions: the microneedle can be used as part of a two-step process whereby the microneedle pierces the skin, creating microchannels and a medicated patch is applied afterwards to facilitate diffusion, or the drug is coated onto the microneedle and upon piercing the skin the coated drug is hydrated and can diffuse into the dermal layers (148; 156; 184; 185).

The commercially available Admin Patch® introduced in **Table 2.2.2.2**, has been used to temporarily disrupt the stratum corneum to create microchannels which could then aid the topical administration of nano-emulsions. This “poke and patch” two-step approach with the microneedle pre-treatment was reported to improve aceclofenac (anti-inflammatory) delivery across rat skin into systemic circulation (185). A similar study found that the poke and patch method employing a microneedle roller permitted the passive transport of various molecules regardless of size. The roller exhibited heightened mechanical strength to deliver potassium chloride (to replenish potassium deficiency) solution rapidly and approximately ten times more potassium chloride solution was delivered following the microneedle treatment than without (156).

Alternatively, porous solid silicon microneedles coated boron doped silicon wafer demonstrated the ability to release drugs upon hydration of the coating from the skin's interstitial fluid. During fabrication, the pores formed boosted the potential yield of drug by increasing the surface area for the coating to adhere, which could be tuned during the manufacturing process. However, the process was difficult and volatile such that small changes in conditions like local solution strength, temperature and sample geometry can cause the process to be halted prematurely (184). Although coated microneedles can be used as a vehicle for a variety of molecules like proteins to deliver vaccines, the fabrication process is challenging. Since proteins are inherently sensitive to degradation, unfolding and aggregation, achieving a uniform coating with "active" components can be difficult. Despite this, the research is promising where successive dip coating increases the quantity of protein on the microneedle surface. This has been shown to allow for homogenous diffusion into the tissue within minutes after a simple manual insertion. This is significant, as microneedles offer a strong immune response when delivering vaccines due to nearby dendrite cells within the dermis. (186).

Despite successfully bypassing the stratum corneum, solid microneedles are not flawless in design. There is a risk of breakage which could leave behind sharps in the stratum corneum. In addition, the quantity of drug that can be delivered is limited with little control over the rate of drug delivery.

2.4.1.2 Dissolvable

Following solid formulations, research began in the development of dissolvable microneedles, where therapeutics are loaded into a biodegradable polymer matrix countering the issues of biocompatibility and needle fragmentation. Loaded drugs are delivered after rapid dissolution of the microneedle following penetration of the stratum corneum. Dissolvable microneedles do not pose the same safety concern as solid microneedles as no sharp needles can remain in the skin, there is also the potential of greater quantity of drug being delivered as the drugs are loaded into the polymer matrix rather than being confined to the external surfaces. In

principle, it also aided fabrication as achieving a uniform coating on pyramidal surfaces can be challenging. (187).

Vora *et al.*, (2020), developed a pullulan-based microneedle array with mechanical integrity and low solubility in lipids to ensure drug release only occurred following penetration of the skin. The array was tested using porcine skin and 80 % dissolution occurred ten minutes after piercing creating microchannels to facilitate transdermal delivery (187). Pullulan is a pertinent choice as it is highly biocompatible, natural polymer so it is readily available and supported the release of insulin trans-dermally to human abdominal skin (188). A balance between polymer and loaded drug needs to be achieved otherwise the structural integrity of the needles can become compromised with high drug loading. This is exemplified in a study by Jeong *et al.*, (2018) who studied the incorporation of cyclosporin A (immunosuppressant), a drug of high molecular weight into hydroxypropyl cellulose needles for transdermal delivery. Increased loading of cyclosporin A made the needles more brittle and likely to fracture. Clearly, caution is needed to avoid over-loading the polymers with the drug component in order to maintain needle strength. When the quantity of drug was fine-tuned, the transdermal delivery displayed a higher efficacy than orally delivered. Pharmacokinetic tests in rats showed that a dose of 5 µg/mL concentration remained in the blood for seventy-two hours in contrast to only twenty-four hours for the orally delivered medication (189).

Two-step fabrication processes can be seen whereby the needles and base plate have different formulations. This can be seen when needles were comprised of chondroitin sulphate and polyvinyl pyrrolidone (PVP) loaded with neurotoxin and where the base plate comprised of carboxymethyl cellulose. Complete dissolution was observed in rats after just ten minutes (190). Similarly, a two-step casting process with PVP loaded with vitamin B12 formed the needle and PVP formed the baseplate. The needles were loaded with 135 µg of vitamin B12 of which 72.92 % was delivered over five hours. Since the drug was only present in the needles, waste was reduced (190; 191).

The biocompatibility and safety of dissolvable microneedles offer a significant advantage over solid approaches. In order for dissolvable microneedle to be viable options for transdermal drug delivery that provide the option for multiple dosing, the yield of drug must be improved by way of drug reservoirs.

2.4.1.3 Hollow

Hollow microneedles are comparable to the traditional subcutaneous needles although they do not reach the depths of the latter, therefore they can retain the minimally invasive character. Intradermal injection performed by classic needle is difficult and requires a high degree of expertise. In contrast, the use of a hollow MN array allows depth to be controlled more easily (dictated by the length of the needles) and doesn't require training (192). Typically, the drug is stored in a liquid reservoir to be delivered upon piercing the skin (193) and are delivered at different rates based on pressure flow (194). One advantage of such systems is that hollow microneedle arrays can now be purchased commercially allowing researchers to refine drug formulations rather than developing time consuming needle designs.

Hollow microneedles can deliver a wide range of substances and are not limited to small molecule targets. A pertinent example is the delivery of Escherichia coli specific T4 bacteriophages (vaccine) using a polycarbonate hollow microneedle to porcine skin. The needles penetrated to a depth of 600 μm however delivery throughout all the layers was difficult. It was reported that the microneedles had a 100 % penetration efficiency regardless of applied force between 0.05-0.4 N/needle (195) emphasizing the ease of use.

Delivery of nucleic acids is a challenge as they are often removed by the spleen, renal and hepatic systems when delivered by traditional injection methods. For this reason, local delivery *via* microneedle is often promoted as a significant advantage. A commercially available MicronJet600 array consisting of hollow needles 600 μm long was used by Golombek *et al.*, (2018), to deliver mRNA labelled with Cy3 (fluorescent label) to a porcine skin model. The injection of a 1.5 μg dose demonstrated high luciferase activity in the surrounding medium forty-eight hours after delivery therefore high efficacy was achieved (193).

Hollow microneedles are not restricted to delivering liquid formulations and in recent years, the delivery of nanoparticles has been demonstrated. Poly Lactic-co-Glycolic Acid (PGLA) nanoparticles encapsulating model antigen ovalbumin (protein) and TLR3 ligand (RNA) were delivered using hollow microneedles. The hollow microneedle delivery brought about a much superior immune response than delivery using dissolving microneedles (196). The same model was used in rats and displayed a unique pharmacokinetic profile characterised by an early burst transit though the draining of lymph nodes and had a higher immune response compared to intramuscular injection. The delivery of the PGLA nanoparticles was brought about using a pre-clinical version of a 3M hollow micro-structured transdermal system. The latter precisely delivered 2 mL to the dermal layers without oozing out of injection site and impinging on any nerves so was painless (197). Arguably the greatest advantage of hollow microneedles is their ability to deliver large quantities of liquid solution. This opens the possibility to fabricate smart nanoparticles which are difficult to deliver using other kinds of microneedles.

2.4.1.4 Swellable

Swellable microneedles often take advantage of hydrogels which are biocompatible polymers with 3D porous structures that can swell in water (40). Upon piercing the skin, the hydrogel needle swells upon contact with the interstitial fluid thus resulting in a phase change that allows the loaded drug to be mobilised to diffuse and be delivered across the skin (198). Some of the more notable advantages to the use of swellable microneedles is that the needles can be removed without leaving polymeric residues. This counters the limitation inherent to dissolvable microneedles where complete dissolution may not be achievable. The swellable system also counters the risk of blockage which can impact on the efficiency of hollow microneedles (199). Through careful design, the swelling feature can be used as a mechanical interlock with tissue upon swelling. This was illustrated with the use of a polystyrene-block-poly(acrylic acid) swellable tip and a non-swellable polystyrene core shown in **Figure 2.4.1.4.1**. The tips enlarged 60 % and released 90 % of the coated insulin after thirty minutes. Burst release was observed initially and sustained for six hours (200).

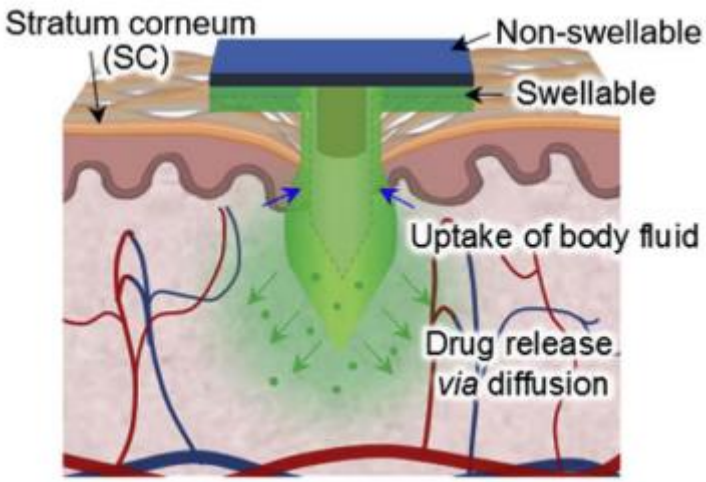

Figure 2.4.1.4.1 Schematic of polystyrene-block-poly(acrylic acid) swellable tip and a non-swellable polystyrene core as mechanical interlock in the skin (200).

Swellable microneedles offer a great degree of flexibility when it comes to rate of drug release by fine tuning the percentage of hydrogel. This was demonstrated by Yin *et al.*, (2018) through the use of a silk fibrin microneedle which exhibited a 500 % swelling capacity. Hydrogels often have poor mechanical properties, so this is an important factor when fine tuning drug release. The silk fibrin microneedles could withstand a force of 0.25 N/needle - sufficient to pierce skin (40). A blend of Gantrez®, poly(ethylene glycol) (PEG) and sodium carbonate was investigated as a means of delivering ketamine (anaesthetic) which is typically delivered by intravenous or intramuscular injection. The drug was immobilised in a film acting as a reservoir, and when introduced to an aqueous solution, the hydrogel blend swelled by 1760 % after twenty-four hours which enabled the delivery of the drug after ninety minutes. The needles exhibited good mechanical strength and were able to pierce parafilm to a depth of 200 µm and can be considered sufficient to pierce the stratum corneum which is 50 µm thick (198). Although hydrogels themselves often lack inherent mechanical strength, through blending with other polymers, the strength can be tuned whilst also allowing for controllable release. Hydrogels are often referred to as smart materials that can be tuned to swell and expel drugs following an external stimulus – not only upon hydration which is a passive form of release.

2.4.1.5 Conductive Microneedles

The design and production of microneedles intended for sensing applications has seen a wide variety of strategies adopted and these have been extensively reviewed (201; 202; 203; 204). In most cases, moulds based on PDMS tend to be the replication workhorses and offers an easy route through which to manipulate the material composition of the MN and thereby refine its properties (205; 206; 207; 208; 209). This micro moulding approach has obvious advantages for drug delivery applications - providing a simple means through which to incorporate the therapeutic agent, but it has also been shown to enable the production of MN arrays for sensing applications. The potential viability of the approach was initially demonstrated using composite palladium / polycarbonate MN structures (210) to yield sensitive electrochemical sensors. The incorporation of carbon nano particles within polystyrene MN structures however greatly increases the analytical remit (Hegarty *et al.*, 2019) and allows the MN to exploit the wealth of detection strategies previous developed at conventional carbon electrodes (211).

The principal issue with the current approaches to carbon-based microneedles relates to the relatively poor electroanalytical performance of the systems. The use of graphitic carbon nano particles offers a relatively inexpensive option for manufacture, but electron transfer can be slow and thereby compromises voltammetric resolution.

2.5 Conclusion

After reviewing the literature, it is clear that traditional methods of drug delivery possess a range of limitations and, in many cases, can be problematic and ineffectual for the patient. Although oral medication is simple to administer but the full potential of the therapeutic is seldom achieved due to physiological conditions along the gastrointestinal and the impact of the first-pass metabolism. Injections provide more direct route to systemic circulation, however, they are invasive and painful which hinders compliance. The latter also bring in to question the waste associated with injections and the risk of misuse and infection by blood

borne pathogens. The transdermal route avoids the pitfalls of traditional delivery mechanisms as provides a fast pathway to systemic circulation whilst being non-invasive. Emerging drug delivery trends are focusing on controlled and targeted drug release, using nanoparticles and implantable devices as vehicles to deliver drugs on demand. Research in these areas is admirable, however the administration needs to be carried out by trained professionals. Controlled transdermal delivery by iontophoresis and ultrasound also requires a level of expertise to achieve drug delivery. Microneedles provide a more simplistic administration that can be carried out by the patient, where an external signal can initiate drug release (*e.g.*, voltage for conductive microneedles).

Chapter 3

Experimental Techniques and Methodology

Overview

This chapter outlines the scientific principles through which the project is based and details the experimental methods employed throughout the project. It is important to note that any specific procedural or instrumentational requirements or modifications to the various experimental set-up are detailed in each chapter.

3.0 Materials and Instrumentation

Chemicals used were purchased predominantly from Sigma-Aldrich (UK) and were the highest grade available and used without further purification unless otherwise specified. Solutions were typically prepared with Britton-Robison (BR) buffers (0.04 M acetic, boric, and phosphoric acids), with the addition of concentrated sodium hydroxide facilitating the adjustment of the pH to an appropriate value. Each buffer was supplemented by the addition of potassium chloride (0.1 M) to provide electrolytes and to define the potentials of silver-silver chloride pseudo-references. Deionised water from Elgastat water system (Elga, UK) was used throughout to prepare all solutions.

Moulds to fabricate microneedle arrays were acquired from Micropoint Technologies Pte Ltd (Singapore) and were pyramidal in format with 200(base) x 500(pitch) x 700 (height) micron dimensions covering a 10 x 10 needle array. A typical silicone mould used in the production of microneedles used in the present project and example of the resulting microneedle array are shown in **Figure 3.0.1**.

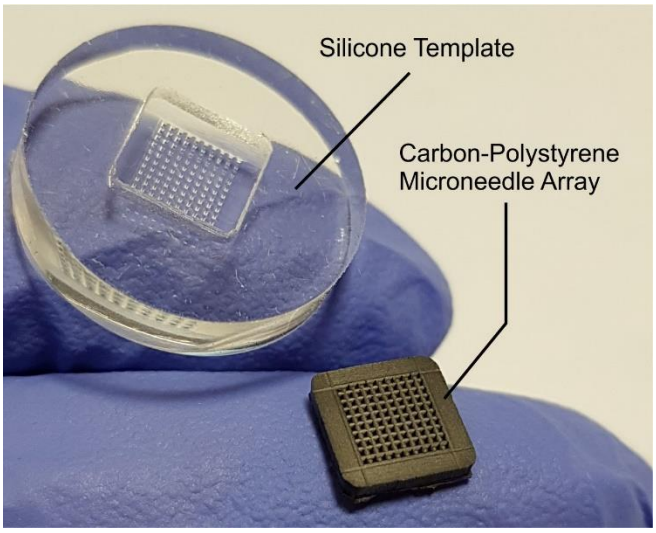

Figure 3.0.1 Silicone mould and resultant microneedle array.

Each microneedle array typically comprises a rectangular block with needle projections on one face as indicated in **Figure 3.0.2A**. The sides of the block and the back panel are coated in enamel paint to serve as an insulating/dielectric layer such that only the face with the

needles can act as an electrode. On a simple level the active geometric area could be considered as 6 mm x 6 mm, but this does not consider the additional area provided by the surface of the needles. Each needle is pyramidal in shape as indicated in **Figure 3.0.2B**.

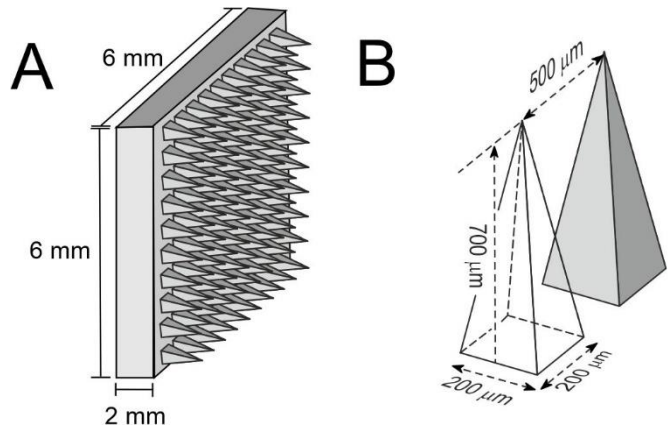

Figure 3.0.2 Typical dimensions of the A) microneedle patch and B) individual needles.

The area of the pyramid can be obtained using **Equation 3.1**.

Eq 3.1

$$A = lw + l\sqrt{\left(\frac{w}{2}\right)^2 + h^2} + w\sqrt{\left(\frac{l}{2}\right)^2 + h^2}$$

Where: l, w and h represent the length, width, and height of the pyramid.

Based on the dimensions outlined in **Figure 3.0.2B**, the total area of each needle (including pyramid base) = 3.23 x 10^{-7} m^2.

There are 100 needles in a patch, therefore the combined surface area = 2.83 x 10^{-5} m^2.

It is necessary to calculate the area of the patch between the individual needles – the base layer – which will be exposed to the solution.

The face of patch without any needles would be 6 mm x 6 mm = 3.6 x 10^{-5} m^2.

The base of each pyramid is 4 x 10^{-8} m^2 and thus 100 bases = 4 x 10^{-6} m^2.

Thus, the area of base layer of the patch exposed to the solution when the needles are present = $3.6 \times 10^{-5} - 4 \times 10^{-6} = 3.2 \times 10^{-5}$ m^2.

We know that the total interfacial area attributed to the needles is 2.83×10^{-5} m^2, therefore, the total geometric area of the microneedle path exposed to the solution is $2.83 \times 10^{-5} + 3.2 \times 10^{-5} = 6.03 \times 10^{-5}$ m^2.

Electrochemical analyses were carried out using either a Palm Sens EmStat 3 or Zimmer Peacock Anapot computer controlled potentiostat. In most cases, a standard three-electrode configuration was employed in which the microneedle patch or a laser induced graphene substrate acted as the working electrode with platinum wire and a Ag|AgCl half cell (3M NaCl, BAS Technicol UK) acting as counter and reference respectively. All measurements were conducted at 22°C ± 2°C. Specific details relating to particular investigations are noted within the corresponding chapters.

3.1 Electrochemical Instrumentation and Methods

Electrochemistry studies the transfer of electrons between the working electrode and electrolyte solution, driven by chemical processes. The resultant electrical response obtained from electrochemical analysis provides qualitative and quantitative data, establishing the kinetics and thermodynamics of a certain reaction (212; 213). In this instance, electrochemistry is utilized to characterise the electroanalytical performance of the conductive microneedle patches and laser induce graphene substrates. It was also used to trigger the release of drug conjugates in addition to discretely determining their presence thus enabling controllable release. This is accomplished by oxidising or reducing a drug tether at the electrode interface at suitable potentials. It is widespread practice from an electrochemical perspective, to modify the working electrode to enhance sensitivity by either chemical (214) or physical (215) means. In this work, a number of surface modification methods have been utilised and are detailed within the relevant sections. Electrochemistry is favourable when compared to traditional

laboratory analysis as a range of electrode types can be used regardless of size, cost, and application (216).

3.2 Fundamental Electrochemistry

3.2.1 Underpinning Concepts

A basic understanding of electrochemistry is critical to the work presented herein as it allows the inter-relation of chemical reactions induced by the transfer of an electrical current to be employed in the design of new biomedical devices. The processes that can influence the transport of charge across electrode-solution interface are of particular importance as proposed devices are, ultimately, intended for direct contact with the skin and underlying interstitial fluid. A host of variables can affect electrochemical behaviour and can include: the material used to construct the device, the composition (and condition) of the interface, mass transport effects and electrical factors such as the potential applied and current obtained. The electrode reaction occurs when electrons are transferred to or from the electrode material being employed. Consider the electrode reaction in **Equation 3.2**.

$$O + ne^- \rightleftarrows R \qquad \textbf{Eq 3.2}$$

This will consist of a sequence of transitions ultimately causing the conversion of O to its reduced form R. These steps are highlighted in **Figure 3.2.1.1**. In this case, the rate of the electrode reaction tends to be controlled by:

i) mass transport (transfer of O from solution bulk solution to the electrode);

ii) the rates of any associated chemical reactions;

iii) the electron transfer kinetics at the immediate electrode-solution interface and;

iv) any other additional reactions that may occur such as adsorption and desorption.

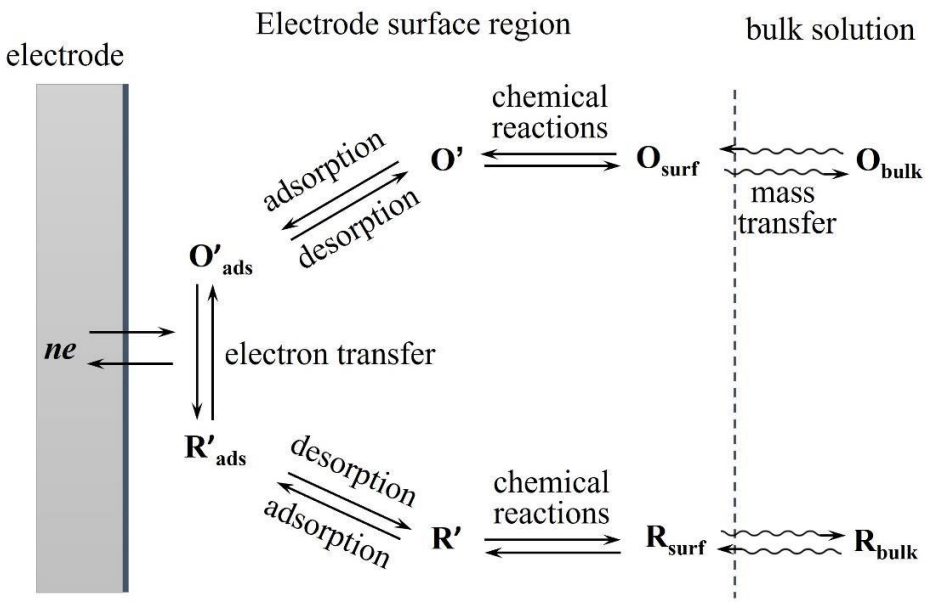

Figure 3.2.1.1 Typical electrode reaction and the sequence of steps involved.

The electrode reaction is driven by the application of an external potential. The latter has the effect of altering the energy of the electrons within the given electrode material. Hence, the energy of the electrons can be increased by imposing more negative potentials (*via* control from a potentiostat). The consequent flow of electrons from the electrode to the solution commences when their energy is greater than the lowest unoccupied molecular orbital (LUMO) of the target analyte (217; 218). This results in the production of a reduction current as indicated in **Figure 3.2.1.2A**.

In a similar manner, the application of a positive potential bias results in the electron energy being lowered below the highest occupied molecular orbital (HOMO) of the target analyte and thereby favours its oxidation at the electrode interface (**Figure 3.2.1.2**). These critical potentials are determined by the standard potential (E^o).

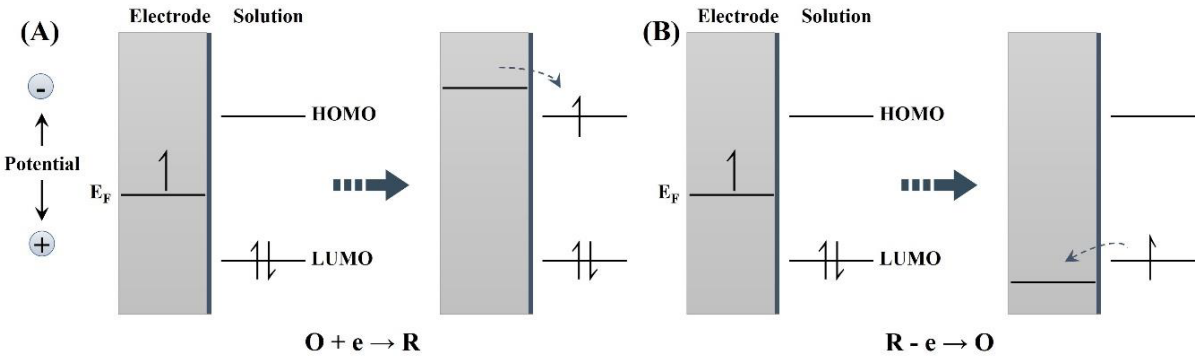

Figure 3.2.1.2 Schematic highlighting the reduction and oxidation processes of a target analyte in solution. Where (A) represents a negative potential raises the Fermi level (*EF*) of the electrode and thereby the reduction of the analyte; (B) highlights the lowering of the *EF* of the electrode by a positive potential bias thereby inducing oxidation of the analyte.

The relationship between the equilibrium potential (E_{eq}), and the concentrations of reactants in the electrode reaction defined earlier in **Equation 3.2** is described by the Nernst Equation (219; 218):

$$E_{eq} = E^0 + \frac{RT}{nF} \ln \frac{a_O}{a_R} \qquad \textbf{Eq 3.3}$$

Where:

E_{eq} = equilibrium potential of the electrode reaction;

E^0 = standard potential of the reaction couple;

R = universal gas constant (8.31447 J K^{-1} mol^{-1});

T = temperature (K);

n = number of electrons transferred per molecule (or ion);

F = Faraday constant (96485 C mol^{-1}) and;

a = activity of the respective oxidised/reduced species (A_O/A_R).

Thus, the potential established at the electrode, under equilibrium conditions, can be obtained by the standard potential and the activity ratio of the reactants involved. It must be noted however that the Nernst equation is only applicable to reversible systems at equilibrium. The latter refers to a given process which is capable of movement in either of two opposite directions from the equilibrium position. In practical terms, it can be achieved in cases where fast electron transfer is possible between an appropriate electrode and the target analyte. At thermodynamic equilibrium, both the rates of oxidation and reduction are the same and hence zero current results.

In conventional applied electrochemistry, it can be problematic to deal with activities when attempting to interpret or elucidate electrode processes due to uncertainties in activity coefficients (γ). As such, the formal potential ($E^{0'}$) is introduced into the Nernst equation and is intended to act as bridge between standard potential and the activity coefficients. This allows the concentration of the redox reactants to the electrode interface to considered as equal to those in the bulk solution. Hence for species X with a concentration [X] mol/L, the activity is:

$$a_x = \gamma_x [x]$$

Eq 3.4

If this is substituted into the Nernst Equation (**Eq 3.3**):

$$E_{eq} = E^0 + \frac{RT}{nF} \ln \frac{\gamma_O [O]_{bulk}}{\gamma_R [R]_{bulk}}$$

Eq 3.5

This can be simplified to:

$$E_{eq} = E^{0'} + \frac{RT}{nF} \ln \frac{[O]_{bulk}}{[R]_{bulk}}$$

Eq 3.6

Where:

$$E^{0'} = E^0 + \frac{RT}{nF}\ln\frac{\gamma_O}{\gamma_R}$$

Eq 3.7

In this case, $[x]_{bulk}$ is the concentration of x within the bulk solution while γ_x is the corresponding activity coefficient. It must be noted that $E^{0'}$ will vary from one medium to another as the activity coefficients are influenced by ionic strength. The Formal potential is determined through experiment so it must also be noted that it will be dependent on factors related to the various ion interactions. The equations highlighted here enable a prediction of the possibility of an electrode reaction occurring, but the rate of the electron transfer will dictate whether or not it occurs in practice.

3.2.2 Electron Transfer Kinetics – Butler Volmer Equation

The electron transfer kinetics for a given electrode process can be greatly influenced by the imposition of a potential at the electrode. Quantitative measurements of the heterogeneous electron transfer rate constant are critical when attempting to interpret the effects of an electrode reaction. Consider the general electrode reaction:

$$O(aq) + e^-(m) \underset{k_{ox}}{\overset{k_{red}}{\rightleftharpoons}} R(aq)$$

Eq 3.8

Where the forward and reverse reactions have first order rate constants k_{red} and k_{ox} respectively. The reduction and oxidation currents i_{red} and i_{ox} from reaction denoted in **Eq 3.8** can be predicted by:

$$i_{red} = -FAk_{red}[O]_0$$

Eq 3.9

$$i_{ox} = FAk_{ox}[R]_0$$

Eq 3.10

where $k_{red}[O]_0$ and $k_{ox}[R]_0$ represent the fluxes of respective reactants to the electrode interface. The net current (i) for the overall reaction is the sum of the forward and reverse currents:

$$i = i_{red} + i_{ox} \quad \textbf{Eq 3.11}$$

Hence:

$$i = FA(k_{ox}[R]_0 - k_{red}[O]_0) \quad \textbf{Eq 3.12}$$

The transition state model in **Figure 3.2.2.1** can be used to illustrate the chemical transition and kinetics and brings together the influence of applied electrode potential on the rate constants. It can be seen in **Figure 3.2.2.1** that the reactants [$O_{(aq)}$ + $e^-_{(m)}$] must overcome an energy barrier in order to transform into the product $R_{(aq)}$ (220).

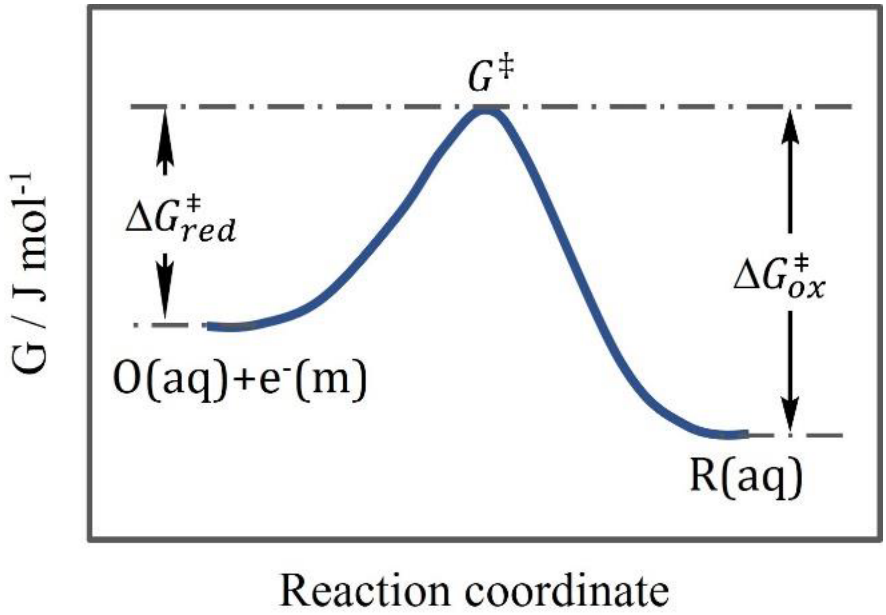

Figure 3.2.2.1 Free energy (G) plot for the reduction of species $O_{(aq)}$ to product $R_{(aq)}$.

Employing transition state theory, the rate of the reduction reaction (k_{red}) is by the transition

$$k_{red} = Aexp\left(\frac{-\Delta G_{red}^{\ddagger}}{RT}\right)$$ **Eq 3.13**

Here $\Delta G_{red}{}^{\ddagger}$ is the free energy of activation and A is the "frequency factor". Given the reaction depicted in **Eq 3.7**, the activation energy for the reduction reaction will be:

$$\Delta G_{red}^{\ddagger} = G^{\ddagger} - G_{ox}$$ **Eq 3.14**

This is the free energy change between the reactant O and the transition state ($G^{\ddagger}$). Also, the free energy associated with the oxidation is the difference between the free energy of R and the transition state as per:

$$\Delta G_{ox}^{\ddagger} = G^{\ddagger} - G_{red}$$ **Eq 3.15**

If the potential of the electron transfer reaction, shown in **Eq 3.8**, is changed to a new E from its equilibrium potential (E_{eq}), the relative free energy of an electron on the electrode will change by:

$$\Delta G = -nF(E - E_{eq}) = -F\eta$$ **Eq 3.16**

This introduces the overpotential η which is the deviation of E from E_{eq} and can be considered a driving force of the current. The overall Gibbs free energy for the reactants (O + e^-) G_{ox} is given by the standard Gibbs free energy of the reactants $G_{ox}{}^0$ and a function of overpotential (**Eq 3.16**). In this case, the free Gibbs free energy for the products stays the same (**Eq 3.18**) as no electron is included in the product component.

$$G_{ox} = G_{ox}^{0} + (-F\eta)$$ **Eq 3.17**

$$G_{red} = G^{0}_{red}$$ **Eq 3.18**

It must also be recognised that the free energy of the transition state $G^{\ddagger}$ is also altered by the overpotential:

$$G^{\ddagger} = G^{0\ddagger} + (-(1-\alpha)F\eta)$$ **Eq 3.19**

Where α denotes the transfer coefficient. This relates to the sensitivity of the transition state to the applied overpotential. The value of α can range from 0 to 1, depending on the shape of the intersection region. In general, the value of α tends to be taken as 0.5 for many reactions. A simplified model, shown in **Figure 3.2.2.2A**, is typically used to demonstrate a linear relationship between the free energy change and the imposed overpotential.

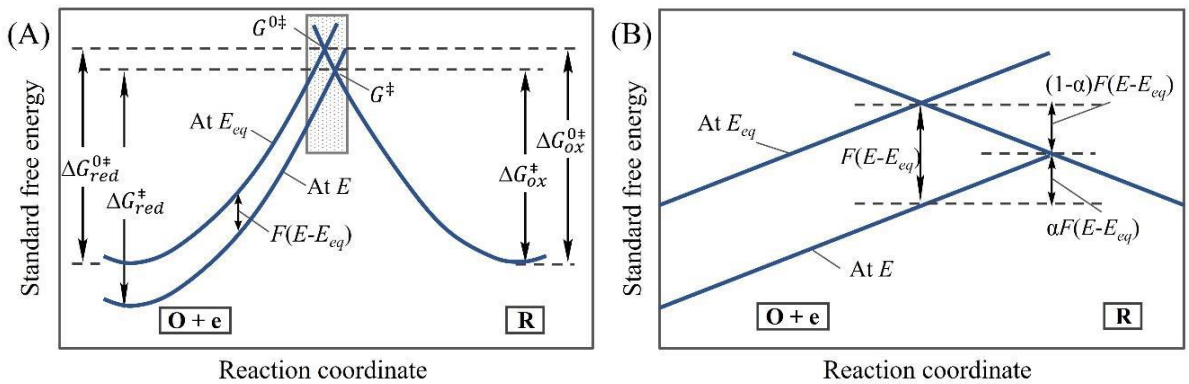

Figure 3.2.2.2 A) Influence of applied potential on the activation standard free energies for the reduction and oxidation reactions, B) is simply a magnification of the intersection region depicted in figure A.

The application of an overpotential will alter the free energies of the reactants and the transition state and, as such, the activation energies will vary accordingly. The activation energies for reduction and oxidation process are given by:

$$\Delta G^{\ddagger}_{red} = \Delta G^{0\ddagger}_{red} + \alpha F\eta$$ **Eq 3.20**

$$\Delta G^{\ddagger}_{ox} = \Delta G^{0\ddagger}_{ox} - (1-\alpha)F\eta$$ **Eq 3.21**

In terms of experimental practice – it is often better to demonstrate that the rate constants depend on the overpotential. Hence, by substituting **Eq 3.20** into the previous equation relating to the reduction rate constant (**Eq 3.13**) it is possible to write:

$$k_{red} = Aexp\left(\frac{-\Delta G_{red}^{0\ddagger}}{RT}\right)\exp\left(\frac{-\alpha F\eta}{RT}\right)$$ **Eq 3.22**

Likewise, a similar argument can be made for the oxidation rate constant:

$$k_{ox} = Aexp\left(\frac{-\Delta G_{ox}^{0\ddagger}}{RT}\right)\exp\left(\frac{(1-\alpha)F\eta}{RT}\right)$$ **Eq 3.23**

Thus, if overpotential (η) independent constants of $k_{red}{}^0$ and $k_{ox}{}^0$ are employed in the **Eq 3.22** and **3.23**, the rate constants can be simplified to:

$$k_{red} = k_{red}^0 \exp\left(\frac{-\alpha F\eta}{RT}\right)$$ **Eq 3.24**

$$k_{ox} = k_{ox}^0 \exp\left(\frac{(1-\alpha)F\eta}{RT}\right)$$ **Eq 3.25**

Where:

$$k_{red}^0 = Aexp\left(\frac{-\Delta G_{red}^{0\ddagger}}{RT}\right)$$ **Eq 3.26**

$$k_{ox}^0 = Aexp\left(\frac{-\Delta G_{ox}^{0\ddagger}}{RT}\right)$$ **Eq 3.27**

From this, it is clear that rate constants for the electron transfer processes are proportional to the exponential of the overpotential and hence the rate of electrode reactions is in fact variable

on the magnitude of the applied potential. This can lead to the Butler-Volmer equation which serves as a versatile tool in understanding the nature of voltammetric profiles obtained at the electrodes (218; 220; 221; 222). The Butler Volmer equation brings together the net current, overpotential and the transfer coefficients and provides a complete description of the current-potential relationship (substituting **Eq 3.26**, **Eq 3.27** into **Eq 3.12**):

$$i = i_0 \left(\frac{[R]_0}{[R]_{bulk}} \exp\left\{ \frac{(1-\alpha)F\eta}{RT} \right\} - \frac{[O]_0}{[O]_{bulk}} \exp\left\{ \frac{-\alpha F\eta}{RT} \right\} \right)$$ **Eq 3.28**

Where:

$$i_0 = FAk^0 [R]_{bulk}^{\alpha} [O]_{bulk}^{1-\alpha}$$ **Eq 3.29**

In this case, i_0 is the standard exchange current which can be thought of as a scaling factor and the standard rate constant (k^0) is a characteristic of the redox couple under investigation. The Butler Volmer equation (**Eq 3.28**) is significant in almost every occasion and when the solution is well stirred and thus the surface concentrations equal the bulk values it can be simplified to:

$$i = i_0 \left(\exp\left\{ \frac{(1-\alpha)F\eta}{RT} \right\} - \exp\left\{ \frac{-\alpha F\eta}{RT} \right\} \right)$$ **Eq 3.30**

3.3 Mass Transport Mechanisms

Molecular movement is characterised by three main types: diffusion, migration, and convection detailed below. During electrochemical reactions, the electrode interacts with the electrolyte solution and the rate at which these reactions occur depends on the potential difference. However, the rate of transport towards the electrode (as indicated in **Figure 3.2.1.1**) also plays a role on the rate of reactions at this boundary.

3.3.1 Diffusion

Diffusion is the movement of molecules from an area of high concentration to an area of low concentration which is defined by Fick's first law detailed in **Equation 3.30**. A concentration gradient is established enabling diffusion at the electrode surface when the concentration of the analyte is less than of the bulk solution or vice versa and can be considered in terms of products of chemical reactions illustrated in **Figure 3.4.1.1**. Diffusion drives material from the bulk solution towards the electrodes surface simultaneously moving the resultant products away from the electrode surface allowing reactions to continue. Fick's second law defines diffusion in terms of time and is detailed in **Equation 3.32** (223).

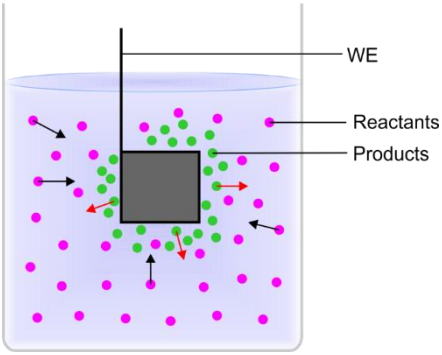

Figure 3.3.1.1 Impact of diffusion on movement of analytes during electrochemical reaction.

Eq 3.31

$$\boldsymbol{Flux = -D_i \frac{\delta_{ci}}{\delta x}}$$

Where:

D_i = diffusion coefficient (cm^2/s) of particle i;

$\frac{\delta ci}{\delta x}$ = concentration gradient at a distance x.

Eq 3.32

$$\boldsymbol{\frac{\delta_c}{\delta_t} = D \frac{\delta^2 c}{\delta x^2}}$$

3.3.2 Convection

Convection refers to the hydrodynamic transport of particles in a solution that can occur due to density gradients or by making use of mechanical forces like stirring or vibration. Convection is the most efficient mode of mass transport.

3.3.3 Migration

Migration is the movement of ionic solutes due to the application of a localised electric field for example, when a positive potential is applied negative ions will be attracted to the electrode and negative ions repelled vice versa in **Figure 3.3.3.1**. In order to reduce the effects of migration during electrochemical analysis it is imperative that the electrolytic solution contains a high concentration (typically 0.1 M) of inert electrolytes. The inert electrolytes would carry most of the charge from the electrodes surface thus leaving the electrochemical species of interest unaffected by migration.

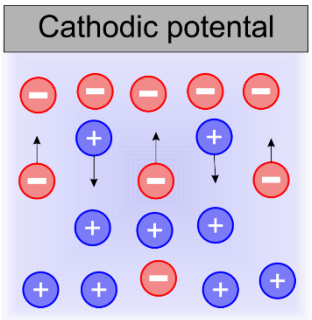

Figure 3.3.3.1 Ionic behaviour when cathodic potential is applied.

3.4 Electrochemical Instrumentation

A computer controlled potentiostat is used to perform most electroanalytical experiments (**Figure 3.4.1A**) and typically applies a three-electrode system (**Figure 3.4.1B**). The latter consisted of a working electrode (WE), a reference electrode (RE) and an auxiliary/counter electrode (RE) where a potential is applied to the working electrode – controlled by the potentiostat and measured relative to reference electrode (218; 224). The significance of each electrode is discussed in turn.

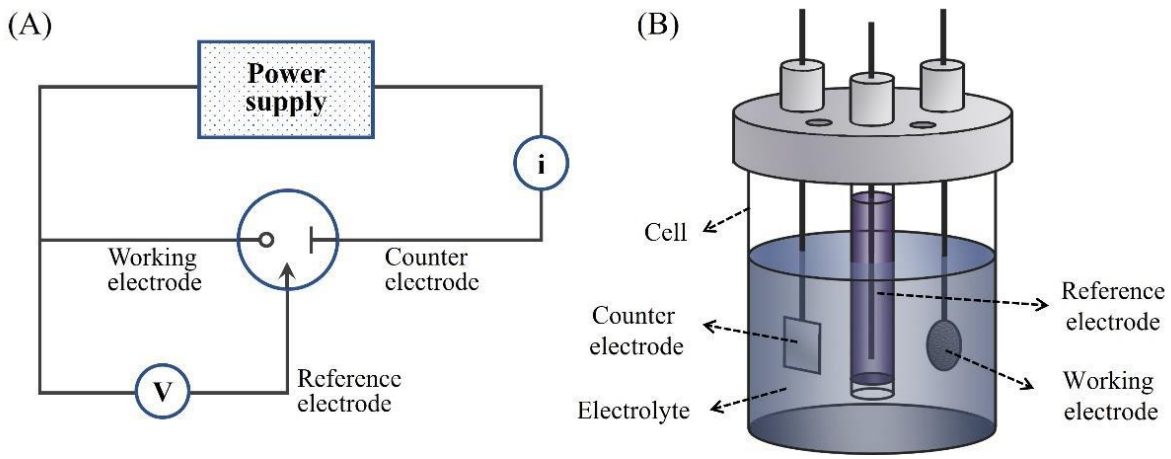

Figure 3.4.1 Schematic of A) a generic potentiostat and B) a conventional three electrode cell.

3.4.1 Working Electrode

The working electrode is of particular interest during electrochemical investigations as this is the location of all significant redox reactions and where electron exchange occurs. The working electrode has an abundance of possible compositions and configurations with common examples being gold, carbon and palladium which can be customised for their role in terms of shape and size, for example the working electrodes employed in this project are carbon-based microneedle arrays and laser induced graphene. When selecting a WE, factors that should be considered are the potential window, catalytic functions, electron kinetics, stability, cost, and size. For instance, fast electron kinetics enables the current flow at the theoretical oxidation potential giving sharp peaks and precise control of the voltage to avoid damage to the electrode or, in the case of this project, unwanted degradation of the drug. Additionally, the material used must be inert, so that any electron exchange is a consequence of the redox reactions. Contamination is a concern for electrode performance and can impact resulting data. The working electrode can be cleaned by polishing or can be enhanced electrochemically by means of anodisation which also decreases the potential required to initiate the redox reactions.

3.4.2 Reference Electrode

The reference electrode is necessary for two and three electrode systems, as it provides a constant and stable potential such that the potential of the working electrode can be reproducibly controlled. Numerous types of reference electrodes are available, in this project, however, a silver-silver chloride (Ag/AgCl) shown in **Figure 3.4.2.1** is used exclusively. The reference electrode acts as a half cell and consists of a silver wire coated with precipitated silver chloride. The wire is enclosed in a glass tube containing 3 M potassium chloride (KCl). This internal potassium chloride solution provides a stable environment isolated from the reactions at the working electrode by way of a porous frit.

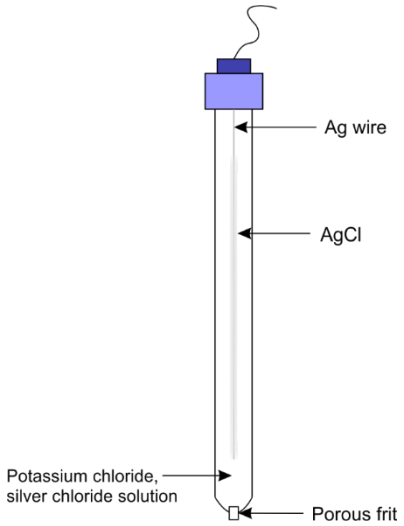

Figure 3.4.2.1 Components of the commercial Ag/AgCl half cell reference electrode.

Within the reference electrode, rapid, reversible reactions occur to make adjustments in order to determine the changes in ionic behaviour in the working solution. The electromotive force (EMF) is established from the maximum difference in redox potentials and, along with standard potential, the cell potentials from two half cell reactions can be calculated more easily. The Nernst equation represents the relationship between the electrochemical cell potential, the relative redox behaviours, and the standard potential in a cell. When applying the Nernst equation to the reference electrode in **Equation 3.33**, n is set to 1 and the redox reactions are substituted with their more experimentally accessible concentrations.

Eq 3.33

$$AgCl_{(s)} + e^- \rightleftharpoons Ag^+_{(aq)} + Cl^-_{(aq)} \; Eo = 0.222 \text{ V}$$

$$E = E° - \frac{2.303RT}{nF} \; log \frac{[B]}{[A]}$$

$$E = E° - \frac{0.05916}{1} \log \frac{[Ag_{(s)}][Cl^-{}_{(aq)}]}{[AgCl_{(s)}]}$$

$$E = E° - 0.05916 \log [Cl_{(aq)}]$$

Where the constants are the same as those documented earlier in **Equation 3.3**. The equation above confirms that the electrode potential due to the redox reaction arising in a Ag/AgCl reference is exclusively dependent on the concentration of chloride ions (when at a constant temperature). Therefore, to ensure a proportional relationship is maintained, the (3 M) potassium chloride solution is integral.

3.4.3 Counter Electrode

The primary function of the counter/auxiliary electrode is to prevent current from passing thought the reference cell. The reference is vulnerable to being damaged by large currents which would result in changes in its potential, thus, becoming an unreliable comparison for the working electrode. Three electrode systems make use of a counter electrode which are very conductive, inert materials like platinum. The mechanism in which the counter electrode operates is that, when a potential is applied to the working electrode to initiate the redox reactions, the current will flow through the counter rather than the reference electrode which will complete the electrical circuit. The opposite reaction to that of the WE occur in the CE, for example, when the WE is oxidised, the CE is reduced. Hence, the material must be inert, so as to not influence results obtained. In this project a platinum wire is used as the counter electrode for three electrode systems unless stated otherwise.

3.5 Electrochemical Techniques

3.5.1 Potential Step Chronoamperometry

Amperometry can be considered as a basic potential step experiment. The generic waveform is highlighted in **Figure 3.5.1.1** where the potential E1 is typically assigned a value where no electrode reaction happens. The potential is then “stepped” to a second potential, E2, in which a faradaic process is induced at the electrode interface. As a consequence, a current is produced and monitored continuously over a set time period. The general current-time profile is detailed in **Figure 3.5.1.1B** where, following the imposition of the step potential (E2), a large current spike is observed which then steadily decays with time. The concentration of the target analyte at the electrode surface will be the same as the bulk prior to the imposition of the step potential but, upon stepping to E2, it will be consumed immediately (in this case an oxidation). A concentration gradient is therefore present and the unoxidized target must diffuse to the electrode surface.

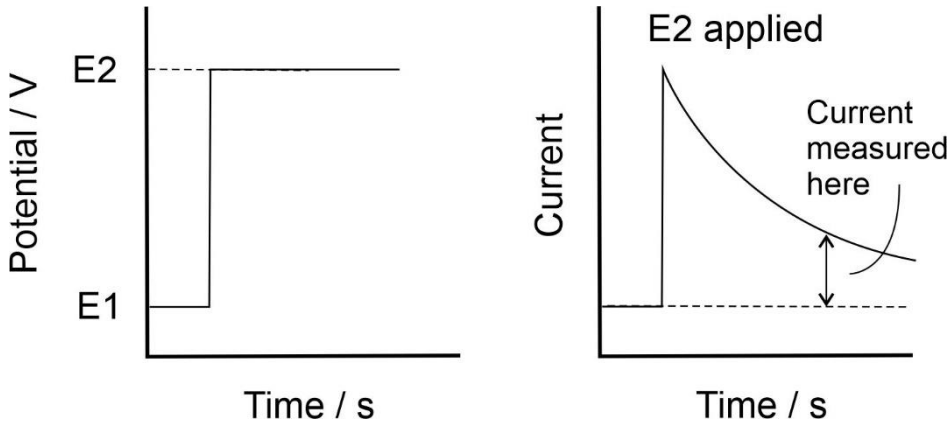

Figure 3.5.1.1 A) Single step amperomertic waveform. B) Generic amperometric response profile for an oxidation process.

The magnitude of the current will be controlled by the electrode area, initial concentration of the target analyte and the rate by which fresh analyte can diffuse to the electrode. The latter is dependent upon the concentration gradient which will drop as the electrode reaction continues with time and, as such, the current drops as a consequence. A quantitative evaluation of the relationship between observed current, *I,* (in this case taking a reduction

process as an example) and reaction time, *t,* can be achieved by substituting $i = nFAk_{red}[O]$ (**Eq 3.9**) into Fick's Second Law (**Eq 3.32**). This yields the Cottrell equation (224; 225; 226):

$$|i| = \frac{nFA[O]D^{\frac{1}{2}}}{\pi^{\frac{1}{2}}t^{\frac{1}{2}}}$$

Eq 3.34

Where n = number of electrons being transferred per reaction and [O] represents the bulk concentration of reactant O.

3.5.2 Cyclic Voltammetry

Cyclic voltammetry is the main diagnostic technique applied in the present project and is used to characterise the electrochemical properties of microneedle substrates and laser induced graphene films. It is also employed to elucidate the reaction mechanisms associated with the electrode promoted drug release where the application of an electrochemical potential can induce a chemical reaction at the electrode interface. The technique is based on a triangular waveform (**Figure 3.5.2.1**) where the potential is varied linearly across the working electrode from a defined potential E1 to a second potential E2 and then swept back to E1 at a constant rate – the scan rate (218; 220; 224).

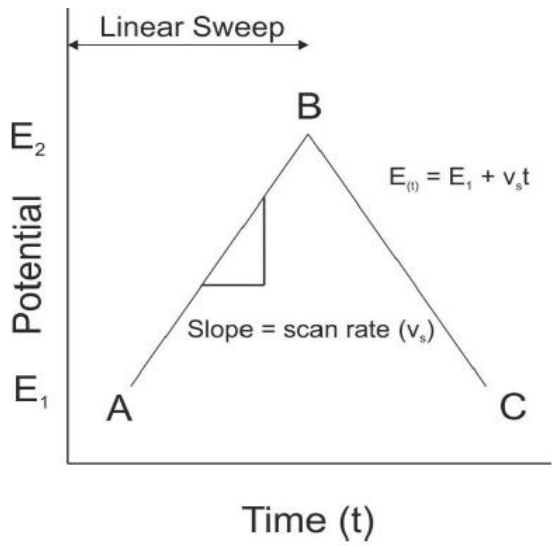

Figure 3.5.2.1 Waveform for a conventional cyclic voltammogram where E1 is the start and end point and E2 is the switching potential.

This potential is controlled and applied by a potentiostat and the current across the working electrode due to the redox reactions of the analyte of interest is traced, known as a cyclic voltammogram.

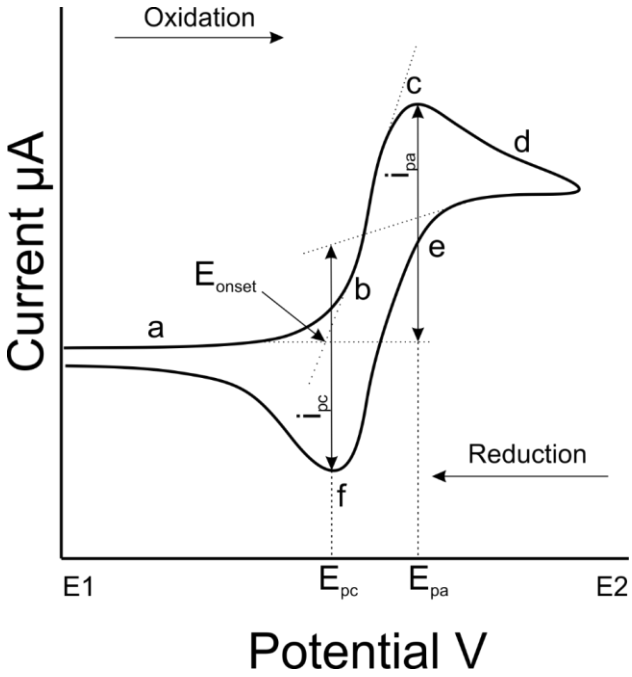

Figure 3.5.2.2 Classic "duck" shaped cyclic voltammogram for a reversible electrode process.

The potentials are typically predetermined by the user in cyclic voltammetry to ensure the full "duck shaped" profile of the redox reactions can be seen. As seen on **Figure 3.5.2.2**, initially as the anodic sweep begins the potential does not meet the analytes threshold for oxidation (a). When this threshold is met known as standard potential onset (E_{onset}), the current increases exponentially to a maximum current known as anodic peak current (i_{pa}) at a potential known as anodic peak potential (E_{pa}) which is driven by the electron exchange due to the analyte being oxidised at the working electrodes surface (b). The steep increase of the current is determined by electron kinetics and less so the rate of diffusion of the oxidant to the electrodes surface. When $E_{1/2}$ is met, the oxidised and reduced species are at equal concentrations satisfying the Nernst equation $E = E_{1/2}$. With subsequent sweeping of the potential, more of the oxidant is depleted creating a concentration gradient creating the peak witnessed in the trace (c) as the current from the depletion of the oxidant is greater than the

increase due to the oxidisation reaction. Following i_{pa}, the current from the more positive potentials is counteracted by diminishing flux of analyte from further distance from the electrode surface. Mass transport is the limiting factor for the current at this point decreasing the current until the potential reaches the defined end potential (d). When the defined potential is met the cathodic sweep begins towards more negative potentials. In the beginning of the cathodic sweep, the analyte continues to be oxidised until the potential reaches a value where the oxidised analyte at the electrode surface can be re-reduced (e). The reduction process mirrors the tract of that for oxidation only differing in direction and similarly a cathodic peak current (i_{pc}) is witnessed at the cathodic peak potential (E_{pc}) (f).

Cyclic voltammetry traces offer an abundance of information about the electrochemical system and analyte – particularly in terms of reversibility of the redox probe at the substrate (220; 224). A systems ability to be reversible depends on its electron transfer kinetics, if the system can abide by Nernstian behaviour *i.e.*, the oxidative and reductive species are at equilibrium at all stages/potentials of the experiment then it is reversible however this is not typical, and systems can be quasi-reversible or irreversible shown in **Figure 3.5.2.3**.

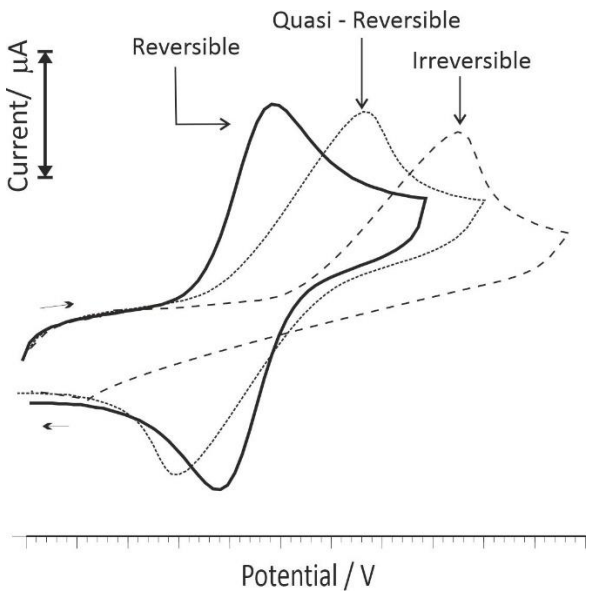

Figure 3.5.2.3 Typical trace from reversible, quasi-reversible and irreversible systems.

A quasi-reversible response requires a greater potential (positive or negative), known as an overpotential (as described earlier in **Section 3.2.2**), to induce oxidation or reduction resulting in an extended voltammogram. Similarly, an irreversible system requires a larger overpotential to initiate redox reactions which is characterised by the maximum peak separation been oxidation and reduction if the latter is visible. Here the electron transfer kinetics are insufficient to maintain equilibrium of redox species. In addition, if there are no electroactive species present, no peaks can be seen and only background capacitance is displayed.

Electrochemically reversible systems follow discrete rules, for instance (218; 220; 224):

- Peak-to-peak separation (ΔE_p), which is the potential difference between anodic and cathodic peak must equal 59/n mV, where n is the number of electrons transferred during a chemical reaction;
- The anodic and cathodic peaks must have a ratio equal to 1;
- Peak currents must be proportional to the square root of the scan rate.

Something that has not been fully discussed, is the role of scan rate, υ, which controls the rate at which potential is swept. Higher resultant currents are detected with a faster scan rate, as there is less time for analytes to diffuse away from the electrodes surface. Electron transfer increases with increasing scan rates also resulting in a greater current magnitude, in fact, the relationship is denoted in Randles-Ševčik **Equation 3.35**, can determine if a reversible system is due to the diffusion of an analyte or an analyte being adsorbed (218; 220; 224; 227; 228).

Eq 3.35

$$I_p = 0.446\, nFAC^0 \left(\frac{nFvD_o}{RT}\right)^{\frac{1}{2}}$$

Where:

n is number of electrons transferred;

F is Faraday constant (96485 C mol^{-1});

A is electrode surface area (cm^2);

C_0 is concentration (mol cm^{-3});

υ is scan rate (V s^{-1});

D_0 is diffusion coefficient of the oxidised analyte (cm2 s^{-1});

R is gas constant (8.314 J K^{-1} mol^{-1});

T is temperature (298.15 K).

When the analyte is adsorbed onto the electrode surface/is not limited by diffusion, the derived current will be linear to the scan rate. In this instance, the analytes concentration C, can be calculated using **Equation 3.36**.

Eq 3.36

$$I_p = \frac{n^2 F^2 T_c}{4RT}$$

3.5.3 Square Wave Voltammetry

Similarly, to cyclic voltammetry, square wave voltammetry uses a three-electrode system, and the current is recorded as a function of the linearly swept potential applied to the working electrode. However, the potential applied for square wave is a staircase waveform or a square wave shown in **Figure 3.5.3.1** meaning that the potential leaps with each step and the polarity is reversed halfway through a full waveform inducing oxidation and reduction peaks. The polarity/direction of the potential is referred to the forward pulse and the reverse pulse. The time to complete a full square wave period is annotated by τ which is inversely proportional to the frequency in Hertz (Hz) typically 1 to 125 Hz.

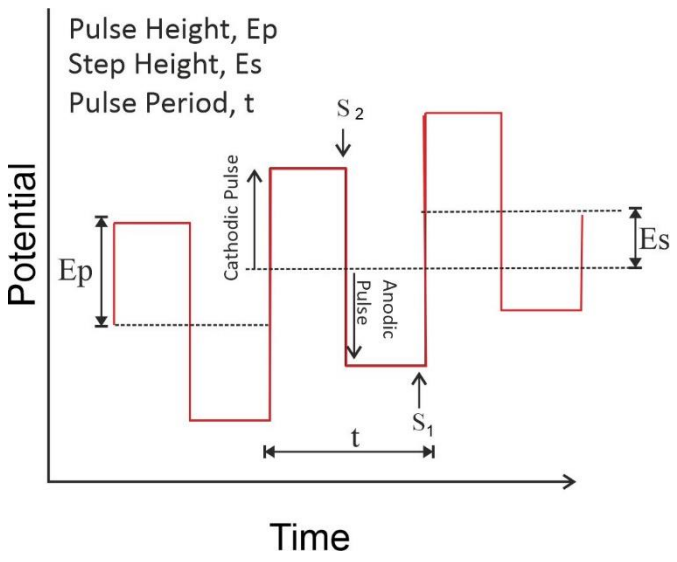

Figure 3.5.3.1 Potential applied during square wave voltammetry in relation to time.

The scan rate (v) can be calculated by **Equation 3.37** below:

Eq 3.37

$$v = \frac{E_{step}}{\tau}$$

Where:

v is scan rate (mV/s);

E_{step} is the step potential (mV);

τ is wave period (s).

The current is recorded at the end of the forward pulse and the end of the reverse pulse and the resultant current (ΔI) that is displayed on a square wave voltammogram is the difference in the oxidation current and reduction current due to the switch in polarity during the waveform, illustrated in **Figure 3.5.3.2**.

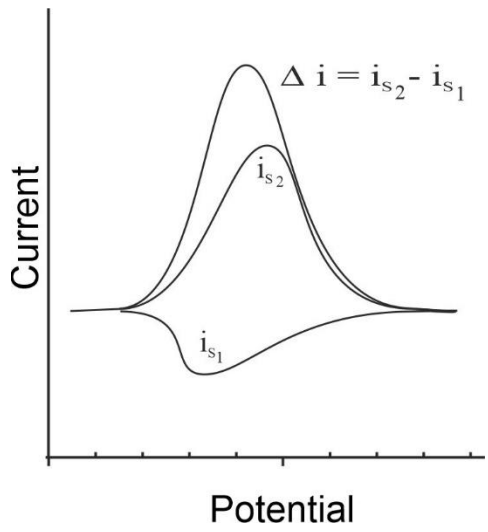

Figure 3.5.2.2 Resultant square wave voltammogram taking the switch in current direction.

A wealth of information about an analyte can be determined from square wave voltammetry, for example the peak height from the voltammogram is proportional to the concentration of electroactive species in solution, demonstrated in **Equation 3.38**.

Eq 3.38

$$\Delta I_p = \frac{nFAD^{\frac{1}{2}}C}{(\pi t_p)^{\frac{1}{2}}} \times \Delta\varphi_p$$

Where:

Δi_p is differential peak current (A);

t_p is pulse width (s);

$\Delta\psi_p$ is dimensionless peak current;

and all other symbols have their common meaning.

Square wave voltammetry is not influenced by capacitive current as cyclic voltammetry as the current is recorded twice in each pulse and there is a delay in current measurement, allowing

ions to reorganise at the electrodes surface. For instance, the Faradaic current, which is due to electron transfer between electrode and analyte is measured during square wave, unlike cyclic where both the Faradaic and capacitive currents are recorded. The reduced influence of capacitance in square wave results in a higher sensitivity as trace concentrations can be suppressed by capacitive background during cyclic voltammetry.

3.6 Surface Characterisation Methods

Many spectroscopic methods were used during this project, and in general spectroscopy is the study of how atoms and molecules interact with electromagnetic radiation and that information can quantitatively understand the sample.

3.6.1 Raman spectroscopy

Raman spectroscopy is a technique that measures the intensity of Raman scattered radiation as a function of its frequency difference from the incident radiation, usually in units of wave numbers, this difference is the Raman shift. It has several uses for example identifying unknown compounds, identifying polymorphs, tracking changes in molecular structures, tracking changes in crystallinity, and evaluating magnitude of residual stress to name a few.

The technique is carried out by applying a laser beam to a sample which induces the polarisation of the sample. This polarised condition is known as a “virtual energy state” which is volatile and unstable. The virtual energy state quickly re-radiates upon relaxation emitting a photon or scatter, which can be characterised as Rayleigh scatter which has the same excitation energy as the incident radiation, stokes where the sample relaxes to its first excitation level therefore has lower energy than the incident radiation and anti-stokes when the relaxation emits higher energy radiation than the incident radiation. The characterisation of excitation and relaxation of the electrons is demonstrated in **Figure 3.6.1.1** and **Figure 3.6.1.2** below.

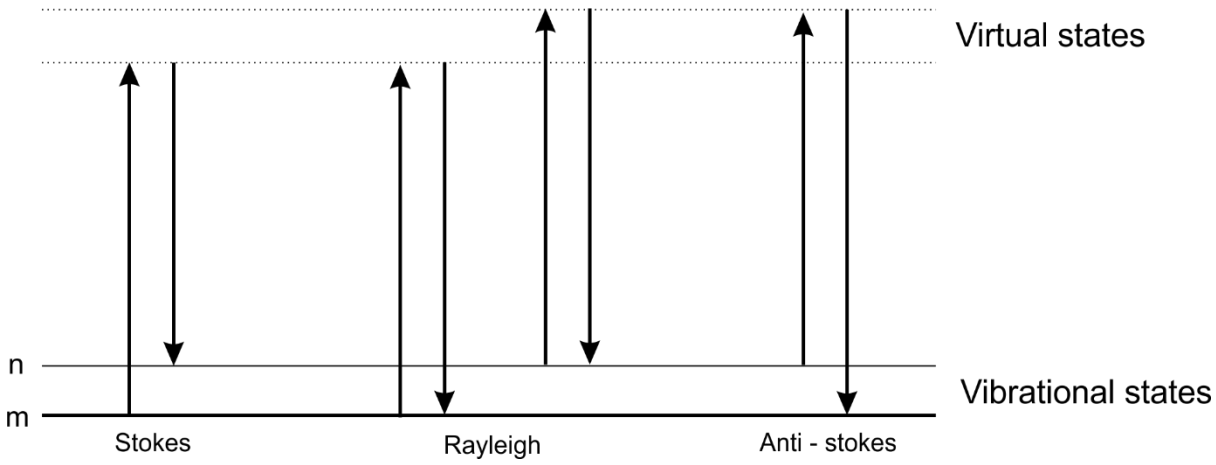

Figure 3.6.1.1 Diagram of Raman scattering processes. The lowest energy state is denoted as m with energy levels increase upwards. Energy of incident radiation (upwards arrows) and energy of scattered radiation (downwards arrows) posses' larger energy than the vibrational states.

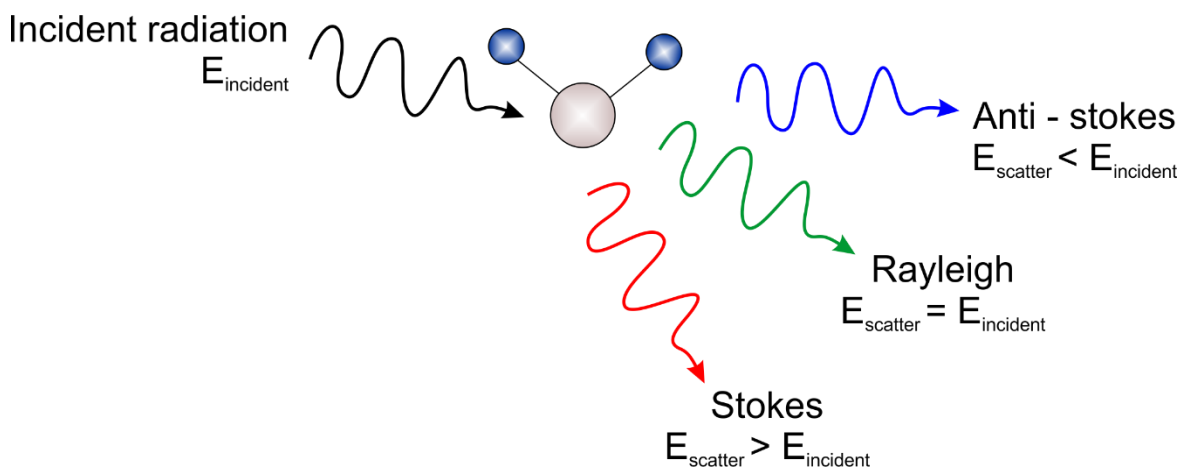

Figure 3.6.1.2 Difference in energy of incident radiation and scatter radiation for different Raman processes.

The profile produced *via* Raman spectroscopy is specific to the sample as information on vibrational modes of the molecule is gathered which display the structure and composition encoded in a set of frequency shifts in Raman scattered radiation providing a "fingerprint" of the sample. Throughout this project Raman spectroscopy was preformed using a Renishaw Raman Microscope (20x objective lens) with a 532 nm laser operating at 10 % power.

Graphitic samples have a characteristic Raman spectrum, defined by two sharp modes: D peak (around 1350 cm^{-1}) and G peak (1580-1600 cm^{-1}). The D peak occurs due to out-of-plane vibrations due to defects within the lattice structure thus indicates level of disorder. High levels of disorder are favourable for electrochemical electrodes as there are more available sites for electron transfer. The G band, however, reports on the graphitic in plane vibrations of sp^2 bonded carbon atoms owing to C-C bond stretching. Raman spectroscopy is a sensitive technique, which can indicate the presence of impurities or changes to lattice structures. Distinctions can be made between graphite and graphene spectra, the latter has a distinctly sharp 2D peak (1610 cm^{-1}) where the G peak splits into 2 peaks. The ratio between D and G peaks (I(D/G) determines the number of defects in a sample, for example, a higher I(D/G) means more defects within a sample.

3.6.2 Scanning Electron Microscopy

A scanning electron microscope (SEM) utilises a high energy, focused beam of electrons to produce a high-resolution image of a solid sample – rather than light that is typically used. It is a powerful magnification tool, where images of a sample's morphology and topography is detailed due to the interactions between the atoms of the sample and the electrons applied. The typical configuration of a SEM and the electrons route of travel is displayed in **Figure 3.6.2.1** and the SEM used in this project is a SU5000 FE-SEM (Hitachi, Japan).

The primary components of a SEM are the electron source, the electromagnetic lenses and the electron detector that computes the signal onto images on the display screen. The electrons are produced thermionically by a tungsten filament within the gun. As a potential is applied, the filament heats up generating electrons that accelerate towards the anode and through the lenses and apertures onto the sample. During operation, the sample chamber and column is kept under vacuum and the sample is scanned.

A range of electrons are emitted (secondary, backscattered, Auger electrons and X-rays) due to the collision of the primary electrons onto the surface of the sample.

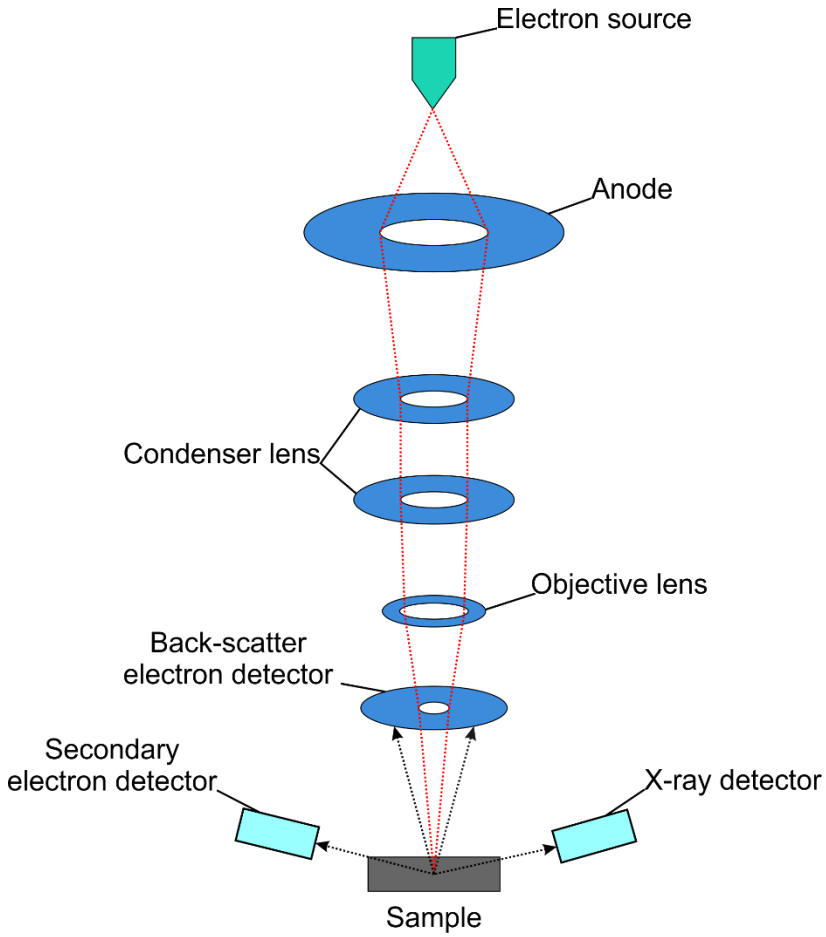

Figure 3.6.2.1 Scanning electron microscope configuration and electron path.

Secondary electrons are released due to the energy transfer during the inelastic collision between primary electrons and loosely bound outer electrons of the atoms, which are excited and expelled. The intensity of secondary electrons is dependant the morphology and topography of the sample of interest and gives information on such characteristics. In contrast, backscattered electrons are produced by elastic collisions which indicates the atomic number of the sample hence its elemental make-up. Finally, X-rays are emitted when inner electrons are excited by the incident electrons. When this happens, the higher energy electron is forced to replace the detached electron leading to energy emanation. This energy is then taken up by another electron, known as an Auger electron which is subsequently released. The combination of emitted X-rays and Auger electrons provides information about the superficial composition of the sample. The signals are detected, and an image is produced.

Samples investigated using SEM must be conductive as electrons are used to produce signals, if a sample was insulated then charging would occur. If a material is a poor conductor, it is common practice to sputter coat the sample with gold, palladium, or carbon. It is also imperative that a sample can withstand being under vacuum for long periods of time. SEM is a non-destructive technique as the bombardment of electrons does not result in volume loss, therefore a sample can be reused and analysed repeatedly.

3.6.3 Energy Dispersive X-ray Analysis

Energy-dispersive X-ray spectroscopy (EDX) analyses the elemental composition of a sample and is generally attached to an electron microscopy instrument such as transmission electron microscopy (TEM) or scanning electron microscopy (SEM). The mechanism through which EDX functions is high energy electrons are focused onto a sample expelling inner electrons. An electron from a higher binding energy fills this hole, replacing the ejected electron, which in turn emits an X-ray of the difference of the electron binding energies. The energy of the emitted X-ray is unique to each element, therefore, a “fingerprint” spectrum can be obtained. Moseley’s law declares direct correlation between the frequency of the emitted X-rays and the atomic number of the atom under analysis. Hence, EDX is valuable in identifying the elements are present and to what extent. In this project the Scanning electron microscope (SEM) employed is SU5000 FE-SEM (Hitachi, Japan) and Energy-dispersive X-ray (EDX) analysis was carried out using a X-Max silicon drift detector (Oxford Instruments, UK) attached directly to the SEM analysis chamber.

Numerous combinations of electron movements can occur following bombardment from X-rays shown in **Figure 3.6.3.1**. Siegbahn notation is used to help describe these phenomena, letter K, L and m refer to the n value the electrons have where K is the closest to the nucleus, while α and β indicate the size of the transition. For example, relaxation from M to L, or L to K is noted as L_α or K_α, the opposite is true for transitioning from M to K which is denoted as K_β. EDX spectrometers are often equipped with an electron microscope like a scanning electron

microscope (SEM) where elements can be mapped on top of electron images. The mapping feature is utilized in this project as well as a graphical output of energy in keV versus peak intensity. The location of peaks indicates the atoms present.

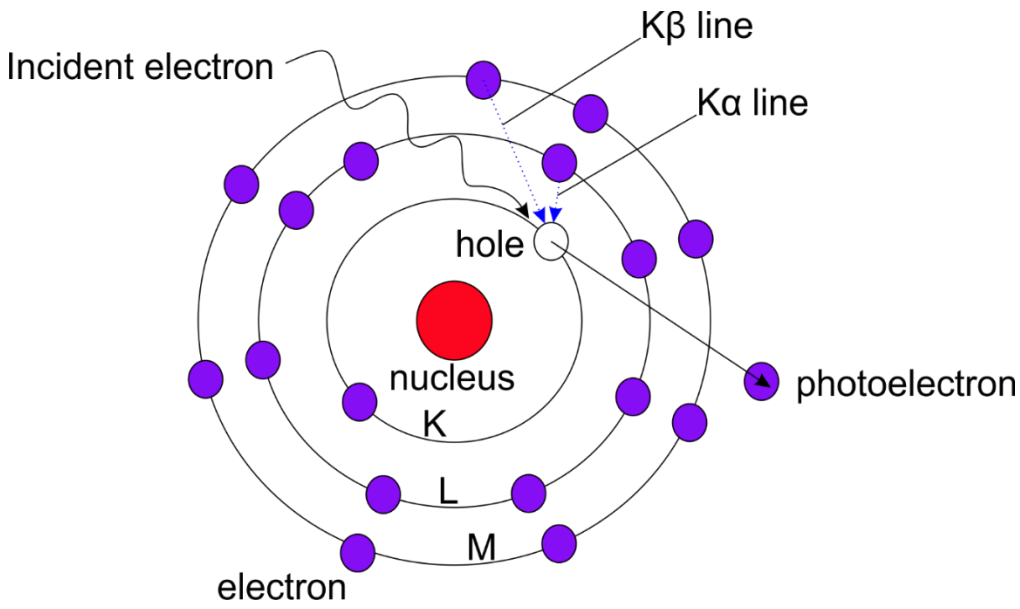

Figure 3.6.3.1 Electron transitions that can occur from bombardment from electrons.

3.6.4 X-Ray Computed Tomography

Computer tomography (CT) uses X-rays to acquire two-dimensional cross-sectional images of a three-dimensional sample. These images are taken at various angles and reconstructed to produce a three-dimensional illustration that that can be sliced to view the internal structures without destroying a sample. The mechanism works by applying a fixed X-ray source onto sample as it passes through towards the detector that measures how the sample interacts with the X-rays that rotates 360° on a single axis. The core components of a CT scanner are the X-ray source which supplies X-rays at variable energies (generally between 70 – 150 kV), the sample stage and the detector. Higher energy X-rays have more penetrating power than lower energy photons and the potential selected depends on the density of the material of the sample. It is notable that the X-rays produced are not monochromatic, but a spectrum of energies. Generally, the lower energy X-rays do not produce an image and are filtered out before reaching the detector. In this project the cross-sectional images of microneedle arrays

were obtained from Bruker Skyscan1275 micro computed tomography (Micro CT). The images are of a lower resolution than two-dimensional imaging techniques, however, the ability to slice the sample to view internal structures is useful to view layered microneedle structures discussed in **Chapter 4**.

3.7 Surface Modification Techniques

3.7.1 Electrochemical Anodisation

The process of anodising an electrochemical electrode is widespread technique to enhance its performance during electroanalytical methods. Anodising introduces additional oxygen functional groups to the surface of the electrode which can result in changes in the crystal structure of the samples layers and microscopic texture. Thus, more edge plane sites are created enabling and increase in the rate of electron transfer kinetics, improving sensitivity and voltammetric response. Anodisation is a simple procedure that is accomplished by using chronoamperometry, mentioned in **Section 3.5.3**, whereby +2 V potential is applied to the working electrode for a set time in 0.1 M sodium hydroxide (NaOH) solution. Through the application of an anodic potential at the working electrode, oxygen is generated, and hydrogen is released at the cathode. The oxidation processes promote nucleophilic attack on the carbon surface leading to an influx of oxygen functionality. These attacks also result in microscopic changes on the surface and the crystalline structures just below the surface leading to more exfoliation of the layers and increase in edge plane sites (229; 230; 231; 232; 233). Details of time and electrode are discussed in relevant chapters.

3.7.2 Laser Ablation

The term “laser” is an acronym of light amplification by stimulated emission of radiation which concisely describes how a laser functions. There is a plethora of laser types, such as “YAG”, diode and CO_2 to name a few, however they all function with the same core elements. The electrons within the lasing medium are stimulated into an excited state two or three levels

above the ground state, until population inversion is achieved, where more electrons are in an excited state than the ground state and when these excited electrons relax, photons are emitted. The photon emitted depends on the state of the electron's energy before the photon is released. The photons released from a laser are monochromatic and coherent meaning they have the same energy and are released in unison producing a fine, concentrated beam of unidirectional light, this is because the emission is not spontaneous but stimulated. At either end of the laser medium there are mirrors reflecting the photons back and forth which, in turn, stimulates more electrons producing a cascade effect and once one of the mirrors has "half-silvered" allowing some light to pass through, the resultant beam is the laser light that is used to cut material or in the case of this project, induce the formation of graphene on polyimide.

A CO_2 laser emits photons of around 10600 nm, in the infrared region of electromagnetic spectrum which produces heat, it essentially melts material to cut it or burns material in the case of graphene production. The high temperatures burn the carbon in polyimide film which releases gases producing the thin, porous layer of carbon known as laser induced/scribed graphene (234).

Laser ablation of polyimide to produce laser induced graphene and of conductive microneedle arrays to produce carbon nanotube-like fibres was achieved using a ULS VLS 2.30 commercial CO_2 laser. The laser was typically in raster mode, at a power of 30 %, a speed of 40 %, resolution 1000 pulse per inch (PPI) unless stated otherwise in the relevant chapters.

3.8 Assay Validation Methods

3.8.1 Ultraviolet-Visible Spectrophotometry

Ultraviolet-visible (UV-Vis) spectrophotometry measures the absorption of light within the ultraviolet and visible ranges (200-800 nm) used in many areas of science. This technique provides quantitative data to determine the presence of an analyte in a solution or how it interacts with light. It calculates how much light a substance absorbs, this is achieved by

measuring the intensity of light that passes through a sample (I) with regards to the intensity of light passed though the solvent known as the reference (I_o). The absorbance is plotted ($A = log\frac{I_0}{I}$) versus the user-defined wavelength range in nm. A ThermoScientific Genesys 150 dual-beam spectrometer (2 nm bandwidth) was used during this project to acquire UV/Vis spectra.

The parameters that are important when selecting a solvent for UV-Vis are whether it absorbs any of the light emitted, therefore common solvents include water, ethanol, and cyclohexane. Additionally, compounds that express high absorptivity, should be diluted to ensure the absorbance is within the detectable range which is no greater than 1.5. Although UV-Vis can help to identify if an analyte is present, likewise, the concentration of analyte can be calculated. Absorbance is proportional to the molar concentration of the solution, displayed in **Equation 3.39** below.

Eq 3.39

$$\varepsilon = \frac{A}{c * l}$$

Where:

ε is the molar absorptivity coefficient;

A is the absorbance;

c is the concentration of the sample (mol/L);

l is the length of light path through the cuvette in (cm).

Within this project UV-vis spectrophotometry was used to characterise absorbance spectra of drugs and compounds as well as determining the release profiles of selected drugs.

Chapter 4

Laser Ablation of Nanocomposite Microneedles for Enhanced Electrochemical Performance Combined with Dual-layer Microneedle Approach using Biocompatible and Dissolvable Array

Overview

This chapter investigates an alternative method to improve the electrochemical properties of polystyrene-carbon (Ps-C) microneedles (MN) by way of electrochemical anodisation and laser ablation. Various techniques are used to assess the suitability of the laser modification method such as cyclic voltammetry, Raman spectroscopy, energy dispersive X-ray analysis (EDX) and scanning electron microscopy (SEM). In addition, a multi-layered approach is investigated using a cellulose acetate phthalate (CAP) microneedle as means to create microchannels for interstitial fluid to access to a secondary layer containing a laser modified microneedle for sensing and controlled drug delivery applications.

4.0 Introduction

Wearable sensors have become a trending topic in relation to monitoring a patient's health status, resulting in rapid innovation of point-of-care devices. This is especially prevalent within disease treatment, whereby a "closed loop" feedback system between sensing and therapy is bridged thus enhancing care management (235). Electrochemical sensors are ideal candidates for health status monitoring due to their exceptional analytical properties, for example, fast response time, high sensitivity, and adaptability, as well as being miniature, simplistic, and inexpensive (236). The most common embodiment of electroanalytical sensors has been planar screen-printed electrode (SPE) systems as typified by the commercial success of home glucose monitors. More recently, 3D systems based on conductive microneedles have been employed where they bring a number of procedural advantages over SPE configurations – particularly in terms of being able to directly access interstitial fluid. The latter can have a similar composition to blood plasma providing a wealth of information about a patients' health (236; 237).

Initially, the electrochemical properties of microneedles were enhanced by metallising, where a coating like gold (238) or platinum (239) were deposited onto a preformed microneedle template with the aim of imparting conductivity. The coatings were achieved by a variety of means like sputtering, electrodeposition, or e-beam evaporation. Teo *et al.*, (2019) produced a flexible microneedle substrate using magnetorheological drawing lithography which was coated with a gold/titanium film and served as a highly sensitive electrochemical sensor to detect glucose, uric acid, and cholesterol simultaneously (237). In this instance, the primary limiting factor is the fabrication method, lithography is a labour intensive, multistep fabrication process which is a challenge to translate into a manufacturing setting, additionally scientific expertise is necessary to use the extensive equipment required (240). Micro-moulding offers a much more simplistic and rapid fabrication process and have been reported that Kim *et al.*, (2015) produced polylactic acid microneedle array that was metallised *via* silver titanium coating (241).

More recently, polymer nanocomposites have been produced where the conductivity is enhanced by incorporating conductive nanoparticles within the matrix, rather than coating the surface, McConville *et al.*, (2016) produced polystyrene-palladium microneedles *via* solvent-based casting but, despite palladium being a popular electrode choice, it is rarely incorporated into microneedles (210). Although metal coatings and nanoparticles provide high conductivity, they are expensive, as an alternative, carbon-based nanoparticles have been employed in polymer nanocomposite microneedle arrays (242). The carbon nanocomposite approach requires an additional wetting process to enhance its electrochemical properties by way of anodisation. Here, laser ablation has been studied as an alternative method to enhance the conductivity of polystyrene-carbon (Ps-C) microneedle array. Through laser processing, the mechanical strength of the needles is compromised, therefore a dual layered array has been employed where cellulose acetate phthalate (CAP) is the piercing mechanism and the laser modified polystyrene-carbon microneedle provides the sensing element.

Cellulose acetate phthalate (CAP) is traditionally utilised as an enteric polymer coating for oral medication (243). It is a derivative of cellulose, consisting of 30-40 % phthalyl, 19-24 % acetyl, and 6 % water which provides sustained drug delivery (244).

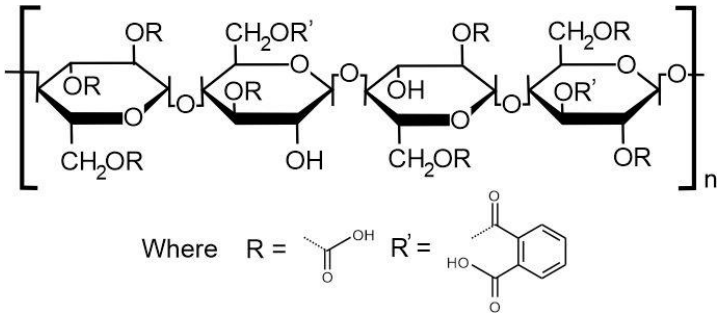

Figure 4.0.1 Structure of cellulose acetate phthalate.

It is a suitable candidate for microneedle fabrication as it is biocompatible (245), and is soluble in pH as low as 6 (246). As the skin is more acidic, the CAP needles will not dissolve until they pierce the skin and come into contact with the interstitial fluid, upon which, CAP will dissolve,

microchannels will be left behind whereby the laser modified polystyrene-carbon microneedle can fulfil its sensing role.

4.1 Experimental Details

4.1.1 Materials and Instrumentation

Carbon nano powder (<100 nm), polystyrene (MW 192,000), cellulose acetate phthalate (MW 2534) and all associated laboratory chemicals were obtained from Sigma-Aldrich, were the highest grade available and were used without further purification. Britton Robinson buffers (acetic, boric, and phosphoric acids, each at a concentration of 0.04 M and adjusted to the appropriate pH through the addition of sodium hydroxide) were used throughout unless otherwise specified.

Electrochemical analysis was carried out using a Palm Sens computer controlled potentiostat with a standard three-electrode configuration in which the microneedle patch was used as the working electrode with platinum and a Ag|AgCl half cell (3M NaCl, BAS Technicol UK) acting as counter and reference respectively. All measurements were conducted at 22°C ± 2°C. Raman spectroscopy was performed using a Renishaw Raman Microscope (20× objective lens) with a 532 nm laser operating at 10% power. Electron micrographs were obtained using su5000 Hitachi field emission scanning electron microscope (Hitachi, Ltd., Ibaraki-Ken, Japan) of accelerating voltage 10-15 kV. Microneedles were sputtered (gold source) under vacuum prior to obtaining micrographs (Emitech K500X Sputter Coater, Quorum Technologies Ltd., England). X-ray images obtained from Bruker skyscan microct. Microneedles were modified using ULS VLS2.30 25 W CO_2 laser cutter on raster mode, speed 30 and resolution of 1000 pulse per inch.

4.1.2 Preparation of Carbon Nanocomposite Microneedles

Polystyrene acted as a binder to carbon nanoparticles in a ratio 1:1 by weight, dissolved in cyclohexanone and stirred to ensure homogenous mixture was achieved (typically two hours).

The mixture was cast into silicone microneedle moulds and a carbon fibre rod placed in the baseplate to facilitate electrical connection. Microneedle moulds were obtained from Micropoint Technologies Pte Ltd (Singapore) and were pyramidal in format with 200(base) x 500(pitch) x 700(height) micron dimensions covering a 10 x 10 needle array as indicated in schematic in **Figure 4.1.2.1**.

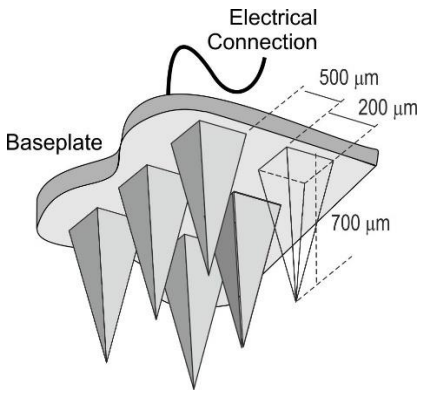

Figure 4.1.2.1 Schematic of conductive microneedle array dimensions produced using Micropoint Technologies Pte Ltd (Singapore) moulds.

The moulds were placed in a vacuum at 30°C and once the pressure had increased to 1000 mbar the air was release (to draw the mixture into the tips of the silicone mould to ensure sharp microneedle production). If required after vacuuming, the mould was topped up with additional solution to account for solvent evaporation. The mixture was left at room temperature for seventy-two hours and removed from the moulds following this. Electron micrographs detailing the typical morphology of the polystyrene-carbon microneedle array (Ps-C MN) are shown in **Figure 4.1.2.2A** and a single needle in **Figure 4.1.2.2B**. The micro-moulding fabrication process results in the production of sharp needle tips, essential to pierce the tough stratum corneum. The baseplate and carbon rod are coated with enamel to define the geometric electrode area.

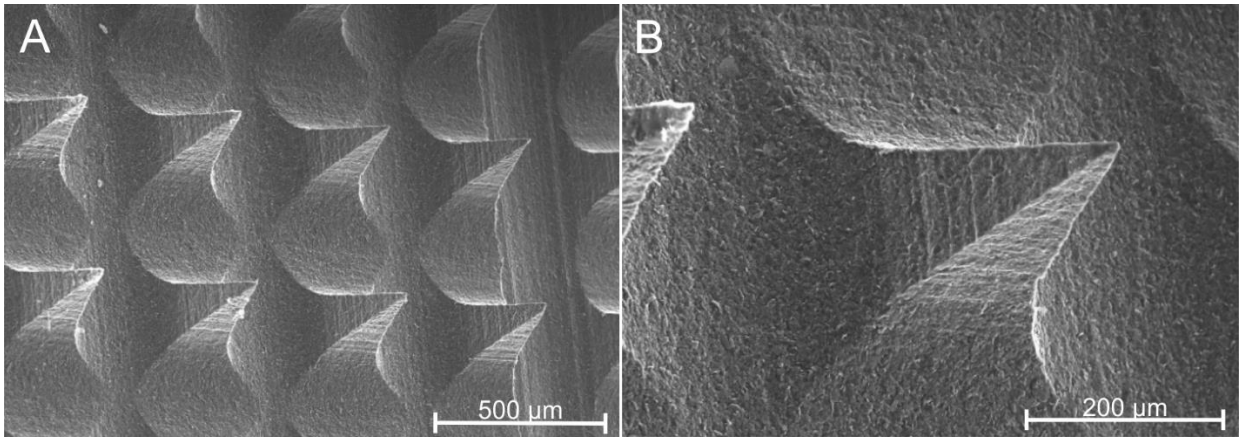

Figure 4.1.2.2 Electron micrograph of A) polystyrene-carbon microneedle array, B) single needle from polystyrene-carbon microneedle 200(base) x 500(pitch) x 700(height).

The microneedle tips were examined by orientating the stage of the electron microscope (**Figure 4.1.2.3**) and their width estimated at 200 µm +/- 1.9 µm in based on a sample of 10 needles.

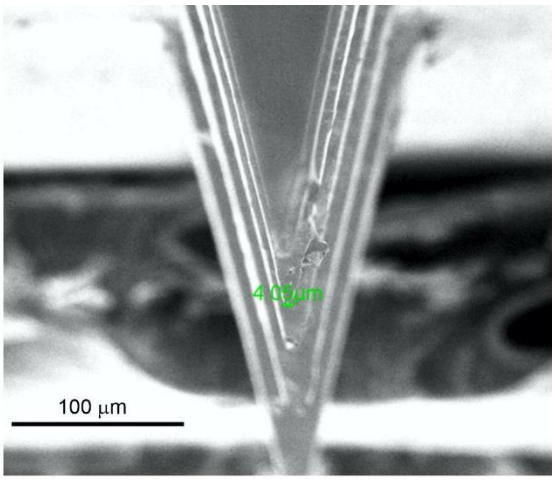

Figure 4.1.2.3 Electron micrograph cross-section of polystyrene-carbon microneedle array.

The conductivity of the resulting 50:50 wt% Ps-C MN formulation was analysed by Mr Cameron Scott using a Keithley 4 point probe (2461 series Source Meter) and found to be 1575.2 S/m ± 96 S/m (N = 5).

4.2 Results and Discussion

4.2.1 Preliminary Electrochemical Analysis

A cyclic voltammogram detailing the electrochemical response of an unmodified Ps-C MN towards ferrocyanide (2 mM, 0.1 M KCl) is shown in **Figure 4.2.1.1** The unmodified microneedle can be seen to display a very large peak separation (ΔE_p = 600 mV) characteristic of slow electron transfer.

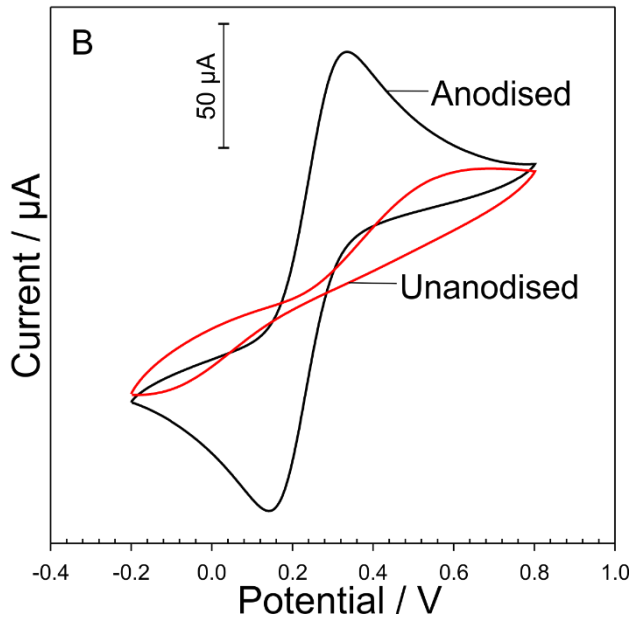

Figure 4.2.1.1 Cyclic voltammograms of detailing the response of polystyrene-carbon microneedles to ferrocyanide (2mM,0.1 M KCl, 50mV/s) before and after electrochemical anodisation in NaOH (0.1 M, +2V, 60s).

Electrochemical anodisation is a well-known process which is often used to enhance the electrochemical properties of carbon electrodes and simply requires immersing the microneedle in alkaline solution (0.1M NaOH) along with the imposition of a large positive potential (+2V) for periods between several seconds to several minutes. The general electrode process involved is indicated in **Equation 4.1**.

$$2H_2O_{(l)} \rightarrow O_{2(g)} + 4H^+_{(aq)} + 4\ e^- \qquad \textbf{Eq 4.1}$$

It could be expected that the positive charge at the electrode interface would lead to nucleophilic attack by hydroxyl ions (from the prevailing NaOH electrolyte) resulting in the immediate interface becoming more hydrophilic. This, in combination with the evolution of oxygen, can lead to the exfoliation/delamination of the graphitic layers creating more edge plane sites with a higher proportion of carbon-oxygen functionalities. This process was investigated here and the corresponding voltammogram is compared to that obtained prior to the surface modification in **Figure 4.2.1.1**.

The anodisation process greatly improved the electrochemical performance where the peak separation of 100 mV is markedly closer to the theoretical Nernstian value of 59 mV for the 1 electron transfer process common to ferrocyanide. Polystyrene loaded with carbon nanoparticles has a similar electrochemical response to graphitic carbon which is dramatically improved after anodisation and it can be anticipated that the process results in the generation of defects and increases the number and variety of oxygen functionalities some of which are indicated in **Figure 4.2.1.2**.

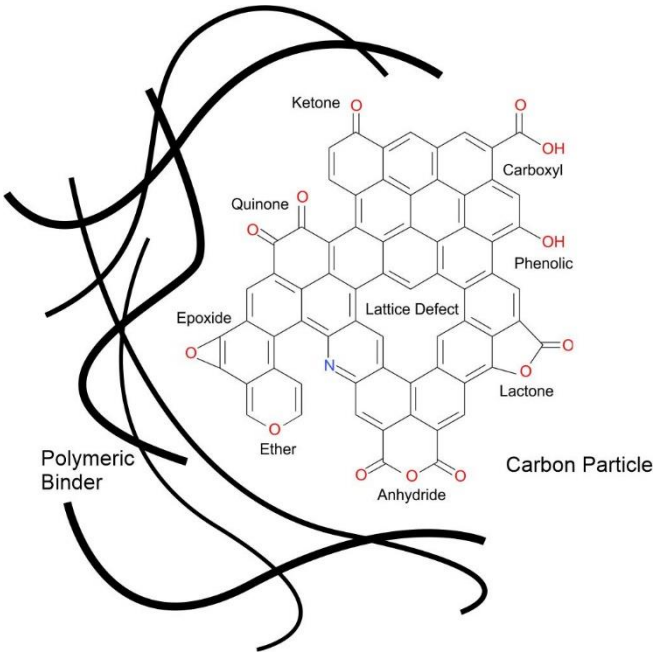

Figure 4.2.1.2 Summary of the functional groups present on the surface of carbon nanoparticles within the polystyrene microneedle matrix (adapted from (247)).

The structural features of carbon are the basal and edge planes which exhibit entirely different electrochemical profiles and while both are present on unmodified carbon MN, basal planes predominate. In contrast, the exfoliation processes that occur during anodisation create more edge planes. The featureless planar nature of the graphite particles within the unmodified Ps-C MN does not facilitate electron transfer as well as edge planes and thus the anodisation process leads to a greater proportion of the latter which, in combination with the oxygen functionalities highlighted in **Figure 4.2.1.2**, lead to much faster electron transfer and the appearance of the conventional / near reversible "duck" shaped CV profile (**Figure 4.2.1.1**).

4.2.2 Raman Analysis of Surface Modification

Raman spectroscopy was preformed to investigate the effect of anodisation on the polystyrene-carbon microneedle. From the spectra detailed in **Figure 4.2.2.1** it can be seen that both samples contained prominent vibrational modes at 1345 cm^{-1}, 1595 cm^{-1} and 2695 cm^{-1}, which correspond to the D, G and 2D bands of graphitic materials (248) retrospectively. The vibrational modes of polystyrene are also present at 2910 cm^{-1} and 3055 cm^{-1} which correspond to the aliphatic C-H bonds and the aromatic C-H bonds retrospectively (249). The D-band (indicates out of plane vibrations in the sp^2 lattice hence defects) increases following anodisation. The I_D/I_G ratio of the unmodified Ps-C MN was calculated as 1.39 versus the anodised Ps-C MN was calculated as 0.98, typically, the I_D/I_G ratio increases when there are more defects (250), which we know to be the case here due to the increased intensity of the D-band after anodisation. However, the ratio doesn't follow this rule as the G-band overlaps with a vibrational mode of polystyrene at 1600 cm^{-1} characteristic of C=C double bonds resulting in a higher intensity. The prominent vibrational modes of aliphatic and aromatic C-H bonds support this as they increase two-fold following anodisation. The process of anodisation and the subsequent generation of oxygen bubbles at the electrode (carbon particle) interface could dislodge particles from the surface and in this case perhaps exposes more of the polystyrene binder.

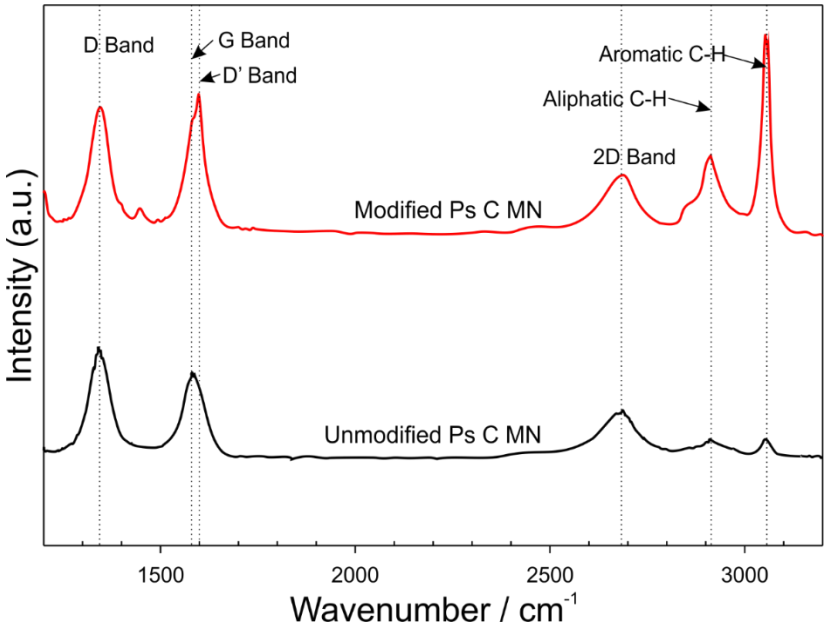

Figure 4.2.2.1 Raman spectra of unmodified and anodised polystyrene-carbon microneedle.

4.2.3 Contact Angle Analysis

It can be expected that the unmodified Ps-C MN will exhibit hydrophobic characteristics given the lack of polar groups within the polystyrene binder and carbon particles. In contrast, the increased population of carbon-oxygen functionalities (**Figure 4.2.1.2**) would be expected to enhance surface wettability through their hydrophilic nature. This was confirmed through comparing the contact angle measurements for the unmodified and anodised MNs. The former was found to be very hydrophobic with the water droplet sitting as a ball on the MN surface (**Figure 4.2.3.1B**) and exhibited a contact angle of 136°. In comparison, the contact angle for polystyrene alone deposited onto a planar silicone sheet (no needles) was found to 90° which is consistent with the literature (251). The inclusion of carbon nanoparticles within the formulation of the planar film led to a further increase in the hydrophobicity with a contact angle of 98°. This is still much lower than that observed at the MN structure, and it could be envisaged that the needle morphology itself impacts on the contact angle measurements. In contrast, the anodised MN led to the spreading of the droplet across the MN plate giving the characteristic “dome” like appearance with a contact angle of 104° and certainly appears to improve surface wettability.

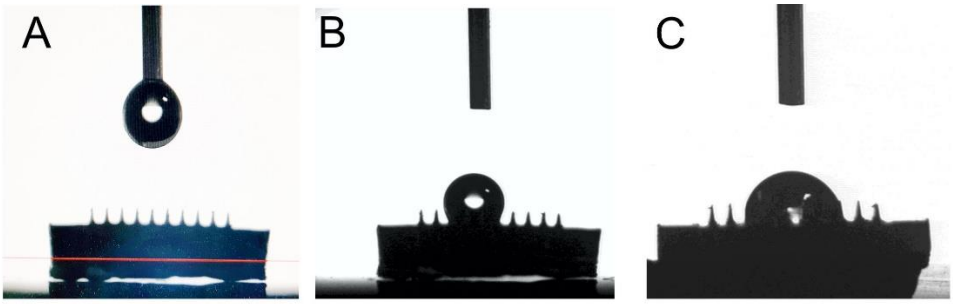

Figure 4.2.3.1 Contact angle measurements of a polystyrene-carbon (Ps-C) microneedle A) before drop release, B) at the unmodified Ps-C MN and C) at the anodised Ps-C MN.

4.2.4 Influence of Laser Treatment on MN Structure and Performance

It is clear that the electrochemical oxidation processes increase oxygen species which in turn influence wettability, surface reactivity, porosity and electron transfer kinetics of the electrode. While the process is effective, it is nevertheless, procedurally cumbersome in terms of the mechanics involved. Instrumental techniques such as plasma (252) and laser ablation (253) have however been promoted as a more efficient modification strategy where the need for wet chemical processing is avoided. These approaches have also been shown to lead to similar enhancements as the electrochemical anodisation. As such, laser processing of the microneedle structures was investigated here whereby laser patterning of the Ps-C MN was performed. The rationale was the laser ablation of the interfacial polymer would improve the electrochemical properties by exposing carbon within the polystyrene binder thereby enhancing the effective surface area. Moreover, work by Ezkiel *et al.*, (2008) demonstrated that ablation in an air atmosphere led to exfoliation of carbon fibre creating edge plane sites which enhanced the electron transfer kinetics. It was envisaged that were this approach successful, it would be advantageous from a manufacturing standpoint simplifying the development process and avoiding the wet chemical stages.

Electron micrographs detailing the results of the laser rastering at various power settings across Ps-C MN patches are detailed in **Figure 4.2.4.1**. Following laser processing of Ps-C MN, sharp needle tips are absent, and the topography resembles mounds rather than the pyramidal shape witnessed in **Figure 4.1.2.1**. The change in morphology exhibited in the

electron micrographs in **Figure 4.2.4.1** can be attributed to a loss of the polystyrene binder and exposure of the carbon nanoparticles. This is perhaps unsurprising when the melting point of polystyrene and carbon are considered, polystyrene has a lower melting point around 270°C whereas the melting point of carbon is around 3550°C. Thus, the laser processing easily ablates the polystyrene compromising the sharp needle tips whilst simultaneously uncovering the carbon nanoparticles.

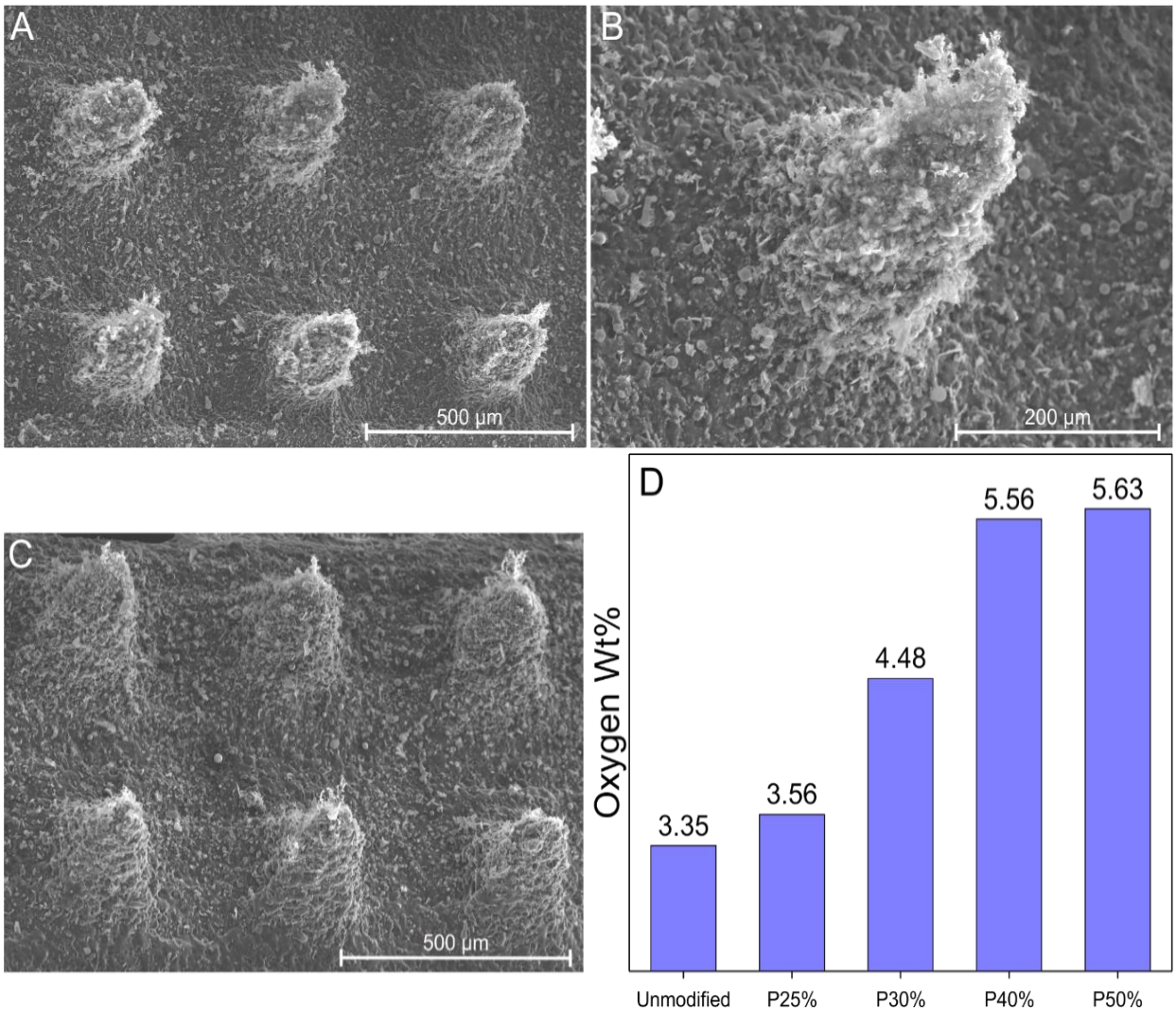

Figure 4.2.4.1 Electron micrograph of polystyrene-carbon microneedle array A) post laser ablation (power 25 %, speed 30, PPI 1000), B) post laser ablation (power 25 %, speed 30, PPI 1000), C) post laser ablation (power 50 %, speed 30, PPI 1000) and D) Oxygen percentage of polystyrene-carbon microneedle array as a consequence of laser ablation at increasing powers obtained from energy dispersive X-ray analysis.

In addition to exposing the carbon nanoparticles, laser ablation increased the percentage of oxygen species, shown in the elemental analysis in **Figure 4.2.4.1D** where the oxygen percentage for an unmodified Ps-C MN is 3.35wt% versus 5.63wt% for modified Ps-C MN (Power 50 %).

It also suggests that increasing the laser power, increases oxygen percentage but caution must be applied to prevent destruction of the microneedle array entirely. It is important to note that EDX provides elemental analysis throughout the entire depth of a sample, and laser ablation is a surface modification, so it is possible that oxygen percentage is in fact higher than calculated at the surface of the Ps-C MN which is the most significant factor for improved electrochemical performance.

Cyclic voltammograms detailing the electrochemical response of Ps-C MN patches following laser ablation towards ferrocyanide (2 mM, 0.1 M KCl, 50 mV/s) are shown in **Figure 4.2.4.2A.** Inspection of the individual voltammograms reveals that although 25 % and 30 % power expose carbon nanoparticles within the Ps-C MN (evidenced by the SEM images in **Figure 4.2.4.1**) but the resulting MN fail to exhibit any significant improvement in electrochemical properties with irreversible behaviour (ΔE_p = 600 mV) and ambiguous peak currents. Processing at higher power with the application of 40% and 50% leads to Ps-C MN exhibiting more reversible profiles (40%: ΔE_p = 200 mV; 50%: ΔE_p = 100 mV). It is clear that increasing the laser power improves the electrochemical properties and this is consistent with the results reported by Ezekiel *et al.*, (2008) for carbon fibre (253). This aligns with elemental analysis indicating increased oxygen functionalities following ablation by higher powers and hence faster electron kinetics. From this we can see that laser ablation provides similar electrochemical profile to anodised systems displayed in **Figure 4.2.4.2B** where peak separation is roughly 100 mV albeit with a decreased peak current. It could be envisaged that the electrochemical anodisation is much more efficient at disrupting the carbon particle structure without loss of the needle integrity – preserving the majority of the carbon surface. In contrast, the need to go higher laser powers to acquire similar electrochemical performance

results in substantial loss of the needle structure itself (as per the SEM images in **Figure 4.2.4.1**) and hence the lower current.

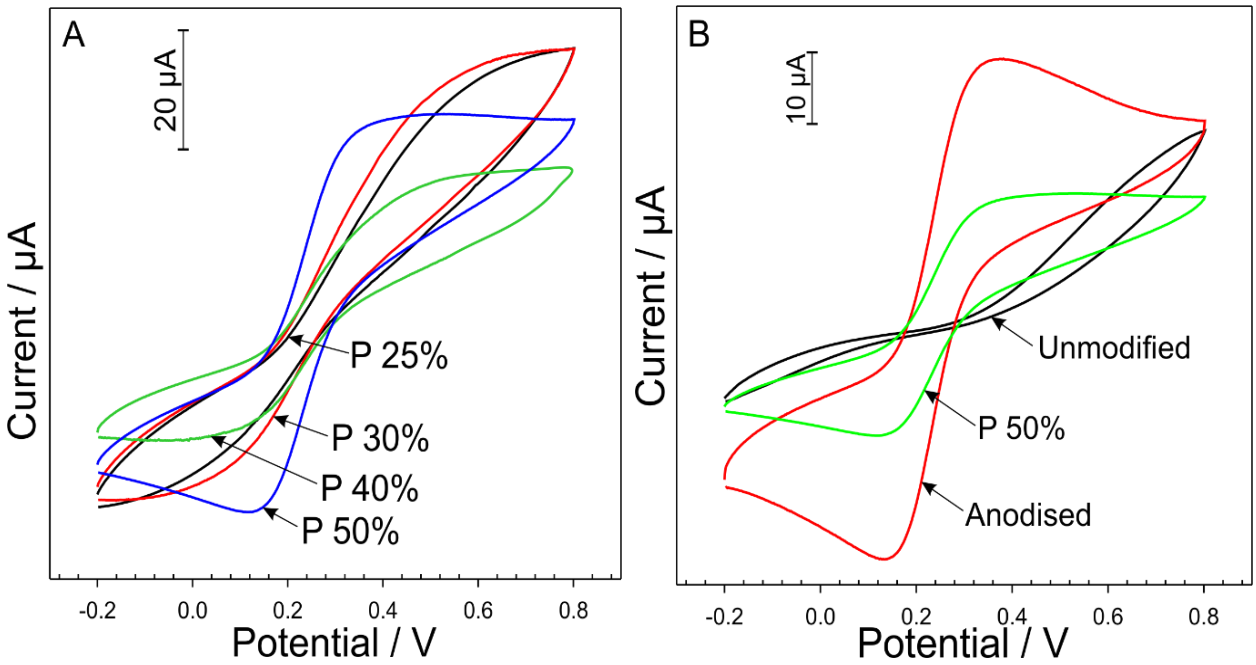

Figure 4.2.4.2 Cyclic voltammogram of A) modified polystyrene-carbon microneedle to ferrocyanide (2mM,0.1 M KCl, 50mV/s) following laser ablation of varying power (Raster mode, speed 30, PPI 1000), B) unmodified polystyrene-carbon microneedle to ferrocyanide (2mM,0.1 M KCl, 50mV/s) versus anodised in NaOH (0.1 M, +2V, 60s) and laser ablated (Power 50 %, raster mode, speed 30, PPI 1000).

4.2.5 Design of a Multilayer MN Patch

The laser modified MNs are redundant in isolation as they do not possess the structural features essential for insertion within the skin. The sharp tips are reduced to blunt particulate mounds which would likely flatten when applied to the skin. However, the large surface area and increased oxygen species can be useful for a variety of sensing contexts or for controlled drug delivery discussed in subsequent chapters. This led to the design of a multilayer MN patch illustrated in **Figure 4.2.5.1** where it was envisaged that skin penetration could be accomplished by a biocompatible (and dissolvable) MN layer allowing interstitial fluid to enter the second layer, thus come into contact with the laser processed MN. This approach could have a number of advantages over the direct application of composite needles. The current

recorded at the MN electrode will be dependent upon the effective electrode area and, as such, damage to the needles during insertion could significantly alter the analytical response. It is possible to envisage shear forces breaking the needles at the point of application as the patch is unlikely to be inserted perpendicular to the skin surface. There is also the fact during insertion, fouling of the electrode surfaces could occur as the needles mechanically push between and through the skin cells. The use of a sacrificial needle system to create a series of microchannels could be useful in protecting the working surfaces of the diagnostic or drug releasing needles. A schematic of the dual layer needle concept is shown in **Figure 4.2.5.1**. The insertion (A) leads to the steady dissolution of the needles leaving behind the microchannels in the upper skin layers (B). This is a conventional approach in “poke and patch” microneedle drug delivery systems (254) where the needle is used solely to puncture the skin and leave entry points for a topically applied drug to access the underlying tissue. In this case the microchannels can serve as a means of transporting the interstitial fluid to the secondary sensing needle array (C) or, alternatively, allowing access to a drug which is tethered to the secondary needles and released upon receiving an appropriate electrochemical trigger (D). The mechanisms relating to the latter opportunity are discussed in more detail within **Chapters 6** and **7**.

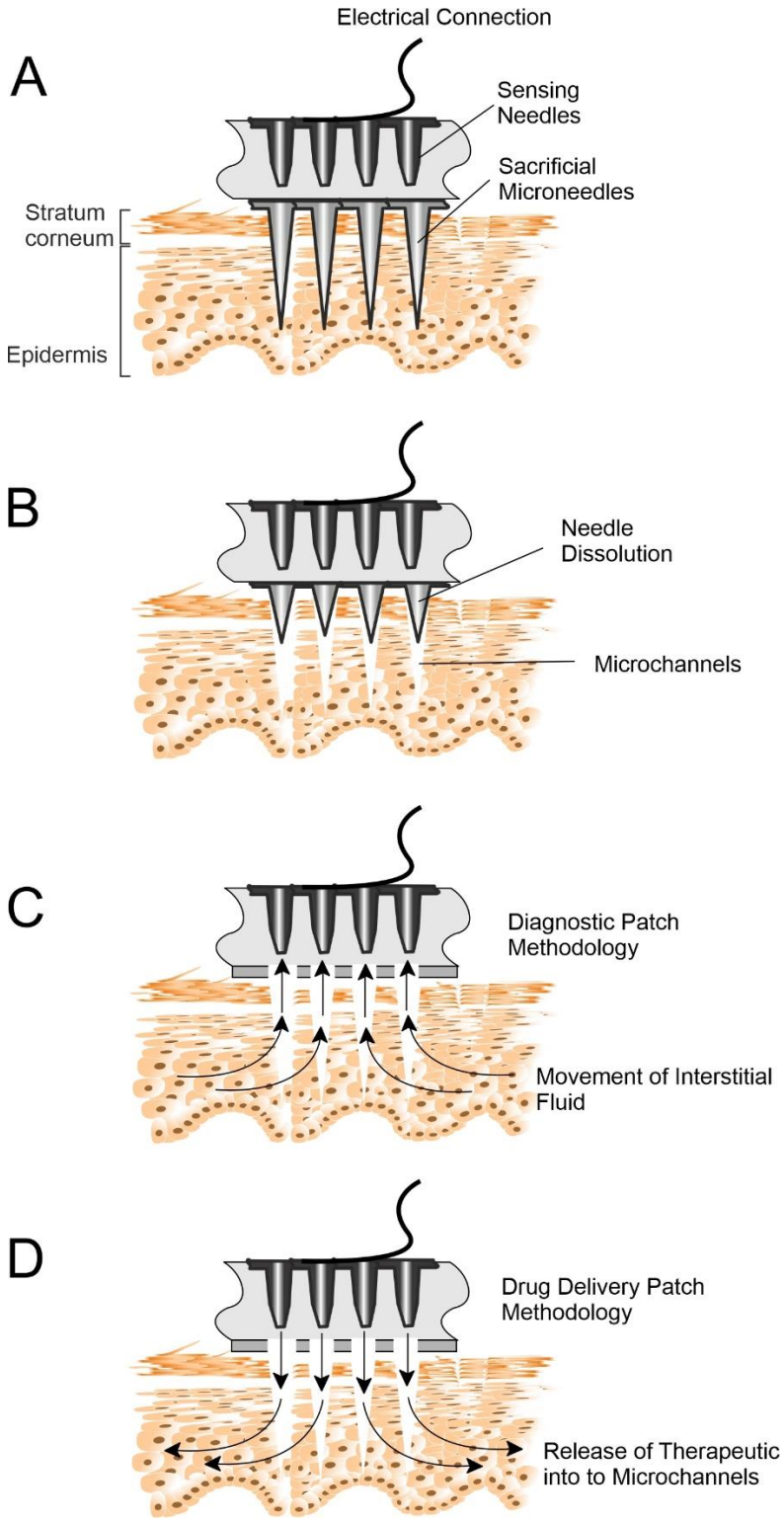

Figure 4.2.5.1 Schematic of multilayer microneedle patch with biocompatible layer to pierce the skin and laser processed layer for sensing or controlled drug delivery.

4.2.6 Cellulose Acetate Phthalate MNs

Cellulose acetate phthalate (CAP) was chosen as the primary constituent of the sacrificial microneedle array. It is a biocompatible substrate that produces sharp microneedles as seen in **Figure 4.2.6.1**. CAP serves as an ideal candidate as it is soluble in neutral / mildly alkaline medium, and it would be anticipated that its dissolution within the skin layers would provide access to the underlying electrode layer of the dual layer MN assembly.

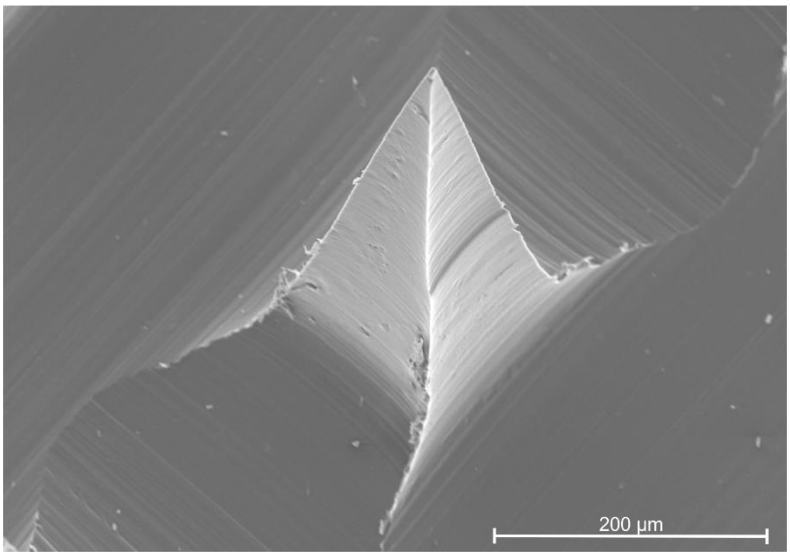

Figure 4.2.6.1 Electron micrograph of cellulose acetate phthalate microneedle 200(base) x 500(pitch) x 700(height).

The electron micrographs in **Figure 4.2.6.2** demonstrate CAPs behaviour when submerged in Britton Robinson pH 7 buffer over time. After five minutes, the sharp needle tip is diminished, whilst maintaining the general pyramidal shape **(Figure 4.2.6.2A)**. With continued dissolution, after ten minutes, the surface of the microneedles become smooth and even less defined (**Figure 4.2.6.2B**). After thirty minutes of sustained immersion in the buffer, the dissolution processes culminate with point fractures in the baseplate (**Figures 4.2.6.2C-F**). It could be envisaged that at this point, migration of the interstitial fluid to the lasered microneedles would, in principle, be possible.

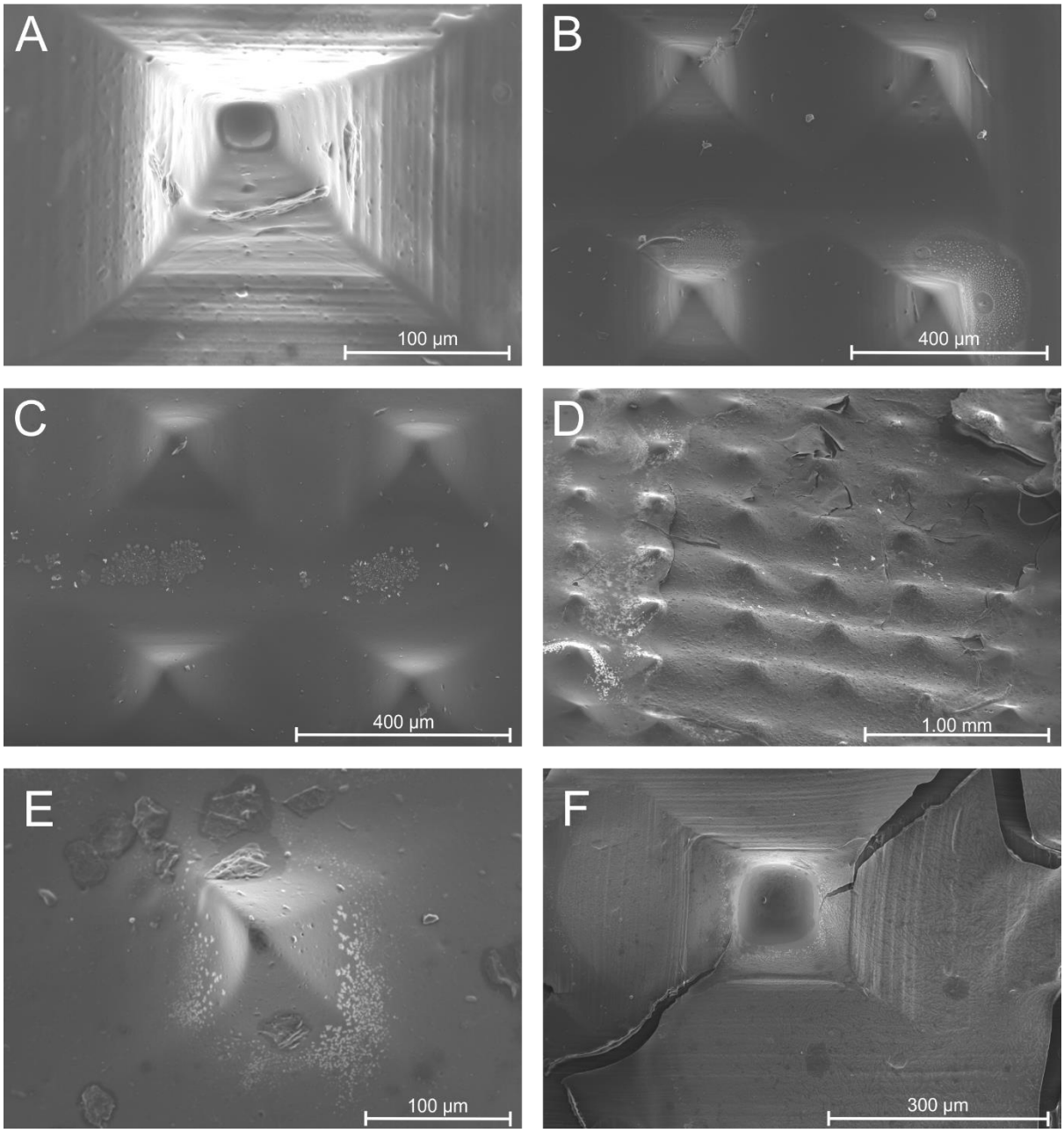

Figure 4.2.6.2 Electron micrograph of cellulose acetate phthalate microneedle submerged in pH 7 buffer for A) five minutes, B) ten minutes, C) thirty minutes, D) thirty minutes displaying fractures in baseplate, E) thirty minutes displaying ambiguous/smooth needle and F) thirty minutes displaying fracture on baseplate.

4.2.7 Multilayer Assembly

Following characterisation of the electrochemical properties of the laser modified Ps-C MN and the dissolution of CAP MN, assembling the dual layered MN array was a natural successor. The CAP / laser modified Ps-C MN assembly was analysed by micro computerized

tomography (µCT) to highlight the core structure and internal void as detailed in **Figure 4.2.7.1**.

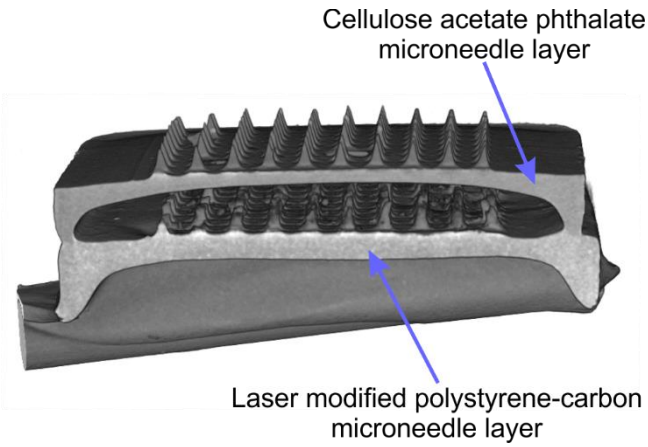

Figure 4.2.7.1 Sliced X-ray image of cellulose acetate phthalate microneedle layered on top of laser modified polystyrene-carbon microneedle.

The MN patches were directly aligned by visual inspection and sealed. A carbon fibre rod maintained electrical contact to the Ps-C MN layer. It can be seen from the µCT that the needles are intact after placement with a clear space for fluid to access the Ps-C array.

4.2.8 Characterisation of Multilayer Assembly

Electron micrographs in **Figure 4.2.8.1** illustrate how the CAP layered - laser modified Ps-C MN assembly behaves after being submerged in Britton Robinson pH 7 buffer for thirty minutes. As expected, the CAP MN has dissolved leaving behind cavities to expose the underlying laser modified Ps-C MN. As the CAP MN dissolves, it appears to become more flexible and bends as highlighted in **Figure 4.2.8.1A**. The CAP MN and Ps-C MN are aligned well as shown in **Figure 4.2.8.1B** and **Figure 4.2.8.1C**, and the integrity of the laser modified Ps-C MN is maintained in **Figure 4.2.8.1D**. It should be noted that in general, direct alignment of the MN is not required as when the CAP needles dissolve, the expectation would be that the fluid would enter the cavity and contact each of the underlying Ps-C MN.

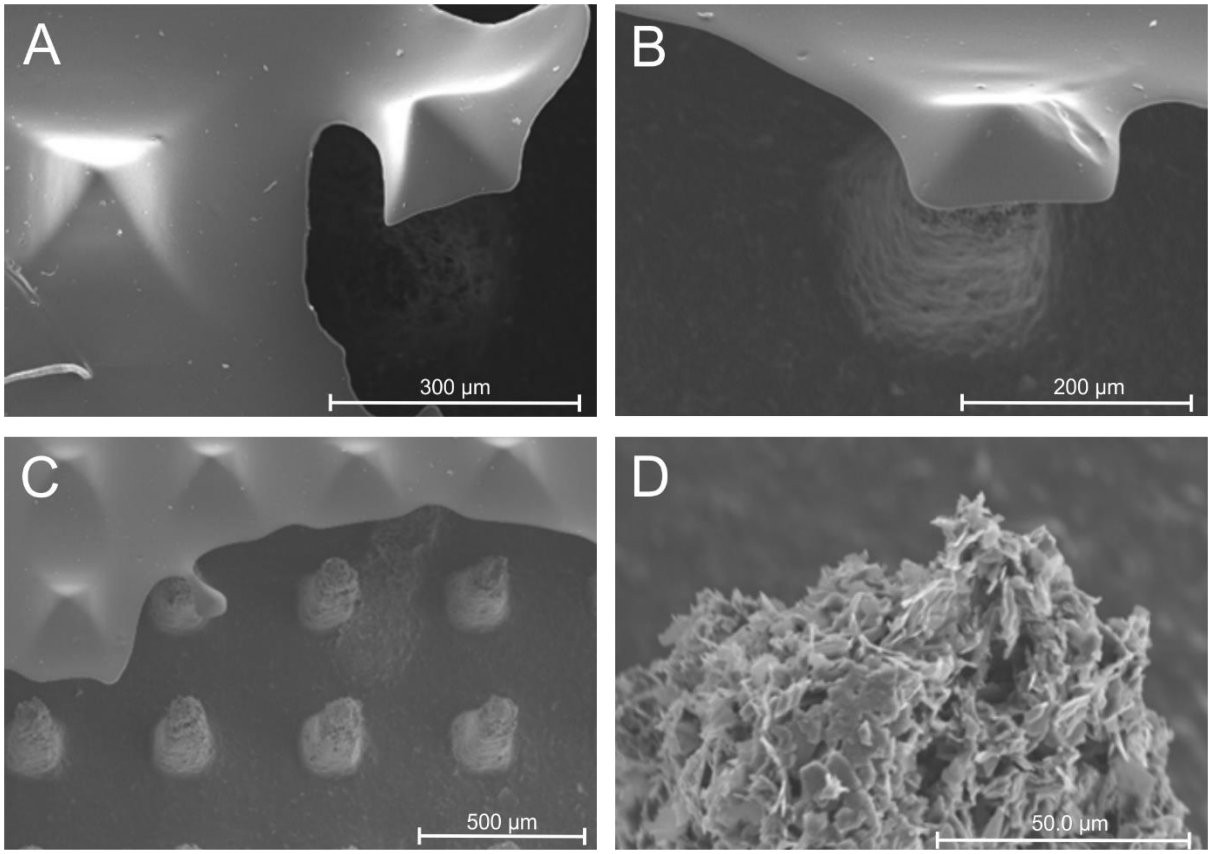

Figure 4.2.8.1 Electron micrographs of dual layer microneedle after thirty minutes in Britton Robinson pH 7 buffer showing A) the flexibility of the CAP MN bending, B) the alignment of the CAP and underlaying modified Ps-C MN, C) the large cavity in the CAP MN exposing the underlaying sensing MN and D) the intact laser modified Ps-C MN.

After studying the dual layer MN *via* electron microscopy, the next step was to assess the electrochemical properties of the array. Cyclic voltammograms detailing the electrochemical response of CAP layered - laser modified Ps-C MN towards ferrocyanide (2 mM, 0.1 M KCl, 50 mV/s) after zero minutes, one minute, fifteen minutes and thirty minutes in pH 7 Britton Robinson buffer are shown in **Figure 4.2.8.1**. As anticipated, the electrochemical performance improves as the CAP layer dissolves with increased time in the pH 7 buffer, to expose the underlaying laser modified Ps-C MN. Very slight bumps are seen after one minute and fifteen minutes, indicting a small volume of solution has reached the underlaying Ps-C MN and can be attributed to pin holes in the enamel used to electrically isolate the backplate of the Ps-C MN. However, after thirty minutes clear redox peaks are visible, and the characteristic quasi

reversible duck profile is observed (ΔE_p = 200 mV) confirming that CAP does not influence the electrochemical performance of the underlaying laser modified Ps-C MN.

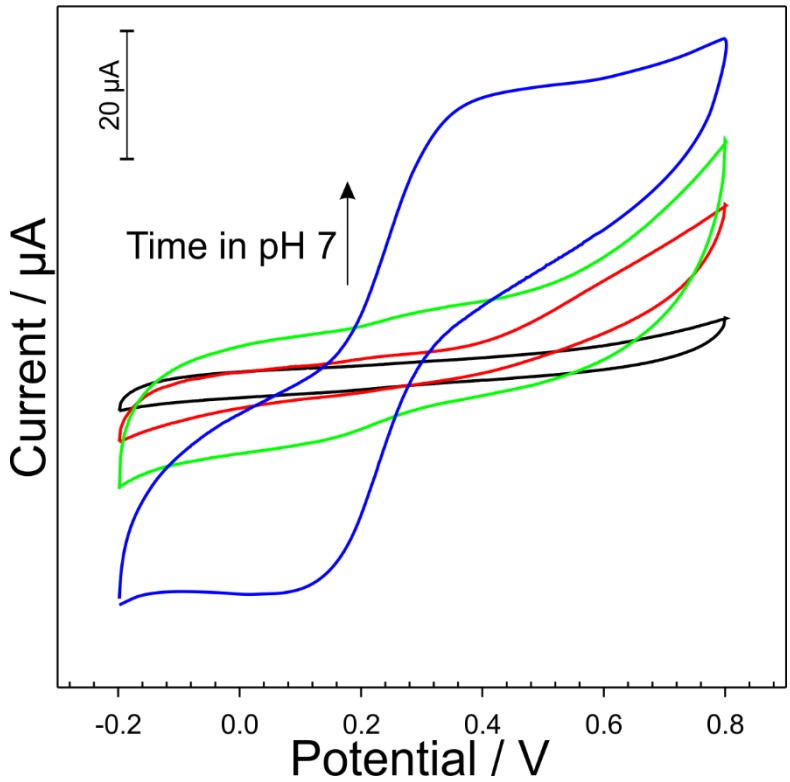

Figure 4.2.8.2 Cyclic voltammogram of cellulose acetate phthalate layered laser modified polystyrene-carbon microneedle to ferrocyanide (2mM,0.1 M KCl, 50mV/s) with increasing time in pH7 (Black zero minutes, red one minute, green fifteen minutes and blue thirty minutes).

4.3 Conclusions

In this chapter alternative methods to improve the electrochemical performance of polystyrene-carbon nanocomposite microneedle arrays were investigated. The microneedle was modified by both electrochemical anodisation and laser ablation to increase oxygen functionalities. Elemental analysis confirmed increased oxygen wt% with increasing laser power which translated to improved electrochemical performance. Electron microscopic studies found that laser modification compromised the structural integrity of the microneedle array – effectively removing the piercing capability. An alternative design concept was

formulated where the enhanced surface area exposed by the laser processing could be used to advantage and an innovative dual layer prototype system was constructed. The latter employed cellulose acetate phthalate as a sacrificial insertion system leaving behind microchannels for interstitial to reach the underlaying lasered carbon layer. The latter could be used for diagnostic or drug delivery applications.

Chapter 5

Nanocomposite Microneedles Based on Cellulose Acetate Phthalate and Carbon Nanoparticles Decorated with Laser Induced Graphene to Improve Electrochemical Performance

Overview

This chapter investigates various laser induced graphene (LIG) formations to be harvested and added to cellulose acetate phthalate-carbon microneedles in order to improve their electrochemical performance. Electrochemical analysis such as cyclic voltammetry and square wave voltammetry are employed to test the response of the system to ferrocyanide and uric acid retrospectively. Electron micrographs detail the morphology of the LIG formation and illustrate the sharpness of the microneedle systems. As well as preliminary studies into the biodegradability of CAP as a binder to address issues of waste generated by sharps using blood glucose sensors used by diabetic patients as a way to quantify waste generated. The CAP system is preliminary assessed as an alternative peroxide sensor.

Some of the work presented in this chapter has contributed to peer reviewed publications:

Robert Barber, Sarah Cameron, **Amy Devine**, Andrew McCombe, L. Kirsty Pourshahidi, Jill Cundell, Souradeep Roy, Ashish Mathur, Charnete Casimero, Pagona Papakonstantinou, James Davis, 2021. Laser induced graphene sensors for assessing pH: Application to

wound management. *Electrochemistry Communications*. 123. https://doi.org/10.1016/j.elecom.2020.106914

Amy Devine, Ellen Hegarty, Catherine Hegarty, James Davis, 2023. Conductive Composite Microneedle Sensors based on Cellulose Acetate Phthalate: Investigating Performance and Biodegradability. *IEEE Sensor Letters*. https://doi.org/10.1109/LSENS.2023.3245024

5.0 Introduction

Graphene materials can be produced by numerous means such as mechanical exfoliation (255), chemical synthesis (256), chemical exfoliation (257; 258), and chemical vapor deposition (259). Mechanical exfoliation is one of the first discovered methods of isolating graphene flakes from graphite. It is relatively simplistic, whereby tape is applied to graphite and peeled off, which breaks the weak van der Waals' forces holding the layers of graphene stacked on top of one another (260; 261) and ultrasonication can achieve similar results (262). Mechanical exfoliation produces high quality graphene layers, however, there are limitations when it comes to scalability and reproducibility (263). Chemical synthesis refers to the chemical reduction of graphene oxide and there are three main routes, the Brodie method (264), Staudenmaier method (265) and Hummers method (266) which involve the oxidation of graphite with acids and oxidants. Chemical synthesis routes are time consuming, involving several hazardous steps (263). Chemical exfoliation is the process of introducing alkali metals into a graphite solution to increase interlayer spacing, thus breaking the van der Waals' forces holding the layers together which is then sonicated to disperse the layers (267). Thermal chemical vapor deposition of graphene involves filling a quartz tube with various gases such as methane, hydrogen and argon containing a metal substrate at high temperatures. Over time a single layer of graphene will be deposited upon cooling (259). Chemical vapour deposition can be plasma enhance allowing for the production of graphene at lower temperatures (268). Chemical vapor deposition is commonly used to produce graphene, however, it requires extensive equipment and materials to fabricate.

In this work, a single-step fabrication process has been adopted where a film of porous graphene is induced onto an insulating polymer substrate (269). There has been considerable interest in the development and characterisation of laser-induced graphene (LIG) as it provides a facile method of additive manufacture of highly conductive substrates, which, in contrast to screen printing systems, allows rapid prototyping of electrochemical sensors. In some respects, the investigations conducted in **Chapter 4** could be considered an attempt at

creating laser induced graphene directly on to the microneedle (MN) surface. The creation of graphene like domains within the MN structure could impart many favourable characteristics such as excellent electrical and thermal conductance, high rate of electron transfer kinetics and large surface area (270). The outcomes from the previous laser investigations however, at least from the perspective of needle integrity, less than successful and hence an alternative approach to LIG based MN fabrication is required.

Polyimide (PI) film is commonly used as a substrate to fabricate LIG, due to the wide absorption range of PI film to a spectrum of laser sources. Both, UV, and IR commercial laser systems can be used to carbonise the abundance of aromatic groups (**Figure 5.0.1**) within the chemical structure (271; 272). The photothermal process that converts polyimide to LIG, breaks the bonds between the carbon with the subsequent liberation of gases giving LIG a porous, foam-like structure (269). Polyimide is a cost-effective substrate used to produce graphene and the laser processing provides freedom when it comes to design without the use of chemicals (273; 274; 275).

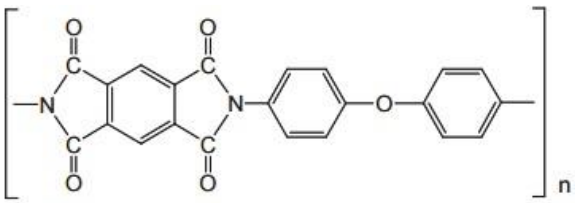

Figure 5.0.1 Structure of polyimide.

The surface morphology produced by laser patterning can be tuned based on the required application and it can range from a foam structure to long, thin nanotube-like structures (276). In producing nanotube-like structures or fibres, the surface area is increased and, in turn, provides opportunities for it to be functionalised with catalysts or drugs (277). Extensive research has been conducted employing carbon nanotubes (CNT) as a means to improve the conductivity of polymer composites. Zhang *et al.*, (2020) combined CNT with cellulose to improve electrical conductivity (278), and similarly Behera *et al.*, (2020) combined CNT with poly(lactic acid) as a biodegradable alternative (279). In either case, the translation of the

approaches for rapid prototyping or mass manufacturing are problem. In contrast, laser induced graphene can be tuned through simply alternating the instrumental parameters of the laser system.

In this work, the primary aim was to investigate the substitution of the carbon nanoparticles with laser induced graphene (LIG) has been investigated where the intention was to harvest LIG from the laser ablation of large areas of polyimide film. This would allow its direct inclusion within the microneedle / moulding formulation process and thereby enable the single step manufacture of conductive microneedles with enhanced electrochemical properties rather than relying on post-production modifications.

A secondary aim was to improve the biodegradability of the MN themselves as a means of avoiding the waste associated with conventional point of care diagnostics (*i.e.*, glucose test strips and lancets) as well as syringe-based drug/vaccine delivery. While polycarbonate and polystyrene have been the polymers of choice as the binder which supports the 3D form (210; 211), neither could be considered as biodegradable. There is an extensive literature base on the use of dissolving microneedle formulations, but such systems are invariably intended to enable rapid swelling to allow delivery of a drug. In this case, the microneedle is intended to act as an electrode and it is clear that premature dissolution of the needle component would destroy its analytical capability. As such, there is a need for a polymeric binder which would be stable under a given set of conditions for a duration appropriate to collect the target data, but which would, over a more moderate period, dissolve leaving only the carbon residue. Cellulose acetate phthalate (CAP) was selected as the binder here on the basis that the material is known to be chemically and mechanically stable in acid condition but begins to dissolve when exposed to mildly alkaline media and is widely used as an enteric coating for oral tablet formations to enable transit of the drug to the intestine. The choice of CAP was also made on the basis of the results from the previous chapter where it was shown to be capable of forming well defined microneedles. The development of a CAP – LIG composite microneedle was therefore proposed as a means of facilitating the single step fabrication of a

disposable sensor system offering both enhanced electrochemical performance and biodegradability.

5.1 Experimental Details

5.1.1 Materials and Instrumentation

Carbon nano powder (<100 nm), polystyrene (MW 192,000), cellulose acetate phthalate (MW 2534) and all associated laboratory chemicals were obtained from Sigma-Aldrich, were the highest grade available and were used without further purification. Britton Robinson buffers (acetic, boric, and phosphoric acids, each at a concentration of 0.04 M and adjusted to the appropriate pH through the addition of sodium hydroxide) were used throughout unless otherwise specified. Microneedle moulds were obtained from Micropoint Technologies Pte Ltd (Singapore) and were pyramidal in format with 200(base) x 500(pitch) x 700 (height) micron dimensions covering a 10 x 10 needle array. The structure of the needle design was previous described in **Section 4.1.2**. Electrochemical analysis was carried out using a Palm Sens EmStat 3 computer controlled potentiostat with a standard three-electrode configuration in which the microneedle patch was used as the working electrode with platinum and a Ag|AgCl half cell (3M NaCl, BAS Technicol UK) acting as counter and reference respectively. All measurements were conducted at 22ºC ± 2ºC.

5.1.2 Production of Laser Induced Graphene

Laser induced graphene was prepared through ablating polyimide film (125 micron, Goodfellow UK) with a ULS VLS2.30 25 W CO_2 laser cutter on raster mode, speed 30 and resolution of 1000 pulse per inch. Large area sections of polyimide were rastered (3000 mm^2) and the resulting LIG deposit removed through either sonication or mechanical abrasion with a stainless-steel scalpel. The LIG particles were collected and mixed with cyclohexanone which was cast into the microneedle mould and dried under a heat lamp. This was repeated until the entire mixture was used up (used for eight microneedle patch arrays) and the normal

microneedle production highlighted in the next section followed. Planar LIG electrodes were patterned on polyimide and thermally encapsulated within polyester laminate sheets (125 micron). The latter were pre-cut with a 3 mm diameter window in order to expose a defined area of LIG. A schematic representation of the assembly is detailed in **Figure 5.1.2.1**.

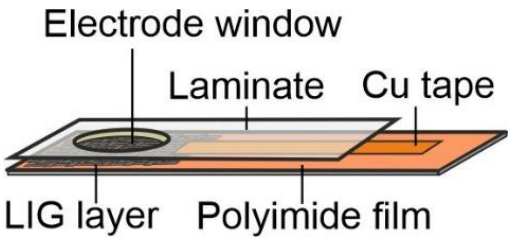

Figure 5.1.2.1 Schematic of planar LIG electrode.

5.1.3 Production of Carbon Composite Microneedles

The carbon microneedles were prepared as previously described in **Chapter 4** with the exception that cellulose acetate was substituted for the polystyrene and laser induced graphene particles for the carbon nanoparticles. The relative ratio of the mixtures was kept at 1:1 by weight, dissolved in cyclohexanone and stirred until a homogenous solution was obtained (typically two hours). The solution was cast into silicone microneedle templates and a carbon fibre stub placed into the base plate to facilitate electrical connection. The moulds were placed in a vacuum at 30°C and the pressure increased to 1000 mbar and the air released again (to force the homogenous solution to the tips of the mould ensuring sharp microneedle production). The templates were topped up with more solution - preferably overflowing the cast to allow for solvent evaporation. The solvent was left to evaporate at room temperature (over forty-eight hours) whereupon the needles could be removed from the patch.

5.2 Results and Discussion

5.2.1 Laser Scribing of Polyimide – A Preliminary Study

An electron micrograph displaying the morphology of polyimide (PI) after laser scribing is shown in **Figure 5.2.1.1**. The unmodified sections of the PI film are smooth and featureless, however, following laser ablation, foam-like carbon structures are produced giving a furrow

like appearance. These structures are formed due to the application of localised heat which degrades the polymer, thus releasing gas causing the polymer to foam. Once cooled, a conductive carbon track is left with a relatively heterogeneous structure as indicated in **Figure 5.2.1.1**.

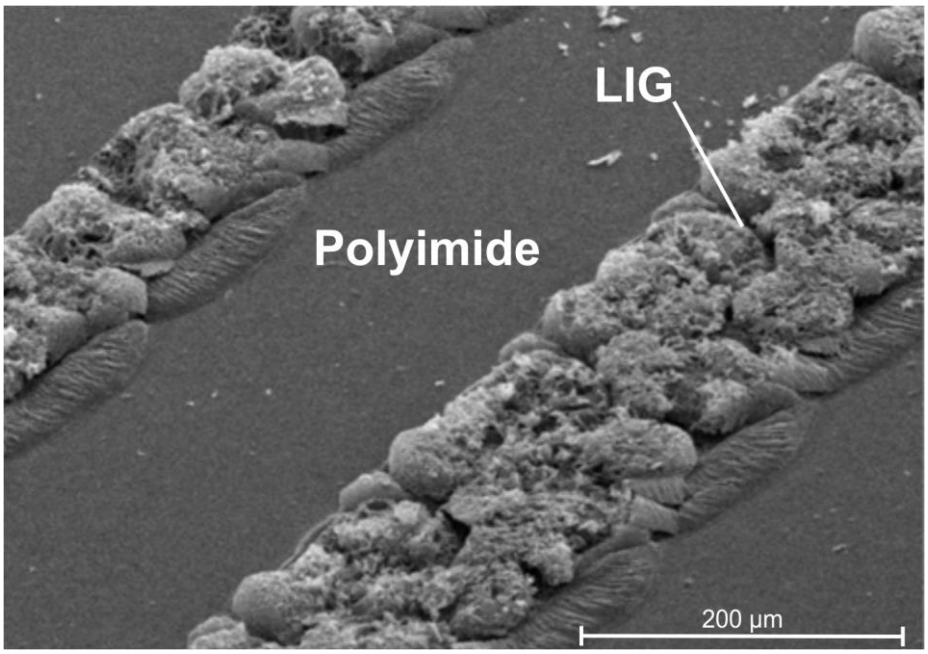

Figure 5.2.1.1 Electron micrograph of polyimide film with laser induced graphene (LIG) tracks.

A cyclic voltammogram detailing electrochemical response of laser induced graphene (LIG) substrate towards ferrocyanide (2 mM, 0.1 M KCl, 50 mV/s) is shown in **Figure 5.2.1.2**. It can be seen that LIG exhibits excellent electrochemical properties with sharply defined redox peaks and a peak separation consistent with the theoretical Nernstian value (E = 60 mV). The reversible nature of ferrocyanide at the LIG electrode stands in marked contrast to the Ps-C MN systems investigated in **Chapter 4**. The fact that the excellent performance can be obtained without any further modification (*i.e.*, anodisation) serves to justify its potential application within MN formulations.

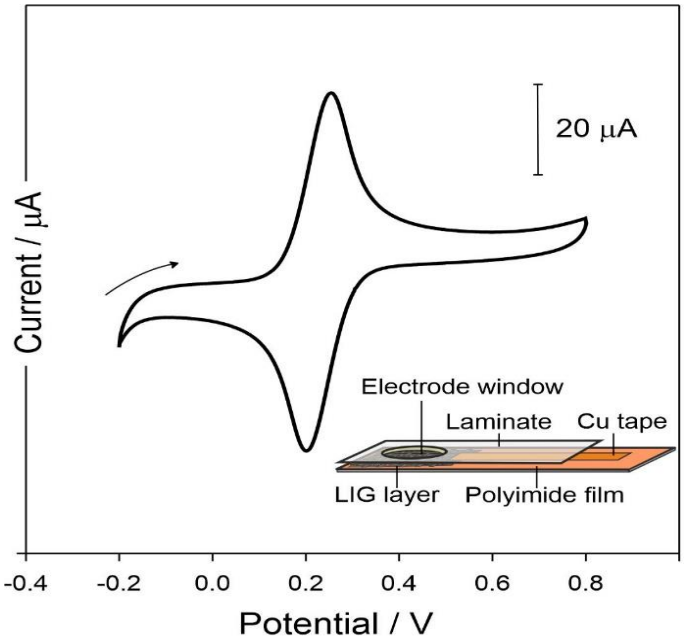

Figure 5.2.1.2 Cyclic voltammogram of laser induced graphene electrode to ferrocyanide (2 mM,0.1 M KCl, 50mV/s). Inset: LIG electrode configuration.

5.2.2 Influence of Laser Power on LIG Formations

It has been documented that altering laser settings can produce a range of LIG formations, in this work, the influence of power was studied initially. The foam-like structures resulting from the application of the CO_2 laser on PI at varying powers are compared in **Figure 5.2.2.1** (speed of 40 %, resolution 1000 pulse per inch (PPI) and raster mode). The overall morphology resembles a loosely formed honeycomb and is highly porous. At lower powers (*i.e.*, 25%), the LIG is moderately fibrous and as the power increases, the fibres are become longer, more apparent and web-like.

5.2.3 Influence of Multiple Passes on LIG Formations

Multiple passes of the laser can improve the graphitisation of non-polyimide substrates thus improving the conductivity (280; 281). In this instance, multiple passes of the laser over the same area of polyimide did not produce visible changes to the LIG morphology seen in **Figure 5.2.3.1**. The initial pass provided sufficient fluence to photothermally break the carbon bonds within the PI surface, thus forming the porous and fibrous morphology.

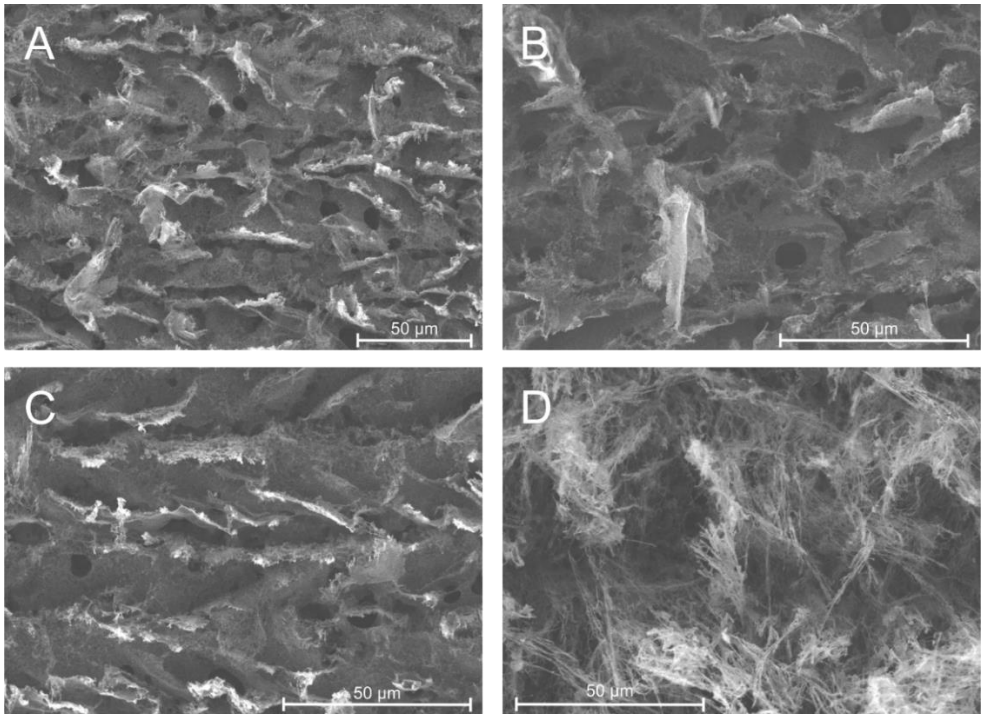

Figure 5.2.2.1 Electron micrograph of laser induced graphene A) power 25 %, B) power 30 %, C) power 35 % and D) power 50 %.

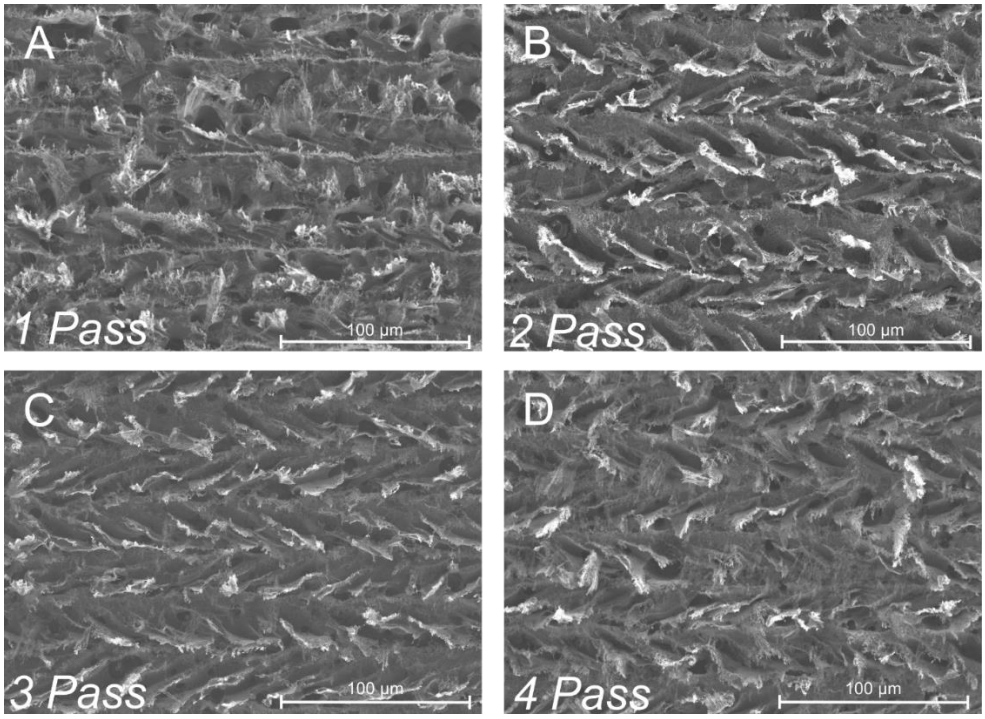

Figure 5.2.3.1 Electron micrograph of laser ablated polyimide after A) 1 pass, B) 2 passes, C) 3 passes and D) 4 passes (PPI 1000, speed 40 and power 30 %).

5.2.4 Cross Sectional Investigation of LIG Formations

The intention was to harvest the LIG formations to be combined with a polymer to produce conductive microneedle arrays, in the hope of enhancing the electrochemical performance, similar to that of the planar LIG electrode shown in **Figure 5.2.1.1**. It is therefore important that the internal layers of graphene are comparable to the superficial layer seen in **Figure 5.2.2.1B** above. This was achieved by stripping the superficial layer of the LIG (Power 30 %) via carbon tape. A porous and fibrous morphology is observed in **Figure 5.2.4.1**.

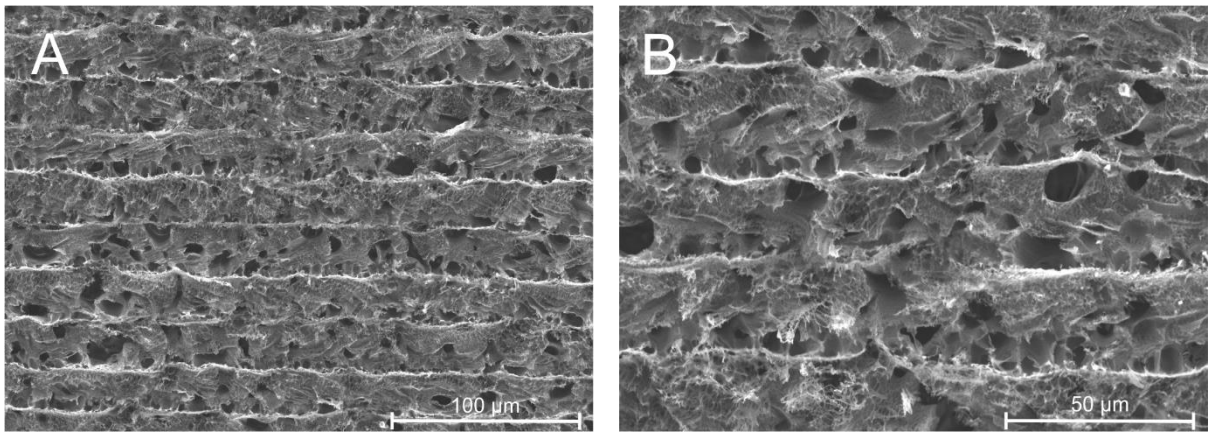

Figure 5.2.4.1 Electron micrograph of laser induced graphene electrode after stripping with carbon tape (PPI 1000, speed 40 and power 30 %).

5.2.5 Electrochemical Characterisation of LIG Substrates

The electrochemical performance of the LIG electrodes were assessed using cyclic voltammetry. Voltammograms detailing the electrochemical response of the planar LIG electrodes towards ferrocyanide (2 mM, 0.1 M KCl, 50 mV/s) are shown in **Figure 5.2.5.1**. After the application of 30 % power, the peak separation is close to theoretical Nernstian value (ΔE_p = 60 mV). There is no significant difference when increasing the power to 40% but there is a stark contrast following 50 % power with a supressed peak current and a separation of 200 mV. Laser ablation of polyimide at 50 % power produces more fibrous features as seen in **Figure 2.2.2.1D** that resemble carbon nanotubes which typically have enhanced conductivity (282) and the extensions would have provided an increase surface area. However, in this instance the electrochemical performance of the more fibrous LIG formations is

compromised therefore, the PI ablated with 30 % power was selected to be harvested and loaded into the composite MN.

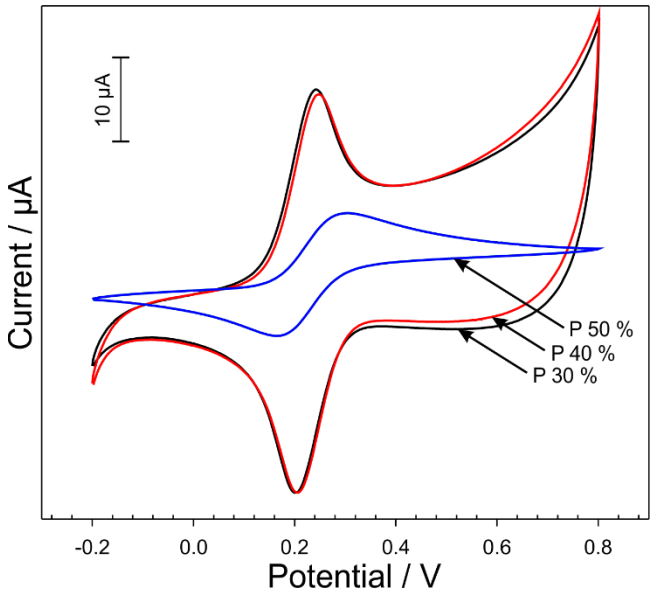

Figure 5.2.5.1 Cyclic voltammogram of laser induced graphene electrode to ferrocyanide (2mM,0.1 M KCl, 50 mV/s) at varying powers, 30 % (Black), 40 % (Red) and 50 % (Blue).

5.2.6 Cellulose Acetate Phthalate Based MN

Cellulose acetate phthalate (CAP) was pursued as a binder for nanocomposite MNs due to its biocompatibility and biodegradability discussed in the previous chapter. In contrast to **Chapter 4** where the MN were composed of pure CAP, in this instance the CAP replaces the polystyrene binder and is mixed with the carbon nanoparticles (or LIG) in a 1:1 weight ratio. Electron micrographs detailing the structure of the resulting CAP-C MN are shown in **Figure 5.2.6.1** and are little different from those observed with polystyrene. Sharp needle tips are evident and are sufficiently robust to pierce skin.

Cyclic voltammograms detailing the electrochemical response of CAP-C MN versus unmodified Ps-C MN towards ferrocyanide (2 mM, 0.1 M KCl, 50 mV/s) are shown in **Figure 5.2.6.2A**. In both instances slow electron transfer is observed with a large peak separation (E = 600 mV). However, within the CAP-C MN trace, the background current and capacitance are high concealing redox peaks, this may be due to the swelling nature of the polymer. In an

attempt to improve the electrochemical properties of the CAP-C MN, LIG was harvested from 3000 mm^2 of LIG and loaded into the mixture. A cyclic voltammogram detailing the response of CAP-C-LIG MN towards ferrocyanide (2 mM, 0.1 M KCl, 50 mV/s) is highlighted in **Figure 5.2.6.2B** The redox peaks are slightly more defined after the LIG addition, however, it is still not optimal, so the next step was to try a layered approach.

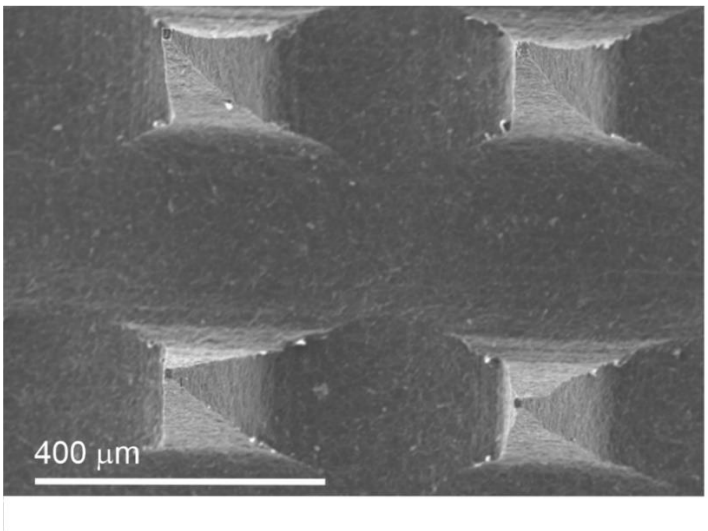

Figure 5.2.6.1 Electron micrograph of cellulose acetate phthalate carbon microneedle (CAP-C MN).

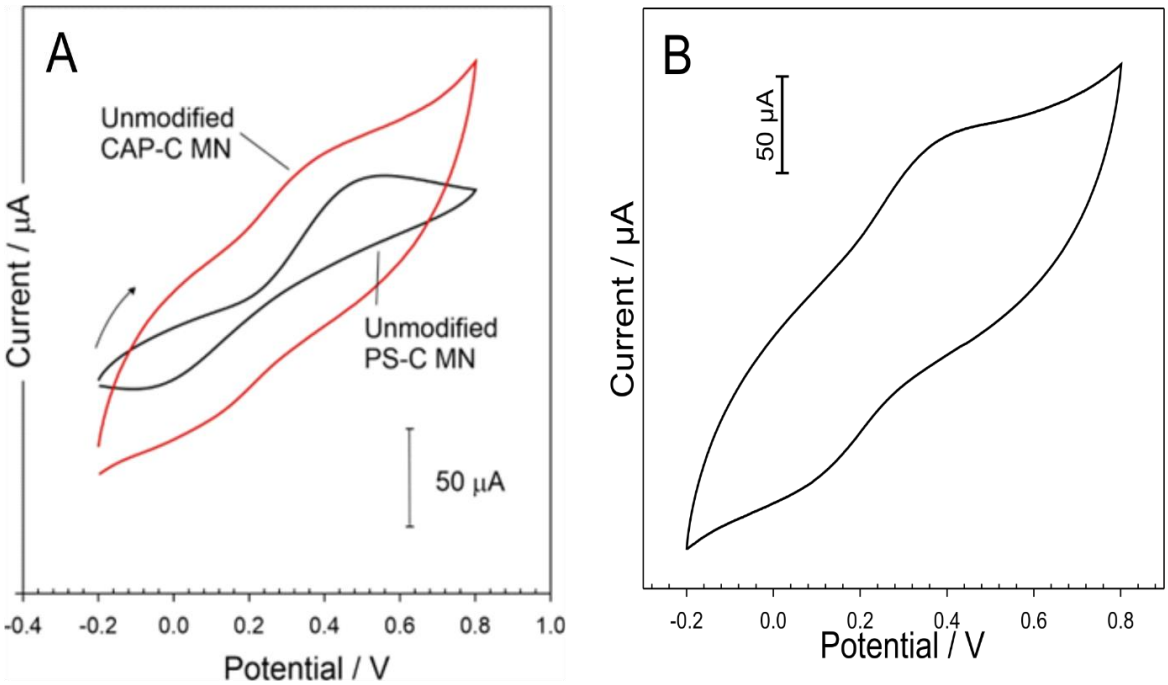

Figure 5.2.6.2 Cyclic voltammograms of A) CAP-C MN and Ps-C MN and B) CAP-C MN loaded with LIG response towards ferrocyanide (2 mM, 0.1 M KCl).

Raman spectroscopy was preformed to assess the CAP-C-LIG MN versus LIG electrode. From the spectra detailed in **Figure 5.2.6.3** it can be seen that both spectra contained prominent vibrational modes at 1345 cm^{-1}, 1580 cm^{-1} and 2695 cm^{-1}, which correspond to the D, G and 2D bands of graphitic materials retrospectively. The D-band (indicates out of plane vibrations in the sp^2 lattice hence defects) which provides more opportunities for functionalisation and improved electrochemical properties. The I_D/I_G ratio of the CAP-C-LIG MN was calculated as 0.74 versus the LIG electrode was calculated as 0.83, indicating that the LIG electrode contains more defects within the lattice.

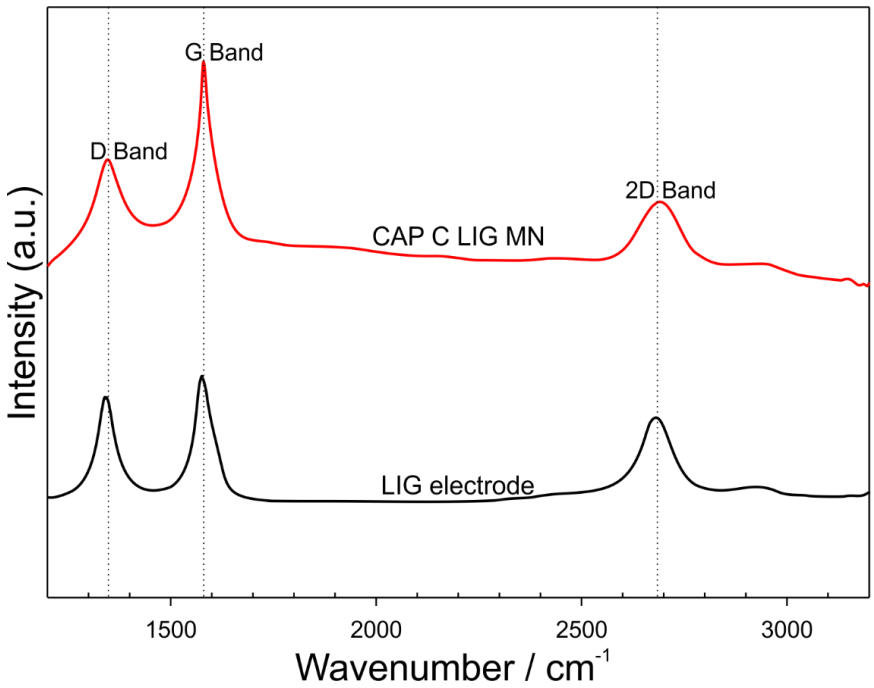

Figure 5.2.6.3 Raman spectra of CAP-C LIG MN and planar LIG electrode.

5.2.7 Layered LIG Approach

A simple mixing of LIG within the CAP-C formulation layered approach, detailed in the schematic in **Figure 5.2.7.1A,** was investigated as a mean of bringing the LIG closer to the electrode-solution interface while the CAP-C within the bulk of the MN serves as an electrical connector and provides the core structure for maintaining the geometry of the microneedles. The LIG was mechanically exfoliated from the lasered PI, suspended in cyclohexanone, and cast into the silicon microneedle mould with the expectation that it would coat the walls of the

pyramidal cavities within the mould. Once the solvent had evaporated, the CAP-C mixture was cast into the template. Cyclic voltammograms detailing the electrochemical response of layered CAP-C LIG-MN towards ferrocyanide (2 mM, 0.1 M KCl, 50 mV/s) is shown in **Figure 5.2.7.1B**. The redox peaks for the layered CAP-C-LIG mixture MN are modest and despite the high capacitance background, appear to be quasi reversible with a peak separation of approximately 100 mV. Briefly rinsing the MN with 0.1 M NaOH however dramatically improved the electrochemical response when compared with the unmodified layered profile in **Figure 5.2.71B**. It was anticipated that the NaOH removed some of the polymer which had been cloaking the LIG at the surface. While the peak separation is similar, the magnitude of the redox peaks is greatly increased and well defined. Electron micrographs detailing the CAP C LIG MN after being rinsed with NaOH is shown in **Figure 5.2.7.2**. The CAP-C core is shown to be relatively sharp and intact, which is decorated with LIG flakes.

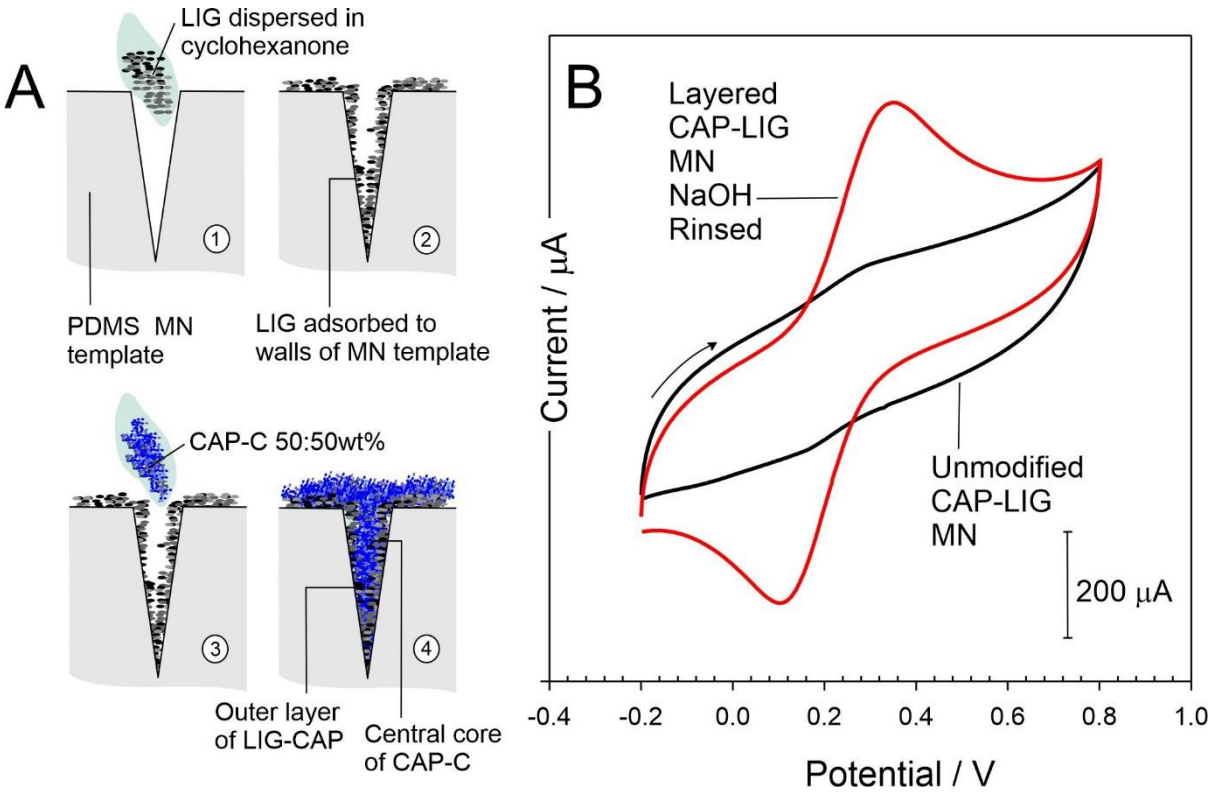

Figure 5.2.7.1 A) Schematic of CAP-C-LIG MN fabrication process and B) cyclic voltammograms of CAP-C-LIG MN response to towards ferrocyanide (2 mM, 0.1 M KCl, 50 mV/s).

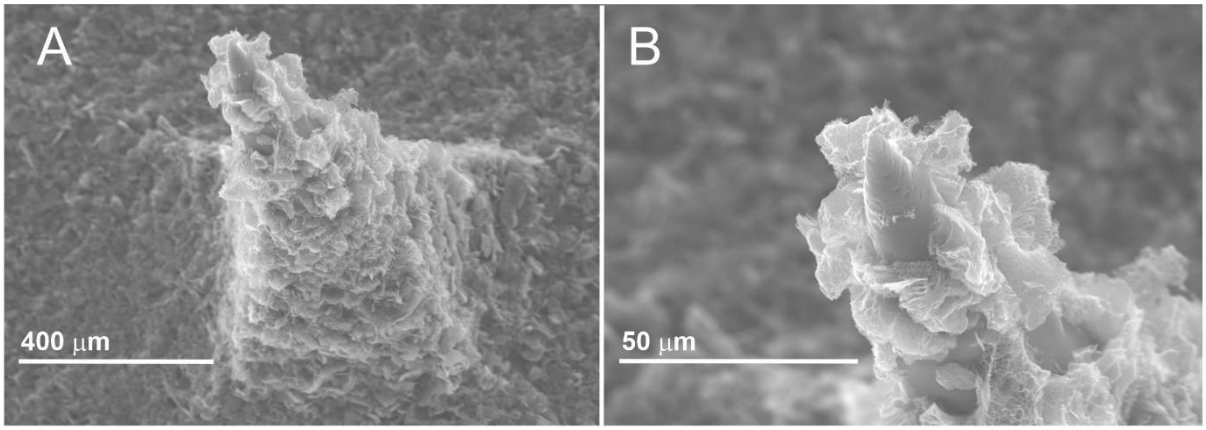

Figure 5.2.7.2 Electron micrograph of layered CAP-C-LIG MN after NaOH rinse.

A CAP-C MN patch was rinsed with NaOH to serve as a control, however the CAP-C MN displayed improved electrochemical profile similar to the layered MN, raising the question if the LIG was responsible for the improved response to ferrocyanide. Cyclic voltammograms detailing the electrochemical response of unmodified CAP-C MN versus modified CAP-C MN towards ferrocyanide (2 mM, 0.1 M KCl, 50 mV/s) are shown in **Figure 5.2.7.3**. The unrinsed MN does not display any obvious redox peaks, following the NaOH rinse however, the redox peaks are defined with a peak separation of E = 100 mV, displaying a near (quasi) reversible response.

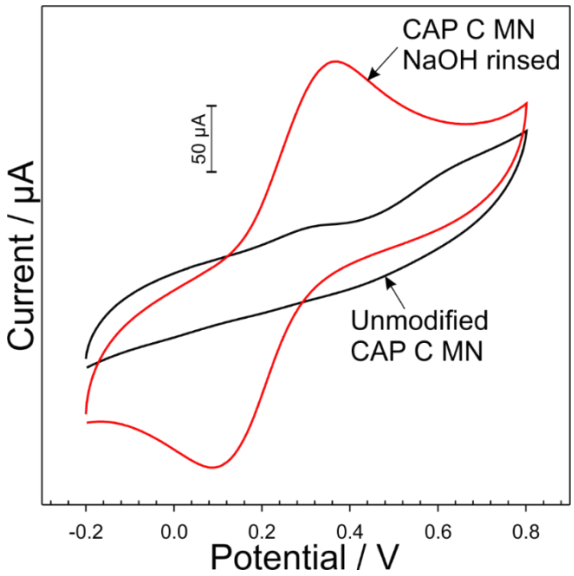

Figure 5.2.7.3 Cyclic voltammograms comparing the response of unmodified CAP-C MN versus NaOH rinsed CAP-C MN to towards ferrocyanide (2 mM, 0.1 M KCl, 50 mV/s).

5.2.8 CAP-LIG Urate Acid Analysis

As it is unclear whether the LIG has any significant impact on the electrochemical properties of the CAP-C MN, we tested the system in a real-world scenario to sense for the presence of uric acid. The latter is a common biomarker in a range of clinical conditions, such as hypertension (283), kidney function (284), stroke and cardiovascular disease (285; 286; 287). Uric acid undergoes a two-electron oxidation at the electrode and the general reaction scheme is detailed in **Figure 5.2.8.1**. The uric acid (I) is electrochemically converted to an unstable imine intermediate (II) which undergoes hydrolysis (II→III) before rearranging to the final breakdown product allantoin (IV).

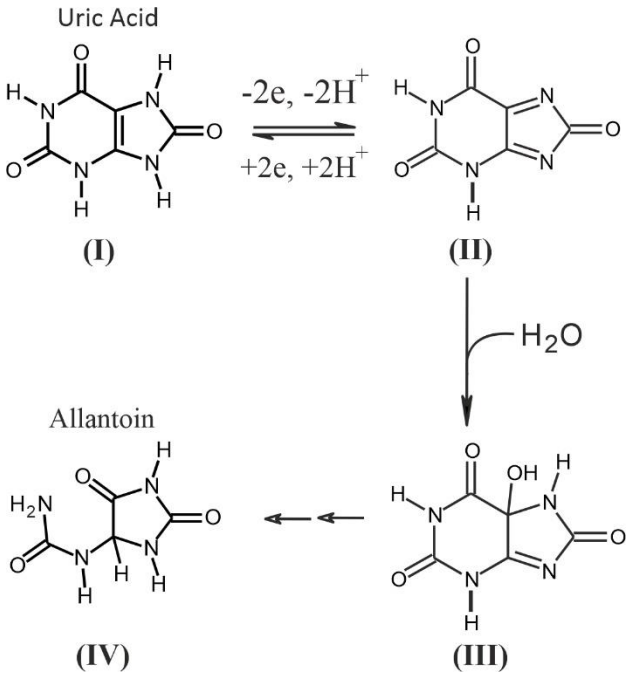

Figure 5.2.8.1 Breakdown pathway of uric acid resulting from oxidation at the electrode.

Electrochemical detection of urate can be difficult due to high over-potentials required to induce electron transfer and hence output a distinct, unambiguous peak and measurable current (288). Uric acid, in particular, coexists with ascorbic acid within biological fluids such as serum, blood and urine. These two biomarkers have very close oxidation potentials which become overlapped during electrochemical analyses, therefore, it is imperative that the oxidation potential is as low as possible to avoid this (211). Square wave voltammograms

detailing electrochemical response of unmodified Ps-C MN versus modified Ps-C LIG MN towards uric acid in pH 6 Britton Robinson buffer is shown in **Figure 5.2.8.2**. A wide oxidation peak is observed at + 0.45 V prior to anodisation. In contrast, the response displayed following anodisation (0.1 M NaOH, +2V, 180 s) reveals a well-defined oxidation peak at +0.3 V with a significantly larger current response. The improved electron transfer kinetics can be attributed to the increased edge planes achieved during the anodisation process and the results are consistent to the investigation performed by Hegarty *et al.*, (2019) (211).

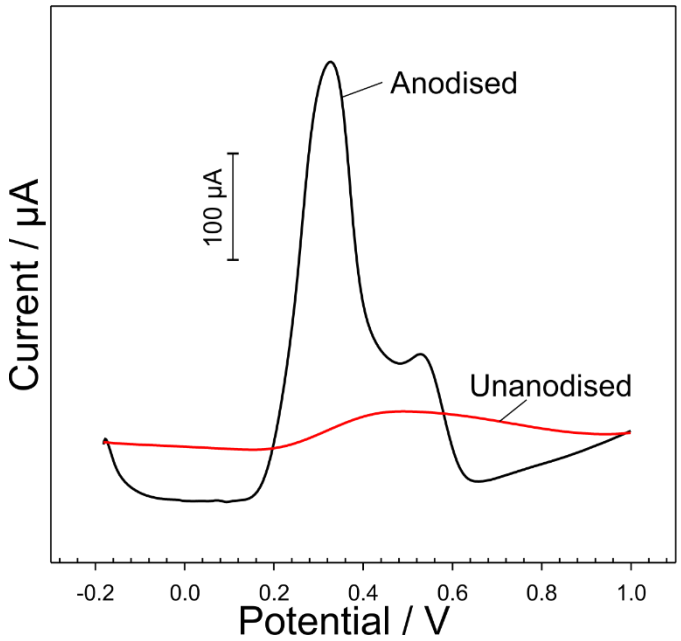

Figure 5.2.8.2 Square wave voltammogram detailing the response of modified and unmodified polystyrene-carbon microneedle towards uric acid in pH 6 buffer.

The cellulose acetate phthalate (CAP) microneedle loaded with carbon nanoparticles before any pre-treatment displays a voltammetric profile similar to that observed with the Ps-C MN in that a broad, ill-defined peak is observed (**Figure 5.2.8.3)** and is attributed to the oxidation of urate. It is noteworthy that the urate oxidation peak for the untreated CAP-C MN occurs at lower potentials (+0.2 V *vs* +0.45 V) to that of the untreated Ps-C MN suggesting that the CAP component has some influence in enhancing the electrochemical properties. The response obtained with the NaOH rinsed electrode is again broadly similar to that of the anodised Ps-C MN (E_{ox} = +0.15 V vs +0.3 V) with a greatly enhanced current, but the peak position is largely

similar to that observed prior to modification. Note that simply rinsing the unmodified Ps-C MN with NaOH did not result in any change in the voltammetric profile.

It is surprising that simply dipping the CAP-C MN in NaOH would improve the response at all, never mind so significantly. Using CAP as a binder must interact with the uric acid, however this is unusual as they are both anionic in pH 6 buffer.

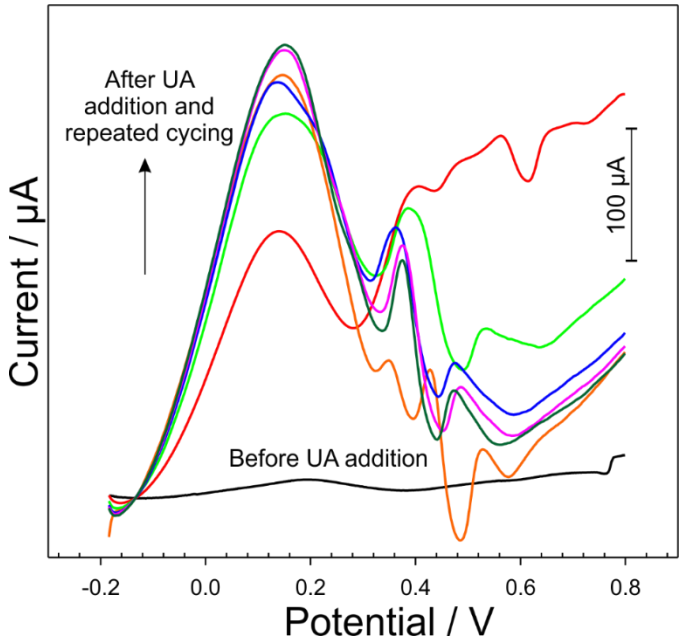

Figure 5.2.8.3 Square wave voltammograms detailing the response of CAP-C MN after dipping in NaOH towards uric acid in pH 6 buffer and after repetitive cycling.

Despite the CAP-C MN's improved response to uric acid, incorporating laser induced graphene that has been harvested from polyimide, the response improves further. Square wave voltammograms detailing the response of CAP-C-LIG MN after being dipped in NaOH towards uric acid is shown in **Figure 5.2.8.4**. The oxidation potential of the uric acid can be observed at +0.075 V proving that the LIG has some influence on improving the electrochemical performance.

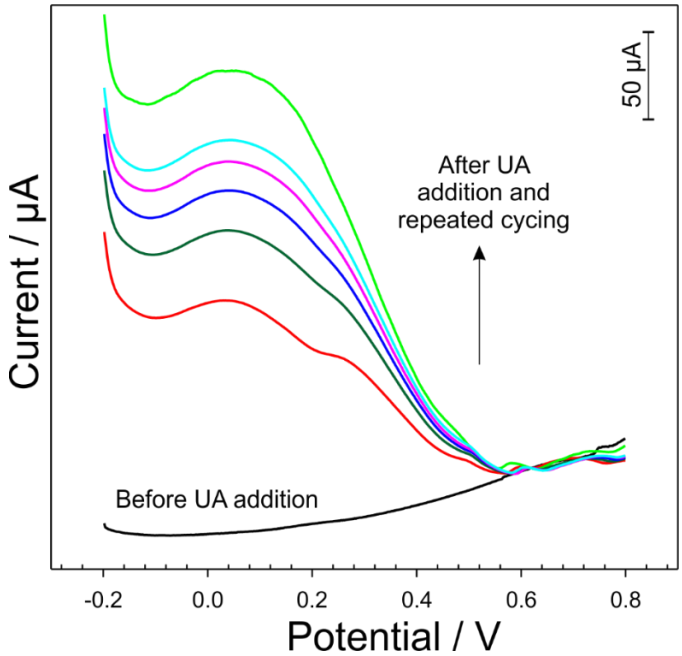

Figure 5.2.8.4 Square wave voltammogram detailing the response of CAP-C LIG MN after dipping in NaOH towards uric acid in pH 6 buffer after repetitive cycling.

5.2.9 Biodegradability – Justification

The devices intended to facilitate home glucose monitoring (HGM) have traditionally relied upon screen printed electrodes (SPE) to deliver the analyses, but it must also be noted that these still require the use of a lancet to enable release of the blood sample from a finger. The strips and lancet will inevitably generate considerable waste (289; 290). It is little surprise therefore that there has been a long-recognised need to re-evaluate both the operational design and disposal of modern point of care testing (POCT) / sensing consumables to provide more sustainable options that minimise the generation or accumulation of clinical waste. It must be noted that the electrochemical properties of many of the carbon based SPEs can be relatively poor. As with most carbon-based electrodes their electrochemical properties can be enhanced through anodisation processes (247; 253). This is evidenced in **Figure 5.2.9.1A** where the cyclic voltammetric responses to ferrocyanide (a well-known mediator in commercial glucose meters) at the unmodified and anodised carbon SPE are compared.

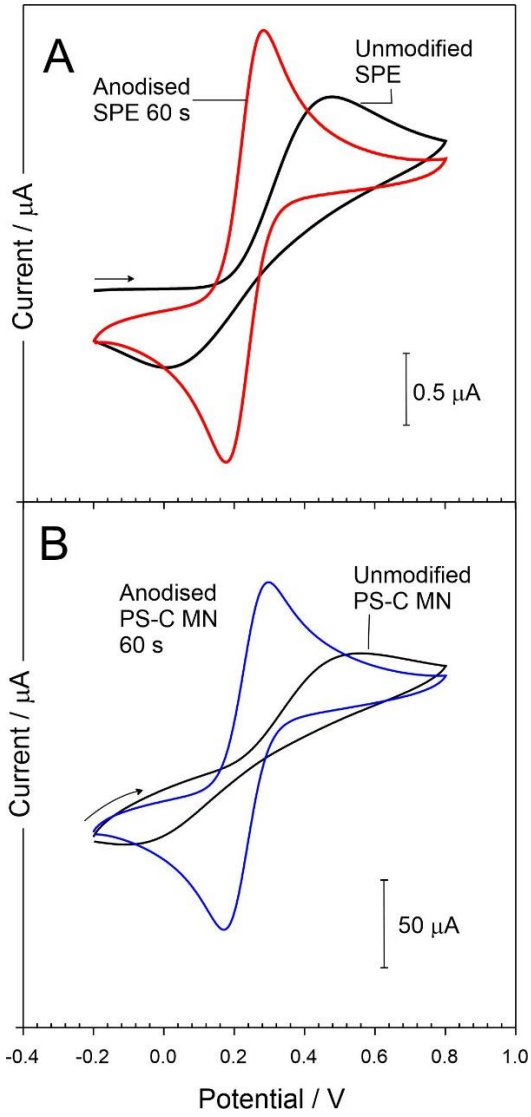

Figure 5.2.9.1 Cyclic voltammograms detailing the response towards ferrocyanide (2 mM, 0.1 M KCl, 50 mV/s) at A) a carbon screen printed electrode and B) a polystyrene-carbon microneedle (Ps-C MN). The responses before and after anodisation in 0.1M NaOH are compared in each case.

It must be noted that the responses observed at the SPE follow similar voltammetric behaviour patterns to the microneedle systems (Ps-C MN compared with the SPE in **Figure 5.2.9.1B**). As such, it is possible to envisage that substituting the MN (either Ps-C or the CAP-C) systems for the SPE could be a viable alternative. The major advance here, however, is that were the SPE systems replaced by the CAP-C MN system – its potential biodegradability could minimise substantial amounts of medical waste.

Modification of the MN immediately after production can certainly improve the electrochemical performance of the system but it also brings some difficulties from the perspective of mass manufacturing sensors. Any additional processing step will be time consuming to implement. In the case of cellulose acetate phthalate as the core binder, it could be anticipated that this would address the issue of biodegradability. Scanning Electron micrographs detailing the dissolution of the CAP-C microneedle in pH 8 BR buffer after one min and thirty minutes are highlighted in **Figure 5.2.9.2A** and **5.2.9.2B** respectively. Close examination reveals the partial dissolution and stand in marked contrast to the pristine structures considered earlier in **Figure 2.6.1** which were recorded prior to any treatment. It must also be noted that the microneedle arrays resulting from PS-C formulations remained unchanged when left in the same buffer medium.

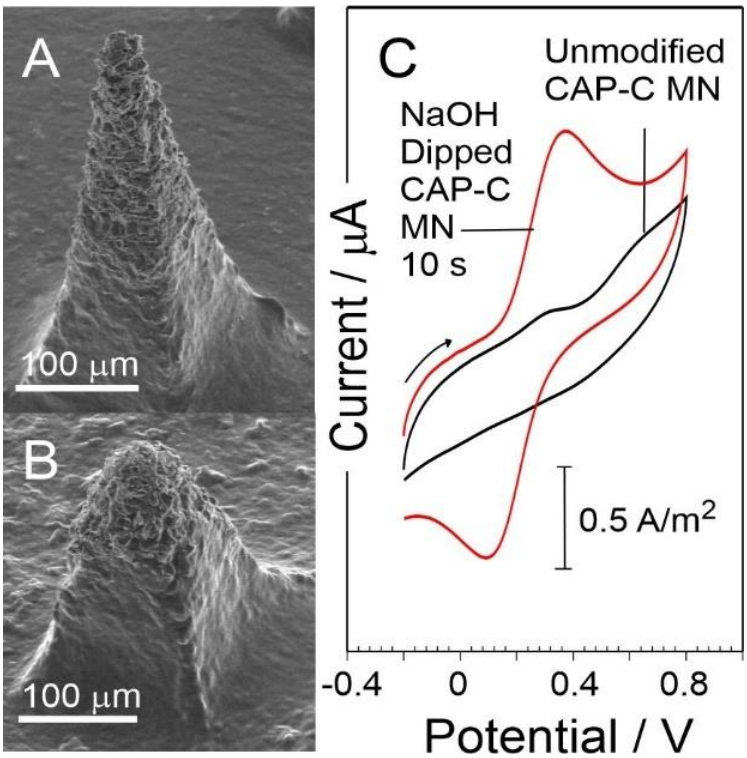

Figure 5.2.9.2 Electron micrographs of the CAP-C MN after exposure to pH 8 BR buffers for A) one min and B) thirty min. C) Voltammetric responses of the CAP-C MN to ferrocyanide (2 mM, 0.1 M KCl, 50 mV/s) pre and post treatment with NaOH (0.1 M,10 s).

Gradual dissolution of the CAP polymer within the alkaline solution was observed with prolonged immersion (>30 min) leading to the loss of needle definition. The voltammetric responses of the CAP-C MN system, under conditions analogous to those used previously for the polystyrene system (**Figure 5.2.9.1B**) are detailed in **Figure 5.2.9.2C**. The oxidation/reduction peaks of the ferrocyanide probe are barely visible with the oxidation process observed only as a poorly defined broad peak at +0.6 V. A large overpotential is needed to induce ferrocyanide oxidation at the unmodified CAP-C MN surface and is consistent with the response observed at the unmodified polystyrene system. However, the CAP-C MN array was found to exhibit a large capacitive background - attributed to combined influences of the polymer's hydrophilic nature its subsequent swelling at the microneedle interface.

Although the response of the PS-C MN systems has been shown to be improved through the additional anodisation step, a similar approach cannot be employed in the case of CAP-C systems as extended immersion in the NaOH would lead to the dissolution of the needles (as indicated in **Figure 5.2.9.2A** and **5.2.9.2B**) as well as a marked reduction in mechanical integrity. It must be recognised however, that the dissolution of CAP in alkaline conditions could be exploited as a core feature of the proposed design – allowing facile biodegradation. Short exposure (10 s) to NaOH was proposed as a viable pre-treatment option which would remove residual / interfacial CAP without significantly affecting the core structure of the needle itself. The voltammetric responses of the CAP-C MN after dipping in 0.1 M NaOH solution for 10s has been included in **Figure 5.2.9.2C** for comparison. The voltammetric profile is markedly improved in terms of the peak resolution and magnitude with the characteristic "duck" profile is seen. The clear improvement in electrode performance can be attributed to the fact that the NaOH removes the some of the CAP film and thereby exposes underlying carbon particle at the interface. In contrast, dipping an unmodified PS-C MN into NaOH at open circuit without the application of an oxidation potential did not lead to any improvement in the cyclic voltammetric response. This could be attributed to the insoluble nature of the polystyrene in

aqueous solution. A more quantitative examination of the dissolution of the CAP-C MN in pH 7 BR buffer is shown in the voltammograms in **Figure 5.2.9.3A**. As the CAP dissolves, there is a sustained reduction in electrode area (as carbon is lost) and hence the peak height response to the ferrocyanide probe diminishes. The electrode was found to be stable for up to ten minutes before the steady degradation in response is observed. Although this would preclude long term / continuous monitoring applications, it could, nevertheless, be exploited in point of care scenarios where a single measurement is performed shortly after insertion – such as in home glucose monitoring.

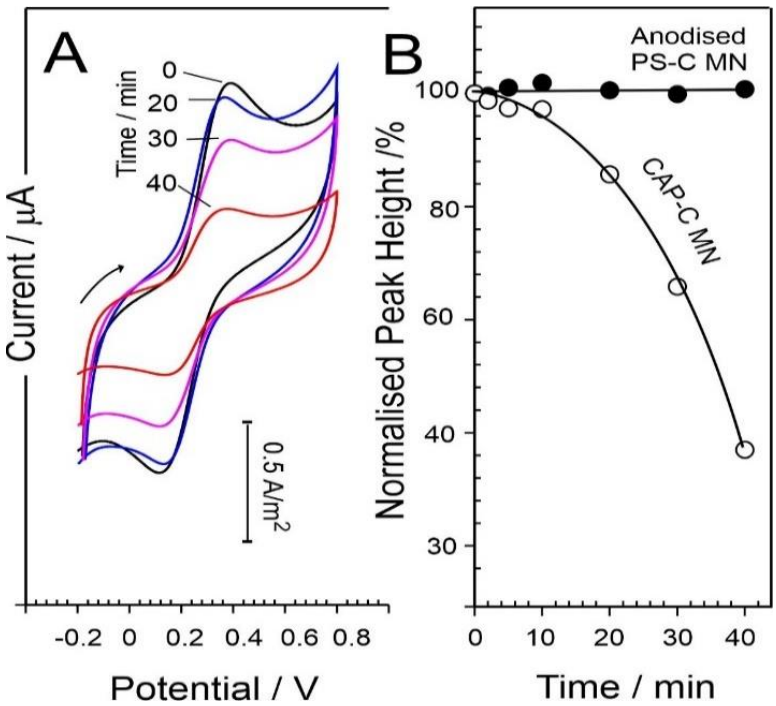

Figure 5.2.9.3 A) Cyclic voltammetric response of a CAP-C MN array to ferrocyanide (2 mM, pH 7 BR buffer, 50 mV/s) over a period of forty minutes. B) Quantitative analysis of the changes in ferrocyanide oxidation peak height with time for both CAP-C and PS-C MN arrays.

Ferrocyanide is a common mediator in commercial HGM systems and therefore it is possible to speculate that the CAP-C MN system could be adapted to glucose enzyme sensing – especially as the voltammetric performance is at least equivalent to the unanodised SPCE response highlighted in **Figure 5.2.9.2C**. Nevertheless, it was important to assess the analytical capability beyond mediator systems and consider the response to peroxide. The

latter is a common by-product in a range of enzyme biosensors and being able to detect it at the CAP-C would provide an indication as to the generic applicability of the system. The performance of the CAP-C MN electrode array towards peroxide was assessed through the amperometry (+1.0 V, 10s, pH 7 buffer) with the response to 25 mM increments shown in **Figure 5.2.9.4**. The current response was found to be linear over 25 μM to 500 μM (I (/A) = 0.0323 [H_2O_2 /mol L-1] + 2x10^{-8}; N = 6; R^2 = 0.998) with a limit of detection of 5.7 μM (based on *3.3*S_b)

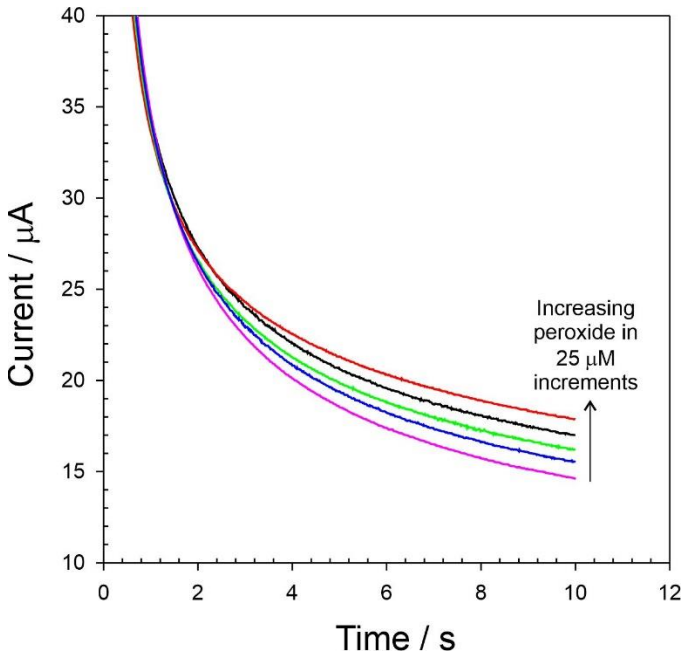

Figure 5.2.9.4 Chronoamperometric responses of the CAP-C MN systems towards peroxide (25 mM additions, pH 7 BR buffer, +1V) over a period of 10 seconds.

5.2.10 Waste Impact Assessment

In order to assess the potential impact such a substitution would have on the latter, an evaluation of the annual quantity of home glucose measurement waste within Northern Ireland was conducted. Estimates by Diabetes UK suggest there are some 105,000 people in Northern Ireland (NI) with the condition with projections for a considerable rise in number in the short term. The magnitude of the latter has been estimated at around 4% per year (291; 292). It must be acknowledged that not all diabetics will utilise HGM devices, and it is impossible get precise figures on the proportion that do so within NI. Figures from the US

suggest that HGM is regularly used by some 25-30 % of the diabetic population which, if applied to the present case, would suggest that some 26-31,000 people in the NI would avail of some form of device (293; 294). Assuming this is indeed the case, current guidance recommends that blood sugar concentrations are measured at least four times per day. This would give rise to almost 125,000 glucose strips (and lancets) being discard each day within NI (294). The recommendation is for spent strips/lancets to be discarded within clinical waste containers. While there is considerable cause for concern in terms of end disposal method for such devices, for the purposes of this estimate an assumption is made that the HGM waste is indeed discarded appropriately. The amount of HGM clinical waste that is theoretically generated per day in NI can be calculated as:

The weight of a single strip would approximate to 0.126 g +/- 0.0103 g (N = 5). A Braun lancet was used as the model and is indicated in **Figure 5.2.10.1A**. The total weight of the lancet is 3.915 g +/- 0.0154 g (N = 3) with the majority of the structure being polypropylene (3.595 g, 92%) with a stainless-steel needle and trigger spring as highlighted in **Figure 5.2.10.1B** where the lancet has been disassembled.

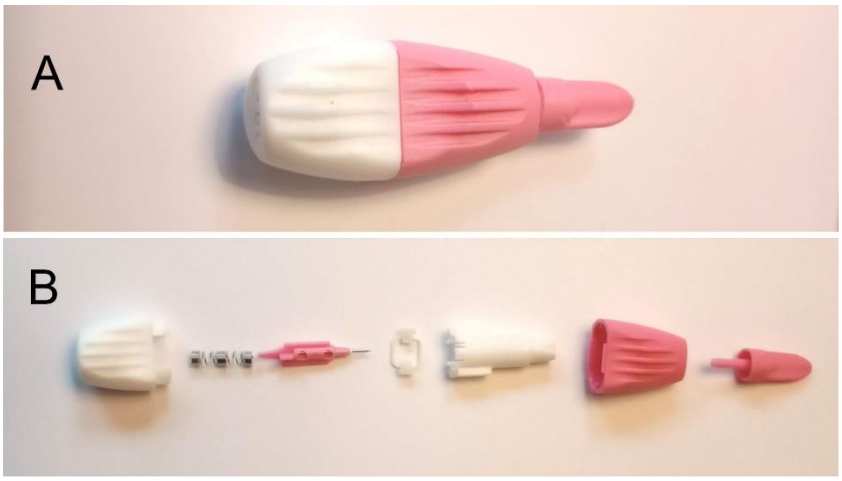

Figure 5.2.10.1 A) Braun lancet for capillary blood sampling and B) the individual constituents.

Considering test strips -> 0.126 g x 4 daily = 0.504 g per person

Thus, taking the estimate of 26,000 diabetics, this would give rise to 13.1kg of strip waste per day and almost 4783 kg per year in Northern Ireland.

However, with each strip – there will also be one lancet. Therefore for 26,000 patients – it could be expected that some 104,000 lancets would be used and discarded.

If we assume 3.92 g per lancet, then this would give rise to 408 kg per day of waste lancets every day in NI. In total, approximately 153586 kg (~154 tonnes) of home glucose monitoring medical waste is generated between lancets and strips - waste that may not even be properly disposed of at present (295).

The carbon footprint of the waste components can also be evaluated. It can be assumed that >90% of the testing strip will be polymer. Likewise, from the dissection of lancet in **Figure 5.2.10.1B** it was found that the polymer composition was found to amount to 92%. Hence it is possible to estimate that just over 141 tonnes will be polymer If we assume that the strips/lancet polymer composition is simply polypropylene (consistent with the Braun Lancet technical specification) then:

1 g of polypropylene contains = 0.86 g of carbon (based on a CH_2-CH_2-CH_2 repeating unit)

If this was incinerated (to 100% efficiency) then the amount of CO_2 produced could be determined by:

Mass of CO_2 = 44 g/mol

$C + O_2 \rightarrow CO_2$

1 mole of carbon gives 1 mole of CO_2

Thus 0.86 g of carbon = 0.86/12 = 0.072 mol and similarly must produce 0.072 mol of CO_2

Weight of CO_2 produced = 0.072 x 44 = 3.14 g

Hence 1 gram of polypropylene at 100% incineration efficiency will produce 3.14g of CO_2

In terms of annual production:

Total weight of polymer = 141299 kg = 1.41 $x10^8$ g

Total CO_2 produced = 4.44 x10^8 g ~ 444 tons

It is clear that with an increasing diabetic population, the amount of waste produced could dramatically increase. Given the microscale geometry of the solid MN, it could be envisaged that the ability to pierce and sample interstitial fluid would effectively remove the need for the lancet – which comprises the bulk of the waste (296).

5.2.11 Biodegradability Preliminary Evaluation

Cellulose acetate phthalate is known to break down in neutral to alkaline environments which is an added advantage when considering the waste generated due to medical waste and conventional drug delivery systems. The stability of the CAP-C microneedle systems was therefore assessed through examining the morphology of the needles after being interred in moist loam soil (in line with ASTM D5988 – 18: Standard Test Method for Determining Aerobic Biodegradation of Plastic Materials in Soil) for one week. The rationale here was that a combination of environmental weathering and microbial processes should dissolve/metabolise the CAP binder ultimately resulting in the complete degradation of the microneedle patch. Electron micrographs detailing the structural integrity of the CAP-C microneedle before and after one week of being interred in the soil are compared in **Figure 5.2.11.1A-D**.

Large cavities are seen on the base plate and needles of the array, we can assume that the moisture in the soil weakened the needles resulting in fractures as well as dissolution of the CAP binder. This is corroborated when compared to a Ps-C MN after one week in loam soil shown in **Figure 5.2.11.2**, where the needles are intact with no craters.

The degradation of the CAP-C microneedle patch is clear from the electron micrographs and stands in marked contrast with the PS-C which are effectively unchanged. It is important to note that the CAP-C MN tips have been removed and hence their piercing capability. The latter is crucial from a health and safety perspective such that any inadvertent secondary application is avoided.

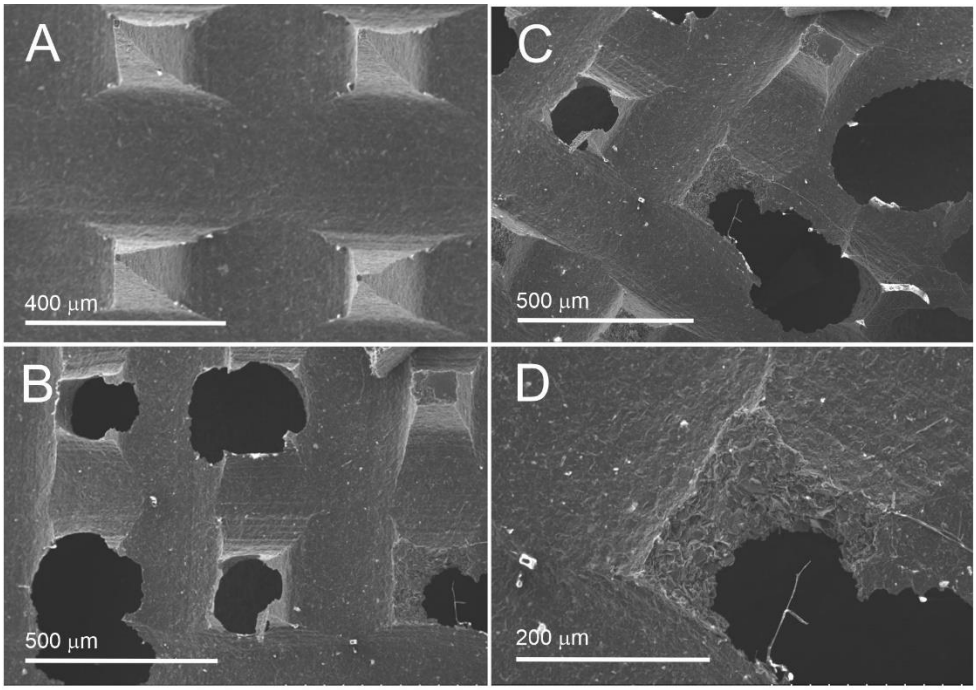

Figure 5.2.11.1 Electron micrographs of the breakdown of CAP-C MN after one week in loam soil.

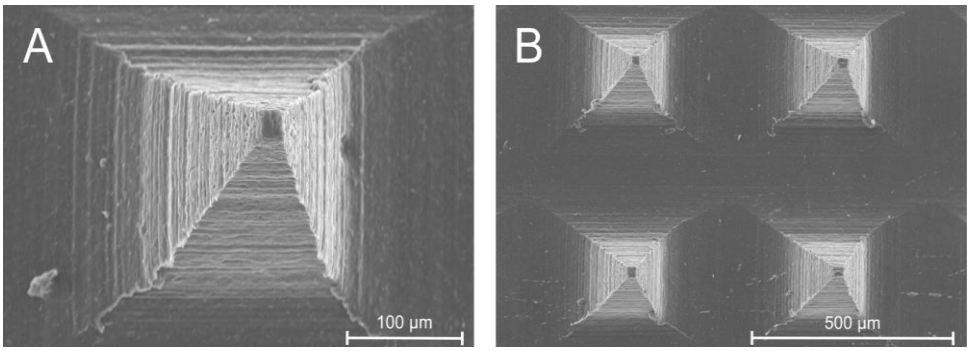

Figure 5.2.11.2 Electron micrographs of Ps-C MN after one week in loam soil.

The rapid degradation of the CAP system advocated here stands in marked contrast to the degradation period expected for polystyrene or polycarbonate. It also improves the acceptability of disposing of the spent MN in domestic/household waste or composting recycling systems. This again is in marked contrast where current recommendations for the disposal of measurement strips and lancets employed in home glucose monitoring related to dedicated waste containers for incineration. There are long standing issues with compliance with prescribed disposal practices and it has been estimated by Thompson and Cook (2021) that in the UK almost 30% of lancets were placed directly into household waste (289). Similar

numbers have been reported internationally and contribute to a worrisome waste and safety problem (289; 290).

5.3 Conclusions

The work presented in this chapter is multi-faceted. Initial electrochemical investigations of the CAP-C MN decorated with LIG would suggest that there is little electrochemical improvement. However, when the system employed to detect uric acid – which typically requires a large over potential – the oxidation potential is lowered significantly. This has real world advantages, where ascorbic acid would normally interfere. Additionally, the use of CAP as a binder introduces possibilities when it comes to tackling sharps waste issues. This issue is especially prevalent for diabetic patients when it comes to blood glucose detection. The waste produced by diabetic patients in NI is estimated and the CAP system is investigated as a suitable alternative to detect peroxide. A preliminary study of the biodegradability of CAP MN is investigated and compared to polystyrene MN array.

Chapter 6

Electrochemically Initiated Release: Exploring New Modalities for Controlled Drug Release

Overview

A series of naphthoquinone-aminophenol derivatives have been synthesized on the basis that their conjugation with a suitable drug candidate could provide a means through which the latter could be released upon the imposition of an appropriate oxidation potential. The approach is based on a three-component assembly in which the naphthoquinone redox centre serves as a reporter unit allowing interrogation without release of the drug. The central aminophenol serves as the tether to which the drug is linked *via* an ether bond. Upon oxidation of the aminophenol - ether component, transition of the latter to the corresponding quinone imine results in the release of the drug. The electrochemical properties of the model system have been investigated and the impact of the release process on the functional groups intrinsic to the drug component is critically considered.

The majority of the work presented in this chapter has formed the basis of a peer reviewed publication:

Amy Devine, Catherine Hegarty, Charnete Casimero, Rebecca Louise Molyneaux, Robert B. Smith, Marco F. Cardosi, James Davis, 2020. Electrochemically initiated release: exploring new modalities for controlled drug release. *Journal of electroanalytical Chemistry*. 872. https://doi.org/10.1016/j.jelechem.2020.113926

6.0 Introduction

Advances in controlled drug delivery systems have continued to develop over the last six decades. At present, three generations have been outlined, the first of which being controlled release *via* drug formulation. This was introduced in 1952 by Smith Kline and French, where dextroamphetamine was released for twelve hours. In the 1970s, a greater knowledge of drug release mechanisms such as dissolution, diffusion, osmosis, and ion exchange mechanisms helped advance controlled drug delivery technology leading into the second generation. Initially, the second generation of controlled drug delivery focused on zero-order delivery systems. At this time, it was thought that zero-order release kinetics were superior, as a constant concentration can be achieved in the blood. This curtailed development of controlled drug delivery systems until, it was realised that it isn't necessary to maintain a constant drug concentration in the blood and in fact zero-order systems don't maintain a constant drug concentration. Reaching the minimum effect concentration is more significant for drug efficacy rather than maintaining a constant threshold. This provided increased flexibility for subsequent drug delivery systems and within the second generation, smart polymers and hydrogels were introduced. These smart materials are triggered by changes in pH, temperature or glucose levels which have been used in implants or smart transdermal patches. Finally, the second generation has seen the development of nanotechnology and nanoparticles for controlled release. Although three generations have been identified, the third is only beginning to emerge as smart systems come to the fore. It is predicted to include feedback systems whereby therapeutics are delivered following a stimulus provided within the patient like glucose levels (297).

Controlled transdermal drug delivery is still in its infancy, whose growth and research enables the development of new therapeutic treatment programs. The transdermal route offers a rapid path for drugs and molecules to be delivered which can then be programmed into smart transdermal patches for controlled release specific to a patient's needs. Transdermal drug delivery methods are usually inexpensive, single use and disposable (298).

It is no surprise that the health sector is hugely influenced by the internet of things (IoT), especially with increasing research into controlled drug delivery systems. The ability to provide more connected health services is to the benefit of both physician and patient where both are properly informed on an individual's health and thereby provides control and independence to the patient. This is achieved by connecting many devices that intercommunicate. For example, the controlled drug delivery system can record and send data on compliance and dosing and can be paired with sensors to determine the concentration within the blood to ensure the critical level is reached for optimal efficacy of the therapeutic (299). The growth of the internet of things within the health sector has been achieved in part by the development of micro electromechanical systems (MEMS) used in low-cost, high-performance sensors and actuators. MEMs using microneedle systems have been employed to achieve controlled transdermal drug release thorough smart triggering systems that are initiated through wireless transmission allowing for control of drug doses over multiple occasions (297). The time and quantity of drug release can be achieved by various means, for example, the control can be achieved due to the interaction of smart materials within their environment like changes in pH, redox interactions, or enzyme or by remote operation controlling conditions like temperature, light, ultrasound, or voltage (300).

Electrochemically triggered release is advantageous as the electrodes employed are inherently miniature, simplistic, requiring low powers whilst offering high sensitivity and stability (275). Bansal *et al.*, (2021) developed an electrochemical electrode based on gold coated with polypyrrole to release glutamate (neurotransmitter), which was stable, displaying no delamination following 1000 cyclic voltammetry scans (301). Similarly, Uppalapati *et al.*, (2018) employed polypyrrole as a coating over drug loaded micelles loaded with dexamethasone (anti-inflammatory) were an electrochemical trigger altered the polypyrrole inducing release (302) .

The approach taken here relies on a potential drug candidate being bonded to a redox anchor which is immobilised onto a conductive substrate such as a microneedle array. The drug

release would then be induced upon applying an oxidation potential that transforms the redox anchor bonded to the drug thus expelling it. The schematic in **Figure 6.0.1** illustrates the drug anchor employed which was based on a naphthoquinone aminophenol derivative, where the drug is attached to the phenolic functionality of the aminophenol unit *via* an ether link. The naphthoquinone and aminophenol components of the derivative studied serve as redox centres. The naphthoquinone unit serves as the reporter unit, where the oxidation of this unit does not induce drug release, but instead determines the presence and quality of the drug at the electrodes surface. It is anticipated that the drug will only be released after the oxidation of the aminophenol unit to the corresponding quinone imine which breaks the ether li resulting in the oxygen reverting to the quinoid carbonyl. The aim is that the naphthoquinone aminophenol unit will remain intact and only the drug will be released into solution.

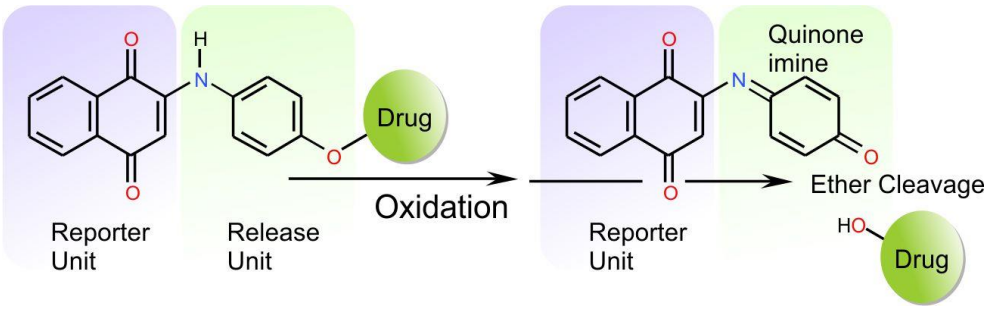

Figure 6.0.1 Oxidative pathway leading to the release of the tethered drug.

Electrochemical release methodologies have had considerable interest which have been reviewed (303). Typically, the release of the therapeutic is dependent upon physical actuation by changing the properties of the barrier membrane induced by an electrochemical trigger (304). The route illustrated in **Figure 6.0.1** relates to the direct release of the drug component. The objective has been to investigate the electrochemical characteristics of the naphthoquinone aminophenol derivative as a redox switch and to evaluate its possible applicability in relation to the range of drugs that could eventually be linked.

6.1 Experimental details

6.1.1 Materials and Instrumentation

All chemicals were acquired from Sigma-Aldrich, were the highest grade available and were used without further purification. Phosphate buffered saline (PBS) at pH 7 was used during the course unless otherwise specified. Electrochemical analysis was conducted using a micro Autolab (Type III) computer controlled potentiostat (Eco-Chemie) with a standard three electrode configuration in which either a glassy carbon electrode (3 mm diameter) or a carbon-polystyrene microneedle patch was used as the working electrode. Platinum wire and a Ag|AgCl half cell (3 M NaCl, BAS Technicol UK) acting as counter and reference in that order. The naphthoquinone derivatives were prepared at the Research Centre for Smart Materials, University of Central Lancashire, Preston UK.

Preparation of Microneedles: Carbon nanoparticles (Sigma UK) were infused with polystyrene powder (100, 000, Sigma) in a ratio of 1:1 by weight, dissolved in cyclohexanone and stirred until a homogenous solution was achieved (typically two hours). The solution was then cast into silicone microneedle templates (Micropoint®) and a carbon fibre stub was positioned into the base plate section to enable electrical connection. The dimensions of the silicone templates were 200(base) x 500(pitch) x 700 (height) micron covering a 10 x 10 needle array. The templates were placed in a vacuum at 30°C and once the pressure had increased to 1000 mbar the air was released again (this was to draw the homogenous solution to the tips of the silicone cast ensuring sharp microneedle production). If required after vacuuming, the templates were topped up with more solution preferably overflowing the cast to allow for solvent evaporation. The solvent was left to evaporate at room temperature (over forty-eight hours) at which point the needles could be removed from the patch. The baseplate and non-needle surfaces were coated with enamel (six hour drying period) to serve as a dielectric.

6.1.2 Preparation of Naphthoquinone Derivatives

A series of substituted 1,4-napthoquinone derivatives were initially prepared by Ms Rebecca Molyneaux under the supervision of Dr Robert Smith (University of Central Lancashire). The

material was supplied on the basis of a kind gift and were used as received. The preparation of the key derivatives used in this project are detailed here for completeness. The synthesis is based on a Michael addition and an example highlighted in **Figure 6.1.2.1**.

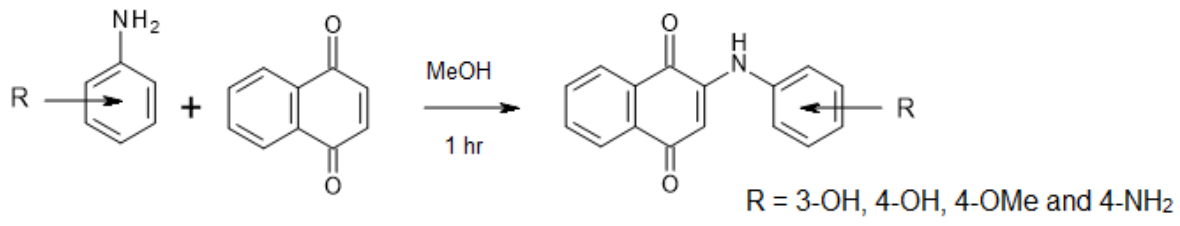

Figure 6.1.2.1 Reaction scheme used in the preparation of the naphthoquinone derivatives.

In general, ethanol (50 mL) was added to a flask containing 1,4-naphthoquinone (1.58 g, 10 mmol) and the resulting mixture heated until the solution was clear. The appropriate amine derivative was then added with constant stirring and left for one hour. A solid precipitate and the solid isolated at the pump. Purification of the resulting solid was achieved through heating in methanol and re-isolating the derivative at the pump. Typical yields ranged from 25% to 54% depending on nature of the chosen derivative. The resulting product was characterised using NMR, FTIR and mass spectroscopy. 1H and 13C NMR spectra were recorded on a Bruker Fourier 300 (300 MHz) spectrometer. In all cases, chemical shifts were reported in ppm relative to the DMSO solvent residual (1H NMR d6-DMSO, 2.500 ppm and 13C NMR d6-DMSO, 39.520 ppm). Similarly, coupling constants are reported in Hertz (Hz) to the nearest 0.5 Hz. Multiplicities are reported as singlets (s), doublets (d) and triplets (t) or a combination of these. In cases where broad peaks were observed, due to either H-bonding or restricted rotation, the broad (br) prefix is noted. Low resolution mass spectra for each compound were recorded on a Finnigan™ LCQ™ Advantage MAX in ESI mode. Infra-red spectra (1800–800 cm−1) were recorded on a Perkin Elmer Spectrum RX 1 with a Specac Golden Gate™ ATR accessory. The characterisation data for each derivative are presented in turn:

2-(3-Aminophenol)-1,4-napthoquinone (0.63g, 25%,deep red solid)

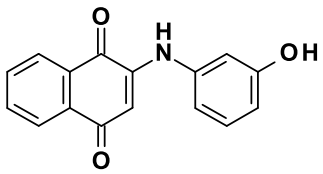

^{1}H NMR (300 MHz, DMSO-d6) δ 9.67 (s, 1H), 9.16 (s, 1H), 8.06 (dd, J = 7.5, 1.5 Hz, 1H), 7.95 (dd, J = 7.6, 1.5 Hz, 1H), 7.86 (td, J = 7.5, 1.5 Hz, 1H), 7.79 (td, J = 7.4, 1.6 Hz, 1H), 7.23 (t, J = 8.1 Hz, 1H), 6.90 – 6.76 (m, 2H), 6.62 (d, J = 8.9 Hz, 1H), 6.16 (s, 1H).

^{13}C NMR (75 MHz, DMSO) δ 183.03, 182.03, 158.47, 146.48, 139.52, 135.34, 133.09, 133.01, 130.91, 130.48, 126.60, 125.72, 114.68, 112.83, 110.74, 102.68.

LCMS (ESI): m/z 265.06.

2-(4-Aminophenol)-1,4-napthoquinone (1.06g , 42%, deep red solid)

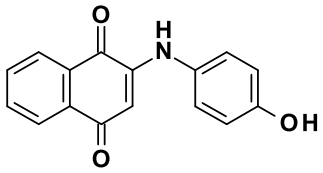

^{1}H NMR (300 MHz, DMSO-d6) δ 9.61 (s, 1H), 9.11 (s, 1H), 8.05 (dd, J = 7.6, 1.5 Hz, 1H), 7.94 (dd, J = 7.6, 1.5 Hz, 1H), 7.85 (td, J = 7.4, 1.4 Hz, 1H), 7.77 (td, J = 7.5, 1.5 Hz, 1H), 7.23 – 7.12 (m, 2H), 6.90 – 6.78 (m, 2H), 5.88 (s, 1H).

^{13}C NMR (75 MHz, DMSO) δ 182.55, 182.16, 155.76, 147.50, 135.33, 133.26, 132.87, 130.88, 129.38, 126.49, 126.26, 125.70, 116.23, 101.16.

LCMS (ESI): m/z 264.95.

2-(4-Methoxyanilino)-1,4-naphthoquinone (1.44 g, 54%, deep purple solid)

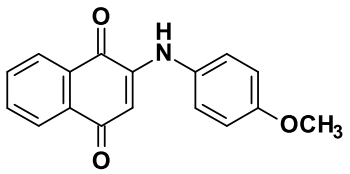

^{1}H NMR (300 MHz, DMSO-d6) δ 9.20 (s, 1H), 8.05 (dd, J = 7.5, 1.5 Hz, 1H), 7.94 (dd, J = 7.6, 1.5 Hz, 1H), 7.85 (td, J = 7.5, 1.5 Hz, 1H), 7.77 (td, J = 7.5, 1.6 Hz, 1H), 7.30 (d, J = 9.0 Hz, 2H), 7.02 (d, J = 8.9 Hz, 2H), 5.93 (s, 1H), 3.78 (s, 3H).

^{13}C NMR (75 MHz, DMSO) δ 182.68, 182.10, 157.35, 147.31, 135.32, 133.18, 132.92, 131.03, 130.87, 126.51, 126.05, 125.70, 114.95, 101.45, 55.75.

LCMS (ESI): m/z 279.51.

2-(4-Aminoanilino)-1,4-naphthoquinone (0.98g, 39%, black solid)

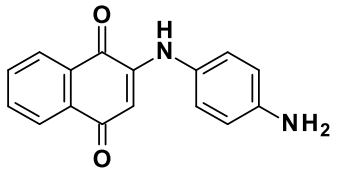

^{1}H NMR (300 MHz, DMSO-d6) δ 9.02 (s, 1H), 8.04 (dd, J = 7.6, 1.4 Hz, 1H), 7.93 (dd, J = 7.7, 1.4 Hz, 1H), 7.84 (td, J = 7.5, 1.5 Hz, 1H), 7.75 (td, J = 7.4, 1.5 Hz, 1H), 7.02 (d, J = 8.7 Hz, 2H), 6.62 (d, J = 8.7 Hz, 2H), 5.85 (s, 1H), 5.26 (s, 2H).

^{13}C NMR (75 MHz, DMSO) δ 182.28, 182.25, 147.47, 147.44, 135.31, 133.43, 132.73, 130.90, 126.44, 126.23, 125.84, 125.67, 114.50, 100.73.

LCMS (ESI): m/z 264.83.

6.2 Results and Discussion

Initially two naphthoquinone anchor units differing only in the positioning of the phenolic group were explored to establish their electrochemical properties. Cyclic voltammograms noting the responses of the 1,4 aminophenol and the 1,3 aminophenol naphthoquinone conjugates at a glassy carbon electrode are compared in **Figure 6.2.1**. Both derivatives display discrete redox positions for naphthoquinone unit and consequent aminophenol oxidation processes. However, when assessing the reversibility of the two systems, there is a distinction between the 1,4 aminophenol derivative and the 1,3 derivative. The former (solid line, **Figure 6.2.1**) displays an almost reversible electrochemical profile which is stable to repetitive cycling, in contrast, the 1,3 derivative (dashed lines, **Figure 6.2.1**) displays an irreversible system with each consecutive scan leading to the depletion of the electrode's response. This is underlined by the decrease in the peak height of the naphthoquinone reduction process due to the formation of oligomeric material caused by the coupling of radical cations accumulating at the surface of the electrode.

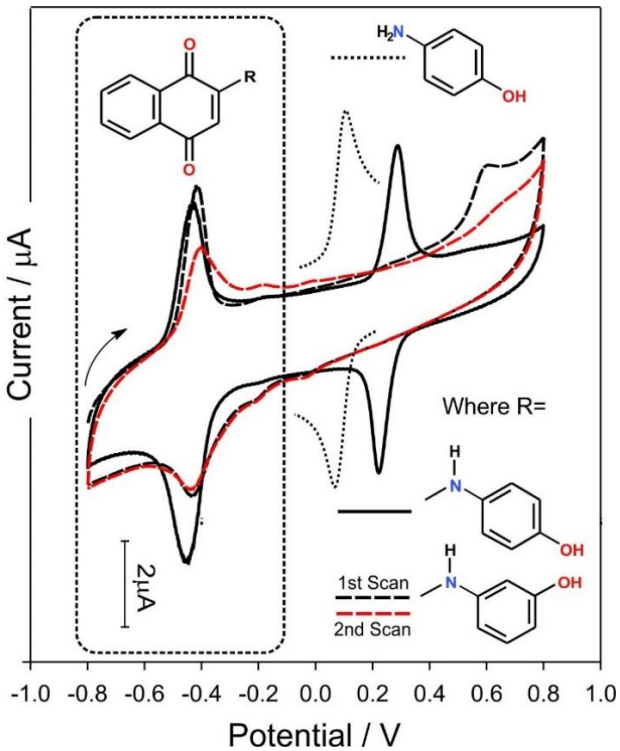

Figure 6.2.1 Cyclic voltammograms detailing the response of the naphthoquinone derivatives (182 µM) at a glassy carbon electrode in pH 7 PBS buffer. Scan rate 50 mV/s.

The response of the glassy carbon electrode towards 1,4 aminophenol has been included in **Figure 6.2.1** (dotted line) which displays a peak position (+0.11 V) that is significantly less positive than the naphthoquinone-1,4 aminophenol conjugate (+0.29 V). In addition, the peak position of the naphthoquinone component of the conjugate (-0.43 V) was discovered to be more negative than that of the unattached quinone (-0.15 V). This shift in the peak positions of the two conjugates can be credited to their impact of each on the other. This can be explained by the electron withdrawing nature of the quinone which has a knock-on effect on the oxidation of the aminophenol making oxidation more difficult with the electron releasing properties of the amine thus making it more difficult to reduce the quinone. The shift in the peak position of the aminophenol component is of greater importance as this would affect the drug release mechanism (**Figure 6.0.1**).

The sharpness of the peaks for the 1,4 aminophenol derivative would suggest that the conjugate has been adsorbed onto the electrode surface. This was verified through the removal of the electrode and numerous rinses (in deionised water). The electrode was scanned again this time in fresh pH 7 PBS buffer with no naphthoquinone conjugate present. Scan rate analysis of the adsorbed conjugate was performed (**Figure 6.2.2A** and **Figure 6.2.2B**) ranging 5 mV/s to 1 V/s and discovered that the peak heights for the naphthoquinone and the aminophenol components (-0.43 V and +0.29 V) increased linearly with scan rate (**Figure 6.2.2B**). The surface coverage (Γ) was estimated using **Equation 6.1**.

$$i_p = \frac{n^2F^2}{4RT} vA\ \Gamma^* \quad \textbf{Eq 6.1}$$

Where:

i_p = Peak current (amps);

v = Scan rate (V/s);

n = Number of electrons;

F = Faraday constant (96485 C mol^{-1});

R = Gas constant (8.314 JK^{-1} mol^{-1});

T = Temperature (298.15 K);

A = Electrode area (cm^2).

Hence a plot of peak height *vs* scan rate should be linear for a surface confined species with a gradient equal to:

$$\frac{n^2F^2}{4RT}A\ \Gamma^*$$

Given the linear plot observed in **Figure 6.2.2B** of peak height *vs* scan rate, the surface coverage was found to be 8.63 x 10^{-11} mol cm^{-2}.

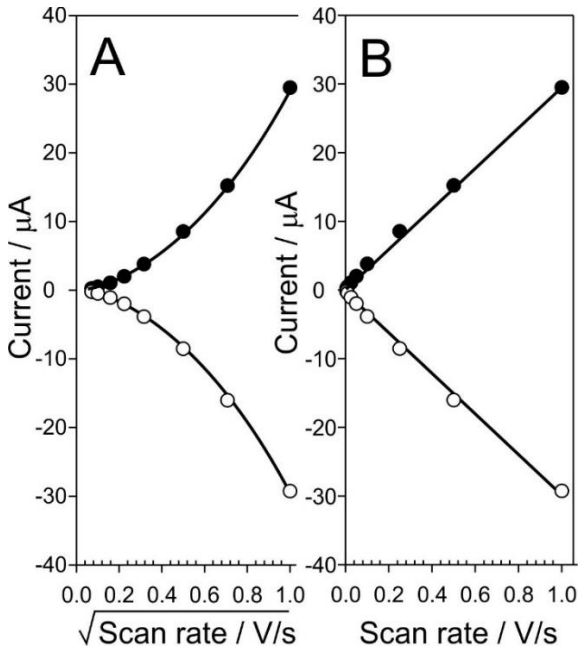

Figure 6.2.2 Influence of scan rate on the peak height of the aminophenol component of the conjugate pre-adsorbed onto glassy carbon electrode.

6.2.1 Release Mechanism

The model drug would be covalently bonded to the 1,4 aminophenol unit *via* an ether link to the OH group, thus, it is expected that upon oxidation of the aminophenol, the latter would transform into the resulting quinone imine consequently expelling the drug. A methoxy functionalised conjugate acted at the model drug for the initial studies due to the eases in synthesis in addition to aiding in the interpretation of the results. The methoxy group, once released, should lead to methanol which is electrochemically inactive in the potential window studied. Hence, this approach was initially assessed using 1,4 methoxyaniline (p-anisidine) as the model drug conjugate as upon oxidation it was envisaged that it would transform to the corresponding quinone-imine. Cyclic voltammograms highlighting the response of p-anisidine at a glassy carbon electrode are detailed in **Figure 6.2.1.1** (dashed lines). An irreversible oxidation process on the first scan is observed at +0.50 V and a resultant secondary reduction process is observed at +0.07 V on the reverse sweep which can be credited to the reduction of the electrochemically generated quinone imine to aminophenol. The oxidation of the latter is observed at +0.105 V and is consistent with the peak position of commercially available 1,4 aminophenol (**Figure 6.2.1.1**, solid line).

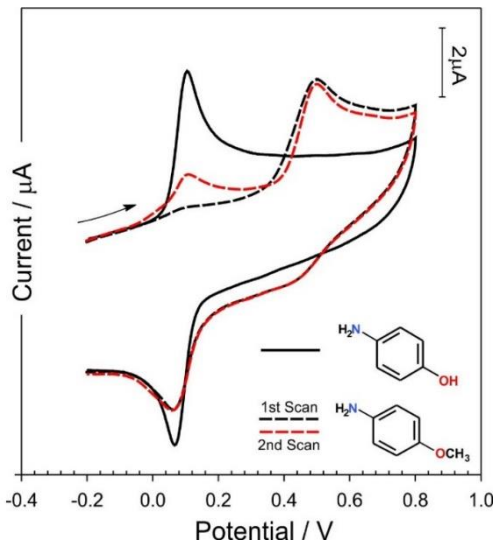

Figure 6.2.1.1 Cyclic voltammograms detailing the response of the 1,4-methoxyaniline (182 μM) at a glassy carbon (dashed line) electrode in pH 7 PBS buffer. The response to 1,4-aminophenol (solid line) has been included for comparison. Scan rate: 50 mV/s.

6.2.2 Microneedle Substrates

After successfully cleaving the methoxy group from the conjugate immobilised on the glassy carbon electrode (**Figure 6.2.1.1**), the next stage was to assess the response of the naphthoquinone-methoxy conjugate at a conductive microneedle array. The miniature size of microneedles shown in **Figure 6.2.2.1A** provides a minimally invasive approach for drug delivery and the electrochemical trigger employed allows for controlled dosing. The production, characterisation, and optimisation of the electrochemical properties of the polystyrene carbon composite microneedles used as the electrode substrates have been previously detailed in **Chapter 4** (211). The planar nature of the naphthoquinone-aminophenol conjugate has been shown to have a high affinity for carbon surfaces and, therefore, for the purposes of simply evaluating the efficacy of the approach, the conjugates were adsorbed on to the array surfaces rather than covalently tethered. Cyclic voltammograms detailing the response of the microneedle array electrode to the adsorbed methoxy conjugate (182 μM, 0.01 M PBS, pH 7) are shown in **Figure 6.2.2.1B** and the various molecular transitions associated with the peak processes highlighted in **Figure 6.2.2.2**.

Two microneedles were assessed (unmodified and anodised) as the substrate to which the methoxy conjugate was adsorbed. The modification was achieved by way of anodic oxidation in 0.1 M NaOH (+2 V, 300 s) which has been shown to improve electron transfer kinetics by introducing oxygen functionalities to the surface (247). The cyclic voltammogram detailing the unmodified MN with adsorbed naphthoquinone methoxy conjugate is featureless, however following anodisation the carbon MN displays most of the peak process observed at the glass carbon electrode. On the first scan, the naphthoquinol component is seen to be oxidised to its quinone form (I→II) at -0.31 V and the methoxy component oxidises at +0.71 V which is shown to be irreversible on the return sweep (II→III) that leads to the ejection of the methoxy group generating methanol. The anchor is consequently reverted to the original aminophenol derivative (III) examined earlier (**Figure 6.2.1**), however this is immediately oxidised to the quinone-imine form (III→IV) and on the reverse sweep, the reduction to the aminophenol

derivative (IV→III) is noted at +0.24 V and, as the reverse sweep continues, the quinone is reduced (III→V).

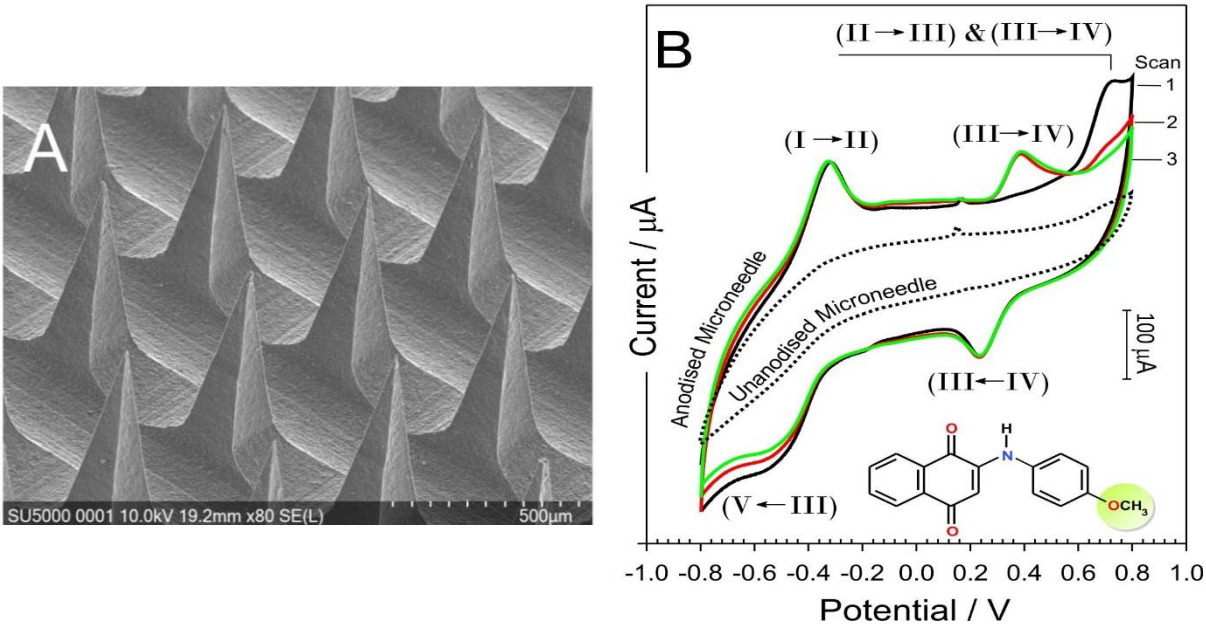

Figure 6.2.2.1 A) Scanning electron micrograph of the nano particulate carbon – polystyrene microneedle array. B) Cyclic voltammograms detailing the response of the methoxy-naphthoquinone derivative (185 µM) at unmodified (dotted line) and anodised (solid line) carbon-polystyrene microneedle arrays in pH 7 buffer. Scan rate: 50 mV/s.

The second scan reveals the oxidation of the aminophenol derivative is seen at +0.39 V consistent with **Figure 6.2.1**. As the methoxy derivative is adsorbed to the surface of the microneedle, the majority of the “model drug” is released on the first scan which is supported by the disappearance of the methoxy oxidation peak at + 0.71 V on successive scans.

The core process is consistent with the simple system excluding the naphthoquinone examined in **Figure 6.2.1.1**. However, the potential required to oxidise the methoxy in the naphthoquinone system is more positive than the 1,4 methoxyaniline system which presents a problem when considering drug candidates. The purpose of the naphthoquinone is to serve as a reporter unit, determining the presence of the drug as a redox centre without inducing its release. It is envisaged the naphthoquinone could be excluded from the final iteration with the

aminophenol unit attached to the carbon substrate, meaning the electron withdrawing influence of the quinone would not shift the potential required to cleave the ether.

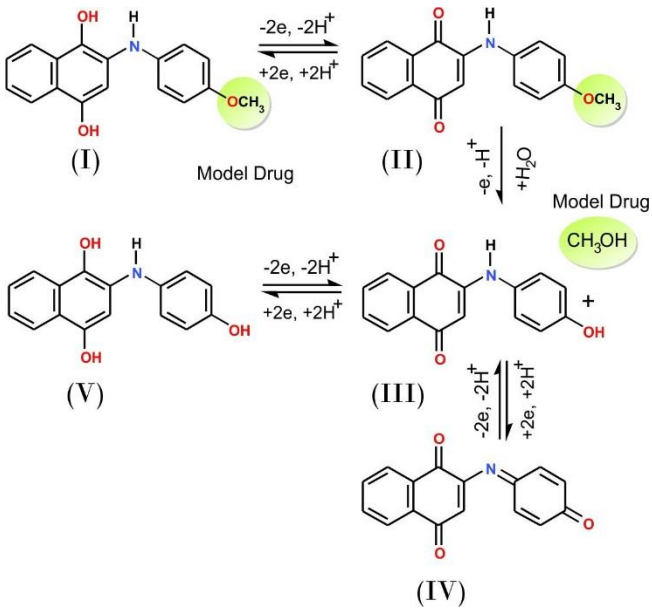

Figure 6.2.2.2 Proposed reaction mechanism attributed to the redox transitions (I→V) observed at the electrode for the methoxy conjugate.

6.2.3 Potential Drug Candidates

The release of a given drug in this system is determined on the oxidation of the aminophenol component, therefore it is important to consider suitable candidates. There are are number of factors that would influence the selection of a drug candiate, one being the complexity of synthesis of the compound, however, in this instance this is out of scope of the investigation. A preliminary challenge would be selecting a drug that will not be altered following the application of the oxidation potential to cleave the ether bond employed as a teather, to ensure the drug remains in its therapeutically active state. Following the oxidation of the ether, the resultant drug exits with an OH group, therefore a potential drug candidate must have an hyrdoxyl group (either an alkyl or aryl) in its active form. A list of common commercial drugs covering a spectrum of clinical conditions and which fulfil this hydroxyl group criterion is highlighted in **Table 6.2.3**. At a quick glance, the chemical structures reveal a wide variety of

functionality, but the question is whether the drug is altered after applying the oxidation potential?

An ideal drug candidate would be one which contained only akyl functionality (such as Gabapentin or Gentamicin) whereupon it is unlikely there would be any oxidation of the core structure at the potentials applied here. The next preferrable structure would contain a phenolic OH (such as Salbutamol) which would have used in the actual ether linkage. Alternatively, compounds containing aromatic structures to which there are no N or O groups directly attached (*i.e.*, Haloperidol) could also be considered as feasible conjugates. Complications arise where the active drug structures themselves contain aromatic functional groups such as amines (Diclofenac), heterocycles (Rotigotine) or other ethers (Atenolol, Bisoprolol). Drugs such as Tramadol, Naproxen or Codeine each possess an OH through which to attach to the electrochemical tether but also possess a separate methoxy functional group. The latter, like the model system highlighted in **Figure 6.2.1.1**, will also be electrochemically active and there is a risk that upon attempting to cleave the ether link tethering the drug, the methoxy group which is intrinsic to the actual drug could also be oxidised. One caveat however is that the ether link tethering the drug is activated as a consequence of the aminophenol structure that constitutes the tether. Though it must be noted that in the present system there is conflict between the electron withdrawing influence of the quinone increasing the oxidation potential. In principle however, the electron releasing properties of the aromatic amine group essentially renders the ether groups easier to oxidise than if it were absent.

The possibility of inadvertently oxidising other functionalities within the drug candidate was assessed through examining the response to codeine (1 mM, pH 7 PBS). Cyclic voltammograms comparing the response to codeine and the initial naphthoquinone-methoxy conjugate are detailed in **Figure 6.2.3.1**.

Drug	Structure	Action	Drug	Structure	Action
Warfarin	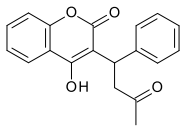	Anti coagulant	Venlafaxine	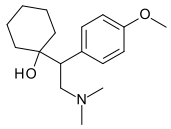	Anti depressant
Codeine	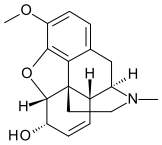	Opioid analgesic	Haloperidol	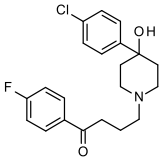	Antipsychotic
Salbutamol	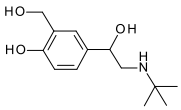	Broncho-dilator	Gabapentin	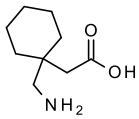	Anti convulsant
Diclofenac	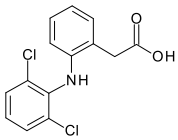	Analgesic	Naproxen	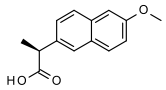	Non-steroidal anti-inflammatory drug
Rotigotine	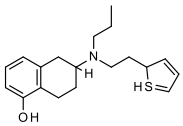	Treatment of Parkinson's symptoms	Gentamicin	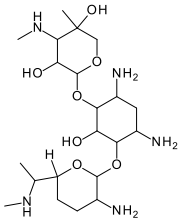	Antibiotic
Tramadol	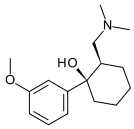	Opioid analgesic	Bisoprolol	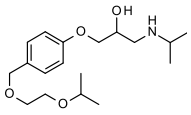	Anti arrhythmic
Atenolol	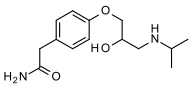	Treatment of high blood pressure	Amoxycillin	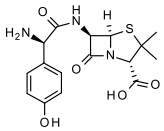	Antibiotic

Table 6.2.3.1 Common prescription drugs which could be considered potential candidates for linkage to the naphthoquinone-aminophenol linker.

The response to codeine is relatively featureless (despite the presence of the methoxy) with an ill-defined oxidation process observed at +1.1 V. This is significantly more positive than that

required to cleave the aminophenol activated ether and thus it could be envisaged that, at least in this case, the release of codeine *via* this conjugate could be possible. Clearly, individual drug systems would need to be appraised before embarking on the complex synthesis required to chemically attach the candidates to the linker. Gabapentin, naproxen, and diclofenac provide an alternative attachment pathway by virtue of their carboxylic acid functionality. The great advantage of the ether bond is that cleavage can only occur upon electrochemical activation and thus greatly minimises the risk of accident release. It could be envisaged that rather than linkage *via* and ether – these can be conjugated through an ester. The electrochemical properties of the latter are investigated in the next chapter.

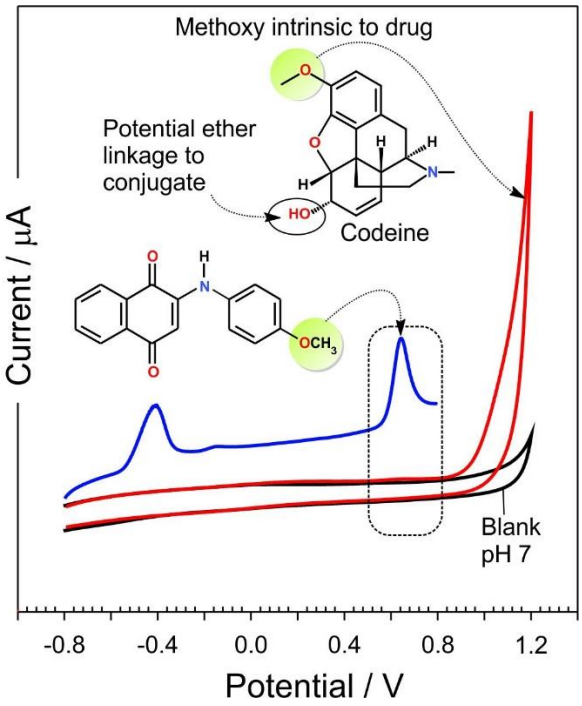

Figure 6.2.3.1 Cyclic voltammograms comparing the response of a glassy carbon electrode to codeine (1 mM, pH 7 PBS) and the naphthoquinone-methoxy conjugate. Scan rate: 50 mV/s.

6.3 Conclusions

The approach outlined in this chapter offers a high level of control over the release process due to the application of the naphthoquinone aminophenol methodology. The use of the ether as a tether is stable and will only cleave following an application of an oxidation potential.

However, the drugs that could be applied to this system are limited as they require hydroxyl functionalities, and the synthesis would need include the individual drug conjugate as a precursor. In an attempt to combat this, the next chapter outlines the use of an ester bond tethered to commercially available drugs thus as an alternative to the extensive synthesis discussed here.

Chapter 7

Activation of Carboxylic Groups *via* DMAP / DCC for Controlled Release of Ester Bound Drugs *via* Electrochemical Trigger

Overview

This chapter employs dicyclohexylcarbodiimide (DCC) and 4- N, N-dimethylaminopyridine (DMAP) which are known to readily activate carboxylic groups towards ester formation. Given the presence of such groups on carbon surfaces, the subsequent activation could be exploited as a means of immobilising drug candidates at the electrode surface. Laser induced graphene (LIG) and polystyrene-carbon (Ps-C) were used as the test substrates. Following the esterification of the drug candidate to the substrate, the application of oxidative and reductive potentials can be used as a means to control drug delivery. Acetaminophen (paracetamol) and salicylic acid were employed as model drug agents and were used to validate the release system in real time by way of cyclic voltammetry and UV-visible spectrophotometry. While oxidative release exploits the inherent electrochemical properties of the drug, cathodic potential changes brought out changes in the local pH which in turn hydrolyse the ester bond. The use of poly(anthranilic acid) was also explored as an electrode modifier which would increase the population of carboxylic groups and thereby increase the drug loading potential and eventual yield.

7.0 Introduction

Within the transdermal drug delivery sphere, control over release of therapeutics *via* electrochemical triggers has gained significant interest. Jin *et al.*, (2012) made the use of a reductive potential which induced the dissolution of alginate crosslinked with iron to deliver drug mimicking protein (304). Other work by Duong *et al.*, (2018) applied a cathodic potential to a polycarbonate microneedle coated with a positively charged pH responsive polymer, where the local pH at the MN surface transformed the polymer to expel the vaccine attached (305). The approach in this work relies on an ester bond attached to a drug candidate that can be broken either by an oxidative potential or by applying a cathodic potential that increases the pH local to the electrode surface that can hydrolyse the ester thus expel the drug.

The previous chapter highlighted the limitation of employing an ether tether using the naphthoquinone aminophenol unit. The ether link, although stable, is difficult to synthesise and also restricts the range of drugs which would be suitable and therefore wouldn't be feasible in a large scale. This leads onto this chapter which focuses on the application of an ester link which would be bound to a drug candidate and broken upon the application of a potential. The use of an ester link is much more simplistic and widens the range of drugs that can be delivered as they only need to possess a hydroxyl group, however, in this study electrochemically active drugs were the focus as a means of validating the release in real time. Initially codeine, salicylic acid and acetaminophen were explored as candidates as they have appropriate chemical structure containing a group that can be detected electrochemically for characterisation and to verify release quickly without the use of additional instruments.

The primary substrate employed in this investigation was laser induced graphene (LIG) which contains an abundance of carboxylic groups and hence provide target sites for drug immobilisation. Direct esterification between an acid (in this case those at the electrode surface) and an alcohol (the drug) is extremely slow, and a catalyst is usually employed. A commonly utilised catalyst that rapidly forms esters is dicyclohexylcarbodiimide (DCC) in the presence of 4- N, N-dimethylaminopyridine (DMAP), which activates the carboxylic groups on

a substrate. Following activation, the drug replaces the DCC and forms an ester bond more readily with the LIG. This activation process for LIG is highlighted in **Figure 7.0.1** and has been used for a range of substrates including cellulose nanofibrils to deliver metronidazole (prodrug) (306).

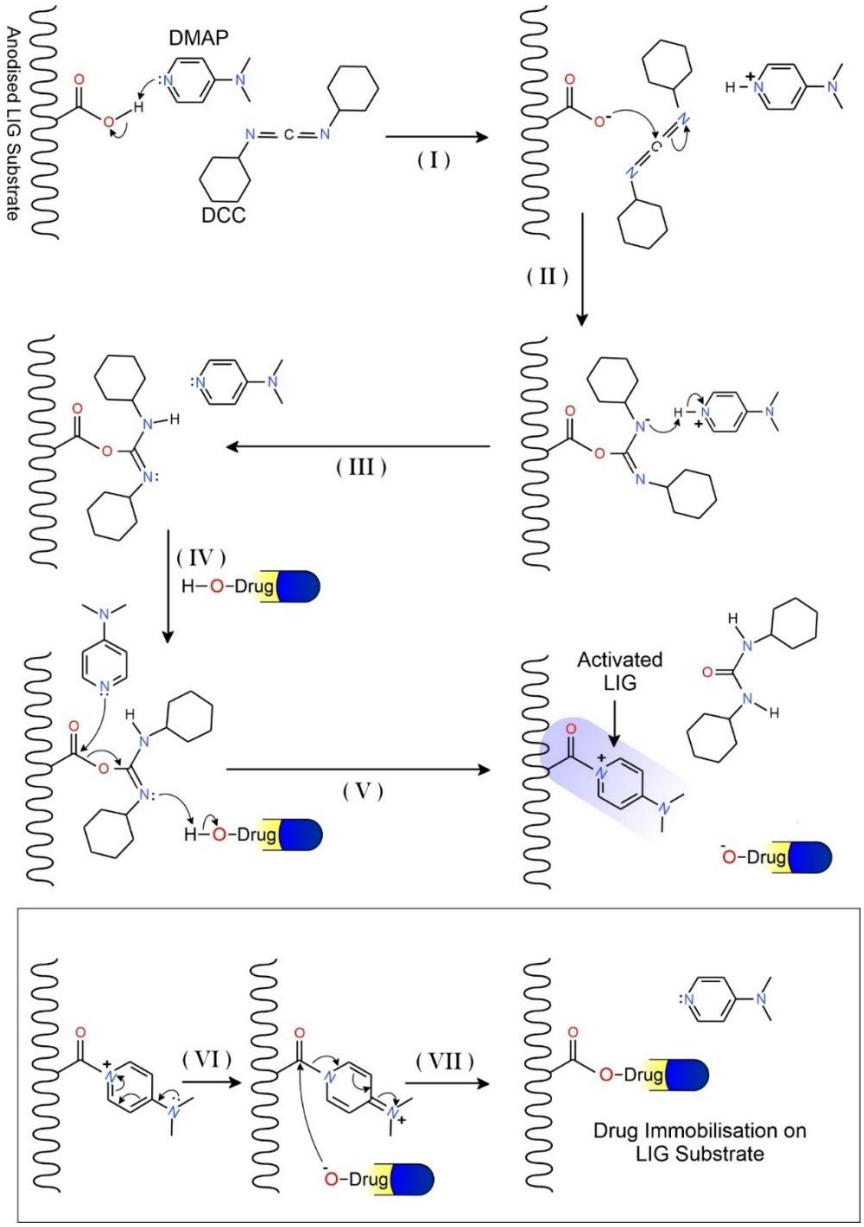

Figure 7.0.1 Activation of carboxylic groups on laser induced graphene (LIG) by dicyclohexylcarbodiimide (DCC) in the presence of 4- N, N-dimethylaminopyridine (DMAP) which is displaced by a drug candidate possessing hydroxyl group to facilitate esterification.

The drug yield in theory could be increased by providing more carboxylic acid sites on the electrode surface, even in the case of LIG where there is a high population of these sites. This is even more relevant for carbon microneedles which do not inherently possess such opportunities for drugs to adhere. The electropolymerisation of anthranilic acid (AA) onto the surface of the carbon surface could be applied to provide more sites for esterification especially if a thick film is produced. The use of the polymerisation of AA is explored in this chapter to increase drug loading.

7.1 Experimental Details

7.1.1 Materials and Instrumentation

All chemicals were acquired from Sigma-Aldrich, were the highest grade available and were used without further purification. Britton Robinson buffers were used throughout unless otherwise specified. The latter consisted of acetic, boric, and phosphoric acids, each at a concentration of 0.04 M and adjusted to the appropriate pH through the addition of sodium hydroxide). Electrochemical analysis was carried out using a Palm Sens computer controlled potentiostat with a standard three-electrode configuration in which LIG substrate or the microneedle patch was used as the working electrode with platinum and a Ag|AgCl half cell (3M NaCl, BAS Technicol UK) acting as counter and reference respectively. All measurements were conducted at 22ºC ± 2ºC. Esterification of electrode surface by dicyclohexylcarbodiimide (DCC) at a concentration of 10 mM in the presence of 1 mM 4- N, N-dimethylaminopyridine (DMAP) was carried out in acetonitrile for acetaminophen or salicylic acid – each at a concentration of 10 mM for 30 minutes to give ample time for reaction of take place. The electrode was rinsed in pH 3 buffer to remove any residual DMAP / DCC or unattached drug. Laser induced graphene (LIG) was fabricated using a ULS VLS2.30 25 W CO_2 laser cutter on raster mode, speed 40, power 30 % and resolution of 1000 pulse per inch. Microneedle moulds were obtained from Micropoint Technologies Pte Ltd (Singapore) and were pyramidal in format with 200(base) x 500(pitch) x 700 (height) micron dimensions covering a 10 x 10 needle array.

7.2 Results and Discussion

7.2.1 Selection of Model Drug Targets

The mechanism employed in this chapter differs from the previous chapter as actual drugs are released rather than methanol. The main criteria in this instance are that the drug candidates possess an OH group available to tether the drug in addition to being electrochemically active such that their presence or release could be confirmed promptly. Cyclic voltammograms noting the responses of codeine, salicylic acid and acetaminophen at a glassy carbon electrode are highlighted in **Figure 7.2.1.1**. The response to codeine is relatively featureless with an ill-defined oxidation process observed at +1.1 V. The response to salicylic acid produces an oxidation peak at +0.7 V which is irreversible. The response to acetaminophen reveals a sharp oxidation peak at +0.5 V and reduction peak at +0.1 V but the peak separation of roughly 400 mV hints at quasi-reversible behaviour. As the salicylic acid and acetaminophen display sharp, well defined oxidation peaks which could be easily observed at the electrode (in contrast to the codeine) – these were taken forward for further investigation.

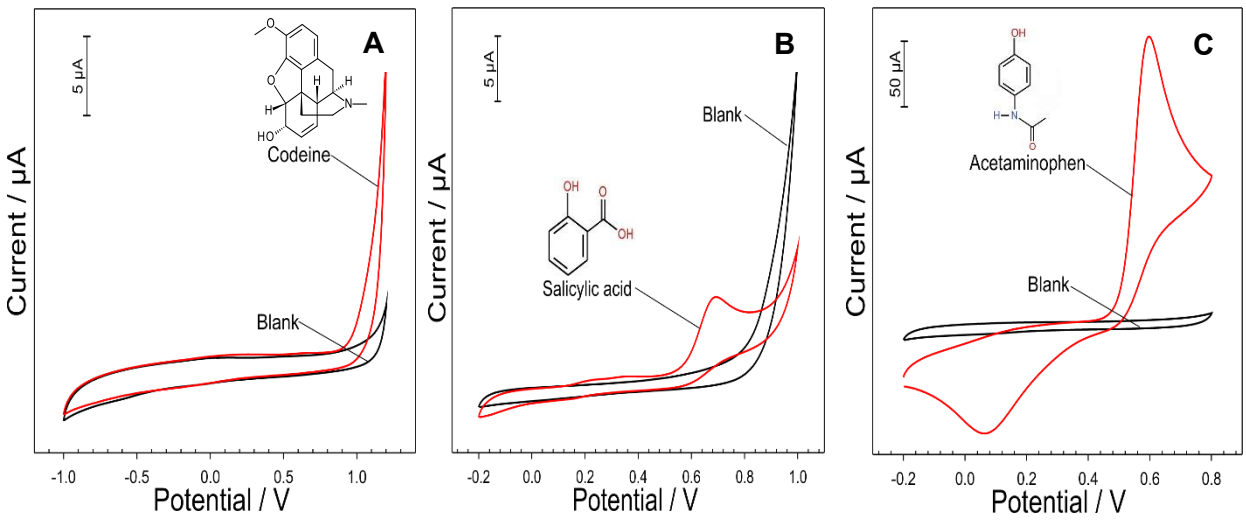

Figure 7.2.1.1 Cyclic voltammograms detailing response of A) codeine (0.19 mM), B) salicylic acid (1.15 mM) and C) acetaminophen (1.87 mM) towards glassy carbon electrode in pH 5 BR buffer. Scan rate: 50mV/s.

Cyclic voltammograms detailing the response of salicylic acid and acetaminophen to laser induced graphene (LIG) is noted in **Figure 7.2.1.2**. The oxidation peak observed with salicylic acid on the glassy carbon electrode was more pronounced compared the response to the LIG electrode and the LIG electrode requires a more positive overpotential to induce oxidation (~+1 V). The overpotential results in by-products due to the irreversible oxidation as indicated by ambiguous reduction and oxidation peaks. The presence of these by-products confirms that the salicylic acid is altered and may not produce the therapeutic action intended, therefore it is unsuitable to be released by the application of an oxidation potential. The response of acetaminophen to LIG, however, is similar to that of the glassy carbon electrode where a quasi-reversible system is observed, albeit the reduction process is less defined.

7.2.2 Oxidative Release of Drug Candidates

The next stage was to assess the DMAP/DCC release system which is illustrated in **Figure 7.2.2.1**. It has already been established from **Chapter 5** that the laser induced graphene substrates possess a population of interfacial carboxylic groups. It was anticipated that a second processing step involving electrochemical anodisation would further increase the proportion of COOH groups and thereby provide a surface tether for the immobilisation of the drugs. The DMAP / DCC mechanism highlighted in **Figure 7.2.2.1** facilitates the esterification of the carbon surface and activated the carboxylic groups for reaction with the hydroxyl group within drug (acetaminophen or salicylic acid). In the case of acetaminophen, it was envisaged that when an oxidative potential is applied, the ester bond is broken as a consequence of the quinone-imine formation highlighted in **Figure 7.2.2.1**.

As such, the oxidised form of acetaminophen could, in principle be released in a controlled manner. Cyclic voltammograms detailing response of LIG DMAP / DCC loaded with acetaminophen is compared to bare LIG in **Figure 7.2.2.2**. An oxidation peak is observed at +0.6 V and displays a quasi-reversible system consistent with the oxidation peak of acetaminophen in isolation in **Figure 7.2.1.1** which indicates that the ester (provided by DAMP / DCC) attached to the drug is broken and is released into solution. The cyclic voltammogram

detailing the response of bare LIG control is featureless in the pH 5 buffer which is unsurprising. The use of pH 5 buffer in this case was chosen to minimise hydrolysis of the ester link.

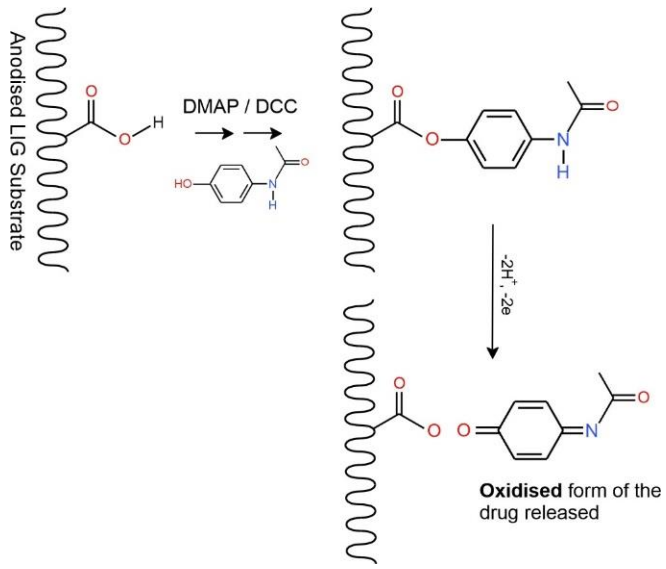

Figure 7.2.2.1 Immobilisation of electro-oxidative release of acetaminophen.

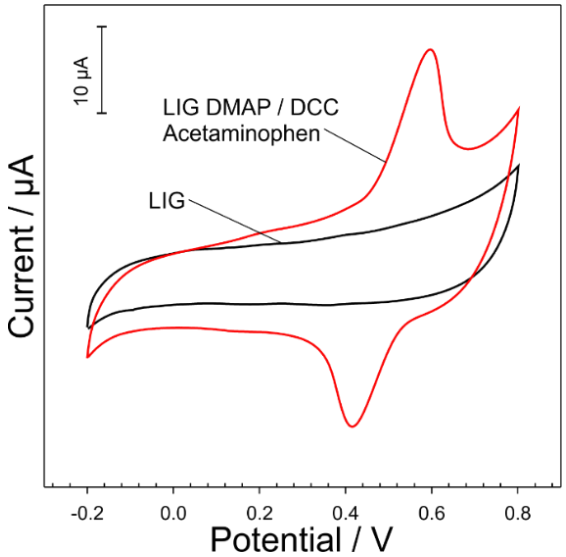

Figure 7.2.2.2 Acetaminophen release mechanism facilitated by DMAP / DCC ester activation and cyclic voltammogram detailing the response of LIG versus LIG DMAP / DCC loaded with acetaminophen in pH 5 BR buffer. Scan rate: 50 mV/s.

The fact that the drug is released in its oxidised form is clearly problematic – especially in terms of therapeutic efficacy. Given the drug exhibits quasi reversible behaviour (**Figure**

7.2.2.2), it could be envisaged that, while a suitably positive potential could be used to release the drug, the second potential step applying a reductive potential could return the drug to its active reduced form. There are obvious limitations in this approach where diffusion of the drug away from the electrode would prevent re-reduction. This is further corroborated in **Figure 7.2.2.3** where successive scans of LIG DMAP / DCC loaded with acetaminophen displays a diminishing oxidation peak (+0.58 V), suggesting that the acetaminophen is released and dissolves into the solution resulting in a smaller peak after each scan. It is important to note that the majority of the acetaminophen is released on the first scan.

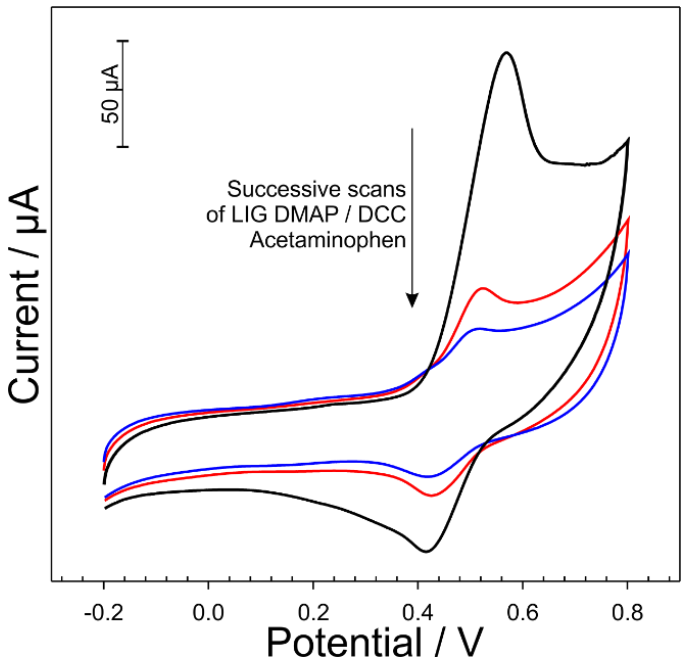

Figure 7.2.2.3 Cyclic voltammograms detailing the response of LIG DMAP / DCC loaded with acetaminophen with repetitive cycling in pH 5 BR buffer. Scan rate: 50 mV/s.

Since acetaminophen cannot pass through the skin barrier, the approach was investigated using an anodised polystyrene-carbon microneedle which could facilitate drug delivery through the skin. Cyclic voltammograms detailing the response of modified Ps-C MN DMAP / DCC loaded with acetaminophen is shown in **Figure 7.2.2.4**. Similarly, **Figure 7.2.2.4** details the oxidation peak decreases following successive scans indicating the removal of the acetaminophen into solution.

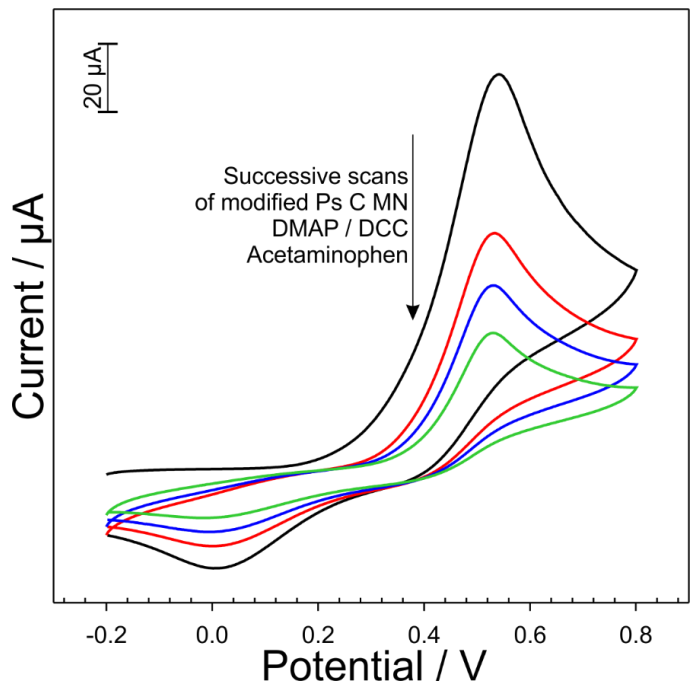

Figure 7.2.2.4 Cyclic voltammograms detailing the response of Ps-C MN DMAP / DCC loaded with acetaminophen with repetitive cycling in pH 5 BR buffer. Scan rate: 50 mV/s

The release mechanism presented here provides a more simplistic fabrication process compared to the naphthoquinone-aminophenol tether discussed in the previous chapter. However, it is not without its limitations, the selected drug must be electrochemically oxidised to break the ester bond which produces a significant molecular change. This becomes as issue if the change is irreversible, which could alter the therapeutic nature of the drug. As the drug candidate would need to be capable of reversible electrode behaviour which would dramatically restrict the candidate drug pool. A pertinent example of this restriction can be seen with irreversible nature of salicylate. It could be envisaged that the salicylate could similarly be tethered to the LIG (or MN) electrode *via* DMPA/DCC as indicated in **Figure 7.2.2.5**.

The same DMAP / DCC system is applied for the delivery of salicylic acid, highlighted in **Figure 7.2.2.5**, where an ester bond is formed between the carboxylic group of the LIG and the hydroxyl group of the salicylic acid, which is broken by the application of the oxidative potential.

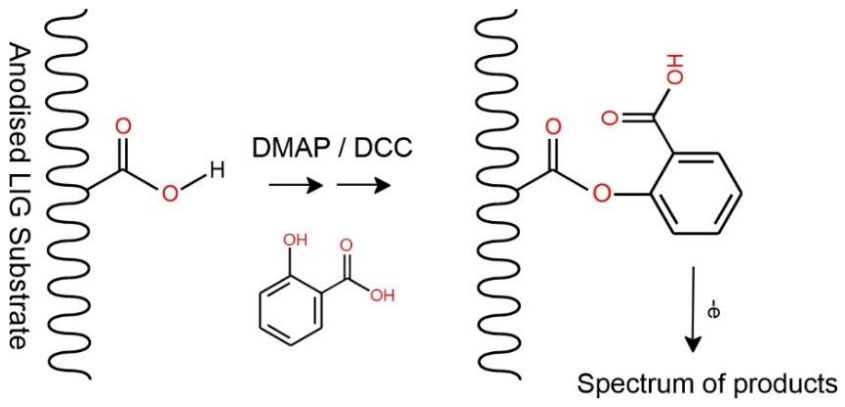

Figure 7.2.2.5 Salicylic acid release mechanism facilitated by DMAP / DCC ester activation.

However, the molecular change to the salicylic due to the oxidative potential produces a range of products. This issue is two-fold, due to the release of a variety of products, the therapeutic intention of salicylic acid cannot be achieved, and these products are irreversible – fouling the surface of the electrode but also creating chemical species which could have undesirable properties.

Square wave voltammograms of LIG DMAP / DCC loaded with salicylic acid are shown in **Figure 7.2.2.6** and demonstrates the oxidative release and subsequent by-products.

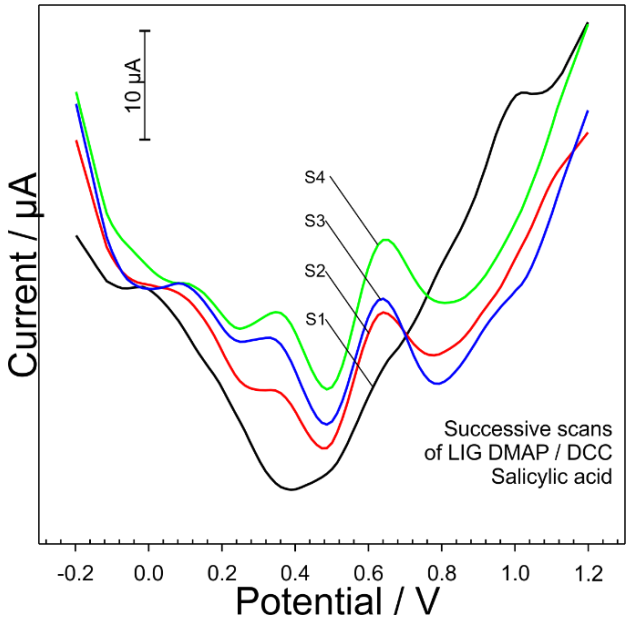

Figure 7.2.2.6 Square wave voltammograms detailing the response of LIG DMAP / DCC loaded with salicylic acid with repetitive cycling in pH 5 BR buffer.

The oxidation peaks of some of the by-products are included in the following scans, for example the at around +0.4 V the peak is likely dihydroxybenzoic when compared to work by Alcalde *et al.*, (2019) where the features of polyphenols were explored (307). Similar work investigating phenolic acids by Magarelli *et al.*, (2013) supports the assumption that the prominent peak around +0.6 V is likely to be gentisic acid (308).

The breaking of the ester bond is observed on the first scan at +1 V where the majority of the bound drug is expelled in an irreversible process. The molecule released is unstable containing a free radical and readily reacts with other released molecules producing a range of by-products. The chemical structure of the by-products produced due to the oxidation of salicylic acid are illustrated in **Figure 7.2.2.6**. As mentioned previously, the oxidation of salicylic acid produces an unstable molecule containing free radicals, and the molecules can react with themselves in two ways, either “head to tail”, shown in instance A where the molecules form a polymer chain, or they can arrange “tail to tail” to form a dimer known as biphenylsalicylic acid (309) in instance B. Despite instance B being a reversible system, the drug is not in its therapeutically active form and the properties may be altered. This leads onto the next approach, which is to hydrolyse the ester bond by changing the local pH by applying a very negative potential which would release drug candidates without altering their structure.

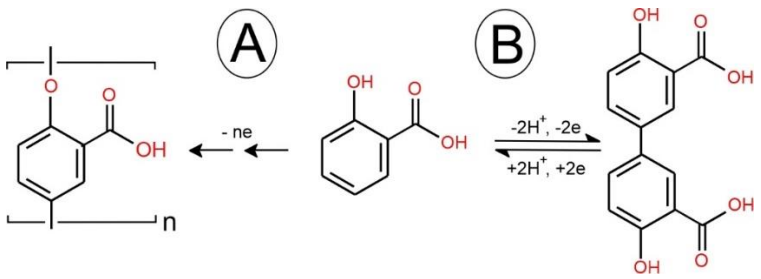

Figure 7.2.2.7 Chemical structure of the possible by-products that can arise due to the application of an oxidative potential towards salicylic acid. (A) polymeric deposits (PSA) and (B) biphenylsalicylic acid (BPSA)

7.2.3 Ester Hydrolysis through Localised Changes in pH

An alternative release method that could potentially preserve the therapeutically active form of the drug was investigated and involved controlling release through manipulation of local pH. The latter could be achieved through controlled electrolysis at the electrode surface increasing interfacial pH and thereby accelerating the hydrolysis of the ester without unduly changing the form of the drug itself. The basic methodology is summarised in **Figure 7.2.3.1**.

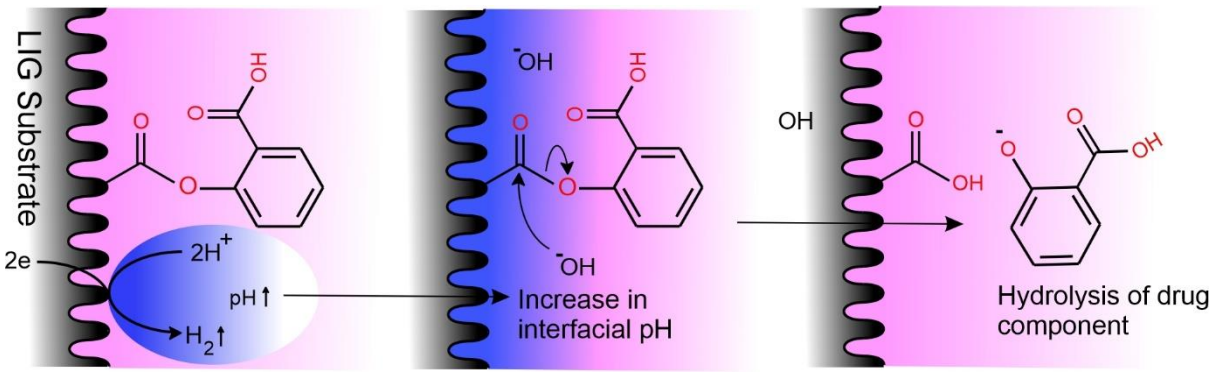

Figure 7.2.3.1 Alternative release mechanism where the local pH is increased by the application of a cathodic potential to hydrolyse the ester bound to the drug.

The ester bound to the selected drug is stable in more acidic environments like pH 5, which would ensure that release would not be released accidentally before puncturing the skin. Upon the imposition of a cathodic potential, the population of hydroxyl ions at the electrode surface would increase the pH locally and hydrolyse the bond thus providing controlled release without altering the molecular structure of the drug. In principle, the drug candidate does not need to be electroactive for the process to be viable as the release is based on simple hydrolysis of the ester bond. A similar method was employed by Anderson *et al.*, (2019) where a cathodic potential of –2 V was used to increase the local pH to induce swelling or cellulose acetate phthalate resulting in the expulsion of a drug candidate (310).

While this process presents an obvious advantage, there are still a number of caveats. The imposition of the cathodic potential to facilitate the hydrogen evolution process could be of issue where the drug has electrochemically reducible functional groups (such as nitro or nitroso groups). In this case, the drug molecule would be substantially changed during the

release process. As such, the method has the potential to dramatically increase the drug candidate pool, but it is not a generic methodology and caution over selection would still be required.

7.2.4 Initial Electro-Hydrolysis of Drug Loaded LIG

As a preliminary test, a potential of -2 V was applied at the LIG DMAP / DCC electrodes loaded with either acetaminophen or salicylic acid and then a series of cyclic voltammograms recorded. From **Figure 7.2.4.1**, it can be seen that the voltammograms are featureless after the application of a cathodic potential (-2 V), suggesting that the drug has been expelled, for comparison cyclic voltammograms of LIG DMAP / DCC electrodes loaded with drug that were not treated with -2 V are included and display the characteristic oxidation peaks reported in **Section 7.2.2**. The release of acetaminophen is more straightforward as its presence/absence can be determined electrochemically. The irreversible nature of the salicylate complicated analysis and UV-Visual spectrophotometry was employed to ensure that it is released following the application of a cathodic potential. The reduction peaks (+0.35 V) in **7.2.4.1B** for the salicylate can be attributed to the electrogenerated products discussed indicated in **Figure 7.2.2.5**.

7.2.5 Electrochemical Hydrolysis of Salicylic Acid Loaded LIG

The spectroscopic methodology employed to study the electro-hydrolysis of the LIG loaded with salicylic acid is summarised in **Figure 7.2.5.1.** UV-vis spectrophotometry was employed before and after the electrochemical hydrolysis of LIG/salicylate with the salicylate yielding an unambiguous absorption profile. One measure that is taken prior to chronoamperometry to ensure that there is no unbound drug on the surface is copious rinsing in pH 3 prior to testing.

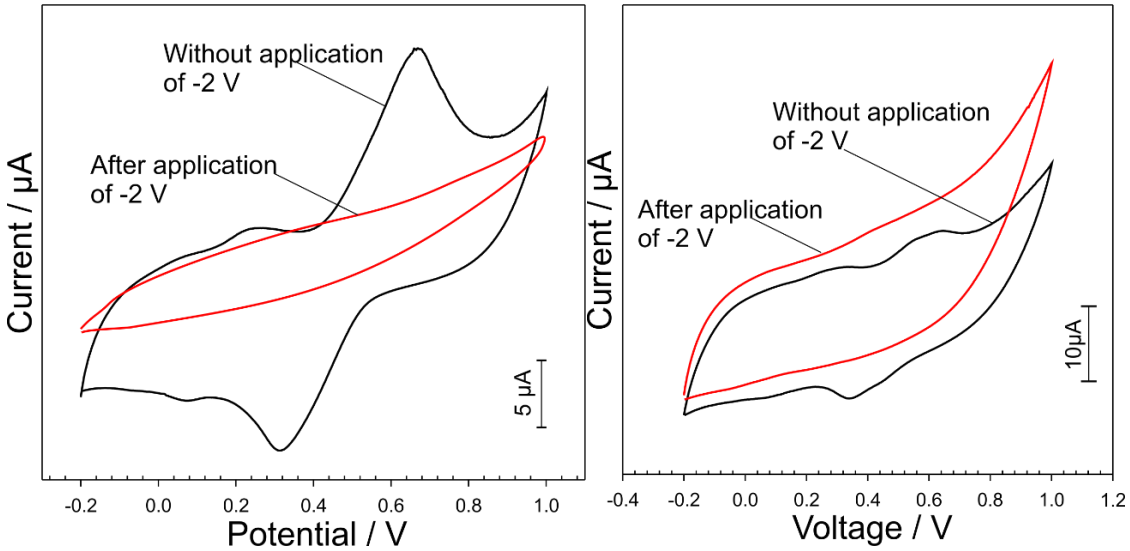

Figure 7.2.4.1 Cyclic voltammograms detailing the response of LIG DMAP / DCC loaded with acetaminophen (Left) and salicylic acid (Right) after the application of –2 V (Red) versus the control where there was no pre-treatment potential of -2 V (Black) in pH 5 BR buffer. Scan rate: 50 mV/s.

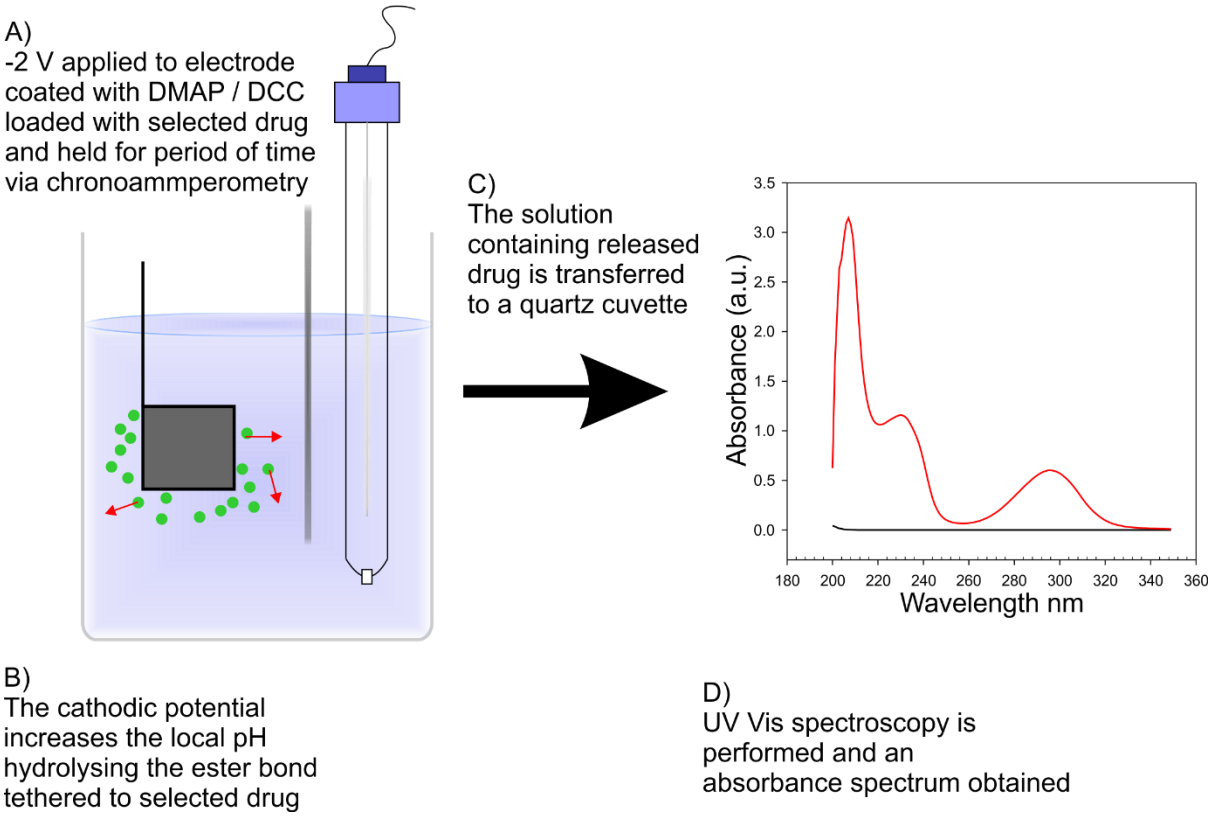

Figure 7.2.5.1 Methodology employed to verify release of drugs following application of -2 V to LIG DMAP / DCC loaded with salicylic acid.

A preliminary investigation detailing the absorbance spectrum of salicylic acid in pH buffer is shown in **Figure 7.2.5.2** and displays prominent absorbance peaks at 210 nm, 230 nm and 295 nm. A calibration curve was plotted using the absorbance values at 300 nm versus the concentration which displayed linear regression ($y = 3330.2\ x - 0.0425$) with an R^2 value of 0.9957.

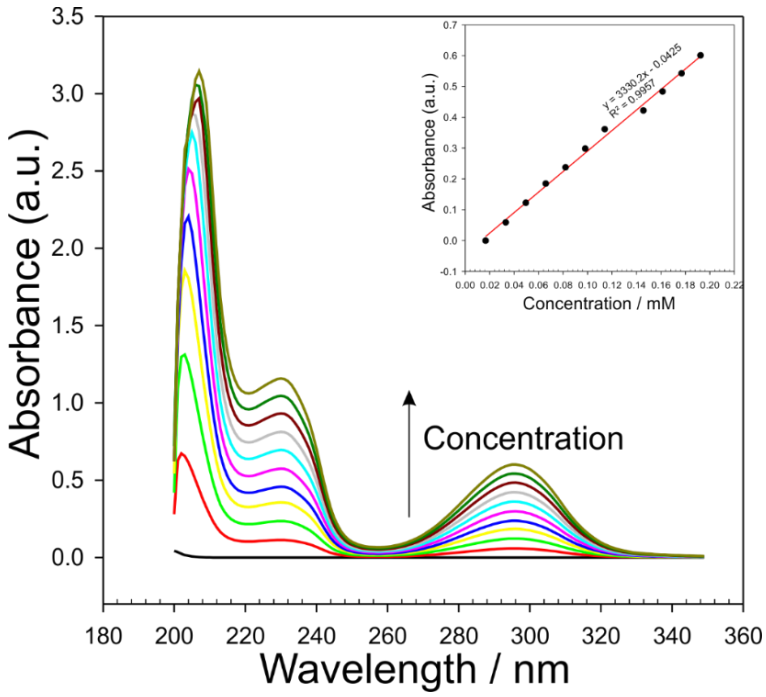

Figure 7.2.5.2 UV Vis spectrum of salicylic acid in pH 5 and the resulting calibration curve.

The next step was to confirm that salicylic acid can be released by electro-hydrolysis, an absorbance spectrum following the application of -2 V to LIG loaded with salicylic acid into 3 mL of pH 5 buffer is seen in **Figure 7.2.5.3** and there is a prominent peak at 295 nm consistent with **Figure 7.2.5.2**.

After one treatment of -2 V for two minutes, using the calibration data in **Figure 7.2.5.2**, it was estimated that 32.9 μM of salicylic acid was released and after a following three minutes a total of 47.6 μM has been released. These were based on a geometric electrode area of 0.1 cm^2. Increasing the yield would require access to more carboxylic acid sites on the LIG. There is however a limit as to the amount of carboxyl groups that can be created through anodisation with increasing duration leading to greater degrees of carbon exfoliation rather than substantial

changes to the interfacial composition. This is supported by XPS studies of anodisation effects on carbon fibre by Casimero *et al.*, (247). An alternative approach however is to use a polymer film which has carboxylic acid side substituents – with control over the thickness of the film providing a means of enhancing the drug yield.

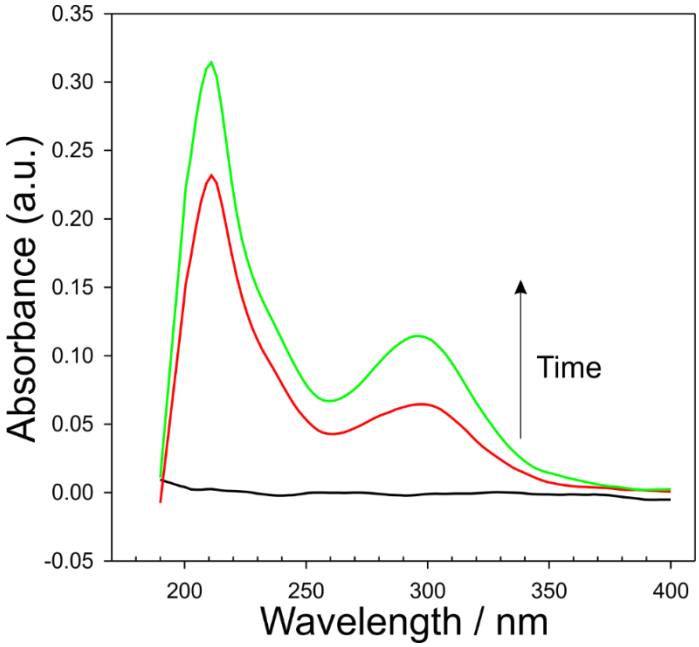

Figure 7.2.5.3 UV Vis spectrum following the electro-hydrolysis of salicylic acid from LIG DMAP / DCC loaded with salicylic acid after applying -2 V in pH 5 BR buffer.

7.2.6 Poly(Anthranilic Acid): Increasing Drug Loading

Anthranilic acid (AA) behaves similarly to other polyanilines being heralded for high electroactivity as well as ease of electropolymerisation. In this instance, the application of poly(anthranilic acid) shown in **Figure 7.2.6.1A**, as a coating would increase the population of carboxylic groups thus increasing the yield of drugs with salicylic acid used as the model drug in **Figure 7.2.6.1B**.

Cyclic voltammograms detailing the electropolymerisation of anthranilic acid in 0.1 M sulfuric acid towards LIG are shown in **Figure 7.2.6.2**.

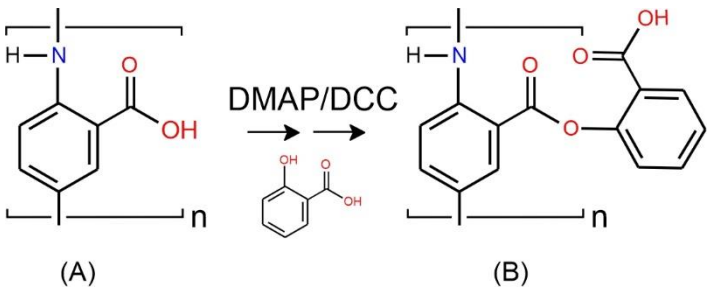

Figure 7.2.6.1 Modification of poly(anthranilic acid) (A) with salicylate (B).

The first scan (black line) has only one peak around +0.9 V and the trace goes back on itself on the return sweep where reduction peaks at +0.4 V and +0.05 V can be seen. Successive scans show the corresponding oxidation peaks due to the polymerisation at +0.9 V at +0.3 V and +0.5 V and the magnitude of the redox peaks increase after each successive scan. These results are consistent with work by Wang *et al.*, (2006) who attributed the redox peaks to three typical forms of polyaniline, leuco emeraldine (LE), emeraldine (EB) and per nigraniline (PA). The more negative redox peaks are due to the conversion of EB and LE states and the more positive redox peaks are due to the conversion of EB and PA (311).

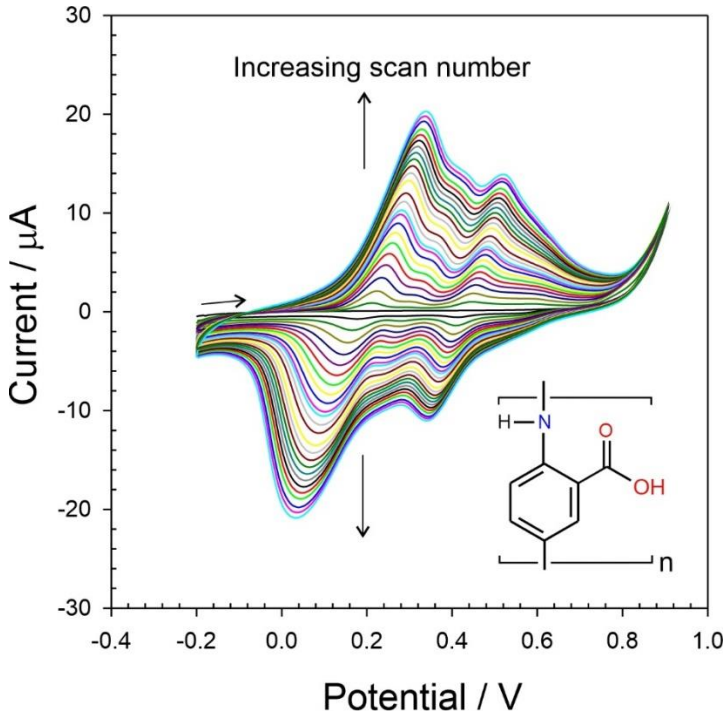

Figure 7.2.6.2 Cyclic voltammograms detailing the response of a LIG electrode towards anthranilic acid in 0.1 M sulfuric acid. Scan rate: 50 mV/s

The next step was to quantify the release of salicylic acid from LIG coated with poly(anthranilic acid). The polymer was deposited using repetitive scan cyclic voltammetry as per **Figure 7.2.6.2** and terminated after 50 scans. Salicylic acid was loaded onto the polymer using the DMAP / DCC procedures previously specified. The absorbance spectra following the application of -2 V at discrete intervals of 30 s were then recorded as per the methodology employed with the anodised LIG film (**Figure 7.3.7.1**). After the first treatment of -2 V for 30 s, it was estimated that 26.2 μM of salicylic acid was released. After another 30 s treatment the concentration is 38.6 μM which was greater than the yield obtained from 5 minutes hydrolysis at the uncoated LIG electrode. After a total of 90 s 49.2 μM of salicylic is released from the LIG, this is promising as a means of increasing the yield of drug release as well as the rate of release.

A preliminary investigation of poly(anthranilic acid) on PS-C microneedles was also conducted. After one treatment of -2 V for 2 minutes 14.8 μM of salicylic acid is released, and after another 2 minutes treatment the concentration is 17.9 μM, then 20.3 μM and finally 22.1 μM. The geometric area of the PS-C MN face is 0.6 cm^2 (**Chapter 3**, **Section 3.0**) which is substantially greater than the LIG electrode used in the previous study. It could have been expected that the yield of salicylate should have been greater, but the opposite is observed. A tentative explanation could be attributed to the composite nature of the underlying electrode with the PS-C MN compared to the inherently conductive LIG such that the hydrogen evolution at the MN interface resulting is a less significant pH change and hence slower hydrolysis. The extent to which the pH can be controlled at the MN is an area for further exploration and it could be anticipated that the inclusion of metallic particles (such as Pd) could enhance the HER reaction and improve yield (albeit through increased material cost).

7.3 Conclusions

The approach in the previous chapter employed the use of an ether link as a tether providing stability, only cleaving following an application of an oxidation potential. However, the drugs that could be applied to this system are limited as they require hydroxyl functionalities, and the synthesis would need include the individual drug conjugate as a precursor. In an attempt to combat this, the use of an ester bond tethered to commercially available drugs were explored in this chapter. Dicyclohexylcarbodiimide (DCC) in the presence of 4- N, N-dimethylaminopyridine (DMAP) is used to activate the carboxylic groups on the carbon substrate and following activation, the drug replaces the DCC and forms an ester bond more readily with the LIG. The controlled release of acetaminophen and salicylic acid is explored by the application of an oxidative potential that breaks the ester bond bound to the hydroxyl group of the therapeutics. This is an acceptable release mechanism for acetaminophen, however, the oxidation of salicylic acid poses an issue, as it is broken down into a range of products which are redundant. To combat this, the voltage is ramped negatively, in order to increase the pH local to the electrode surface thus hydrolysing the ester bond and subsequent release of the drug. The release of therapeutics is verified electrochemically and by UV-Visible spectrophotometry, and it was apparent that yield is a limiting factor for this mechanism. One approach explored was increasing the population of carboxylic groups on at the electrode surface by coating it with poly(anthranilic acid) by electropolymerizing anthranilic acid in sulfuric acid. The expectation was that the polymer coating would increase the yield however this was not the case and further investigations are required.

Chapter 8

Conclusions and Further Work

8.0 Conclusions

Adherence to prescribed medication has been a longstanding challenge for patients with chronic conditions like asthma, hypertension, and diabetes, those of which rarely exist in isolation. Proper adherence plays an important role in the clinical benefit of therapies and poor adherence is the primary reason for suboptimal clinical benefit. The issue of poor adherence is complex, as many patients that suffer with chronic conditions, suffer with numerous other aliments simultaneously – known as comorbidities – which also need to be managed. As a result, patients may have many treatment regimens to follow. The average geriatric patient takes 4 – 5 different medications a day, as well as the additional challenges elderly patients face, like diminishing cognitive and physical abilities like memory, hearing, vision, and movement. Thus, they can become more reliant on external assistance and are less able to manage their own treatment.

Numerous chronic conditions require injections to manage their illness, for example, patients with type 1 diabetes must inject insulin and cancer patients often receive therapy *via* intravenous lines. Subcutaneous and intravenous injections can provide rapid delivery of a wide range of drugs, but these are predominantly administered by a trained professional. Injections produce large volumes of sharps waste, and some patients are reluctant to adhere to injections due to fear and anxiety.

In this work, microneedles are exploited as a vehicle that would disrupt the stratum corneum that can be used in smart patch technology. The overarching aims can be summarised as improving electrochemical properties of carbon nanocomposite microneedle arrays and tethering model drugs to the surface of the conductive microneedles *via* ether and ester bonds, where an applied voltage can initiate the release of the bound drug. The vision is that this work will help lay the groundwork for transdermal automated drug delivery systems or smart wearable systems, where dose timing and frequency can be controlled, bettering adherence to complex regimens and anxiety surrounding administration. It could be anticipated that, through combining transdermal patches with smart wearable systems, autonomous drug

delivery can be achieved that can facilitate improvements in adherence and offering patient friendly option to manage their therapy. At the outset of the present investigation, it was hoped that the work would provide the groundwork for a smart patch system that exploits microneedle technology to control transdermal drug delivery *via* electrochemical stimulus.

Carbon based electrochemical sensors, especially screen-printed electrodes are common-place and widely available, for instance blood glucose sensors. More recently, carbon nanocomposite microneedles have been explored as well as laser induced graphene. In **Chapter 4**, alternative method to improve electrochemical properties of nanocomposite polystyrene-carbon (Ps-C) microneedles (MN) by way of electrochemical anodisation and laser ablation is explored. Wearable sensors have become a trending topic in relation to monitoring patients' health status, resulting in rapid innovation of point-of-care devices. This is especially prevalent within disease treatment, whereby a "closed loop" feedback system between sensing and therapy is bridged thus enhancing care management. The electrochemical properties of the polystyrene-carbon microneedles were assessed and the chemical modification by electrochemical anodisation explored and characterised and increased oxygen functionality was shown to greatly improve the electrode responses. Laser processing of the microneedle structures was investigated as an alternative. The key rationale was that ablation of the interfacial polymer would improve the electrochemical properties by exposing carbon within the polystyrene binder thereby enhancing the effective surface area. This was found to improve electrochemical performance with additional oxygen functional groups corroborated by energy dispersive X-ray analysis, however, when observed in electron micrographs, the structural integrity of the needles was compromised.

While it is possible to conclude that the laser modified MNs are redundant in isolation, the large surface area and increased oxygen species can be useful for a variety of sensing contexts or for controlled drug delivery. This led to the design of a multilayer MN patch where it was envisaged that skin penetration could be accomplished by a biocompatible (and dissolvable) MN layer allowing interstitial fluid to enter the second layer, thus come into contact

with the laser processed MN. Cellulose acetate phthalate (CAP) was chosen as the primary constituent of the sacrificial microneedle array. Electron micrographs confirm that upon submerging the layered microneedle array in alkaline buffer for a period of time, holes in the CAP layer provide access to the sensing layer beneath and cyclic voltammograms confirm that the electrochemical properties of the sensing layer are maintained.

There has been considerable interest in the development and characterisation of laser-induced graphene (LIG) as it provides a facile method of additive manufacture of highly conductive substrates, which, in contrast to screen printing systems, allows rapid prototyping of electrochemical sensors. This was explored in **Chapter 5** where LIG was harvested and added to cellulose acetate phthalate-carbon microneedles in order to improve their electrochemical performance. It was anticipated that this would allow its direct inclusion within the microneedle / moulding formulation process and thereby enable the single step manufacture of conductive microneedles with enhanced electrochemical properties rather than relying on post-production modifications. The use of CAP was also found to be advantageous from the perspective of biodegradability where it was postulated that MN could be used as a viable alternative to screen printed electrode/lancet applications. CAP was to exhibit a window of stability which would be suitable for single shot diagnostics, but which could readily degrade under environmental stress thereby offering a means of avoiding the waste associated with conventional point of care diagnostics (*i.e.*, glucose test strips and lancets) as well as syringe-based drug/vaccine delivery.

After assessing the capability of different formulation of microneedles for conductivity and sensing abilities, **Chapter 6** explored their use as substrates for solid state drug release. A series of naphthoquinone-aminophenol derivatives were used on the basis that their conjugation with a suitable drug candidate could provide a means through which the latter could be released upon the imposition of an appropriate oxidation potential. The novel strategy offers a high level of control over the release process due to the application of a tailored potential but the range of drugs that could be applied to this system were found to be limited

as they require hydroxyl functionalities. The strategy was also complex in that it required custom synthesis of the redox tether-drug conjugate. In an attempt to combat this, **Chapter 7** focused on the application of an ester link which would be bound to a drug candidate and broken upon the application of a potential. The use of an ester link is much more simplistic and widens the range of drugs that can be delivered as they only need to possess a hydroxyl group. Improvement to drug yield were also considered with the use of poly(anthranilic acid) as the surface modifier which would increase the population of carboxylic acid sites through which a drug could be bound.

8.1 Further Work

The aim of this project was to investigate and develop novel methods of transdermal drug delivery that could be employed into the design of a “smart patch”, that would allow the controlled release or dosing of therapeutics. The focus of the research targeted microneedle structures and sought to explore new concepts in their design and formulation, as well as new drug release mechanisms. The core approach centred on electrical/electrochemical transduction as the release mechanism and the challenge lay in developing new materials that were consistent with microneedle fabrication, but which could enable the controlled delivery.

The core remit of the research programme was to provide proof of principle for the development of a microneedle system that could ultimately serve as a means of electrochemically releasing a drug. Two strategies have been critically appraised, and the ester linkage is clearly the more favourable. Much more work would need to be done in terms of assessing the release kinetics and ensuring that the drugs released are unaffected by the release mechanism. The hydrolysis of the ester link once within the skin also creates an issue where extracellular components may inadvertently increase the rate at which the tether is broken. It could be envisaged however that the dual MN layer explored in **Chapter 4** may be of benefit here – acting as a protective barrier as well as a reservoir for ester linked drugs. The

ether link is certainly the more stable but procedurally difficult and it is unlikely pharmaceutical companies would adopt this route unless the efficacy of the system had clinical outcomes that were significantly greater than conventional approaches.

The poly(anthranilic acid) system has only been briefly assessed yet this would be a pathway for further exploration – especially as MN offer a very limited yield. The combination of the ester tethering with PAA could yet counter many of the limitations that presently beset MN delivery whilst offering a greater degree of control. Again, more detailed studies would be required in terms of drug release profiles.

Ultimately, it could be anticipated that, through combining transdermal patches with smart wearable systems, autonomous drug delivery can be achieved that can facilitate improvements in adherence and offering patient friendly option to manage their therapy. In **Chapter 1**, **Figure 1.0.2** shows a conceptual illustration of how microneedles could ultimately be incorporated into a wearable system to control transdermal drug delivery. As yet, this remains a concept but it is clear that advances in wearable technology continue apace.

References

1. **World Health Organisation (WHO).** WHO Library Cataloguing-in-Publication Data. *https://www.who.int/chp/knowledge/publications/.* [Online] Jan 2003. [Cited: 27 Dec 2021.] https://www.who.int/chp/knowledge/publications/adherence_full_report.pdf.

2. *Measuring medication adherence: Are missed doses reported more accurately than perfect adherence?* **Wagner, G.J. and Rabkin, J.G.** 4, 2000, Psychological and Socio-medical Aspects of AIDS/HIV, Vol. 12, pp. 405-408.

3. *Social determinants of health associated with epilepsy treatment adherence in the United States: A scoping review.* **Gaudecker, Jane R. von, et al.** November, 2021, Epilepsy & Behavior, Vol. 124.

4. *Factors influencing poor medication adherence amongst patients with chronic disease in low-and-middle-income countries: A systematic scoping review.* **Chauke, Gloria Dunisani, et al.** 6, 2022, Heliyon, Vol. 8.

5. *Use of the transtheoretical model in medication adherence: A systematic review.* **Imeri, Hyllore, et al.** 5, 2022, Research in Social and Administrative Pharmacy, Vol. 18, pp. 2778-2785.

6. *Managing acute illness.* **Jones, Roger, et al.** s.l. : The King's Fund, 2012.

7. *Defining chronic diseases and health conditions in childhood (0–18 years of age): national consensus in the Netherlands.* **Mokkink, Lidwine B, et al.** 2008, European Journal of Pediatrics, Vol. 167, pp. 1441-1447.

8. *Evaluation of infectious and non-infectious complications in patients with primary immunodeficiency.* **Bazregari, Saeed, et al.** 4, 2017, Central European Journal of Immunology, Vol. 42, pp. 336-341.

9. *Use Your Words Carefully: What Is a Chronic Disease?* **Bernell, Stephanie and Howard, Steven W.** 159, 2016, Front Public Health, Vol. 4.

10. *Asthma.* **Papi, Alberto, et al.** 10122, 2017, The Lancet, Vol. 391, pp. 783-800.

11. *Hypertension as a chronic disease: What can be done at a regional level?* **Cardiol, Can J.** 6, 2008, The Canadian Journal of Cardiology, Vol. 24, pp. 483-484.

12. *Association between copayment, medication adherence and outcomes in the management of patients with diabetes and heart failure.* **Gourzoulidis, George, et al.** 4, 2017, Health Policy, Vol. 121, pp. 363-377.

13. *Impact of community pharmacists in COPD management: Inhalation technique and medication adherence.* **Hesso, Iman, Gebara, Shereen Nabhani and Kayyali, Reem.** September, 2016, Respiratory Medicine, Vol. 118, pp. 22-30.

14. *The end of AIDS: HIV infection as a chronic disease.* **Deeks, Steven G, Lewin, Sharon R and Havlir, Diane V.** 9903, 2013, The Lancet, Vol. 382, pp. 1525-33.

15. *Comorbidity indexes: review of the literature and application to studies of elderly population.* **Harboun, M and Ankri, J.** 3, 2001, Revue D'epidemiologie et de Sante Publique, Vol. 49, pp. 287-98.

16. *Polypharmacy: A Global Risk Factor for Elderly People.* **Dagli, Rushabh J and Sharma, Akanksha.** 6, 2014, Journal of International Oral Health, Vol. 6.

17. *A scoping review on medication adherence in older patients with cognitive impairment or dementia.* **Hudani, Zain K. and Rojas-Fernandez, Carlos H.** 6, 2016, Research in Social and Administrative Pharmacy, Vol. 12, pp. 815-829.

18. *To adhere or not to adhere: Rates and reasons of medication adherence in hematological cancer patients.* **Hall, Alix E., et al.** January, 2016, Critical Reviews in Oncology/Hematology, Vol. 97, pp. 247-62.

19. *A study of medication compliance in geriatric patients with chronic illness.* **Punnapurath, Savithri, et al.** 4, 2021, Journal of Family Medicine and Primary Care, Vol. 10, pp. 1644-1648.

20. *Dissolving and biodegradable microneedle technologies for transdermal sustained delivery of drug and vaccine.* **Hong, Xiaoyun, et al.** 2013, Drug Design, Development and Therapy, Vol. 7, pp. 945-952.

21. *American Nurses Association Independent Study Module, Needlestick Safety and Prevention.* **Foley, M and Leyden, A. T.** 2003, pp. 1-33.

22. *Hollow polymer microneedles array resistance and insertion tests.* **Lhernould, Marion Sausse, Deleers, Michel and Delchambre, Alain.** 2015, International Journal of Pharmaceutics, Vol. 480, pp. 8-15.

23. *Cutaneous immunization: an evolving paradigm in influenza vaccines.* **Gill, Harvinder S, et al.** 4, 2014, Vol. 11, pp. 615-627.

24. *Needle-free vaccine delivery.* **Giudice, Erin and Campbell, James D.** 1, 2006, Advance Drug Delivery, Vol. 58, pp. 68-89.

25. *Children With Diabetes: The Impact of Fear of Needles 1 Case Study.* **Rzeszut, Jennifer.** s.l. : Elsevier Inc., 2011, Journal of Pediatric Nursing, Vol. 21, pp. 589-592.

26. *A patchless dissolving microneedle delivery system enabling rapid and efficient transdermal drug delivery.* **Lahiji, Shayan F., Dangol, Manita and Jung, Hyungil.** 2015, Scientific Reports, pp. 1-7.

27. *Minimally Invasive Protein Delivery with Rapidly Dissolving Polymer Microneedles.* **Sullivan, S.P, Murthy, Niren and Prausnitz, Mark R.** 5, 2008, Advanced Materials, Vol. 20, pp. 933-938.

28. *Loss of orally administered drugs in GI tract.* **Gavhane, Yogeshkumar Nanasaheb and Yadav, Adhikrao Vyankatrao.** 4, 2012, Saudi Pharmaceutical Journal, Vol. 20, pp. 331-344.

29. *Microneedles: An emerging transdermal drug delivery system.* **Bariya, Shital H., et al.** 1, 2012, Journal of Pharmacy and Pharmacology, Vol. 64, pp. 11-29.

30. *In Vitro and In Vivo Characterization of MEMS Microneedles.* **Teo, MAL, et al.** 1, 2005, Biomedical Microdevices, Vol. 7, pp. 47-52.

31. *Enhancement of transdermal drug delivery via synergistic action of chemicals.* **Karande, Pankaj and Mitragotri, Samir.** 11, 2009, Biomembranes, Vol. 1788, pp. 2362-2373.

32. *Cost-effective Fabrication of Chitosan Microneedles for Transdermal Drug Delivery.* **Sadeqi, A., et al.** 2018, 40th Annual International Conference of the IEEE Engineering in Medicine and Biology Society, pp. 5737-5740.

33. *Trends in drug- and vaccine-based dissolvable microneedle materials and methods of fabrication.* **Moore, Lyndsey E., Vucen, Sonja and Moore, Anne C.** 2022, Biopharmaceutics, Vol. 173, pp. 54-72.

34. *Penetration-Enhanced Ultrasharp Microneedles and Prediction on Skin Interaction for Efficient Transdermal Drug Delivery.* **Roxhed, Niclas, et al.** 6, 2007, Journal of Microeletromechanical Systems, Vol. 16, pp. 1429-1440.

35. *Swellable microneedles based transdermal drug delivery: Mathematical model development and numerical experiments.* **Yadav, Prateek Ranjan, et al.** January, 2022, Chemical Engineering Science, Vol. 247.

36. *Solid Microneedles for Transdermal Delivery of Amantadine Hydrochloride and Pramipexole Dihydrochloride.* **Hoang, Mylien T., Ita, Kevin B and Bair, Daniel A.** 4, 2015, Microneedle Patches: Developing Strategies for Delivery, Vol. 7, pp. 379-396.

37. *Microneedles in Drug Delivery: Progress and Challenges.* **Avcii, Muhammet and Celik, Ayhan.** 11, 2021, Micromachines, Vol. 12.

38. *Microneedle patches for vaccine delivery.* **Suh, Hyemee, Shin, Juhyung and Kim, Yeu-Chun.** 1, 2013, Clinical and Experimental Vaccine Research, Vol. 3.

39. *Polymeric Microneedle Arrays: Versatile Tools for an Innovative Approach to Drug Administration.* **Dardano, Principia, et al.** 8, 2019, Advanced Therapeutics, Vol. 2.

40. *Swellable silk fibroin microneedles for transdermal drug delivery.* **Yin, Zhuping, et al.** 2018, International Journal of Biological Macromolecules, Vol. 106, pp. 48-56.

41. *"Smart" materials-based near-infrared light-responsive drug delivery systems for cancer treatment: A review.* **Raza, Ali, et al.** 1, 2019, Journal of Materials Research and Technology, Vol. 8, pp. 1497-1509.

42. *Thermo-responsive polymers: Applications of smart materials in drug delivery and tissue engineering.* **Sponchioni, Mattia, Palmiero, Umberto Capasso and Moscatelli, Davide.** 2019, Materials Science and Engineering: C, Vol. 102, pp. 589-605.

43. *Battery-Free and Wireless Smart Wound Dressing for Wound Infection Monitoring and Electrically Controlled On-Demand Drug Delivery.* **Xu, Gang, et al.** 26, 2021, Advanced Functional Materials, Vol. 31.

44. *Smart wearable systems: Current status and future challenges.* **Chan, Marie, et al.** 3, s.l. : Elsevier, 2012, Artificial Intelligence in Medicine, Vol. 56, pp. 137-156.

45. *Electronic drug delivery systems: An overview.* **Vadlapatla, Rajesh, Wong, Eva Y. and Gayakwad, Sanjaykumar G.** 2017, s.l. : Elsevier, 2017, Journal of Drug Delivery Science and Technology, Vol. 41, pp. 359-366.

46. *All disease begins in the gut: Influence of gastrointestinal disorders and surgery on oral preformance.* **Hatton, Grace, et al.** 1, 2018, International Journal of Pharmaceutics, Vol. 548, pp. 408-422.

47. *Advances in Oral Drug Delivery.* **Alqahtani, Mohammed, Kazi, Mohsin and Mohammad, A.** 2021, Frontiers in Pharmacology, Vol. 12.

48. *Challenges and Recent Progress in Oral Drug Delivery Systems for Biopharmaceuticals.* **Homayun, Bahman, Lin, Xueting and Choi, Hyo-Jick.** 2, 2019, Pharmaceuticals, Vol. 11.

49. *Impact of gastrointestinal tract variability on oral drug absorption and pharmacokinetics: An UNGAP review.* **Vinarov, Zahari, et al.** 2021, European Journal of Pharmaceutical Sciences, Vol. 162.

50. *Intestinal Lymph Flow, and Lipid and Drug Transport Scale Allometrically From Pre-clinical Species to Humans.* **Trevaskis, N.L, et al.** 458, 2015, Front Physiol, Vol. 11.

51. *Multidimensional analysis of human intestinal fluid composition.* **Pyper, K, et al.** 2020, Eur J Pharm Biopharm, Vol. 153, pp. 226-240.

52. *Meal Effects Confound Attempts to Counteract Rabeprazole-Induced Hypochlorhydria Decreases in Atazanavir Absorption.* **Faber, K.P, et al.** 2017, Pharm Res, Vol. 34, pp. 619-628.

53. *Efficacy and Pharmokinetics of Glecaprevir and Pibrentasvir with Concurrent Use of Acid-Reducing Agents in Patients With Chronic HCV Infection.* **Flamm, S, et al.** 2019, Clin. Gastroenterol. Hepatol., Vol. 17, pp. 527-535.

54. *Navigating the human gastrointestinal tract for oral drug delivery: Unchartered waters and new frontiers.* **Koziolek, M, et al.** 2016, Adv drug Deliv rev, Vol. 101, pp. 75-88.

55. *Role of Physiological Intestinal Water in Oral Absorption.* **Sutton, S.C.** 2, 2009, The AAPS Journal, Vol. 11, pp. 277-285.

56. *Mechanistic Fluid Transport Model to Estimate Gastrointestinal Fluid Volume and Its dynamic change over time.* **Yu, A, et al.** 2017, The AAPS Journal, Vol. 19, pp. 1682-1690.

57. *Current challenges and future persepectives in oral absorption research: An opinion of the UNCAP network.* **Vinarov, Zahari, et al.** 2021, Advanced Drug Delivery Reviews, Vol. 171, pp. 289-331.

58. *Impact of gastrointestinal physiology on drug absorption in special populations - an UNGAP review.* **Stillhart, C, et al.** 2020, Eur. J. Pharm. Sci., Vol. 147.

59. *Impact of gastrointestinal disease states on orla drug absorption - implications for formulation design - a PEARRL review.* **Effinger, A.** 2019, J. Pharm. Pharmacol., Vol. 71, pp. 674-698.

60. *Diabetes-induced mechanophysiological changes in the small intestine and colon.* **Zhao, M., Liao, D and Zhao, J.** 2017, World J. Diabet., Vol. 8, pp. 249-269.

61. *Effect of diabetes mellitus on pharmacokinetic and pharmodynamic properties of drugs.* **Dostalek, M., Akhlaghi, F and Puzanovova, M.** 2012, Clin. Pharmacokinet., Vol. 51, pp. 481-499.

62. *Physiologically based and population PK modeling in optimizing drug development: a predict-learn-confirm analysis.* **Suri, A., et al.** 3, 2015, Clin. Pharmacol. Ther., Vol. 98, pp. 336-344.

63. *Physiologically-based pharmacokinetic modeks fir children: stsarting to reach maturation?* **Verscheijden, L.F.M, et al.** 2020, Pharmacol. Ther., Vol. 211.

64. *Magnetic resonance imagine quantification of gastrointestinal liquid volumns and distribution in the gastronintestinal tract of children.* **Papadatou-Soulou, E., et al.** 9, 2019, Mol. Pharm., Vol. 16, pp. 3896-3903.

65. *Impact of regional differences along the gastrointestinal tract of healthy adults on oral drug absorption: An UNGAP Review.* **Vertzoni, M, et al.** 2019, Eur J Pharm, Vol. 134, pp. 153-175.

66. *Adverse drug reactions due to drug-drug interactions with proton pump inhibitors: assessment of systematic reviews with AMSTAR method.* **Yucel, E, et al.** 2016, Expert Opin. Drug Saf., Vol. 15, pp. 223-236.

67. *Effects of meal and incretins in the regulation of splanchnic blood flow.* **Koffert, J, et al.** 2017, Endocrine connections, Vol. 6, pp. 179-187.

68. *Drug absorption VII: Influcence of mesenteric blood flow on intestinal drug absorption in dogs.* **Crouthamel, W.G., et al.** 1975, J. Pharm. Sci., Vol. 64, pp. 664-671.

69. *Excipient Variability and Its Impact on Dosage Form Functionality.* **Dave, V.S, et al.** 3, 2015, J. Pharm. Sci., Vol. 104, pp. 906-915.

70. *Potential for Pharmaceutical Excipients to Impact Absorption: a Mechanistic Review for Bcs Class 1 and 3 Drugs.* **Flanagan, T.** 2019, Eur. J Pharm. Biopharm., Vol. 141, pp. 130-138.

71. *Potential pharmacokinetic interaction between orally administered drug and osmotically active excipients in pediatric polypharmacy.* **Matsui, Kazuki, et al.** 2021, European Journal of Pharmaceutical Sciences, Vol. 165.

72. *Digoxin-inactivating bacteria: identification in human gut flora.* **Saha, JR, et al.** 325, 1983, Science, Vol. 220, pp. 325-7.

73. *Reflection Paper on the Pharmaceutical Development of Medicines for Use in the Older Population.* **European Medicines Agency.** 2020.

74. *Under-represenation of elderly in clinical trials: an analysis of the initial approval documents in the Food and Drug Administration database.* **Ruiter, R., Burggraaf, Jacobus and Rissmann, R.** 2019, J. Chin. Pharmacol., Vol. 85, pp. 838-844.

75. *Swallowing Disorders - european Union Geriatric Medicine Society white paper: oropharyngeal dysphagia as geriatric syndrome.* **Baijens, L.W, et al.** s.l. : 11, 2016, Clin. Interv. Aging, pp. 1403-1428.

76. *Dysphagia: prevalence, management and the community nurse.* **Smithard, D.G.** 2015, Commun. Pract., Vol. 88, pp. 32-35.

77. *First-Pass Elimination Basic Concepts and Clinical Consequences.* **Pond, S.M and Tozer, T.N.** 1, 1984, Clinical Pharmacokinetics, Vol. 9, pp. 1-25.

78. *First-Pass Effect: Significance of the Intestine for Absorption and Metabolism.* **Doherty, Margaret and Pang, K.S.** 4, 1997, Drug and Chemical Toxicology, Vol. 20, pp. 329-44.

79. **Cross, Matthew E. and Plunkett, Emma V. E.** First-pass metabolism and bioavailability. [book auth.] Matthew E. Cross. *Physics, Pharmacology and Physiology for Anaesthetists.* Birmingham : Cambridge University Press, 2014, pp. 179-180.

80. *Enzyme-catalyzed processes of first-pass hepatic and intestinal drug extraction.* **Shen, DD, Kunze, KL and Thummel, KE.** 1997, Advanced Drug Delivery Reviews, Vol. 27, pp. 99-127.

81. *Challenges for the oral delivery of macromolecules.* **Goldberg, M. and Gomez-Orellana, I.** 2003, Nat. Rev. Drug Discov., Vol. 2, pp. 289-295.

82. *Physical methods for enhancing drug absorption from the gastrointestinal tract.* **Luo, Zhi, Paunovic, Nevena and Leroux, Jean-Christophe.** 2021, Advanced Drug Delivery, Vol. 175.

83. **Khonsary, SA.** *Guyton and Hall: Textbook of Medical Physiology.* Los Angeles : Surgical Neurology International, 2017.

84. **NICE.** British National Formulary (BNF). *National Institute for Health and Care Excellence.* [Online] 2022. https://bnf.nice.org.uk/drug/.

85. *Far from "just a poke": Common painful needle procedures and the development of needle fear.* **McMurtry, M, et al.** 10, 2015, Clinical Journal of Pain, Vol. 31, pp. 3-11.

86. *The number of injected same-day preschool vaccines relates to preadolescent needle fear and HPV uptake.* **Baxter, Amy, et al.** 33, 2017, Vaccine, Vol. 35, pp. 4213-4219.

87. *Survey of the prevalence of immunization non-compliance due to needle fears in children and adults.* **Taddio, Anna, et al.** 32, 2012, Vaccine, Vol. 30, pp. 4807-12.

88. *Patient errors in use of injectable antidiabetic medications: A need for improved clinic-based education.* **Wei, Erin, et al.** 5, 2020, Journal of the American Pharmacists Association, Vol. 60.

89. *Worldwide Injection Technique Questionnaire Study: Population Parameters and Injection Practices.* **Frid, Anders, et al.** 9, 2016, Mayo Clinic Proceedings, Vol. 91, pp. 1212-23.

90. *26519 Patient safety alert: Preventing infection from misuse of medication vials.* **Taylor, James S, Patel, Jay and Otto, Elizabeth.** 3, 2021, Journal of the American Academy of Dermatology, Vol. 85.

91. *Evolution of the Global Use of Unsafe Medical Injections, 2000-2010.* **Pepin, J, et al.** 8, 2013, PLoS One, Vol. 7.

92. *Skin permeabilization for transdermal drug delivery: recent advances and future prospects.* **Schoellhammer, CM, Blankschtein, D and Langer, R.** 3, 2014, Expert Opin Drug Delivery, Vol. 11, pp. 393-407.

93. *A review of measures used to examine medication adherence in people with ADHD at initiation, implementation and discontinuation of pharmacotherapy.* **Khan, Muhammad Umair and Aslani, Parisa.** 3, 2020, Research in Social and Administrative Pharmacy, Vol. 16, pp. 277-289.

94. *Recommendations for the assessment and optimization of adherence to disease-modifying drugs in chronic inflammatory rheumatic diseases: A process based on literature reviews and expert consensus.* **Gossec, L, et al.** 1, 2019, Joint Bone Spine, Vol. 86, pp. 13-19.

95. *Inhaled corticosteroid-phobia and childhood asthma: Current understanding and management implications.* **Hui, Rex Wan Hin.** 2020, Paediatric Respiratory Reviews, Vol. 33, pp. 62-66.

96. *Medication adherence for secondary stroke prevention and its barriers among lebanese survivors: A cross-sectional study.* **Saade, S, et al.** August 2020, 2021, Clinical Epidemiology and Global Health, Vol. 9, pp. 338-346.

97. *Compliance to topical anti-glaucoma medications among patients at a tertiary hospital in North India.* **Rajurkar, K, et al.** 2, 2018, Journal of Current Ophthalmology, Vol. 30, pp. 125-129.

98. *Does the Formulation of Oral Solid Dosage Forms Affect Acceptance and Adherence in Older Patients? A Mixed Methods Systematic Review.* **Shariff, ZB, et al.** 2020, Journal of the American Medical Directors Association, Vol. 8, pp. 1015-1023.

99. *Battery-free implantable insulin micropump operating at transcutaneously radio frequency-transmittable power.* **Yan, B, et al.** 5-6, 2019, Med. Dev. Sensors, Vol. 2.

100. *Bioactive hydrogel-based scaffolds for the regeneration of dental pulp tissue.* **Samiei, M, et al.** 2021, J. Drug Deliv. Sci. Technol., Vol. 64.

101. *The newest generation of drug-eluting stents and beyond.* **Lee, D.H. and de la Torre Hernadez, J.M.** 1, 2018, Eur. Cardiol., Vol. 13, pp. 54-59.

102. *Biodegradable wafers releasing Temozolomide and Carmustine for the treatment of brain cancer.* **Shapira-Furman, T., et al.** 2019, Journal of Controlled Release, Vol. 295, pp. 93-101.

103. *Wearable and implantable devices for drug delivery: Applications and challenges.* **Kar, A, et al.** January, 2022, Biomaterials, Vol. 283.

104. *On the mechanisms of biocompatibilty.* **Williams, D.F.** 20, 2008, Biomaterials, Vol. 29, pp. 2941-2953.

105. *Electrospinning: applications in drug delivery and tissue engineering.* **Sill, T.J and von Recum, H.A.** 13, 2008, Biomaterials, Vol. 29, pp. 1989-2006.

106. *Recent development of polymer nanofibres for biomedical and biotechnological applications.* **Zhang, Y.** 2005, J. Mater. Sci. Mater. Med., Vol. 16, pp. 933-946.

107. *Diclofenac sustained release from sterilised solf contact lens materials using optimised layer-by-layer coating.* **Silva, D., et al.** 2020, Int. J. Pharm., Vol. 585.

108. *Advanced materials and processing for drug delivery: the past and the future.* **Zhang, Y., Chan, H.F and Leong, K.W.** 1, 2013, Adv. Drug Deliv. Rev., Vol. 65, pp. 104-120.

109. *Dual-responsive drug delivery systems prepared by blend electrospinning.* **Li, H., et al.** 1-2, 2018, Int. J. Pharm., Vol. 543, pp. 1-7.

110. *Nerve growth factor (NGF)-conjugated electrospun nanostructures with topographical cues for neuronal differentiation of mesenchymal stem cells.* **Cho, Young Il, et al.** 12, 2010, Acta Biomaterialia, Vol. 6, pp. 4725-4733.

111. *Coaxial electrospun fibres: applications in drug delivery and tissue engineering.* **Lu, Y., et al.** 2016, Wiley Interdisiplinary Reviews: Nanomedicine and Nanobiotechnology, Vol. 8, pp. 654-677.

112. *Regenerative medicine and drug delivery: Progress via electrospun biomaterials.* **Doostmohammadi, M, Forootanfar, H and Ramakrishna, S.** April 2019, 2020, Materials Science and Engineering C, Vol. 109.

113. *Development of novel chitosan based ketorolac implant controlled release.* **Rahman, SAU, et al.** 13, 2018, Biomedical Research, Vol. 29, pp. 2735-2739.

114. *Leveraging advances in chemistry to design biodegradable polymeric implants using chitosan and other biomaterials.* **Sharma, Bhasha, Sharma, Shreya and Jain, Purnima.** 2021, International Journal of Biological Macromolecules, Vol. 169, pp. 414-427.

115. *PLGA porous scaffolds by polydopamine-assisted immobilisation of NGF for spinal cord injury repair.* **Pan, Su, et al.** 4, 2019, Materials Research Express, Vol. 6.

116. *Smart stimuli-responsive implantable drug delivery systems for programmed and on-demand cancer treatment: An overview on the emerging materials.* **Mazidi, Zahra, et al.** P1, 2022, Chemical Engineering Journal, Vol. 433.

117. *Ultrasound propulsion of micro-/nanomotors.* **Xu, T., Xu, LP and Zhang, X.** 2017, Applied Mater. Today, Vol. 9, pp. 493-503.

118. *Electroconductive smart polyacrylamide-polypyrrole (PAC-PPY) hydrogel: a device for controlled release of risperidone.* **Saha, S., et al.** 35, 2015, RSC Adv., Vol. 5, pp. 27665-27673.

119. *Smart magnetocaloric coating for implants: Controlled drug release for targeted delivery.* **Komlev, A.S, Gimaev, R.R and Zverev, V.I.** 2021, Physics Open, Vol. 7.

120. *Advanced Near-Infrared Light Responsive Nanomaterials as Therapeutic Platforms for Cancer Therapy.* **Chien, Y.H, et al.** 3, 2019, Advanced Therapeutics, Vol. 2.

121. *Recent Advances of D-α-tocopherol Polyethylene Glycol 1000 Succinate Based Stimuli-responsive Nanomedicine for Cancer Treatment.* **Guan, Y., et al.** 2, 2020, Current medical science, Vol. 40, pp. 218-231.

122. *Hierarchical structured and programmed vehicles deliver drugs locally to inflamed sites of intestine.* **Li, W, et al.** 2018, Biomaterials, Vol. 185, pp. 322-332.

123. *Redox-Responsive Nanogel with Intracellular Reconstruction and Programmable Drug Release for Targeted Tumor Therapy.* **Tian, Y.u, et al.** 8, 2019, Macromol. Rapid Commun., Vol. 40.

124. *Smart drug delivery of p-Coumaric acid loaded aptamer conjugated starch nanoparticles for effective triple-negative breast cancer therapy.* **Mariadoss, A.V.A, et al.** December 2021, 2022, International Journal of Biological Macromolecules, Vol. 195, pp. 22-29.

125. *Preparation and optimization of biodegradable star-block copolymer micelles for temperature-triggered drug release.* **Li, J, et al.** 2014, Materials Letters, Vol. 131, pp. 5-8.

126. **Deb, P.K, et al.** Chapter 6 - Pharmaceutical and Biomedical Applications of Polymers. *Basic Fundamentals of Drug Delivery.* s.l. : Academic Press, 2019, pp. 203-267.

127. *Molecular dynamics simulation study of curcumin interaction with nano-micelle of PNIPAAm-b-PEG co-polymer as a smart efficient drug delivery system.* **Rezaeisadat, M, Bordbar, A.K and Omidyan, R.** 2021, Journal of Molecular Liquids, Vol. 332.

128. *Polymeric hydrogel Nanocapsules: a Thermo and pH dual-responsive carrier for sustained drug release.* **Nan, J, et al.** 2014, Nano-Micro Lett., Vol. 6, pp. 200-208.

129. *Thermo/redox/pH-triple sensitive poly(N-isopropylacrylamide-co-acrylic acid) nanogels for anticancer drug delivery.* **Zhan, Y, et al.** 20, 2015, Journal of Materials Chemistry B.

130. *Poly(N-isopropylacrylamide) derived nanogels demonstrated thermosensitive self-assembly and GSH-triggered drug release for efficient tumor Therapy.* **Chen, J, et al.** 29, 2019, Polymer Chemistry.

131. *Curcumin-loaded biocompatible thermoresponsive polymeric nanoparticles for cancer drug delivery.* **Sanoj Rejinold, N, et al.** 1, 2011, Journal of Colloid and Interface Science, Vol. 360, pp. 39-51.

132. *Tumor targeted delivery of umbelliferone via a smart mesoporous silica nanoparticles controlled-release drug delivery system for increased anticancer efficiency.* **Kundu, M, et al.** June, 2020, Materials Science and Engineering C, Vol. 116.

133. *Micelle directed chemical polymerization of polypyrrole particles for the electrically triggered release of dexamethasone base and dexamethasone phosphate.* **Uppalapati, D, et al.** 1-2, 2018, International Journal of Pharmaceutics, Vol. 543, pp. 38-45.

134. *Graphene oxide@gold nanorods for chemo-photothermal treatment and controlled release of doxorubicin in mice Tumor.* **Khan, M. S, et al.** 2017, Colloids and Surfaces B: Biointerfaces, Vol. 160, pp. 543-552.

135. *Transport of particles by magnetic forces and cellular blood flow in a model microvessel.* **Freund, J.B and Shapiro, B.** 2012, Physics of Fluids, Vol. 24.

136. *Development of a Two-Way Coupled Eulerian–Lagrangian Computational Magnetic Nanoparticle Targeting Model for Pulsatile Flow in a Patient-Specific Diseased Left Carotid Bifurcation Artery.* **Hewlin, Rodward L., Ciero, Ashley and Kizito, John P.** 2, 2019, Cardiovascular Engineering and Technology, Vol. 10, pp. 299-313.

137. *Shear-Activated Nanotherapeutics for Drug Targeting to Obstructed Blood Vessels.* **Korin, N, et al.** 2012, Science, Vol. 337, pp. 738-42.

138. *Flow topology and targeted drug delivery in cardiovascular disease.* **Meschi, Sara S., Farghadan, Ali and Arzani, Amirhossein.** 2021, Journal of Biomechanics, Vol. 119.

139. *Recent advances in transdermal drug delivery.* **Subedi, RK, et al.** 3, 2012, Arch Pharm Res, Vol. 33, pp. 339-351.

140. *Transdermal drug delivery.* **Prausnitz, MR and Langer, R.** 2008, Nat Biotechnol, Vol. 26, pp. 1261-1268.

141. *Nanotechnology and the transdermal route: A state of the art review and critical appraisal.* **Cevc, G and Vierl, U.** 3, 2010, Journal of Controlled Release, Vol. 141, pp. 277-299.

142. *Transdermal drug delivery: Innovative pharmaceutical developments based on disruption of the barrier properties of the stratum corneum.* **Alkilani, AZ, McCrudden, MTC and Donnelly, RF.** 4, 2015, Pharmaceutics, Vol. 7, pp. 438-70.

143. *Device-assisted transdermal drug delivery.* **Lee, H, et al.** 127, 2018, Advanced Drug Delivery Reviews, Vol. 1, pp. 35-45.

144. *The optimal choice of medication administration route regarding intravenous, intramuscular, and subcutaneous injection.* **Jin, J.-f., et al.** 9, 2015, Patient Prefer. Adherence, Vol. 2, pp. 923-42.

145. *Impact of transdermal drug delivery on treatment adherence in patients with Alzheimer's disease.* **Molinuevo, J.L. and Arranz, F.J.** 1, 2014, Expert Review of Neurotherapeutics, Vol. 12, pp. 1-7.

146. *Challenges and innovations of drug delivery in older age.* **Khan, Muhammad Suleman and Roberts, Michael S.** 2018, Advanced Drug Delivery Reviews, Vol. 135, pp. 3-38.

147. *Surgical anatomy of the skin.* **Mohamed, Sarah and Hargest, Rachel.** 1, 2021, Surgery (Oxford), Vol. 40, pp. 1-7.

148. *State of the art in Stratum Corneum research: The biophysical properties of ceramides.* **Schmitt, Thomas and Neubert, Reinhard H. H.** 2018, Chemistry and Physics of Lipids, Vol. 216, pp. 91-103.

149. **U.S Department of Health and Human Services.** U.S National Library of Medicine. *ClinicalTrials.gov.* [Online] 2023. [Cited: 06 February 2023.] https://clinicaltrials.gov/ .

150. **Allen, D.** *Transdermal Delivery Market Predicted to Reach $31.5 Billion by 2015: PharmaLive Special Report.* s.l. : Pharmaceutical & Medical Packaging News, 2011.

151. *A Review: Different Generation Approaches of Transdermal drug delivery systems.* **Bhatt, DC and Mohd, Aqil.** 2010, J Chem Pharm, Vol. 2, pp. 184-193.

152. *Enhanced skin permeation of sex hormones with novel topical spray vehicles.* **Morgan, TM, Reed, BL and Finnin, BC.** 10, 1998, J Pharm Sci, Vol. 87, pp. 1213-1218.

153. *Heat: A Highly Efficient Skin Enhancer for Transdermal Drug Delivery.* **Szunerits, S and Boukherroub, R.** 2018, Nanobiotechnology, Vol. 6.

154. *Review of Microneedle based Transdermal Drug Delivery Systems.* **Parhi, Rabinarayan and Supriya N, Divya.** 3, 2019, International Journal of Pharmaceutical Sciences and Nanotechnology, Vol. 12.

155. *Overview of recent advancements in the iontophoretic drug delivery to various tissues and organs.* **Helmy, Abdelrahman.** 2021, Journal of Drug Delivery Science and Technology, Vol. 61.

156. *Transdermal delivery of potassium chloride with solid microneedles.* **Abiandu, Ifeoma and Ita, Kevin B.** 2019, Journal of Drug Delivery Science and Technology, Vol. 53.

157. *Iontophoresis-mediated direct delivery of nucleic acid therapeutics, without use of carriers, to internal organs via non-blood circulatory pathways.* **Hasan, M, et al.** January, 2022, Journal of Controlled Release, Vol. 343, pp. 392-399.

158. *Transdermal drug delivery: Overcoming the skin's barrier function.* **Naik, Aarti, Kalia, YN and Guy, RH.** 9, 2000, Pharmaceutical Science and Technology Today, Vol. 3, pp. 318-326.

159. *Combination of lipid nanoparticles and iontophoresis for enhanced lopinavir skin permeation: Impact of electric current on lipid dynamics.* **Moura, R.B.P, et al.** May, 2022, European Journal of Pharmaceutical Sciences, Vol. 168.

160. *Potential of iontophoresis as a drug delivery method for midazolam in pediatrics.* **Djabri, Asma, Guy, Richard H and Delgado-Charo, M Begona.** 128, 2019, European Journal of Pharmaceutical Sciences, Vol. 1, pp. 137-143.

161. *Iontophoretic skin delivery systems: Success and failures.* **Bakshi, P, et al.** 586, 2020, International Journal of Pharmaceutics, Vol. 30.

162. *The effect of non-invasive dermal electroporation on skin barrier function and skin permeation in combination with different dermal formulations.* **Kis, Nikolett, et al.** 2022, Journal of Drug Delivery Science and Technology, Vol. 69.

163. *Electroporation-enhanced transdermal drug delivery: Effects of logP, pKa, solubility and penetration time.* **Chen, Xiao, et al.** 151, 2020, European Journal of Pharmaceutical Sciences, Vol. 1.

164. *Development of voltage gated transdermal drug delivery platform to impose synergistic enhancement in skin permeation using electroporation and gold nanoparticle.* **Anirudhan, T. S. and Nair, S.S.** 2019, Materials Science and Engineering C, Vol. 102, pp. 437-446.

165. *Applications of choline-based ionic liquids in drug delivery.* **Li, Xiaodan, et al.** 2022 : s.n., International Journal of Pharmaceutics, Vol. 612.

166. *Roles of molecular interaction and mobility on loading capacity and release rate of drug-ionic liquid in long-acting controlled release transdermal patch.* **Yang, Degong, Fang, Liang and Yang, Chunrong.** 2022, Journal of Molecular Liquids, Vol. 352.

167. *Enhancement of transdermal delivery of artemisinin using microemulsion vehicle based on ionic liquid and lidocaine ibuprofen.* **Zhang, Yongqiang, et al.** February, 2020, Colloids and Surfaces B: Biointerfaces, Vol. 189.

168. *Risk-focused investigation on ionic liquids against their applied background in transdermal delivery.* **Zhang, Tenghe, et al.** 2022, Journal of Molecular Liquids, Vol. 353.

169. *Ionic liquid transdermal delivery system: Progress, prospects, and challenges.* **Lu, Beibei, et al.** 2022, Journal of Molecular Liquids, Vol. 351.

170. *Ultrasound-mediated topical delivery of econazole nitrate with potential for treating Raynaud's phenomenon.* **Daftardar, Saloni, et al.** 580, 2020, International Journal of Pharmaceutics, Vol. 30.

171. *Recent advances in mechanical force-assisted transdermal delivery of macromolecular drugs.* **Wang, Ruxuan, et al.** 2021 : s.n., International Journal of Pharmaceutics, Vol. 602.

172. *Acoustic streaming: an in vitro study.* **Clarke, L., Edwards, A and Graham, E.** 4, 2004, Ultrasound Med. Biol., Vol. 30, pp. 559-562.

173. *Ultrasound and transdermal drug delivery.* **Lavon, Ilana and Kost, Joseph.** 15, 2004, Drug Discovery Today, Vol. 9, pp. 670-676.

174. *Mathematical and physical modelling of bubble growth due to ultrasound.* **Meidani, A.R Naji and Hasan, M.** 4, 2004, Applied Mathematical Modelling, Vol. 28, pp. 333-351.

175. *Recent progress in transdermal sonophoresis.* **Ita, Kevin.** 4, 2015, Pharmaceutical Development and Technology, Vol. 22, pp. 458-466.

176. *Quantitative Analysis of Acoustic Pressure for Sonophoresis and Its Effect on Transdermal Penetration.* **Kurashina, Yuta, et al.** 5, 2022, Ultrasound in Medicine and Biology, Vol. 48, pp. 933-944.

177. *Ultrasound-induced deformation of PLGA-microPlates for on-command drug release.* **Sciurti, E, et al.** May, 2020, Microelectronic Engineering, Vol. 229.

178. *Transdermal Delivery of Enfuvirtide in a Porcine Model Using a Low-Frequency, Low-Power Ultrasound Transducer Patch.* **Snook, Kevin A, et al.** 2, 2019, Ultrasound in Medicine and Biology, Vol. 45, pp. 513-525.

179. *Controlled intra- and transdermal protein delivery using a minimally invasive Erbium:YAG fractional laser ablation technology.* **Bachhav, Y.G, A, Heinrich and Kalia, YN.** 2, 2013, Vol. 84, pp. 355-64.

180. *Microsecond thermal ablation of skin for transdermal drug delivery.* **Lee, Jeong Woo, et al.** 1, 2011, Journal of Controlled Release, Vol. 154, pp. 58-68.

181. *Er:YAG fractional laser ablation for cutaneous co-delivery of pentoxifylline and D-α-tocopherol succinate: A new approach for topical treatment of radiation-induced skin fibrosis.* **Gou, S, et al.** May, 2019, European Journal of Pharmaceutical Sciences, Vol. 135, pp. 22-31.

182. *Challenges to laser-assisted drug delivery: Applying theory to clinical practice.* **Ibrahim, Omer, et al.** 1, 2020, Advances in Cosmetic Surgery, Vol. 50, pp. 20-27.

183. *Current trends in polymer microneedle for transdermal drug delivery.* **AL-Japairai, Khater Ahmed Saeed, et al.** 2020, International Journal of Pharmaceutics, Vol. 587.

184. *Development of silicon microneedle arrays with spontaneously generated micro-cavity ring for transdermal drug delivery.* **Das, Alakananda, Singha, Chirantan and Bhattacharyya, Anirban.** s.l. : Microelectronic Engineering, 2019, Vol. 210, pp. 14-18.

185. *Combined use of biocompatible nanoemulsions and solid microneedles to improve transport of a model NSAID across the skin: In vitro and in vivo studies.* **Ilić, Tanja, et al.** s.l. : European Journal of Pharmaceutical Sciences, 2018, Vol. 125, pp. 110-119.

186. *Feasibility study for intraepidermal delivery of proteins using a solid microneedle array.* **Witting, Madeleine, et al.** 1-2, s.l. : International Journal of Pharmaceutics, 2015, Vol. 486, pp. 52-8.

187. *Pullulan-based dissolving microneedle arrays for enhanced transdermal delivery of small and large biomolecules.* **Vora, Lalitkumar K., et al.** s.l. : International Journal of Biological Macromolecules, 2020, Vol. 146, pp. 290-298.

188. *Pullulan microneedle patches for the efficient transdermal administration of insulin envisioning diabetes treatment.* **Fonseca, Daniela F.S., et al.** s.l. : Carbohydrate Polymers, 2020, Vol. 241.

189. *Local dermal delivery of cyclosporin A, a hydrophobic and high molecular weight drug, using dissolving microneedles.* **Jeong, Hye Rin, et al.** s.l. : European Journal of Pharmaceutics and Biopharmaceutics, 2018, Vol. 127, pp. 237-243.

190. *Flexible two-layer dissolving and safing microneedle transdermal of neurotoxin: A biocomfortable attempt to treat Rheumatoid Arthritis.* **Yao, Wendong, et al.** s.l. : International Journal of Pharmaceutics, 2019, Vol. 563, pp. 91-100.

191. *Rapidly dissolving bilayer microneedle arrays – A minimally invasive transdermal drug delivery system for vitamin B12.* **Ramöller, Inken K., et al.** s.l. : International Journal of Pharmaceutics, 2019, Vol. 566, pp. 299-306.

192. *Hollow microneedle-mediated micro-injections of a liposomal HPV E743–63 synthetic long peptide vaccine for efficient induction of cytotoxic and T-helper responses.* **van der Maaden, Koen, et al.** s.l. : Journal of Controlled Release, 2018, Vol. 269, pp. 347-354.

193. *Intradermal Delivery of Synthetic mRNA Using Hollow Microneedles for Efficient and Rapid Production of Exogenous Proteins in Skin.* **Golombek, Sonia, et al.** s.l. : Molecular Therapy - Nucleic Acids, 2018, Vol. 11, pp. 382-392.

194. *Hollow microneedle-mediated intradermal delivery of model vaccine antigen-loaded PLGA nanoparticles elicits protective T cell-mediated immunity to an intracellular bacterium.* **de Groot, AM, et al.** s.l. : Journal of Controlled Release, 2017, Vol. 266, pp. 27-35.

195. *Microneedle-mediated transdermal bacteriophage delivery.* **Ryan, E, et al.** 2, s.l. : European Journal of Pharmaceutical Sciences, 2012, Vol. 47, pp. 297-304.

196. *Development of PLGA nanoparticle loaded dissolving microneedles and comparison with hollow microneedles in intradermal vaccine delivery.* **Mönkäre, Juha, et al.** s.l. : European Journal of Pharmaceutics and Biopharmaceutics, 2018, Vol. 129, pp. 111-121.

197. *Intradermal delivery of vaccine nanoparticles using hollow microneedle array generates enhanced and balanced immune response.* **Niu, Lin, et al.** s.l. : Journal of Controlled Release, 2019, Vol. 294, pp. 268-278.

198. *Hydrogel-forming microneedle arrays as a therapeutic option for transdermal esketamine delivery.* **Courtenay, AJ, et al.** s.l. : Journal of Controlled Release, 2020, Vol. 322, pp. 177-186.

199. *Hydrogel-forming microneedles enhance transdermal delivery of metformin hydrochloride.* **Migdadi, EM, et al.** 2018, Vol. 285, p. 142151.

200. *A self-adherent, bullet-shaped microneedle patch for controlled transdermal delivery of insulin.* **Seong, Keum Yong, Seo, Min-Soo, et al.** s.l. : Journal of Controlled Release, 2017, Vol. 265, pp. 48-56.

201. *Tackling the challenges of developing microneedle-based electrochemcial sensors.* **Abdullah, Hilmee, Phairatana, Tonghathai and Jeerapan, Itthipon.** 11, 2022, Microchimica Acta, Vol. 189.

202. *Microneedle for transdermal diagnostics: Recent advances and new horizons.* **Liu, Gui-Shi, et al.** 2020, Biomaterials, Vol. 232.

203. *Toward Biofunctional Microneedles for Stimulus Responsive Drug Delivery.* **Cahill, Ellen M. and O'Cearbhaill, Eoin D.** 7, 2015, Bioconjugate Chemistry, Vol. 26, pp. 1289-96.

204. *Microneedles-based electrochemical sensors: New tools for advanced biosensing.* **Dardano, P., Rea, I and De Stefano, L.** 2019, Current Opinion in Electrochemistry, Vol. 17, pp. 121-127.

205. *Controlled Drug Delivery Using Microdevices.* **Sharma, T. Sanjay, et al.** 9, 2016, Current Pharmaceutical Biotechnology, Vol. 17, pp. 772-87.

206. *Rapidly Dissolvable Microneedle Patches for Transdermal Delivery of Exenatide.* **Zhu, Z, et al.** 12, 2014, Pharmaceutical Research, Vol. 31, pp. 3348-60.

207. *Novel Surface Modified Polymer Microneedle based Biosensors for Interstitial Fluid Glucose Detection.* **Barrett, C, et al.** 2019, IEEE Sensors.

208. *A novel scalable manufacturing process for the production of hydrogel-forming microneedle arrays.* **Lutton, R.E.M., et al.** 1, 2015, International Journal of Pharmaceutics, Vol. 494, pp. 417-29.

209. *Live Vaccinia Virus-Coated Microneedle Array Patches for Smallpox Vaccination and Stockpiling.* **Choi, In-Jeong, et al.** 2, 2021, Pharmaceutics, Vol. 13.

210. *Transdermal microneedle sensor arrays based on palladium: Polymer composites.* **McConville, Aaron and Davis, James.** 2016, Electrochemistry Communications, Vol. 72, pp. 162-165.

211. *Microneedle array sensors based on carbon nanoparticle composites: interfacial chemistry and electroanalytical properties.* **Hegarty, Catherine, et al.** 2019, Journal of Materials Science, Vol. 54, pp. 10705-10714.

212. **Gileadi, Eliezer and Eliaz, Noam.** *Physical Electrochemistry: Fundamentals, Techniques and Applications.* s.l. : John Wiley & Sons, 2019.

213. **Bagotsky, Vladimir S. and Skundin, A.M.** *Fandamentals of Electrochemistry.* s.l. : John Wiley & Sons, 2005.

214. *Progress in the electrochemical modification of graphene-based materials and their applications.* **Chakrabarti, M.H., et al.** 2013, Electrochimica Acta, Vol. 107, pp. 425-440.

215. *Use of exfoliated graphite filler to enhance polymer physical properties.* **Debelak, Bryan and Lafdi, Khalid.** 9, 2007, Carbon, Vol. 45, pp. 1727-1734.

216. *Electrochemical paper-based analytical devices (ePADs) toward biosensing: recent advances and challenges in bioanalysis.* **Solhi, Elham, Hasanzadeh, Mohammad and Babaie, Parinaz.** 11, 2020, Analytical Methods, Vol. 12.

217. *A Practical Beginner's Guide to Cyclic Voltammetry.* **Elgrishi, N, et al.** 2, 2017, Journal of Chemical Education, Vol. 95, pp. 197-206.

218. **Bard, A.J.** *Electrochemical methods: fundamentals and applications.* s.l. : John Wiley & Sons, 2022.

219. *On the electromotive forces which are aroused by magnwtism in metal plates through which a stream of heat flows.* **Nernst, W.** 1887, Annals of Physics, Vol. 267, pp. 760-789.

220. **Fisher, A.C.** *Electrode dynamics.* s.l. : Oxford: Oxford University Press, 1996. Vol. 1.

221. *Studies in heterogeneous equilibria. Part III. A kinetic theory of reversible oxidation potentials at inert electrodes.* **Butler, J.A.V.** 1924, Transations of the Faraday Society, Vol. 19, pp. 734-739.

222. *Zur theorie der wasserstoff uberspannung.* **Erdey-Gruz, T and Volmer, M.** 1930, Zeitschriff fur physikalische Chemie, Vol. 150, pp. 203-213.

223. *On liquid diffusion.* **Fick, A.V.** 1855, The London, Edinburgh, and Dublin Philosophical Magazine and Journal of Science, Vol. 10, pp. 30-39.

224. **Brett, C.** *Electrochemistry: principles, methods, and applications.* s.l. : Oxford University Press, 1993. Vol. 544.6.

225. *Residual current in galvanic polarization, regarded as a diffusion problem.* **Cottrell, F.G.** 1903, Zeitschrift fur Physikalische Chemie, Vol. 42, pp. 385-431.

226. *Application of the Cottrell equation to chronoamperometry.* **Cottrell, F.G.** 385, 1902, Zeitschrift fur Physikalische Chemie, Vol. 42.

227. *A cathode ray polarograph. Part II. - the current-voltage curves.* **Randles, J.E.** 1948, Transactions of the Faraday Society, Vol. 44, pp. 327-338.

228. *Oscillographic polarography with periodical triangular voltage.* **Sevcik, A.** 1948, Collection of Czechoslovak Chemical Communications, Vol. 13, pp. 349-377.

229. *Activation of Highly Ordered Pyrolytic Graphite for Heterogeneous Electron Transfer: Relationship between Electrochemical Performance and Carbon Microstructure.* **Bowling, Robert J., packard, Richard T and McCreery, Richard L.** 1989, American Chemical Society, Vol. 111.

230. *Enhanced electrochemical performance at screen-printed carbon electrodes by a new pretreating procedure.* **Wei, Hang, et al.** 2, 2007, Analytica Chimica Acta, Vol. 588, pp. 297-303.

231. *Advanced Carbon Electrode Materials for Molecular Electrochemistry.* **McCreery, Richard L.** 7, 2008, Chemical Reviews, Vol. 108.

232. *A novel procedure for fabricating flexible screenprinted electrodes with improved electrochemical performance.* **Du, C X, et al.** 2016, Global Conference on Polymer and Composite Materials, Vol. 137.

233. *Effect of electrochemical anodization and growth time on continuous growth of carbon nanotubes on carbon fiber surface.* **Jiang, Haotian, et al.** 20, 2022, Ceramics International, Vol. 48, pp. 29695-29704.

234. *Laser-Induced Graphene.* **Tour, James and Ye, Ruquan.** 7, 2018, Acc. Chem. Res., Vol. 51.

235. *Advances in chemical sensing technology for enabling the next-generation self-sustainable integrated wearable system in the IoT era.* **Wen, Feng, et al.** May, 2020, Nano Energy, Vol. 78.

236. *Microneedle based electrochemical (Bio)Sensing: Towards decentralized and continuous health status monitoring.* **García-Guzmán, Juan José, et al.** 2021, TrAC - Trends in Analytical Chemistry, Vol. 135.

237. *Simultaneous detection of glucose, uric acid and cholesterol using flexible microneedle electrode array-based biosensor and multi-channel portable electrochemical analyzer.* **Gao, Jie, et al.** November 2018, 2019, Sensors and Actuators, B: Chemical, Vol. 287, pp. 102-110.

238. *Biosensing in dermal interstitial fluid using microneedle based electrochemical devices.* **Madden, J, et al.** May, 2020, Sensing and Bio-Sensing Research, Vol. 29.

239. *Minimally invasive and continuous glucose monitoring sensor based on non-enzymatic porous platinum black-coated gold microneedles.* **Chinnadayyala, SR., et al.** 2021, Electrochimica Acta, Vol. 369.

240. *3D printing as a transformative tool for microneedle systems: Recent advances, manufacturing considerations and market potential.* **Economidou, Sophia N. and Douroumis, Dennis.** 2021, Advanced Drug Delivery Reviews, Vol. 173, pp. 60-69.

241. *Curved microneedle array-based sEMG electrode for robust long-term measurements and high selectivity.* **Kim, Minjae, et al.** 7, 2015, Sensors (Switzerland), Vol. 15, pp. 16265-16280.

242. *Microneedle-based devices for point-of-care infectious disease diagnostics.* **Dixon, Rachael V., et al.** 8, 2021, Acta Pharmaceutica Sinica B, Vol. 11, pp. 2344-2361.

243. *Characterization of Cellulose Acetate Phthalate (CAP).* **Roxin, Pernilla, Karlsson, A and Singh, SK.** 11, 2008, Vol. 24, pp. 1025-41.

244. *Hyaluronic acid embedded cellulose acetate phthlate core/shell nanoparticulate carrier of 5-fluorouracil.* **Garg, Ashish, et al.** 2016, International Journal of Biological Macromolecules, Vol. 87, pp. 449-59.

245. *Influence of processing and curing conditions on beads coated with an aqueous dispersion of cellulose acetate phthalate.* **Williams, Robert O. and Liu, J.** 3, 2000, European Journal of Pharmaceutics and Biopharmaceutics, Vol. 49, pp. 243-52.

246. *Cellulose acetate phthalate as an enteric coating material.* **MALM, C. J., Emerson, J and Hiait, GD.** 10, 1951, Journal of the American Pharmaceutical Association, Vol. 40, pp. 520-525.

247. *Ultrasonic exfoliation of carbon fiber: electroanalytical perspectives.* **Casimero, Charnete, et al.** 3, 2020, Journal of Applied Electrochemistry, Vol. 50, pp. 383-394.

248. *Raman spectroscopy optimizes graphene characterization.* **Wall, Mark.** 4, 2012, Advanced Materials and Processes, Vol. 170.

249. *Design of composite microneedle sensor systems for the measurement of transdermal pH.* **Hegarty, Catherine, et al.** August 2018, 2019, Materials Chemistry and Physics, Vol. 227, pp. 340-346.

250. *Enhanced out of plane electrical conductivity in polymer composites induced by CO2 laser irradiation of carbon fibers.* **Karakassides, A, et al.** 10, 2020, Applied Sciences (Switzerland), Vol. 10.

251. *Preparation of Ultra Thin Polystyrene, Polypropylene and Polyethylene Films on Si Substrate Using Spin Coating Technology.* **Lock, Evgeniya, Walton, Scott and Fernsler, Richard.** s.l. : Nrl, 2008, Vol. January.

252. *Atmospheric Pressure Plasma Treated Carbon Fibre Weave: A Flexible Approach to Wound Monitoring.* **Phair, J, et al.** August, 2013, Electrochemistry Communications, Vol. 33, pp. 99-101.

253. *Laser-anodised carbon fibre: Coupled activation and patterning of sensor substrates.* **Ezekiel, HB, et al.** 11, 2008, Journal of Physics and Chemistry of Solids, Vol. 69, pp. 2932-2935.

254. *Microneedle-based delivery: An overview of current applications and trends.* **Guillot, AJ, et al.** 6, 2020, Pharmaceutics, Vol. 12, pp. 1-28.

255. *Electric Field in Atomically Thin Carbon Films.* **Novoselov, K.S, et al.** 5696, 2004, Science, Vol. 306, pp. 666-669.

256. *Chemical Methods for the Production of Graphenes.* **Park, S and Ruoff, RS.** 2009, Nature Nanotechnology, Vol. 4, pp. 217-224.

257. *Honeycomb Carbon: A Review of Graphene.* **Allen, M.J, Tung, VC and Kaner, RB.** 1, 2010, Chemical Reviews, Vol. 110, pp. 132-145.

258. *A Chemical Route to Carbon Nanoscrolls.* **Viculis, L.M, Mack, JJ and Kaner, RB.** 2003, Science, Vol. 299.

259. *Large Area, Few-Layer Graphene Films on Arbitrary Substrates by Chemical Vapor Deposition.* **Reina, A, et al.** 1, 2009, Nano Letters, Vol. 9, pp. 30-35.

260. *Graphene in 3-Dimensions: Towards Graphite origami.* **Ebbesen, T.W and Hiura, H.** 1995, Advanced Materials, Vol. 7, pp. 582-586.

261. *Tailoring Graphite with the Goal of Achieving Single Sheets.* **Lu, X, et al.** 1999, Nanotechnology, Vol. 10, pp. 269-272.

262. *Graphene Shape Control by Multistage Cutting and Transfer.* **Ci, L, et al.** 44, 2009, Advanced Materials, Vol. 21, pp. 4487-4491.

263. *Sythesis and Fabrication of Graphene and Graphene Oxide: A Review.* **Adetayo, Adeniji and Runsewe, Damilola.** 2019, Journal of Composite Materials, Vol. 9.

264. **Das, S.** Sythesis and Characterisation of Graphene. *Carbon Nanomaterials for Advanced Energy Systems.* Hoboken, NJ : John Wiley & Sons Inc., 2015.

265. *Verfahren zur Darstellung der Graphitsaure.* **Staudenmaier, L.** 2, 1898, Deutschen Chemischen Gesellschaft, Vol. 31, pp. 1481-1487.

266. *Preparation of Graphitic oxide.* **Hummers, W.S and Offeman, RE.** 1958, Journal of the American Chemical Society, Vol. 80.

267. **Rao, C.N.R.** Graphene: Sythesis, Properties, and Phenomena. Weinheim, Germany : John Wiley & Sons, Inc, 2013.

268. *Catalyst-Free Efficient Growth, Orientiation and Biosensing Properties of Multilayer Graphene Nanoflake Films with Sharp Edge Planes.* **Shang, N.G, et al.** 2008, Advanced Functional Materials, Vol. 18.

269. *Laser-induced porous graphene films from commercial polymers.* **Lin, J, et al.** 2014, Nature communications, Vol. 5.

270. *Graphene-based biosensors.* **Szunerits, Sabine and Boukherroub, Rabah.** 3, 2018, Interface Focus, Vol. 8.

271. *Facile fabrication of flexible all solid-state micro-supercapacitor by direct laser writing of porous carbon in polyimide.* **In, JB, et al.** 83, 2015, Carbon, pp. 144-151.

272. *Aromatic polyimides as carbon precursors.* **Inagaki, Michio, Ohta, Maoto and Hishiyama, Yoshihiro.** 2013, Carbon, Vol. 61, pp. 1-21.

273. *Laser-induced graphene fibers.* **Duy, LX, et al.** 2018, Carbon, Vol. 126, pp. 472-479.

274. *Laser fabrication of graphene-based electronic skin.* **Liu, YQ, et al.** 2019, Frontiers in Chemistry, Vol. 7.

275. *Advanced Carbon for Flexible and Wearable Electronics Chunya.* **Wang, C, et al.** 2018, Advanced Drug Delivery Reviews, Vol. 132.

276. *Laser-Induced Graphene: From Discovery to Translation.* **Ye, R, James, DK and Tour, JM.** 1, 2019, Advanced Materials, Vol. 31.

277. *Graphene-Based Fibers: Recent Advances in Preparation and Application.* **Xu, Tong and Zhang, Zhipan, Qu, Liangti.** 5, 2019, Advanced Materials, Vol. 32.

278. *Conductive hybrid filaments of carbon nanotubes, chitin nanocrystals and cellulose nanofibers formed by interfacial nanoparticle complexation.* **Zhang, K, et al.** 2020, Materials and Design, Vol. 191.

279. *Enhanced thermal stability, toughness, and electrical conductivity of carbon nanotube-reinforced biodegradable poly(lactic acid)/poly(ethylene oxide) blend-based nanocomposites.* **Behera, K, et al.** 2020, Polymer, Vol. 186.

280. *Laser-Induced Graphene by Multiple Lasing: Toward Electronics on Cloth, Paper, and Food.* **Chyan, Y., et al.** 3, 2018, ACS Nano, Vol. 12, pp. 2176-2183.

281. *Unraveling the dependency on multiple passes in laser-induced graphene electrode for supercapacitor and H2O2 sensing.* **Kaur, S, et al.** 2021, Materials Science for Energy Technologies, Vol. 4, pp. 407-412.

282. *SWCNT-bridged laser-induced graphene fibers decorated with MnO2 nanoparticles for high-performance flexible micro-supercapacitors.* **Yuan, Min.** 2021, Carbon, Vol. 183.

283. *Hypertension in Children: Role of Obesity, Simple Carbohydrates, and Uric Acid.* **Orlando, A, et al.** 129, 2018, Frontiers in Public Health, Vol. 6.

284. *Time to target uric acid to retard CKD progression.* **Kumagai, T, et al.** 2, 2016, Clinical and Experimental Nephrology 2016 21:2, Vol. 21, pp. 182-192.

285. *Sex-specific relationship between serum uric acid and risk of stroke: A dose-response meta-analysis of prospective studies.* **Zhong, C, et al.** 4, 2017, Journal of the American Heart Association, Vol. 6.

286. *Uric acid and cardiovascular risk: What genes can say.* **Kei, A, et al.** 1, 2018, International Journal of Clinical Practice, Vol. 72.

287. *Carbon nanoparticles with tosyl functional group for distinguishing voltammetric peaks of ascorbic acid and uric acid.* **Amiri, Mandana, Imanzadeh, Hamidah and Banaei, Alireza.** 2015, Materials Science and Engineering C, Vol. 47, pp. 189-95.

288. *Electrochemical response of ascorbic and uric acids at organoclay film modified glassy carbon electrodes and sensing applications.* **Mbouguen, JC, et al.** 1, 2011, Talanta, Vol. 85, pp. 754-62.

289. *Unsafe sharps disposal among insulin-Using patients with diabetes mellitus: An emerging global crisis.* **Thompson, B. M. and Cook, CB.** 2022, J. Diabetes Sci. technol, Vol. 16, pp. 1376-1380.

290. **Gold, K.** Analysis: the impact of needle, syringe, and lancet disposal on the community the potential impact of pharmaceuticals and personal. *www.safeneedledisposal.org.* [Online] 2011. [Cited: 28 Feb 2023.]

291. **Diabetes UK.** the importance of diabetes care and prevention in rebuilding and transforming the health system in Northern Ireland. *Diabetes Is Serious.* [Online] 2022. https://diabetes-resources-production.s3.eu-west-1.amazonaws.com/resources-s3/public/2022-

04/Diabetes%20is%20Serious%20Report%20Digital_0.pdf?VersionId=lLpcXWRXhAli4Y3D_y7B.

292. —. Diabetes UK. Northern Ireland. *Diabetes UK In Your Area.* [Online] 2023. https://www.diabetes.org.uk/in_your_area/n_ireland.

293. **Hoskins, Mike.** Healthline. *When People Without Diabetes "Play" with Glucose Monitoring.* [Online] 2019. https://www.healthline.com/diabetesmine/non-diabetes-using-continuous-glucose-monitor.

294. **Diabetes.co.uk.** Diabetes.co.uk. *How often do I need to test my blood glucose?* [Online] 2019. https://www.diabetes.co.uk/diabetes_care/how-often-should-i-blood-test.html.

295. *Microneedle Manufacture: Assessing Hazards and Control Measures.* **Martin, A, et al.** 4, 2017, Safety, Vol. 3.

296. *A pilot study in humans of microneedle sensor arrays for continuous glucose monitoring.* **Sharma, S, et al.** 18, 2018, Analytical Methods.

297. *MEMS devices for drug delivery.* **Lee, Hyunjoo J., et al.** 2018, Advanced Drug Delivery Reviews, Vol. 128, pp. 132-147.

298. *Organic electrochromic timer for enzymatic skin patches.* **Kai, Hiroyuki, et al.** 2019, Biosensors and Bioelectronics, Vol. 123, pp. 108-113.

299. *Knowledge growth and development: internet of things (IoT) research, 2006-2018.* **Dachyar, M, Zagloel, TYM and Saragih, LR.** 8, 2019, Heliyon, Vol. 5.

300. *Drug delivery systems for programmed and on-demand release.* **Davoodi, Pooya, et al.** 2018, Advanced Drug Delivery Reviews, Vol. 132, pp. 104-138.

301. *An interpenetrating and patternable conducting polymer hydrogel for electrically stimulated release of glutamate.* **Bansal, Mahima, et al.** 2021, Acta Biomaterialia, pp. 124-135.

302. —.**Uppalapati, Dedeepya.** 1-2, 2018, International Journal of Pharmaceutics, Vol. 543.

303. *Electrochemically triggered releas of drugs.* **Szunerits, Sabine, Teodorescu, Florina and Boukherroub, Rabah.** 2019, European Polymer Journal, Vol. 83, pp. 467-477.

304. *Electrochemically controlled drug-mimicking protein release from iron-alginate thin-films associated with an electrode.* **Jin, Z, et al.** 1, 2012, ACS Applied Materials and Interfaces, Vol. 4, pp. 466-75.

305. *Smart vaccine delivery based on microneedle arrays decorated with ultra-pH-responsive copolymers for cancer immunotherapy.* **Duong, HTT, et al.** 2018, Biomaterials, Vol. 185, pp. 13-24.

306. *Two-step immobilization of metronidazole prodrug on TEMPO cellulose nanofibrils through thiol-yne click chemistry for in situ controlled release.* **Durand, H, et al.** March, 2021, Carbohydrate Polymers, Vol. 262.

307. *Exploring the antioxidant features of polyphenols by spectroscopic and electrochemical methods.* **Alcalde, Berta, Grandos, Merce and Saurina, Javier.** 11, 2019, Antioxidants, Vol. 8.

308. *Development and validation of a voltammetric method for determination of total phenolic acids in cotton cultivars.* **Magarelli, G, et al.** 2013, Microchemical Journal, Vol. 109, pp. 23-28.

309. *Rapid determination of salicylic acid at screen printed electrodes.* **Rawlinson, Sean, et al.** 2018, Microchemical Journal, Vol. 137, pp. 71-77.

310. *Electrochemically Controlled Dissolution of Nanocarbon-Cellulose Acetate Phthalate Microneedle Arrays.* **Anderson, Ashleigh, et al.** 39, 2019, ACS Applied Materials and Interfaces, Vol. 11, pp. 35540-35547.

311. *In situ electrochemical and surface plasmon resonance (SPR) studies of aniline-carboxylated aniline copolymers.* **Wang, Yanju and Wolfgang, Knoll.** 1-2, 2006, Analytica Chimica Acta, Vol. 558, pp. 150-157.